



UNIVERSIDADE FEDERAL  
DO RIO DE JANEIRO



FEDERAL UNIVERSITY OF RIO DE JANEIRO  
PHYSICS INSTITUTE, SOLID PHYSICS DEPARTMENT

UNIVERSITY OF ANTWERP  
FACULTY OF SCIENCE, CONDENSED MATTER THEORY GROUP

**The first order equations for the  
Ginzburg-Landau theory and the vortex states  
near a permalloy disk**

Thesis submitted for the degree of Doctor of Science (Physics) at the Federal  
University of Rio de Janeiro, and the degree of Doctor of Science: Physics, at the  
University of Antwerp, in a joint PhD agreement, to be defended by

**Rodolpho RIBEIRO GOMES**

**Advisor:** Mauro M. Doria (UFRJ)

**Co-advisor:** Milorad V. Milošević (UAntwerp)

Rio de Janeiro, March 2018

The first order equations for the  
Ginzburg-Landau theory and the vortex states  
near a permalloy disk

---

De eerste orde-vergelijkingen voor de  
Ginzburg-Landau-theorie en de vortex-toestanden  
bij een permalloy-schijf

Rodolpho Ribeiro Gomes

# Abstract

## The first order equations for the Ginzburg-Landau theory and the vortex states near a permalloy disk

Rodolpho Ribeiro Gomes

Advisor: Mauro M. Doria

Co-advisor: Milorad V. Milošević

*Abstract* of the PhD thesis submitted to the Graduate Program in Physics of the Institute of Physics of the Federal University of Rio de Janeiro - UFRJ, as part of the requirements to the obtention of the title of Doctor in Sciences (Physics) at the Institute of Physics of the Federal University of Rio de Janeiro, and the title of Doctor in de Wetenschappen: Fysica, at the Faculty of Science of the University of Antwerp - UAntwerp, in a joint PhD agreement.

The vortex states in superconductors are studied by means of the phenomenological Ginzburg-Landau theory. In the first part of the thesis vortex states are considered in a very long superconducting cylinder with and without the presence of an applied field with special attention paid to the effect of the boundary to an external insulating region. In the second part of the thesis an infinitely long and thin superconducting film is in the presence of an inhomogeneous magnetic field and of an applied current that leads to the nucleation of vortex-antivortex pairs.

The first part is based on A. A. Abrikosov's treatment of the Ginzburg-Landau theory, which consists in using the so-called first order equations to obtain approximate solutions of the Ginzburg-Landau equations. The first order equations solve exactly

Ampère's law and also an integrated version of the non-linear Ginzburg-Landau equation. It stems from this approach that without the presence of the applied field no vortex states are possible in an infinitely long superconductor, but the presence of an external boundary changes this picture. Then vortex states become possible and their energy can be lower than that of the normal state, although they are never stable, which means that their lowest energetic configuration is in the boundary. We also show in this thesis that A. A. Abrikosov's classification of superconductors in type-I and type-II only applies to an infinitely long superconductor with no external boundary. In case of the presence of an external boundary this classification no longer applies and has to be reviewed. We show here that the boundary introduces a negative surface energy able to sustain vortex states above the upper critical field for superconductors with a type-I profile, namely, a  $\kappa$  parameter below the critical one in A. A. Abrikosov's traditional classification.

The second part concerns the understanding of some properties of the phase of the order parameter, which is probed by a lattice of permalloy disks sitting slightly above an infinitely long superconducting film. We formulate the Ginzburg-Landau theory on a lattice through the link variables and conduct a time-dependent process to relax to the equilibrium configuration. The magnetization is azimuthal in the permalloy disk except near to the center where there is an out-of-plane component that gives rise to a spike of non-zero magnetic field. Interestingly we find that below each permalloy disk the phase of the order parameter displays an unusual behavior, it forms several concentric circles of phase discontinuities. In order to get a better insight into the permalloy problem, we analyze the interaction of the superconducting film with other similar magnetic systems, equally located near the superconducting film, namely, a polygon of magnetic dipoles and a magnetic annulus. The polygon of magnetic dipoles mimics in an oversimplified way the magnetic moments that constitute the permalloy disk away from its core. The magnetic dipoles are positioned in a ring

in an in-plane azimuthal arrangement. The magnetic annulus is a perforated disk, namely a permalloy disk removed from its core, with all the constitutive magnetic moments in an azimuthal configuration. Thus, the magnetic annulus corresponds to a permalloy disk without the out-of-plane magnetization core. We obtain the order parameter in the presence of these three magnetic states (polygon, annulus and permalloy) and find phase discontinuity rings and the unbinding of vortex-antivortex pairs in the presence of an applied external current.

**Keywords:** superconductivity, Ginzburg-Landau theory, vortex states, superconductor-ferromagnet heterostructures.

# Resumo

## As equações de primeira ordem para a teoria de Ginzburg-Landau e os estados de vórtices próximos a um disco de permalloy

Rodolpho Ribeiro Gomes

Orientador: Mauro M. Doria

Coorientador: Milorad V. Milošević

Resumo da Tese de Doutorado apresentada ao Programa de Pós-Graduação em Física do Instituto de Física da Universidade Federal do Rio de Janeiro - UFRJ, como parte dos requisitos para a obtenção do título de Doutor em Ciências (Física) no Instituto de Física da Universidade Federal do Rio de Janeiro, e o título de Doctor in de Wetenschappen: Fysica, na Faculty of Science da University of Antwerp - UAntwerp, em um acordo de doutorado em co-tutela.

Os estados de vórtices em supercondutores são estudados por meio da teoria fenomenológica de Ginzburg-Landau. Na primeira parte da tese estados de vórtices são considerados em um cilindro supercondutor, muito longo, com e sem a presença de um campo aplicado e com especial atenção para o efeito da interface com uma região externa isolante. Na segunda parte da tese um filme fino supercondutor infinito está na presença de um campo magnético não-homogêneo e de uma corrente aplicada, o que leva a nucleação de pares de vórtice-antivórtice.

A primeira parte é baseada no tratamento de A. A. Abrikosov para a teoria de Ginzburg-Landau, que consiste em usar as chamadas equações de primeira ordem para obter soluções aproximadas das equações de Ginzburg-Landau. As equações

de primeira ordem resolvem exatamente a lei de Ampère e também uma versão integrada da equação de Ginzburg-Landau não-linear. Obtém-se desta abordagem a não existência de vórtices sem a presença de um campo aplicado em um supercondutor infinitamente longo, porém a presença de uma borda externa altera este quadro. Neste caso, estados de vórtices se tornam possíveis e eles podem apresentar menor energia do que o estado normal, embora eles nunca sejam estáveis, o que significa que na configuração de menor energia eles estão na borda. Nós também mostramos nesta tese que a classificação de A. A. Abrikosov dos supercondutores em tipo-I e tipo-II se aplica somente a um supercondutor infinito sem borda externa. No caso da presença de uma borda externa, esta classificação não mais se aplica. Nós mostramos aqui que a borda introduz uma energia de superfície negativa capaz de manter estados de vórtices acima do campo crítico superior para supercondutores na categoria tipo-I, isto é, aqueles com o parâmetro  $\kappa$  abaixo do valor crítico definido pela classificação tradicional de A. A. Abrikosov.

A segunda parte da tese diz respeito a compreensão de algumas propriedades da fase do parâmetro de ordem, que é examinada por uma rede de discos de permalloy posicionados ligeiramente acima de um filme fino supercondutor infinito. Nós expressamos a teoria de Ginzburg-Landau em um reticulado através das variáveis de ligação e conduzimos um processo de relaxação, dependente do tempo, para a configuração de equilíbrio. A magnetização no disco de permalloy é azimutal com exceção das proximidades do centro, onde há uma componente perpendicular que dá origem a um pico de campo magnético não-nulo. Interessantemente encontramos que abaixo de cada disco de permalloy a fase do parâmetro de ordem mostra um comportamento não usual, ela forma diversos círculos concêntricos de descontinuidade de fase. Para obter um melhor entendimento no problema do permalloy, nós analisamos a interação do filme supercondutor com outros sistemas magnéticos similares, igualmente localizados próximo ao filme supercondutor, especificamente, um polígono de dipolos

magnéticos e um annulus magnético. Os dipolos magnéticos do polígono estão posicionados nos vértices de um polígono inscrito em um círculo, com componente paralela ao plano em um arranjo azimutal de forma a imitar de forma simplificada os momentos magnéticos que constituem o disco de permalloy fora do núcleo. O annulus magnético é um disco perfurado, isto é, um disco de permalloy do qual foi removido o núcleo, com todos os momentos magnéticos que o constituem em uma configuração azimutal. Portanto, o annulus magnético corresponde a um disco de permalloy sem a magnetização perpendicular do núcleo. Nós obtemos o parâmetro de ordem na presença destes três estados magnéticos (polígono, annulus e permalloy), e encontramos anéis de discontinuidade de fase assim como a separação de pares de vórtice-antivórtice na presença de uma corrente externa aplicada.

**Palavras-chave:** supercondutividade, teoria de Ginzburg-Landau, estados de vórtices, heteroestruturas supercondutor-ferromagneto.

# Abstract

## De eerste orde-vergelijkingen voor de Ginzburg-Landau-theorie en de vortex-toestanden bij een permalloy-schijf

De vortextoestanden in supergeleiders worden bestudeerd met behulp van de fenomenologische Ginzburg-Landau-theorie. In het eerste deel van het proefschrift worden beschouwd als een zeer lange supergeleidende cilinder met en zonder de aanwezigheid van een toegepast veld met speciale aandacht voor het effect van de grens op een extern isolerend gebied. In het tweede deel van het proefschrift bevindt zich een oneindig lange en dunne supergeleidende film in de aanwezigheid van een inhomogeen magnetisch veld en van een aangelegde stroom die leidt tot de nucleatie van vortex-antivortexparen.

Het eerste deel is gebaseerd op A. A. Abrikosov's behandeling van de Ginzburg-Landau theorie, die bestaat uit het gebruik van de zogenaamde eerste orde-vergelijkingen om benaderende oplossingen van de Ginzburg-Landau-vergelijkingen te verkrijgen. De eerste orde vergelijkingen lossen exact de wet van Ampère op en ook een geïntegreerde versie van de niet-lineaire Ginzburg-Landau-vergelijking. Het komt voort uit deze benadering dat zonder de aanwezigheid van het toegepaste veld geen vortextoestanden mogelijk zijn in een oneindig lange supergeleider, maar de aanwezigheid van een externe grens dit beeld verandert. Dan worden vortextoestanden mogelijk en hun energie kan lager zijn dan die van de normale toestand, hoewel ze nooit stabiel zijn, wat betekent dat hun laagste energetische configuratie zich in de grens bevindt. We

laten in dit proefschrift ook zien dat A. A. Abrikosov's classificatie van supergeleiders in type I en type II alleen van toepassing is op een oneindig lange supergeleider zonder externe grens. In het geval van de aanwezigheid van een externe grens is deze classificatie niet langer van toepassing en moet worden herzien. We laten hier zien dat de grens een negatieve oppervlakte-energie introduceert die in staat is vortex-toestanden boven het bovenste kritische veld te onderhouden voor supergeleiders met een type-I-profiel, namelijk een  $\kappa$ -parameter onder de kritische in A. A. Abrikosov's traditionele classificatie.

Het tweede deel betreft het begrip van enkele eigenschappen van de fase van de ordeparameter, die wordt gesondeerd door een rooster van permalloy-schijven die enigszins boven een oneindig lange supergeleidende film zitten. We formuleren de Ginzburg-Landau theorie op een rooster door de linkvariabelen en voeren een tijdsafhankelijk proces uit om te relaxeren naar de evenwichtsconfiguratie. De magnetisatie is azimuth in de permalloy-schijf behalve nabij het centrum waar een uit het vlak gelegen component is die aanleiding geeft tot een piek van niet-nul magnetisch veld. Interessant is dat we zien dat onder elke permalloy-schijf de fase van de orderparameter een ongebruikelijk gedrag vertoont, en dat deze verschillende concentrische cirkels van faseafdelingen vormt. Om een beter inzicht te krijgen in het permalloy-probleem, analyseren we de interactie van de supergeleidende film met andere soortgelijke magnetische systemen, die zich gelijkelijk in de buurt van de supergeleidende film bevinden, namelijk een polygoon van magnetische dipolen en een magnetische ring. De polygoon van magnetische dipolen bootsen een simplistische manier de magnetische momenten na die de permalloy schijf vormen weg van zijn kern. De magnetische dipolen zijn gepositioneerd in een ring in een azimuth-opstelling in het vlak. De magnetische ring is een geperforeerde schijf, namelijk een permalloy schijf verwijderd uit zijn kern, met alle constitutieve magnetische momenten in een azimuth configuratie. Aldus komt de magnetische ring overeen met een permalloy-schijf

zonder de uit het vlak gelegen magnetisatiekern. We verkrijgen de ordeparameter in de aanwezigheid van deze drie magnetische toestanden (polygoon, ring en permalloy) en vinden fasediscontinuïteitringen en de onverbindend van vortex-antivortexparen in de aanwezigheid van een toegepaste externe stroom.

**Sleutelwoorden:** supergeleiding, Ginzburg-Landau theorie, vortex-toestanden, supergeleider-ferromagneet-heterostructuren.

# Acknowledgments

I am very grateful for the opportunity to have Prof. Dr. Mauro M. Doria as my supervisor. I thank him for his infinite patience, great enthusiasm and encouragement to face the challenges along the PhD period.

I thank Prof. Dr. Milorad V. Milošević to supervise my work during the PhD sandwich period, for the opportunity to be in contact with exciting problems and sharing his insights into these problems.

I thank the friends and office mates both at the Instituto de Física da Universidade Federal do Rio de Janeiro, Brazil (Charlie, Jilder, Luiz and Rodrigo), and at the University of Antwerp, Belgium (Davi, Diego Lucena, Diego Rabelo, Hossein, Jorge Luiz, Jorge Luiz “Capuã”, Jeroen Mulkers, Jesus, Lingfeng, Rebeca, Victor, Željko) for all the help received and the shared good moments.

I am grateful for all the help received from the personnel of the graduate offices at both Universidade Federal do Rio de Janeiro (Carlos José, Cassius, Patrícia, Pedro) and University of Antwerp Physics Department (Hilde, Nikolas, Véronique).

I thank my parents, Edna and Edilson, for the continuous effort to give me the best basic education possible that they could provide.

I thank my brothers Thyago and Ralphy, and my sisters Raphaella and Rachel for the support and motivation when I needed.

I deeply thank my ever friend Suelen for the support received when she was at my side, and also when she was not physically with me. I would like to express my strong feeling of gratitude to her permanent availability to give suggestions regarding a decision or any future course of action.

Finally, I thank the agency CNPq (from 07/2015 to 06/2016) and the CMT

group, headed by Prof. Dr. François Peeters, at University of Antwerp (from 08/2016 to 12/2016) for the financial support, the latter received during my PhD sandwich period in Belgium.

# Contents

<b>Contents</b>	<b>xv</b>
<b>List of figures</b>	<b>xix</b>
<b>1 Introduction</b>	<b>1</b>
1.1 Goals and objectives . . . . .	1
1.2 Thermodynamics of superconductors and the order of the phase transition . . . . .	10
1.3 The London theory of superconductivity and the diamagnetic and paramagnetic currents . . . . .	11
1.3.1 Condensation energy and the second order transition . . . . .	17
1.4 The Ginzburg-Landau theory and the first order equations . . . . .	19
1.4.1 Interaction between vortices and current . . . . .	21
<b>2 Excited vortex states (EVS) in mesoscopic superconductors</b>	<b>23</b>
2.1 Introduction . . . . .	23
2.2 The Gibbs free energy of a long superconductor and the variational second order equations . . . . .	28
2.3 Dual view of the kinetic energy and the first order equations . . . . .	30
2.3.1 The boundary conditions, the magnetization and the Gibbs free energy . . . . .	33
2.4 The dimensionless units . . . . .	36
2.5 The vortex excited state and conformal mapping . . . . .	38

2.6	Long cylinder with a circular cross section . . . . .	41
2.6.1	Vorticity $L$ at the center . . . . .	42
2.6.2	Vorticity $L = 1$ at any position . . . . .	46
2.7	Conclusion . . . . .	53
<b>3</b>	<b>Vortex states in type <math>I</math> mesoscopic superconductors</b>	<b>55</b>
3.1	Introduction . . . . .	55
3.2	Ginzburg-Landau for type $I$ superconductors . . . . .	60
3.3	The Bogomol'nyi equations and the first order equations . . . . .	68
3.4	The existence of vortex states above the field $H_{c2}$ . . . . .	71
3.4.1	The existence of vortex states slightly above the field $H_{c2}$ . . . . .	74
3.5	Vortex solutions . . . . .	75
3.5.1	Vortices at the center . . . . .	75
3.5.2	Magnetic flux piercing the superconducting cylinder . . . . .	78
3.5.3	Results . . . . .	80
3.5.4	Single vortex slightly displaced from the center . . . . .	84
3.6	Conclusion . . . . .	89
<b>4</b>	<b>Numerical methods</b>	<b>90</b>
4.1	Time-dependent Ginzburg-Landau equations . . . . .	91
4.1.1	Link variables method $U - \psi$ . . . . .	94
4.1.2	Boundary conditions . . . . .	97
4.1.3	Ginzburg-Landau equation for the order parameter . . . . .	99
4.1.4	Physical and numerical characteristics of the superconducting film . . . . .	102
4.2	Micromagnetic simulations . . . . .	103
4.2.1	Magnetic simulation cell . . . . .	105
4.2.2	Contributions to the magnetic energy . . . . .	107
4.2.3	Micromagnetic simulations on GPU: MuMax3 . . . . .	112

4.2.4	Physical and numerical characteristics of a permalloy disk . . .	113
4.2.5	Landau-Lifshitz-Gilbert equation . . . . .	115
<b>5</b>	<b>Rings of phase discontinuity</b>	<b>119</b>
5.1	Introduction . . . . .	119
5.2	The Permalloy disk . . . . .	122
5.2.1	Physical parameters . . . . .	126
5.2.2	Vector potential of a permalloy disk . . . . .	127
5.2.3	Superconducting density and phase . . . . .	130
5.3	Magnetic annulus . . . . .	131
5.3.1	Vector Potential of a magnetic cell . . . . .	132
5.3.2	Superconducting density and phase . . . . .	134
5.4	Polygons of magnetic dipoles . . . . .	135
5.4.1	Vector Potential of a polygon of magnetic dipoles . . . . .	137
5.4.2	Square - 4 magnetic dipoles . . . . .	138
5.4.3	Octagon - 8 magnetic dipoles . . . . .	144
5.4.4	Hexadecagon - 16 magnetic dipoles . . . . .	151
5.5	Conclusion . . . . .	156
<b>6</b>	<b>Nucleation of vortex-antivortex pairs near to an array of defects</b>	<b>159</b>
6.1	Introduction . . . . .	159
6.2	Encrusted disks with local suppression of the order parameter . . . .	163
6.3	Annulus and the superconducting film . . . . .	169
6.4	Permalloy disk and the superconducting film . . . . .	177
6.5	Conclusion . . . . .	181
<b>7</b>	<b>Summary</b>	<b>183</b>
	<b>Bibliography</b>	<b>188</b>
<b>A</b>	<b>The kinetic energy decomposition</b>	<b>208</b>

**B Calculation of the integrals**

# List of Figures

- 1.1 The magnetization  $-4\pi M$  versus the applied field  $H$  is shown here for both type  $I$  and type  $II$  superconductors. The Meissner phase is characterized by a vanishing magnetic induction,  $B = 0$ . The common wisdom is that the former only has one critical field,  $H_c$ , whereas the latter has two  $H_{c1}$  and  $H_{c2}$ . At the field where superconducting and normal state coexist the Gibbs free energy of both phases are equal. 4
- 1.2 The coexistence line between normal and superconducting states are shown in a  $H$  versus (T) diagram for both type  $I$  and type  $II$  superconductors. . . . . 5
- 1.3 The Cooper pair density  $|\psi|^2$  is shown here near to the critical fields  $H_{c2}$  and  $H_c$  for both type  $I$  and  $II$  superconductors. The type  $I$  displays a hysterical behavior meaning that by lowering the field one can go below  $H_c$  and remain in the normal state until  $H_{c2}$  is reached where the density abruptly jumps to a finite value. Increasing the field will keep the superconducting density beyond  $H_{c2}$  until  $H_c$  is reached. The type  $II$  is a smooth transition with no hysteresis whatsoever. . 6

1.4 The phase of the order parameter associated to a vortex ( $a$ ), a antivortex ( $a', b$ ) and a pair vortex-antivortex ( $c$ ) are shown here. The phase is identical to the angle defined from the semi-axis starting at the vortex origin ( $a$ ). For the antivortex the phase is equal to minus the angle ( $a'$ ). In both cases a hue from blue to red is associated to the angle. For the pair vortex-antivortex the line of discontinuity blue-red is reduced to the segment uniting the two cores ( $c$ ). The creation of a pair vortex-antivortex in a given point of a circle and its subsequent annihilation in the point diametrically opposed leaves a ring of discontinuity blue to red. The scale shown in the colorbar is normalized by  $2\pi$  . . . . . 8

1.5 The process of creation of a vortex at the surface of a superconductor is depicted here in three steps. In the first the superconductor only has shielding currents aiming to blockade the applied field inside the superconductor. In the second step the vortex still remains its currents attached to the surface, which clearly shows that the currents encircling its core are paramagnetic thus contrary to the diamagnetic Meissner current. The last step shows the vortex detached from the surface clearly showing the opposition of currents. . . . . 14

2.1 The superconducting density as a function of the relative distance to the cylinder's center for vorticity ranging from  $L = 0$  to  $L = 4$  in case of a vortex fixed at the center ( $\kappa = 2.1$ ). . . . . 44

2.2 The local magnetic field as a function of the relative distance to the cylinder's center for vorticity ranging from  $L = 0$  to  $L = 4$  in case of a vortex fixed at the center ( $\kappa = 2.1$ ). To recover the Niobium values at the temperature of  $T = 7.7 K$  the vertical axis must be multiplied by  $H_{c2}(T = 7.7 K) = 780 \text{ Oe}$  . . . . . 45

- 2.3 The Gibbs free energy difference between the superconducting and the normal states as a function of the cylinder's radius for vorticity ranging from  $L = 0$  to  $L = 4$  in case of a vortex fixed at the center ( $\kappa = 2.1$ ). The excited vortex state only exists in the negative range of this difference. . . . . 46
- 2.4 The Gibbs free energy difference between the superconducting and the normal states as a function of the vortex's position inside the cylinder for the case of vorticity one. Two radius of cylinders are considered ( $\kappa = 2.1$ ). The excited vortex state only exists in the negative range of this difference. . . . . 49
- 2.5 The magnetic field at the center of the vortex as a function of the position of the vortex inside the cylinder ( $\kappa = 2.1$ ). To recover the value for Niobium at the temperature of  $T = 7.7 K$  the vertical axis must be multiplied by  $H_{c2}(T = 7.7 K) = 780 Oe$ . . . . . 50
- 2.6 The magnetization as a function of the position of the vortex inside the cylinder ( $\kappa = 2.1$ ). To recover the value for Niobium for the temperature of  $T = 7.7 K$  the vertical axis must be multiplied by  $H_{c2}(T = 7.7 K)/8\pi\kappa^2 = 7.0 Oe$ . . . . . 51

2.7 The superconducting density, the local magnetic field, the electric current density and the order parameter phase are depicted at three different positions of the vortex inside the cylinder,  $a_0/R = 0.1$  ((a) to (d)), 0.5 ((e) to (h)), and 0.9 ((i) to (l)). Figures (a), (e) and (i) display the density in (color on line) scheme ranging from low density (cyan) to high density (magenta). The (color on line) scheme is distinct for each of these three figures, as the density varies from zero at the center of the vortex to  $c_0^2$  at the boundary, whose value varies according to the position of the vortex inside the cylinder (see Eqs.(2.66), (2.46), (2.73) and (2.74)). The local magnetic field is shown in figures (b), (f) and (j), and the color scheme is distinct for each of these three figures. It ranges from the maximum at the center of the vortex (magenta), according to Eq.(2.32) and Eq.(2.51), to zero at the boundary (cyan). Figures (c), (g) and (k) show the vortex current around the vortex obtained from Eq.(2.16). Figures (d), (h) and (l) show the phase of the order parameter. The discontinuity line splitting the white to the black region shows the existence of a single vortex inside the cylinder. 52

3.1 The critical field,  $H_c(t)/H_c(0)$  and the field above which vortex states can be found,  $H_{c2}(t)/H_{c2}(0) = \tilde{\alpha}(t)$ , are shown in reduced units. The condensate parameter,  $\tilde{\beta}(t)$ , is also displayed here. . . . . 61

3.2 The current of a single vortex ( $L = 1$ ) at the center of the cylinder is shown here, as obtained from Eq.(3.65). The (paramagnetic) circulation around the vortex core prevails near the center but weakens towards the border and is overcome by the (diamagnetic) shielding currents. In between the current vanishes at  $\sqrt{2/H_a}$ , here taken as  $H_a = \tilde{\alpha}(0.9)$ . The radius of the cylinder, taken as  $R = 6.5$ , does not determine the radius of zero current. . . . . 77

- 3.3 The line  $1 - 2\kappa^2\tilde{\beta}(0.9)$  and the ratio  $I_2/I_4$  are both shown ( $\kappa = 0.015$ ,  $t = 0.9$ ) here as a function of applied magnetic field. The ratio  $I_2/I_4$  only depends on  $\phi = H_a R^2$ . . . . . 80
- 3.4 The line  $1 - 2\kappa^2\tilde{\beta}(0.9)$  and the ratio  $I_2/I_4$  ( $L = 1$ ) are shown ( $\kappa = 0.015$ ,  $t = 0.9$ ) for  $R = 5.5$  and  $R = 6.0$  as a function of the applied magnetic field. . . . . 81
- 3.5 A single vortex at the center of the cylinder has its pair density at the surface shown ( $\kappa = 0.015$ ,  $t = 0.9$ ) for cylinder radii  $R = 5.5$  and  $R = 6.0$ . . . . . 82
- 3.6 The difference in Gibbs energy between superconducting (one vortex at the center) and normal states is shown ( $\kappa = 0.015$ ,  $t = 0.9$ ) for cylinder radii  $R = 5.5$  and  $R = 6.0$  within a range of magnetic field shows that the negative range of the Gibbs energy difference is radically different for the two cylinders. The negative range for  $R = 5.5$  is shown in the vicinity of  $H_{c2} = \tilde{\alpha}(0.9)$  in the insertion. . . . . 83
- 3.7 The line  $1 - 2\kappa^2\tilde{\beta}(0.9)$  and the ratio  $I_2/I_4$  ( $L = 1$ ) are shown here ( $\kappa = 0.015, t = 0.9$ ). The ratio is plotted for a selected set of cylinder radii and magnetic field range above the field range. The ratio must fall below the line in order that the single vortex state exist above  $H_{c2}$ . 84
- 3.8 The difference in Gibbs energy between superconducting (one vortex at the center) and normal states is shown ( $\kappa = 0.015$ ,  $t = 0.9$ ) for a selected set of cylinder radii and magnetic field range above the field  $H_{c2} = \tilde{\alpha}(t)$ . The negative range is where the single vortex state can exist. . . . . 85
- 3.9  $I_2$  is shown ( $\kappa = 0.015$ ,  $t = 0.9$ ) for selected set of cylinder radii and magnetic field range above the field  $H_{c2} = \tilde{\alpha}(t)$ . The states are diamagnetic since  $I_2 > 1$  in the whole field range for all radii. . . . . 86

- 3.10  $I_2$  is shown ( $\kappa = 0.015$ ,  $t = 0.9$ ) for cylinder radii  $R = 5.5$  and  $R = 6.0$  above the field  $H_{c2} = \tilde{\alpha}(t)$ . Notice that in the former case  $I_2 = 0$  for  $H_{c2} = 1.128\tilde{\alpha}(0.9)$ . . . . . 87
- 4.1 Representation of the superconducting simulation region of thickness  $t_s$ , sides  $L_x$  and  $L_y$ , and a ferromagnetic disk of thickness  $t_m$ , radius  $R$  and positioned at a distance  $d$  above the superconducting region. . 104
- 4.2 Representation of a face-centered cubic unit cell where the magnetic moments of the atoms at the vertices are shown as black arrows (continuous line) and the magnetic moments of the atoms at the faces are shown as blue arrows (dotted line). . . . . 106
- 4.3 Representation of a simulation cell, of sides  $d$ , with an equivalent magnetic moment corresponding to the average of the magnetic moments of all crystalline cells, of sides  $a_0$ , which one of them is represented at the left frontal corner. . . . . 107
- 4.4 Representation of the magnetization vector that oscillates around the effective field in a cone (a) under the effect of the tangential term  $\vec{m} \times \vec{H}_{eff}$  and in a damped oscillation it tends to the alignment with the effective field (b) under the effect of the radial term  $\vec{m} \times \vec{m} \times \vec{H}_{eff}$ . 118
- 5.1 Superconducting phase of one single vortex (a) and one antivortex (b). The phase varies from  $\theta = 0$  (blue) to  $\theta = 2\pi$  (red). . . . . 120
- 5.2 Representation of the magnetic moments of a permalloy disk in a magnetic vortex state. The magnetic moments outside the center are in an in-plane azimuthal arrangement (red) and at the center they presents an out-of-plane orientation (blue), as shown in the inset. . . 123
- 5.3 Perpendicular component of the permalloy disk's stray field. The disk is positioned at a distance  $d = 0.3 \xi$  above the middle plane of the niobium film. The values shown in the colorbar are in units of  $H_{c2}$ . . 129

5.4	Superconducting density ( $a$ ) and phase ( $b$ ) of the niobium film under the effect of the permalloy disk's stray field. The disk is positioned at a distance $d = 0.3 \xi$ above the middle plane of the niobium film. . . .	130
5.5	Representation of the arrangement of the magnetic moments inside the magnetic annulus, which is equivalent to a permalloy perforated disk without the out-of-plane magnetic moments at the center. In the annulus all the magnetic moments are in the in-plane azimuthal arrangement. . . . .	132
5.6	Superconducting density ( $a$ ) and phase ( $b$ ) at the equilibrium state for the SC film under the magnetic annulus, which position is indicated by the black solid circumference in the center. . . . .	134
5.7	Octagon of magnetic dipoles inscribed in a circumference of radius $R$ . The position of each dipole is determined by the angle $\varphi_{dip}$ . . . . .	136
5.8	Superconducting density $ \psi ^2$ ( $a, b, c$ ) and phase $\theta$ ( $d, e, f$ ). Each row represents a different state, where it is shown two intermediate states ( $a, d$ ), ( $b, e$ ) and the equilibrium one ( $c, f$ ). The phase varies from $\theta/2\pi = 0$ and $\theta/2\pi = 1$ . . . . .	140
5.9	Superconducting current density corresponding to the three states shown in Fig. 5.8. . . . .	143
5.10	Superconducting density ( $a, b, c$ ) and phase ( $d, e, f$ ) for two intermediate states ( $a, d$ ) and ( $b, e$ ) of the relaxation process which results in the equilibrium state ( $c, f$ ). The phase varies from $\theta/2\pi = 0$ and $\theta/2\pi = 1$ . . . . .	146
5.11	Superconducting current corresponding to the three states shown in Fig. 5.10. . . . .	149
5.12	Superconducting density ( $a, b, c$ ) and phase ( $d, e, f$ ) for two intermediate states ( $a, d$ ) and ( $b, e$ ) of the relaxation process and the final equilibrium state ( $c, f$ ). . . . .	152

5.13	Superconducting current corresponding to the three states analyzed in Fig. 5.12. . . . .	155
6.1	Number of VAV pairs, generated inside the region of suppressed superconductivity, as a function of the applied current. . . . .	164
6.2	Superconducting density (upper row) and phase (lower row) for different values of applied current $j_a$ in each column. The values of the current are as follows: $j_a = 0.05 j_0$ for panels (a) and (e), $j_a = 0.10 j_0$ for panels (b) and (f), $j_a = 0.15 j_0$ for panels (c) and (g), $j_a = 0.20 j_0$ for panels (d) and (h). For the superconducting density: dark red (blue) corresponds to $ \psi ^2 = 1$ ( $ \psi ^2 = 0$ ), while for the phase: dark red (blue) relates to $\theta = 2\pi$ ( $\theta = 0$ ). . . . .	165
6.3	Superconducting density (upper row) and phase (lower row) for applied current $j_a = 0.25 j_0$ . Each column presents the density and phase for a different state obtained from the relaxation process. For the superconducting density: dark red (blue) corresponds to $ \psi ^2 = 1$ ( $ \psi ^2 = 0$ ), while for the phase: dark red (blue) relates to $\theta = 2\pi$ ( $\theta = 0$ ). . . . .	166
6.4	Superconducting density (upper row) and phase (lower row) for applied current $j_a = 0.30 j_0$ . Three stages of the relaxation process are presented in the sequence of columns. For the superconducting density: dark red (blue) corresponds to $ \psi ^2 = 1$ ( $ \psi ^2 = 0$ ), while for the phase: dark red (blue) relates to $\theta = 2\pi$ ( $\theta = 0$ ). . . . .	167
6.5	Superconducting density (upper row) and phase (lower row) for applied current $j_a = 0.35 j_0$ . Each column correspond to a distinct state obtained from the iterative procedure. For the superconducting density: dark red (blue) corresponds to $ \psi ^2 = 1$ ( $ \psi ^2 = 0$ ), while for the phase: dark red (blue) relates to $\theta = 2\pi$ ( $\theta = 0$ ). . . . .	168

- 6.6 Figure adapted from Ref. [58]. The bounded VAV pair in panel (a) results of the superposition of a uniform current with two opposite sense current loops as shown in (b). Panel (c) shows the vortex dipole observed by J. Y. Ge *et al.* The red (blue) region corresponds to a region of positive (negative) magnetic field. . . . . 168
- 6.7 Number of VAV pairs generated by a magnetic annulus positioned above the film. The distance  $d = 0.3 \xi$ ,  $d = 0.6 \xi$  and  $d = 0.9 \xi$  are shown respectively by the green line with circles, the blue dashed line with squares and the red line with triangles. . . . . 170
- 6.8 Superconducting density (upper row) and phase (lower row) for applied current  $j_a = 0.10 j_0$  and distance  $d = 0.3 \xi$ . The sequence of states shown in columns (a, d), (b, e) and (c, f), respectively, present stages of the relaxation process where a nucleated VAV pair annihilates at the center under the annulus. . . . . 171
- 6.9 Superconducting density (upper row) and phase (lower row) with applied current  $j_a = 0.15 j_0$  and annulus at a distance  $d = 0.3 \xi$  above the SC film. . . . . 172
- 6.10 Superconducting density (upper row) and phase (lower row) with applied current  $j_a = 0.15 j_0$  and annulus at a distance  $d = 0.6 \xi$  above the SC film. . . . . 173
- 6.11 Superconducting density (upper row) and phase (lower row) with applied current  $j_a = 0.20 j_0$  and annulus at a distance  $d = 0.6 \xi$  above the SC film. . . . . 174
- 6.12 Superconducting density (upper row) and phase (lower row) with applied current  $j_a = 0.30 j_0$  and annulus at a distance  $d = 0.6 \xi$  above the SC film. . . . . 174

6.13 Superconducting density (upper row) and phase (lower row) with applied current $j_a = 0.20 j_0$ and annulus at a distance $d = 0.9 \xi$ above the SC film. . . . .	175
6.14 Superconducting density (upper row) and phase (lower row) with applied current $j_a = 0.30 j_0$ and annulus at a distance $d = 0.9 \xi$ above the SC film. . . . .	176
6.15 Perpendicular component $h_z$ of the disk's stray field without any applied current $j_a = 0$ . The annulus are positioned at distances $d/\xi = 0.3, 0.6, 0.9$ . . . . .	177
6.16 Number of VAV pairs generated by a permalloy disk positioned above the film. The distance $d = 0.3 \xi$ , $d = 0.6 \xi$ and $d = 0.9 \xi$ are shown respectively by the green line with circles, the blue dashed line with squares and the red line with triangles. . . . .	178
6.17 Superconducting density (upper row) and phase (lower row) with applied current $j_a = 0.30 j_0$ and disk at a distance $d = 0.6 \xi$ above the SC film. . . . .	179
6.18 Superconducting density (upper row) and phase (lower row) with applied current $j_a = 0.35 j_0$ and disk at a distance $d = 0.6 \xi$ above the SC film. . . . .	180
6.19 Superconducting density (upper row) and phase (lower row) with applied current $j_a = 0.25 j_0$ and disk at a distance $d = 0.9 \xi$ above the SC film. . . . .	181



# Chapter 1

## Introduction

In this chapter we review some key features of the macroscopic Ginzburg-Landau (GL) theory that are necessary to understand the new results obtained in this thesis. These new results address important questions concerning the understanding of the theory of superconductivity.

We present here the objectives of our research together with the introduction of the superconducting properties that are more relevant to the development of our work. These properties are connected to the critical fields and the superconducting phase of the order parameter in vortex states. Next, we introduce some thermodynamical aspects and the description of the superconducting currents through the London theory. We conclude with the presentation of some points in Ginzburg-Landau theory related to the so-called first order equations that are the subject of the first part of the thesis.

### 1.1 Goals and objectives

In 1911 H. Kamerlingh Onnes [116] observed that the electric resistivity of mercury abruptly drops to zero below the temperature of  $T_c = 4.2 K$ . W. Meissner and R. Ochsenfeld in 1933 [99] discovered a second phenomenon that characterizes the superconductivity, the expulsion of the magnetic field from the inner region of a

given material when it goes to the superconducting state. In the beginning of the decade of 1950, V. L. Ginzburg and L. D. Landau proposed a phenomenological macroscopic theory [62] to describe superconductors near the critical temperature, and posteriorly J. Bardeen, L. N. Cooper and J. R. Schrieffer formulated a microscopic theory [5] that permitted to comprehend the mechanism that generates the conventional superconductivity. In 1986, G. Bednorz and K. A. Müller, discovered the so-called high-temperature superconductors (high- $T_c$ ) [6], that are of type *II* and presents a critical temperature of order  $10^2 K$ . The explanation for the superconductivity in the high- $T_c$  materials is still an open question that is a subject of research.

The first part of this thesis, that consists of chapters 2 and 3, is based on A. A. Abrikosov's treatment of the GL theory that culminated with his proposal in which superconductors can be separated in two groups called type *I* and type *II* [1] depending on their behavior in the presence of an applied external magnetic field  $H$ . A. A. Abrikosov's treatment of the GL theory is based on the so-called first order equations which provide solutions that approximately solve the variational second order equations. More specifically they solve exactly Ampère's law and also an integrated version of the non-linear GL equation. In case of no applied field A. A. Abrikosov's treatment shows that there are no vortex states in the superconductor. However, we show here, in chapter 2, that this is true only in case of an infinitely long superconductor. The presence of an external boundary to a non-superconducting external region modifies this result and it becomes possible to have vortex solutions. They are not stable, which means that their lowest energy is in the boundary where the vortex leaves the superconductor. Nevertheless, it remains the question whether this vortex configuration has lower energy than the normal state, which is addressed here.

We also show in chapter 3 of this thesis that A. A. Abrikosov's classification only applies to an infinitely long superconductor with no external boundary to a

non-superconducting medium. In case of the presence of an external boundary this classification no longer applies and has to be utterly reviewed, as proven here using A. A. Abrikosov's first order equations method applied to the GL theory. According to A. A. Abrikosov's results, type *I* superconductors, when exposed to an external magnetic field that is gradually increased, presents the Meissner effect up to a critical field  $H = H_c$ , when the material changes abruptly to the normal state. The energy difference between the normal and the superconducting state is equal to  $H_c^2/8\pi$ . Nevertheless, if the material geometry permits, it is possible that before the applied field reaches the critical value, namely, for  $H < H_c$ , the material presents the coexistence of superconducting and normal regions, remaining in the so-called intermediate state. On the other hand, the type *II* superconductors expel the applied magnetic field from its interior only up to a smaller field,  $H_{c1} < H_c$ . Then, for a stronger field the material shows normal state filaments immersed in the superconducting region, in the so-called mixed state. These filaments are the vortices and have paramagnetic currents around them, which are generated to partially compensate the kinetic energy due the diamagnetic currents produced by the external applied field. The material remains in this state with lower energy than that of the normal state up to the point that the applied field reaches the upper critical limit  $H_{c2} > H_c$ , when the superconductor smoothly goes to the normal state. This is because the density of vortices becomes so high that their cores begin to touch each other and the dominating phase is that of the cores, namely, the normal state. D. Saint-James and P. G. de Gennes [126] found that it is still possible to find superconductivity in a thin layer around the surface of the superconductor below the so-called surface critical field  $H_{c3} = 1.69 H_{c2}$ .

Fig. 1.1 describes the magnetization curves for type *I* and *II* for an infinite (no-boundaries) bulk superconductor. Starting from the general relation  $B = H + 4\pi M$ , the Meissner phase is easily understood. In the Meissner phase, characterized by  $B = 0$  inside the superconductor, the magnetization increases proportionally to

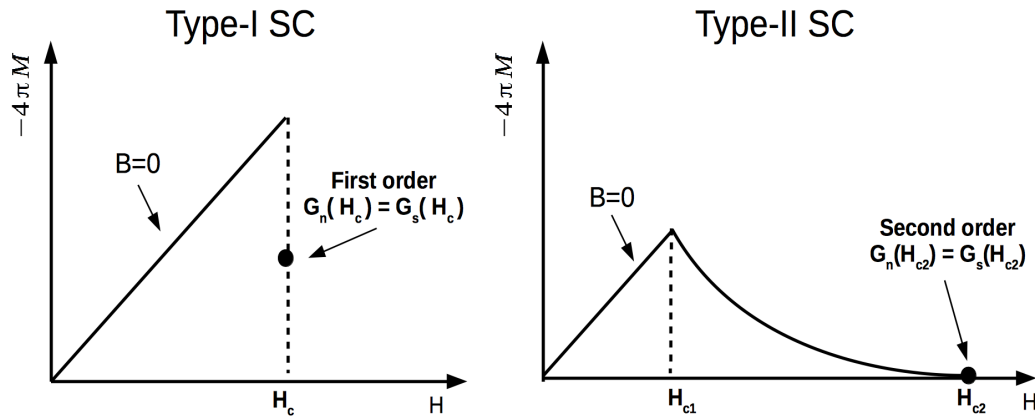


Figure 1.1: The magnetization  $-4\pi M$  versus the applied field  $H$  is shown here for both type *I* and type *II* superconductors. The Meissner phase is characterized by a vanishing magnetic induction,  $B = 0$ . The common wisdom is that the former only has one critical field,  $H_c$ , whereas the latter has two  $H_{c1}$  and  $H_{c2}$ . At the field where superconducting and normal state coexist the Gibbs free energy of both phases are equal.

the applied magnetic field until the thermodynamic critical field  $H_c$  is reached and the normal state is established. We stress in this figure that for the magnetic field where superconducting and normal states coexist, their Gibbs free energy are equal. The Gibbs free energy is the appropriate thermodynamic potential to describe the transition in a superconductor because it only depends on the applied field and on the temperature,  $G(H, T)$ . Therefore, for type *I* superconductor,  $G_N(H_c) = G_S(H_c)$  while for type *II* superconductor,  $G_N(H_{c2}) = G_S(H_{c2})$  (or  $G_N(H_{c3}) = G_S(H_{c3})$ ).

Fig. 1.2 shows these coexistence lines separating superconducting and normal states in a diagram  $H$  vs  $T$ . As it is detailed discussed in section 3.1, for type *I* superconductor it is common place to have this coexistence line at  $H_c(T)$  and for type *II* at  $H_{c2}(T)$ , or  $H_{c3}(T)$ , the latter caused by surface effects. Take the following definitions of the critical fields.

$$H_c \approx \sqrt{H_{c2}H_{c1}}, \quad (1.1)$$

$$H_{c2} = \sqrt{2}\kappa H_c, \quad (1.2)$$

$$H_{c3} \approx 1.69H_{c2}, \quad (1.3)$$

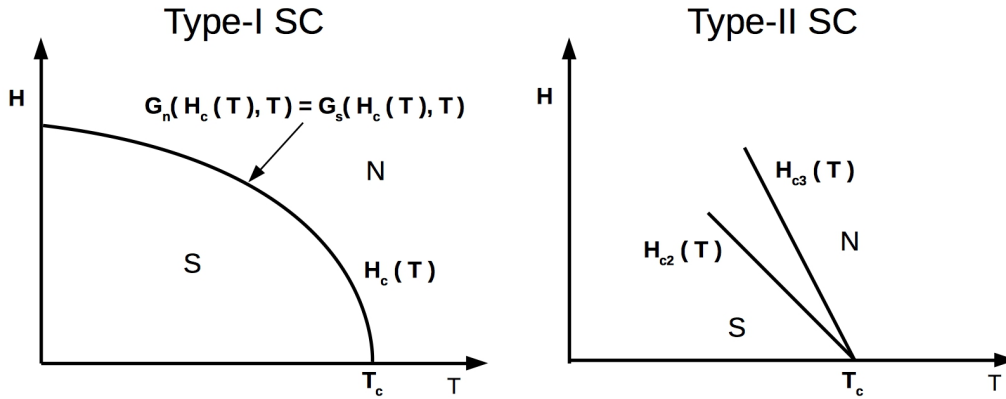


Figure 1.2: The coexistence line between normal and superconducting states are shown in a  $H$  versus  $(T)$  diagram for both type *I* and type *II* superconductors.

where the material parameter  $\kappa \equiv \lambda/\xi$ , the so-called Ginzburg-Landau parameter, is the ratio between the magnetic penetration depth  $\lambda$  and the coherence length  $\xi$ . These definitions naturally introduce the critical material parameter  $\kappa_c = 1/\sqrt{2}$ . For instance, the two types of superconductors, called *I* and *II*, are derived from it since for  $\kappa \rightarrow 1/\sqrt{2}$ ,  $H_{c2} \rightarrow H_c$ , and consequently also  $H_{c1} \rightarrow H_c$ , such that for  $\kappa_c = 1/\sqrt{2}$  the three fields are equal,  $H_{c2} = H_{c1} = H_c$ . Therefore, in this way the magnetization curves of the type *II* superconductor goes into the type *I* superconductor, as shown in Fig. 1.1. However, some of the common belief associated to these fields must be reviewed, as discussed in chapter 3 because it is restricted to infinitely long superconductors.

We start looking at the above relations for a type *I* superconductor which according to the common belief are associated to the material parameter range  $\kappa < \kappa_c$ . Indeed, according to M. Tinkham [140], and many other authors [126, 49, 98, 96], the fields  $H_{c2}$  and  $H_{c3}$  also exist for a type *I* superconductor. While for type *II* superconductors ( $\kappa > 1/\sqrt{2}$ ) it holds that  $H_c < H_{c2} < H_{c3}$ , for the type *I* two scenarios are possible. Notice that  $H_{c3} = 2.37\kappa H_c$  and this defines another “special” material parameter value, namely,  $\kappa_0 = 1/(1.69\sqrt{2}) = 0.417$ . For  $\kappa_0 < \kappa < \kappa_c$  we

have that  $H_{c2} < H_c < H_{c3}$  while for  $\kappa < \kappa_0$  it holds that  $H_{c2} < H_{c3} < H_c$ . Hence, there are materials with  $\kappa$  between  $\kappa_0$  and  $\kappa_c$ , that is, in the range  $0.42 \leq \kappa \leq 0.707$  where  $H_{c2} < H_c < H_{c3}$ . M. Tinkham defines these superconductors as *type 1.5 superconductors* a term that has been taken by V. V. Moshchalkov and co-workers, in a different context, to describe multiband superconductors [110]. We find in this thesis that such properties of superconductors found in the realm of type *I*, can be explained in the context of the first order equations.

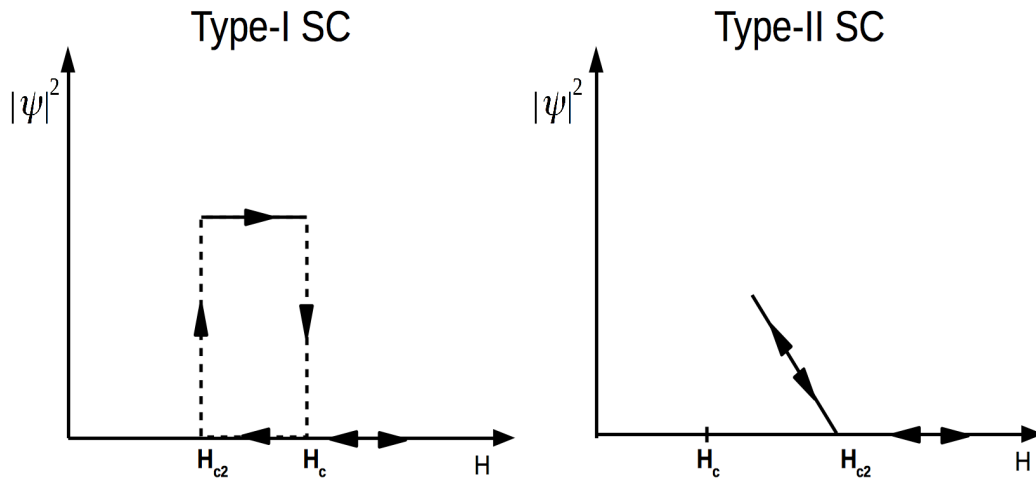


Figure 1.3: The Cooper pair density  $|\psi|^2$  is shown here near to the critical fields  $H_{c2}$  and  $H_c$  for both type *I* and *II* superconductors. The type *I* displays a hysterical behavior meaning that by lowering the field one can go below  $H_c$  and remain in the normal state until  $H_{c2}$  is reached where the density abruptly jumps to a finite value. Increasing the field will keep the superconducting density beyond  $H_{c2}$  until  $H_c$  is reached. The type *II* is a smooth transition with no hysteresis whatsoever.

The meaning of the fields  $H_{c2}$  and  $H_c$  in type *I* superconductors is explained by M. Tinkham in his book *Introduction to Superconductivity* [140] and shown in Fig. 1.3 (equivalent to Fig. 4.7, page 136 of Tinkham's book). The superconducting state in the macroscopic approach of the GL theory is described by a complex order parameter  $\psi = |\psi|e^{i\theta}$  such that  $|\psi|^2$  gives the density of Cooper pairs in a given point in space. Fig. 1.3 shows the behavior of this density as a function of the field and constant temperature. For the type *I* superconductor the applied field is lowered from  $H > H_c$  (normal state) to  $H < H_c$ . The state is supposed to change

from normal to superconductor but it does not. This change only takes place at a lower field, that is, when the upper critical field is reached. At  $H = H_{c2}$  the density  $|\psi|^2$  abruptly changes from zero to its expected value. Then, by increasing the field the density remains constant until  $H_c$  is reached to suddenly drop to zero afterwards. Therefore, in the region  $(H_{c2}, H_c)$  the value of  $|\psi|^2$  is process dependent. Thus, there is hysteresis which is a clear sign of a first order transition. For type *II* superconductors Fig. 1.3 shows that  $|\psi|^2$  smoothly goes to zero with no hysteresis, a sign that the phase transition is of the second order. Hence, in the first part of the thesis we take A. A. Abrikosov's treatment of the GL theory to describe a superconductor with boundaries unveiling novel properties for superconductors of type *I* and bringing new understanding of the critical fields  $H_{c2}$  and  $H_{c3}$ .

The second part of this thesis, that starts in chapter 4 and is developed along chapters 5 and 6, concerns about the properties of the phase of the order parameter,  $\theta$ , which is probed by a lattice of permalloy disks slightly above an infinite long superconducting film.

In chapter 4 we determine the requirements to have one magnetic vortex in each permalloy disk. The magnetic vortex field consists of a spike of non-zero field concentrated in the permalloy disk's center. Interestingly, in chapter 5, we find that below each permalloy disk the phase of the order parameter displays an unusual behavior, it forms several concentric disks of phase discontinuities. In order to get a better insight into the problem, we discuss, before, some fundamental properties of the phase.

Suppose a vortex inside a superconductor at a given point, referred to as the origin. Then, the order parameter vanishes at this origin,  $|\psi(0)| = 0$  and from it we draw a semi-axis that begins at this origin. This defines an angle and the phase of the vortex,  $\theta$ , is equal to it. Then,  $0 \leq \theta \leq 2\pi$  and consequently there

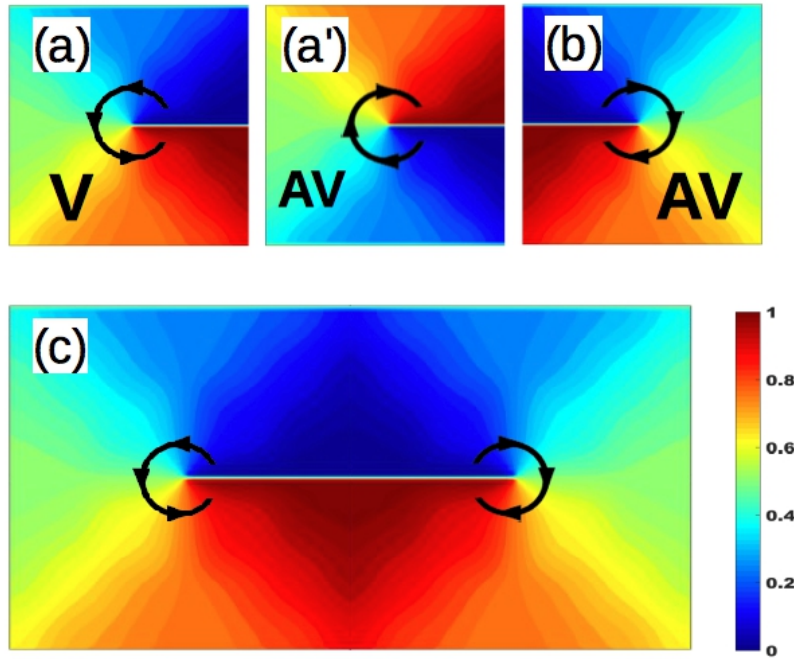


Figure 1.4: The phase of the order parameter associated to a vortex (*a*), a antivortex (*a'*, *b*) and a pair vortex-antivortex (*c*) are shown here. The phase is identical to the angle defined from the semi-axis starting at the vortex origin (*a*). For the antivortex the phase is equal to minus the angle (*a'*). In both cases a hue from blue to red is associated to the angle. For the pair vortex-antivortex the line of discontinuity blue-red is reduced to the segment uniting the two cores (*c*). The creation of a pair vortex-antivortex in a given point of a circle and its subsequent annihilation in the point diametrically opposed leaves a ring of discontinuity blue to red. The scale shown in the colorbar is normalized by  $2\pi$ .

is a discontinuity at this semi-axis, as it jumps from  $\theta = 0$  to  $\theta = 2\pi$ . Colors are associated to the angle, thus running from blue,  $\theta = 0$ , to red,  $\theta = 2\pi$ , such that the discontinuity is characterized by a jump in color, from red to blue, as pictorially represented in Fig. 1.4. As the angle goes from 0 to  $2\pi$  the color smoothly shifts from blue to red passing through all colors of the rainbow hue. Notice that the semi-axis of discontinuity is arbitrarily oriented in space, and this gives rise for the definition of two possible states, the vortex, defined by the order parameter  $\psi = |\psi|e^{i\theta}$ , and the anti-vortex, which corresponds to  $\psi = |\psi|e^{-i\theta}$ . The anti-vortex features the hue blue to red running in the opposite sense, as shown in Fig. 1.4(*a'*). The definition of a vortex or an anti-vortex is always related to the direction of the external magnetic field. Paramagnetic contributions are given by vortices while diamagnetic are given

by anti-vortices. The phase of a pair vortex-antivortex is obtained by aligning the vortex and antivortex discontinuity lines, as shown in Fig. 1.4(c). The discontinuity lines associated to the vortex and the anti-vortex are semi-infinite lines but for the pair their sum reduces to a segment joining their origins.

On the light of the above, let us consider the following “Gedankenexperiment”. Suppose an infinitely long superconductor absolutely at rest, namely, without the presence of any external influence acting on it, such as an applied field, a current, etc. Assume that energy is given in a given point of the superconductor to create a pair vortex-antivortex (VAV). Vortex and antivortex are allowed to move away from their point of creation, but constrained to move along the perimeter of a circle. They move away from each other to finally annihilate each other in the diametrically opposed position. Hence, the final state is equivalent to the initial one, as none of them contains vortices, and the energy is the same. The annihilation of the VAV pair releases the given energy back to the environment. Interestingly, the phases of the superconductor retains the information of this event. While the initial state has constant phase in space, the final state features a ring of phase discontinuity blue to red.

This process of VAV creation can be observed in a superconducting Corbino disk. In this geometry the current flows radially. The resulting force on the vortex and also on the antivortex is azimuthal, namely, tangent to the circle defined by the point where they were created. Therefore, it is enough to have a defect point in the Corbino disk to initiate the nucleation process of vortex-antivortex pairs, according to M. Hayash and H. Ebisawa [73]. In chapter 5 we find the onset of phase discontinuity rings below the permalloy disk and in chapter 6 we study its effects on the onset of vortex-antivortex pairs in the presence of an applied external current.

In the next sections we detail some basic properties needed to understand the results explained in the following chapters.

## 1.2 Thermodynamics of superconductors and the order of the phase transition

The first law of Thermodynamics is written for a superconductor as

$$TdS = dU - \frac{V}{4\pi} \vec{H} \cdot d\vec{B}, \quad (1.4)$$

where  $T$ ,  $S$ ,  $U$ ,  $V$  and  $\vec{B} = \vec{H} + 4\pi\vec{M}$  are the temperature, entropy, internal energy, volume and magnetic induction, respectively. The Gibbs and Helmholtz potentials are defined as

$$G(T, \vec{H}) = F - \frac{V}{4\pi} \vec{B} \cdot \vec{H}, \quad (1.5)$$

where  $F = U - TS$  is the Helmholtz free energy. From the first law it follows that,

$$dG = -SdT - \frac{V}{4\pi} \vec{B} \cdot d\vec{H}. \quad (1.6)$$

As an example to understand some thermodynamic properties of superconductors we consider a long cylinder of type  $I$  superconductor in an uniform longitudinal magnetic field  $\vec{H}$  oriented along the major axis such that contributions near to the top and bottom of the cylinder are not dominant. Suppose that there is a line  $H_c(T)$  separating the normal to the superconducting regions in the  $H$  vs  $T$  phase diagram, given by the phenomenological approximate relation,

$$H_c(T) = H_c(0) \left[ 1 - \left( \frac{T}{T_c} \right)^2 \right]. \quad (1.7)$$

It can be proven by Thermodynamics that the difference between the Gibbs free energies of the normal and superconducting states is given by,

$$G_N(H, T) - G_S(H, T) = \frac{V}{8\pi} [H_c(T)^2 - H^2]. \quad (1.8)$$

From this expression several conclusions can be drawn such as in the coexistence line, defined by  $H = H_c(T)$ , the Gibbs free energies are equal,  $G_N(H, T) = G_S(H, T)$  and in the superconducting region,  $H < H_c(T)$ , the superconducting state has lower Gibbs free energy,  $G_N(H, T) > G_S(H, T)$ .

The order of the transition is determined by computing derivatives of the Gibbs free energy with respect to the temperature. The entropy and the specific heat are the first and the second order derivatives and follow from  $S = -\partial G/\partial T|_H$  and  $C = T\partial S/\partial T|_H$ , respectively. From the above expressions one obtains that,

$$S_S(H, T) - S_N(H, T) = \frac{V}{4\pi} H_c(T) \frac{dH_c(T)}{dT}, \quad (1.9)$$

$$C_S(H, T) - C_N(H, T) = \frac{VT}{4\pi} \left[ \left( \frac{dH_c(T)}{dT} \right)^2 + H_c(T) \frac{d^2 H_c(T)}{dT^2} \right]. \quad (1.10)$$

In summary, a discontinuity in the entropy means a first order transition whereas a discontinuity in the specific heat means a second order transition. The above expressions are useful to draw several conclusions about the thermodynamics of type *I* superconductors. For instance, the superconducting state is less entropic than the normal state,  $S_S(H, T) < S_N(H, T)$ , as long as  $dH_c(T)/dT < 0$ .

### 1.3 The London theory of superconductivity and the diamagnetic and paramagnetic currents

The London theory, developed by the London brothers [92] in 1935, was the first successful attempt to describe the superconductivity properties from a phenomenological point of view.

The motion of electrons in an applied electric field is governed by Newton's law,

$$n_s m_e \frac{d\vec{v}_s}{dt} = n_s q_e \vec{E}, \quad (1.11)$$

where  $m_e$  is the electron mass,  $q_e$  is the electron charge,  $\vec{v}_s$  is the velocity of the superconducting electrons that can be considered as a superfluid of density  $n_s$ .

The superconducting current density is given by  $\vec{J} = n_s q_e \vec{v}_s$ . In the gauge that  $\vec{E} = -\partial\vec{A}/c\partial t$ , one obtains that

$$\vec{J} = -\frac{c}{4\pi\lambda^2}\vec{A}, \quad (1.12)$$

where we defined the so-called London penetration length,

$$\lambda^2 = \frac{m_e c^2}{4\pi n_s q_e^2}. \quad (1.13)$$

By considering the Ampère's law

$$\nabla \times \vec{h} = \frac{4\pi}{c}\vec{J}, \quad (1.14)$$

and applying the curl to both sides of the above equation, one obtains that

$$\vec{h} - \lambda^2 \nabla^2 \vec{h} = 0, \quad (1.15)$$

where we have used that  $\nabla \cdot \vec{h} = 0$ .

Let us take the infinitely long superconducting cylinder of radius  $R$  such that in its interior the local magnetic field is given by  $\vec{h} = h(r)\hat{z}$  where  $r$  is the distance to the central axis. In this case, the London equation becomes,

$$\frac{d^2 h}{d\rho^2} + \frac{1}{\rho} \frac{dh}{d\rho} - h = 0, \quad (1.16)$$

where  $\rho \equiv r/\lambda$ . The most general solution for this equation is given in terms of the modified Bessel functions,

$$h(\rho) = c_1 I_0(\rho) + c_2 K_0(\rho). \quad (1.17)$$

These functions have the following asymptotic limits. For  $\rho \ll 1$ ,

$$I_0(\rho) \approx 1, \quad (1.18)$$

$$K_0(\rho) \approx -\ln(\rho), \quad (1.19)$$

and for  $\rho \gg 1$ ,

$$I_0(\rho) \approx \frac{1}{\sqrt{2\pi\rho}} e^\rho, \quad (1.20)$$

$$K_0(\rho) \approx \frac{\pi}{\sqrt{2\pi\rho}} e^{-\rho}. \quad (1.21)$$

Both are useful to describe the superconductor,  $I_0$  to describe the shielding Meissner current near to the surface of the cylinder and  $K_0$  to describe a vortex state inside the cylinder.

The current is straightforwardly obtained from Ampère's law,

$$\vec{J} = -\frac{c}{4\pi} \frac{dh}{dr} \hat{\theta}. \quad (1.22)$$

It can be drawn from the last two equations that the shielding Meissner current around the edge of the cylinder and the one around the filament (vortex) have opposite directions. While the former is diamagnetic the latter is paramagnetic. This is a direct consequence to the fact that  $K_0$  ( $I_0$ ) is a monotonically decreasing (increasing) function and therefore  $dK_0/d\rho < 0$  ( $dI_0/d\rho > 0$ ).

Fig. 1.5 shows the nucleation process of a vortex from the surface. The Meissner

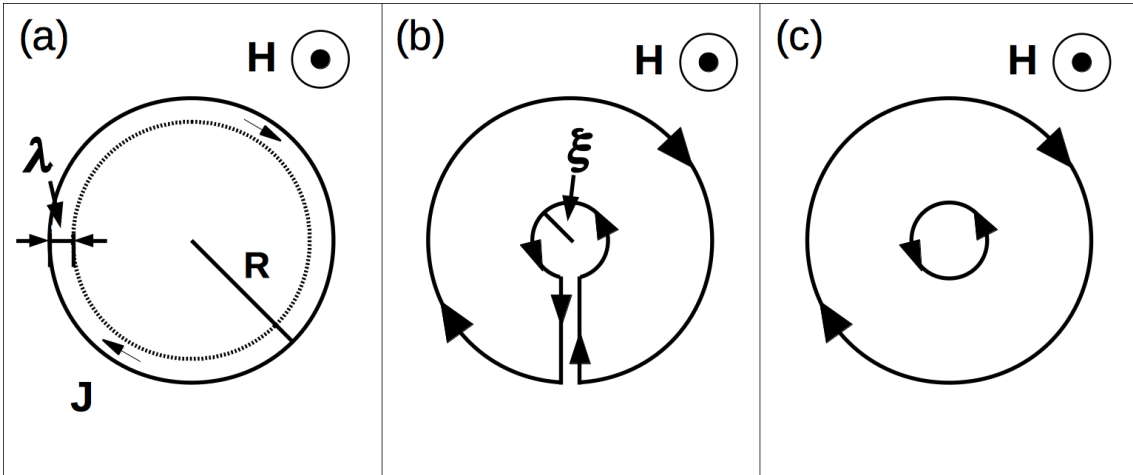


Figure 1.5: The process of creation of a vortex at the surface of a superconductor is depicted here in three steps. In the first the superconductor only has shielding currents aiming to blockade the applied field inside the superconductor. In the second step the vortex still remains its currents attached to the surface, which clearly shows that the currents encircling its core are paramagnetic thus contrary to the diamagnetic Meissner current. The last step shows the vortex detached from the surface clearly showing the opposition of currents.

shielding currents circulate so to create a magnetic field opposite to the applied one and for this reason are diamagnetic. The vortex (filament) bulges from the surface as a protuberance and slowly makes its way inside the superconductor to finally rupture its connection to the surface. The resulting current circulation around the vortex is paramagnetic.

To gain more insight into this problem we firstly consider the superconducting cylinder with no vortex in its interior. Then, the local field is given by,

$$h(r) = H \frac{I_0(r/\lambda)}{I_0(R/\lambda)}. \quad (1.23)$$

The above solution yields at the edge of the local applied field  $h(R) = H$ . At the center  $h(0) = H/I_0(R/\lambda)$ . And so vanishes, since according to the asymptotic formula for  $R \gg \lambda$ ,  $h(0) \sim \exp(-R/\lambda)$ , thus yielding the Meissner effect.

Next, consider the cylinder with a filament in its center of radius  $\xi$  that we shall

identify with the core of a vortex. For the sake of the argument, suppose that the edge of the cylinder ( $r = R$ ) is far away, such that the Meissner field, that was calculated above, near the center is negligible. Consider an extreme type  $II$  superconductor characterized by  $\lambda \gg \xi$ . in this case, we take the asymptotic expression for  $K_0$  to write that near this filament ( $r \gtrsim \xi$ ) it holds that,

$$h(r) = H' \frac{\ln(r/\lambda)}{\ln(\xi/\lambda)}. \quad (1.24)$$

The interpretation of the field  $H'$  inside the filament relies on the single valuedness of the superconducting order parameter, which is associated to the quantization of the magnetic flux. Recall that the superconducting order parameter is a complex wave function,  $\psi = |\psi|e^{i\theta}$ , and its gradient is given by,

$$\nabla\psi = i\psi\nabla\theta + e^{i\theta}\nabla|\psi|. \quad (1.25)$$

Thus, the current density is given by

$$\vec{J} = \frac{\hbar q}{m} |\psi|^2 \left( \nabla\theta - \frac{q}{\hbar c} \vec{A} \right), \quad (1.26)$$

where the charge of the superfluid particles is  $q$ , and the mass is  $m$ . The equation (1.26) divided by  $\hbar q |\psi|^2 / m$  and integrated over a closed path gives

$$\frac{mc}{q^2} \oint \frac{\vec{J}}{|\psi|^2} \cdot d\vec{l} = \frac{\hbar c}{q} \oint \nabla\theta \cdot d\vec{l} - \oint \vec{A} \cdot d\vec{l}. \quad (1.27)$$

The order parameter must be a single valued function and the phase must be equal to the angle plus a multiple of  $2\pi$  upon returning to the same angle. This property is guaranteed by imposing that the path integral of the phase  $\theta$  along the chosen closed path must be a multiple of  $2\pi$ , which means  $\oint \nabla\theta \cdot d\vec{l} = 2\pi n$ , where  $n$  is an

integer number. Thus, Eq.(1.27) can be written as

$$\frac{mc}{q^2} \oint \frac{\vec{J}}{|\psi|^2} \cdot d\vec{l} + \oint \vec{A} \cdot d\vec{l} = n\Phi_0, \quad (1.28)$$

where  $\Phi_0 = \frac{hc}{q}$  is the magnetic quantum flux. This equation shows that currents are adjusted inside the superconductor so as to render that the total magnetic flux through the region delimited by the closed path around the hole be always an integer multiple of the quantum flux. Assuming that  $R \rightarrow \infty$ , there are shielding currents only close to the filament, and so, line integration is only around the filament.

$$\frac{4\pi\lambda^2}{c} \oint_{r=\xi} \vec{J} \cdot d\vec{l} + \oint_{r=\xi} \vec{A} \cdot d\vec{l} = n\Phi_0. \quad (1.29)$$

This becomes,

$$2\pi\lambda^2 H' \left[ \frac{1}{\ln(\lambda/\xi)} + \frac{1}{2} \left( \frac{\xi}{\lambda} \right)^2 \right] = n\Phi_0. \quad (1.30)$$

For the extreme type *II* superconductor,  $\lambda \gg \xi$ , the flux inside the filament is negligible. Hence, the second term is negligible in comparison with the first, and one obtains that,

$$H' = 2H_{c1}, \quad (1.31)$$

where  $H_{c1} = \frac{\Phi_0}{4\pi\lambda^2} \ln\left(\frac{\lambda}{\xi}\right)$ , for the case of the lowest free energy state, which corresponds to  $n = 1$ .

The lower critical field,  $H_{c1}$ , determines the energy per length of a vortex filament according to the argument below. Consider the Gibbs energy of the superconductor of type *II* immediately before the Meissner phase and immediately after the nucleation of the first vortex line. Their Gibbs free energies are equal,  $G_S(H_{c1})|_{no\ vortex} = G_S(H_{c1})|_{one\ vortex}$ , however  $G_S(H_{c1})|_{one\ vortex} = F_{one\ vortex}L - H_{c1}BV/4\pi$  whereas

$G_S(H_{c1})|_{no\ vortex} = 0$ , where  $F_{one\ vortex}$  is the sought energy of a vortex line per length and  $L$  its length. The magnetic induction of a single vortex line is  $B = \int d^3x h/V = \Phi_0/Area$  where  $V = AreaL$ . Therefore, one obtains that  $F_{one\ vortex} = H_{c1}\Phi_0/4\pi$ .

The first measurement of the quantization of the magnetic flux was realized in 1961 [36, 39], and it was verified that the charge involved in the superconductivity phenomena is of a pair of electrons  $q = 2|q_e|$ . A direct demonstration of the effect of the magnetic flux quantization in a superconducting material was given by the Little-Parks effect [90, 66] that measures the dependence of the critical temperature  $T_c$  with the applied magnetic field for a superconducting cylinder thin sheet under the effect of a uniform axially applied magnetic field.

### 1.3.1 Condensation energy and the second order transition

Lev Landau introduced the concept of an order parameter  $\psi$  to describe a second order phase transition. For a superconductor this order parameter must be complex as discussed previously. In case of a homogeneous infinitely long superconductor the Cooper pair density does not vary with the position, which means that  $|\psi(\vec{r})|^2 \equiv |\psi|^2$ . Moreover, the value of the order parameter must be determined with respect to the temperature.

The Gibbs and Helmholtz free energies are equivalent for  $H = 0$ ,  $G \equiv F$  and, according to Landau,

$$\frac{G_S(\psi)}{V} = \frac{G_N}{V} + \alpha|\psi|^2 + \frac{\beta}{2}|\psi|^4, \quad (1.32)$$

where  $\alpha$  and  $\beta$  are phenomenological parameters with a characteristic value for each material, with  $\beta$  a constant and  $\alpha(T) = -\alpha_0(1 - T/T_c)$ , is a generally used expression with  $\alpha_0$  a positive constant.

The order parameter that minimizes the free energy density is a solution of,

$$\alpha\psi + \beta|\psi|^2\psi = 0. \quad (1.33)$$

Notice that the phase of  $\psi$  is arbitrary and constant. We choose  $\psi$  to be a real function. There are two solutions, where the first one is given by  $\psi = 0$  that corresponds to the normal state, and the second one that is valid for  $T < T_c$  and consequently  $\alpha < 0$ , is given by  $|\psi|^2 = -\alpha/\beta$ . For the modulus of the order parameter, we obtain

$$|\psi| = \sqrt{\frac{-\alpha}{\beta}}. \quad (1.34)$$

The free energy density difference is

$$\frac{G_N}{V} - \frac{G_S}{V} = \frac{\alpha^2}{2\beta}, \quad (1.35)$$

which is called the condensation energy. It corresponds to the amount of energy that is released by the electrons in the normal state when the superconducting transition is achieved. This equation corresponds to a special limit of Eq.(1.8) with  $H = 0$ ,

$$G_N(0, T) - G_S(0, T) = \frac{V}{8\pi} H_c(T)^2, \quad (1.36)$$

if we take that,

$$\frac{H_c(T)^2}{4\pi} = \frac{\alpha^2}{\beta}. \quad (1.37)$$

The order of this transition is obtained by calculating the difference in entropy

$$\frac{S_N}{V} - \frac{S_S}{V} = \frac{\alpha}{\beta} \frac{\partial \alpha}{\partial T}. \quad (1.38)$$

Since  $\alpha(T)$  vanishes at the critical temperature,  $\alpha(T_c) = 0$ , the entropy is continuous at the transition. The specific heat is not continuous, and so, the Landau theory

describes a second order phase transition at  $T_c$ .

## 1.4 The Ginzburg-Landau theory and the first order equations

The theory formulated by J. Bardeen *et al.* [5] describes microscopically the superconductivity in good agreement with the experimental data for the cases where the energy gap between the normal and the superconducting state is spatially constant. For the cases where the superconducting gap is spatially inhomogeneous, namely, in the intermediate state of superconductors, a more appropriate approach is the macroscopic theory developed by V. L. Ginzburg and L. D. Landau in 1950 [62]. Interestingly, the GL theory was not well accepted until the year of 1959, when L. P. Gor'kov [67] demonstrated that the GL theory could be derived from the BCS theory when the temperature is very close to the critical temperature  $T_c$ . The GL theory is based on the second order phase transition observed in the superconductors at zero applied field and also on the success of London theory. It is expressed in terms of an order parameter  $\psi(\vec{r})$  that is local. The local density of superconducting electrons is obtained from the order parameter,  $n_s(\vec{r}) \equiv |\psi(\vec{r})|^2$ . The order parameter is assumed to be small enough and vary slowly in space, such that it is possible to expand the Helmholtz free energy density  $F/V$  in a power series of  $|\psi(\vec{r})|^2$ , in the following way,

$$\begin{aligned} \frac{F_S}{V} = \frac{F_N}{V} + \int_V \frac{d\vec{r}}{V} \left\{ \frac{1}{2m} \left| \left( \frac{\hbar}{i} \nabla - \frac{q}{c} \vec{A}(\vec{r}) \right) \psi(\vec{r}) \right|^2 \right. \\ \left. + \alpha(T) |\psi(\vec{r})|^2 + \frac{\beta}{2} |\psi(\vec{r})|^4 + \frac{\vec{h}^2(\vec{r})}{8\pi} \right\}, \end{aligned} \quad (1.39)$$

where  $F_N$  represents the free energy of the normal state,  $\vec{A}$  is the vector potential that produces the magnetic field  $\vec{h} = \nabla \times \vec{A}$ ,  $V$  is the volume of the superconductor,  $m$  and  $q$  represents the mass and electric charge for the charge carriers, which are the Cooper pairs. The variational method is used to obtain a system of two coupled

differential equations for  $\psi$  and  $\vec{A}$ , that render the free energy a minimum,

$$\frac{1}{2m} \left( \frac{\hbar}{i} \nabla - \frac{q}{c} \vec{A} \right)^2 \psi + \alpha\psi + \beta|\psi|^2\psi = 0, \quad (1.40)$$

$$\frac{c}{4\pi} \nabla \times \nabla \times \vec{A} - \frac{q\hbar}{2mi} (\psi^* \nabla \psi - \psi \nabla \psi^*) + \frac{q^2}{mc} \psi^* \psi \vec{A} = 0. \quad (1.41)$$

Our goal here is to describe succinctly A. A. Abrikosov's treatment of these equations based on the first order equations. In the presence of an applied magnetic field and assuming it is very close to the upper critical field such that higher powers of the order parameter can be neglected, Eq.(1.40) can be replaced by,

$$\frac{1}{2m} \left( \frac{\hbar}{i} \nabla - \frac{q}{c} \vec{A} \right)^2 \psi \approx -\alpha\psi. \quad (1.42)$$

In case the magnetic field is essentially given by the applied one,  $\nabla \times \vec{A} = \vec{H}$ , the above equation is equivalent to the Schrödinger equation for a particle in a magnetic field where  $-\alpha$  plays the role of the energy. It is well known that the problem of a particle in a magnetic field is equivalent to the harmonic oscillator, which has ladder operators that take an eigenstate with a given energy to another eigenstate with the next higher (or lower) energy. We can unveil such structure by defining operators  $D_j \equiv (\hbar/i)\partial_j - qA_j/c$ , and it suffices to consider  $j = 1, 2$  since we consider an infinitely long superconductor with applied field perpendicular to this plane. Without any loss of generality, we use the identity  $D_1^2 + D_2^2 = D_- D_+ + i[D_2, D_1]$ , where we have defined the operators  $D_{\pm} \equiv D_1 \pm i D_2$ . Next, by using  $[D_1, D_2] = -(\hbar q/ic)H$ , it follows that,

$$\frac{1}{2m} \left( D_- D_+ + \frac{\hbar q}{c} H \right) \psi \approx -\alpha\psi. \quad (1.43)$$

Therefore, the ground state condition is given by

$$D_+ \psi = 0, \quad (1.44)$$

provided that  $\hbar q H / 2 m c = -\alpha$ . The above equation became known as the first order equation. This field  $H$  is the upper critical field since we can write this last condition as,

$$H = H_{c2} = \frac{\Phi_0}{2\pi\xi^2}, \quad (1.45)$$

where  $\xi^2 = \hbar^2 / 2m(-\alpha)$ .

Next, we seek to solve Ampère's law, namely, Eq.(1.41), under the condition that Eq.(1.44) holds. At this point, A. A. Abrikosov was able to find the exact solution of this problem, that became known as the second first order equation.

$$\nabla \times \vec{A} = \left( H - \frac{\hbar q}{m c} |\psi|^2 \right) \hat{z}. \quad (1.46)$$

The first order equations are well discussed in section 2.3. From the first order equations A. A. Abrikosov obtained the vortex lattice, whose parameters were obtained by introducing this solution into the Gibbs free energy and seeking for the minimum energy.

### 1.4.1 Interaction between vortices and current

The energy of two vortices can be expressed by,

$$F = 2F_{one\ vortex} + \frac{\Phi_0}{8\pi} 2h(\vec{r}_1 - \vec{r}_2), \quad (1.47)$$

where  $F_{one\ vortex}$  is the energy of an isolated vortex,  $h(\vec{r}_1 - \vec{r}_2)$  is the field created by vortex 2 in space and felt by vortex 1 in its core. By considering this interaction term as a potential energy we can obtain the interaction force per unit length felt by the vortex 1 as  $-dF/d\vec{r}_1$ , which yields the force  $j_{12}\Phi_0/c$ , where  $j_{12}$  is the current density induced by the second vortex at the center of the first vortex. This suggests

that for an externally applied current  $\vec{j}_a$  in the  $xy$  plane circulating around a vortex whose magnetic field points in the  $z$  direction, the general expression for the Lorentz force on the vortex core, per unit length, is given by,

$$\vec{f} = \frac{1}{c} \vec{j}_a \times (\Phi_0 \hat{z}). \quad (1.48)$$

A VAV pair experiments an attractive interaction among them and eventually annihilate themselves if no external force stops them from doing so. This is true in the bulk and also in a superconducting thin film of thickness  $d$ , as shown by J. Pearl [119]. A vortex and an antivortex, separated by a distance  $r_{12}$ , experiment an attractive long range force in the latter case given by  $f_{12} \approx 1/r_{12}^2$ , for  $r_{12} \gg \lambda_{eff} = 2\lambda^2/d$ . Nevertheless, an external current applied perpendicularly to a VAV pair can revert this tendency and make them separate from each other by increasing the applied current. In chapter 5, we present a hybrid superconductor-ferromagnet system where this situation is verified and the circles of phase discontinuities emerge.

# Chapter 2

## Excited vortex states (EVS) in mesoscopic superconductors

In this chapter, we address the discussion about the excited vortex states (EVS) for an infinitely long cylinder. We present the A. A. Abrikosov approach, the so-called first order equations formalism, that led him to the discovery of vortices in bulk superconductors. We develop the extension of the first order equations to consider vortex states in mesoscopic superconductors. We present the relation of the first order equations with the non-linear Ginzburg-Landau approach through a decomposition of the kinetic energy that makes explicit the contributions due to the existence of a boundary in a superconductor. Finally, we apply the first order equations formalism to solve the problem of a vortex left inside a cylinder after the external magnetic field is switched off, which is the EVS.

### 2.1 Introduction

Individual vortices in type *II* superconductors were first seen by U. Essmann and H. Trauble through the Bitter decoration technique [47, 48]. Since then, several other techniques have been developed for this purpose [7], such as scanning SQUID

microscopy [150], high-resolution magneto-optical imaging [65, 115], muon spin rotation ( $\mu$ SR) [135, 113], scanning tunnelling microscopy [136, 137], and magnetic force microscopy [136]. These advancements in the visualization of individual vortices opens the gate to investigate new properties, such as those of the *excited vortex state* (EVS).

A type *II* superconductor in the presence of an external applied magnetic field contains vortices in its interior whose density is fixed by the external applied magnetic field. Once the applied field is switched off this state becomes unstable and vortices must leave the superconductor. However their exit can be hindered by microscopic inhomogeneities which pin them inside the superconductor. Here, we make an important distinction concerning this state, with a vortex left inside the superconductor, according on how its energy compares with that of the normal state. Although the left vortex state is always unstable, only in case its energy is lower than that of the normal state we call it EVS. Consider the left vortex state immediately after the applied field is switched off. Vortices have topological stability but only inside the superconducting state. Thus, as long as the superconducting state exists they cannot be created or destroyed and therefore can only enter or exit through the boundary. However if the superconducting state ceases to exist vortices vanish all together inside the material. Therefore, the obtainment of the Gibbs free energy difference between the superconducting state, which contains the left vortex state inside, and the normal state must be done to determine whether the superconducting state still exists. In case this energy difference is positive one expects the collapse of the superconducting state and the onset of the normal state, possibly because of non-linear thermal effects that will develop and pinning will not be able to uphold this transition. In case this energy difference is negative the EVS exists and can remain inside the superconductor provided that pinning impedes the motion of vortices towards the superconductor boundary.

In the London limit the energy of the vortex state is clearly positive since it is the sum of all two-vortex repulsive interactions. This is equivalent to say that the energy is the sum of the vortex lines self energies plus the sum over the repulsive interaction between different vortices. Once again, it becomes clear that vortices inside the superconductor can only be sustained by the external pressure exerted by the applied field and once this pressure ceases to exist they scape leaving behind the state of no vortex. However, the study of the EVS cannot be done in this context of the London theory since it does not describe the condensate energy. Within the London theory it is not possible to compare the energy of the vortex state with the normal state. Therefore, the EVS must be studied in the context of the Ginzburg-Landau (GL) theory.

The EVS is intrinsically paramagnetic [139, 38, 88], which means that its magnetization points in the same direction of the switched off applied field. A simple way to understand this property is to analyse the two types of currents in a superconductor, that are illustrated in Fig. 1.5 in section 1.3. In the Meissner phase there are only shielding currents at the boundary, which are diamagnetic, namely, they create an equal and opposite field to the applied one in its interior resulting into a net null field. However the current around the vortex core is opposite to the shielding current, a property that explains why the increase in the number of vortices weakens the diamagnetic response set by the shielding currents. This increase reaches the critical point where the magnetization vanishes and then the upper critical field is reached. Consider that, for the sake of the argument, after the sudden switch off the applied field the shielding currents immediately disappear. This must occur in some moment otherwise there will be a left field of opposite direction to the applied one. The vortices caught in this sudden transformation either remain pinned or start their move towards the boundary. In case the Gibbs energy difference is positive the whole superconducting state will move towards its collapse, but if negative there will be a

EVS left inside, which corresponds to a vortex state without the shielding currents and therefore with a purely paramagnetic response. There is no Lorentz force to push vortices at the boundary since the shielding currents are absent. Vortices have no impediments at the boundary, there is no Bean-Livingstone barrier in zero applied field [134, 75].

In this chapter we propose a general method to calculate the Gibbs free energy difference between the left vortex and the normal states valid near the superconducting to normal transition, where the order parameter is small. This method is general since it applies to any vortex configuration in any geometry of the cross section area. The method applies to very long superconducting cylinders such that the vortex lines are parallel to each other and oriented along its major axis. As shown here, the order parameter that describes the left vortex state can be obtained from the well-known mathematical problem of conformal mapping. Remarkably, the order parameter is just an analytical function with constant modulus at the boundary of a given cross section geometry. In the power of the order parameter we obtain the Gibbs energy difference, the local magnetic field and currents inside the superconductor. Besides, we also obtain other interesting features, such as the magnetic field at the center of the vortex core, and also the paramagnetic magnetization. As it was shown in section 1.3, it is well-known that at low vortex density the magnetic field inside the vortex core is twice the value of the lowest critical field [18]. For higher densities a vortex lattice sets in and the magnetic field inside the vortex core varies according to the coupling constant  $\kappa$  (the ratio between the penetration and the coherence lengths) and the vortex density [19]. Here, we report the surprising result that as vortices move towards the boundary the magnetic field at their cores, and also the paramagnetic magnetization, change according to their positions. The magnetization vanishes when vortices reach the boundary.

The present approach stems directly from A. Abrikosov's seminal work [1] that led to the discovery of vortices. There, he found two identities that we refer here as the first order equations. They were later rediscovered by E. B. Bogomol'nyi [15] in the context of string theory and found to solve exactly the second order variational equations, that stem from the free energy, for a particular value of the coupling ( $\kappa = 1/\sqrt{2}$ ). These first order equations are able to determine the order parameter and the local magnetic field. A. Abrikosov used them just in case of bulk superconductor, which means a superconductor with no boundary to a non superconducting region. Therefore, he assumed a lattice such that periodic boundary conditions apply. Obviously, the bulk is an idealized system that simplifies the theory but hinders important boundary effects. Here, we essentially extend this very same treatment to the case of a superconductor with a boundary. Interestingly, in case of the bulk, and of no applied external field, the first order equations predict no vortex solution. The only possible solution is that of a constant order parameter. However, as shown here, the existence of a boundary changes dramatically the scenario and vortex solutions become possible even without the presence of an applied field. Thus, the profound connection between the mathematical theory of conformal mapping and the vortex solutions relies on the existence of boundaries. The theory of conformal mapping was developed in the nineteenth century. The Riemann mapping theorem of 1851 states that any simply connected region in the complex plane can be conformally mapped onto any other, provided that neither is the entire plane. The mapping useful to us is the one that takes any finite geometry into the disk [17] which is essentially a variant of the Schwarz-Christoffel conformal transformation [44] of the upper half-plane onto the interior of a simple polygon. The Schwarz-Christoffel mapping [141] is used in potential theory and among its applications are minimal surfaces and fluid dynamics.

Although, in this chapter, we are mainly interested in the EVS problem, it must be stressed that the present method also applies to the situation of an applied

external field, as it was presented in section 1.1 and is developed in chapter 3 for type  $I$  superconductors. The only condition imposed is to be close to the superconducting to normal transition, i.e., near to the upper critical field line. The zero field case just corresponds to the particular case near to the critical temperature,  $T_c$ . However, in the general case, the connection between the order parameter solution and the conformal mapping only holds in case of a circular cross section. Recently, a new method to solve the linearized GL problem for mesoscopic superconductors was proposed by means of conformal mapping [121]. Thus, our approach is distinct from this one since we are also able to obtain the local magnetic field from the order parameter whereas the above method is not.

## 2.2 The Gibbs free energy of a long superconductor and the variational second order equations

Effects of the top and the bottom of a very long superconductor are neglected such that symmetry along the major axis is assumed. Any cross sectional cut at a given  $x_3$  plane reveals the same area  $\Sigma$  and the same physical properties. The external constant magnetic field is oriented along the major axis,  $\vec{H} = H_a \hat{x}_3$ . Hence, the order parameter is only expressed by coordinates in this plane,  $\psi(x_1, x_2)$ , and the only one non-zero component of the local magnetic field is perpendicular to this plane,  $h_3(x_1, x_2) = \partial_1 A_2(x_1, x_2) - \partial_2 A_1(x_1, x_2)$ . The difference between the superconducting and normal Gibbs free energy densities, defined as  $\Delta\mathcal{G}$ , is given by,

$$\begin{aligned} \Delta\mathcal{G} &\equiv \mathcal{G}_s - \mathcal{G}_n \\ &= \int_{\Sigma} \frac{d^2x}{\Sigma} \left\{ \alpha(T)|\psi|^2 + \frac{\beta}{2}|\psi|^4 + \frac{|\vec{D}\psi|^2}{2m} + \frac{(h_3 - H_a)^2}{8\pi} \right\}. \end{aligned} \quad (2.1)$$

The normal state,  $\mathcal{G}_s = \mathcal{G}_n$ , is reached for  $\psi = 0$  and  $h_3 = H_a$ . In this chapter, we consider the commonly used definitions for the GL parameters introduced in

section 1.3.1, that consists in  $\beta > 0$  and  $\alpha(T) = \alpha_0(\frac{T}{T_c} - 1)$ , with  $\alpha_0$  a positive constant. In chapter 3 we introduce a different definition for these parameters in order to describe the vortex state for type *I* superconductors. The vector notation is two-dimensional, such as  $\vec{D} = D_1\hat{x}_1 + D_2\hat{x}_2$  with the operator  $D_j \equiv (\hbar/i)\partial_j - qA_j/c$ ,  $j = 1, 2$ , that was defined in chapter 1, but it is repeated here for completeness. The well-known second order equations are obtained by doing variations with respect to the fields, namely,  $\delta\vec{A}$  and  $\delta\psi^*$ , and lead to the non-linear GL equation that was given in section 1.4 for the general three-dimensional superconductor. Here, we rewrite the GL equations by making use of the two-dimensional notation in a compact form

$$\frac{\vec{D}^2\psi}{2m} + \alpha\psi + \beta|\psi|^2\psi = 0, \quad (2.2)$$

and to Ampère's law,

$$\vec{\nabla} \times \vec{h} = \frac{4\pi}{c}\vec{J}, \quad (2.3)$$

where the current density is given by,

$$\vec{J} = \frac{q}{2m} \left( \psi^* \vec{D}\psi + c.c. \right). \quad (2.4)$$

Boundary conditions must be added to find the physical solutions. They correspond to no current flowing out of the superconductor, as vacuum is assumed outside, and the local field inside must be equal to the applied field outside. Let  $\Upsilon$  be the perimeter of area  $\Sigma$ . Thus at the boundary it must hold that,

$$\hat{n} \cdot \vec{J}|_{\vec{x} \text{ at } \Upsilon} = 0, \quad (2.5)$$

$$h_3|_{\vec{x} \text{ at } \Upsilon} = H_a, \quad (2.6)$$

where  $\hat{n}$  is perpendicular outward to the boundary. Since the current is given by

Eq.(2.4) the following condition on the derivative of the order parameter,

$$\hat{n} \cdot \vec{D}\psi|_{\vec{x} \text{ at } \gamma} = 0, \quad (2.7)$$

is enough to guarantee Eq.(2.5), while Eq.(2.6) determines the local magnetic field.

## 2.3 Dual view of the kinetic energy and the first order equations

The kinetic energy density admits a dual formulation due to the mathematical identity proven in the appendix A, given by Eq.(A.13),

$$\frac{|\vec{D}\psi|^2}{2m} = \frac{|D_+\psi|^2}{2m} + \frac{\hbar q}{2mc} h_3 |\psi|^2 + \frac{\hbar}{2q} (\partial_1 J_2 - \partial_2 J_1). \quad (2.8)$$

As it was presented in section 1.4, the operator  $D_+$  is defined as  $D_+ \equiv D_1 + i D_2$  and the current is given by Eq.(2.4). This decomposition of the kinetic energy as a sum of three terms is exact, and its derivation [149] is given in the appendix A. Therefore, the kinetic energy density,

$$F_k = \int_{\Sigma} \frac{d^2x}{\Sigma} \frac{|\vec{D}\psi|^2}{2m}, \quad (2.9)$$

is also given by,

$$F_k = \int_{\Sigma} \frac{d^2x}{\Sigma} \left( \frac{|D_+\psi|^2}{2m} + \frac{\hbar q}{2mc} h_3 |\psi|^2 \right) + \frac{\hbar}{2q} \frac{1}{\Sigma} \oint_{\gamma} d\vec{l} \cdot \vec{J}. \quad (2.10)$$

In this dual view, there is a superficial (perimetric) contribution due to the current. For a bulk superconductor, where  $\Sigma \rightarrow \infty$ , the superficial current vanishes either because the currents are localized within some region in the bulk away from the boundary or because of periodic boundary conditions, the latter case being that one

considered by Abrikosov [1]. However in case of a finite area, such as for a mesoscopic superconductor, the current at the boundary must be considered and does not vanish.

The most interesting property of this dual view of the kinetic energy is that the current also acquires a new formulation. The current can be simply obtained by the variation of the kinetic energy with respect to the vector potential,

$$\delta F_k = -\frac{1}{c} \int_{\Sigma} \frac{d^2x}{\Sigma} \vec{J} \cdot \delta \vec{A}, \quad (2.11)$$

and the use of the dual formulation leads to

$$J_1 = \frac{q}{2m} [(D_+\psi)^*\psi + \psi^*(D_+\psi)] - \frac{\hbar q}{2m} \partial_2 |\psi|^2, \quad (2.12)$$

$$J_2 = i \frac{q}{2m} [(D_+\psi)^*\psi - \psi^*(D_+\psi)] + \frac{\hbar q}{2m} \partial_1 |\psi|^2. \quad (2.13)$$

The superficial current term does not contribute since at the edge the variation of the vector potential vanishes, namely,  $\delta \vec{A} = 0$ , for  $\vec{x}$  at  $\Upsilon$ .

In this chapter we seek the minimum of the free energy through solutions of the first order equations that were first introduced in section 1.4, and are repeated, for completeness, below,

$$D_+\psi = 0, \text{ and}, \quad (2.14)$$

$$h_3 = H' - 2\pi \frac{\hbar q}{mc} |\psi|^2, \quad (2.15)$$

instead of solutions of the second order equations, given by Eqs.(2.2) and Eq.(2.3). On Eq.(2.15),  $H'$  is a constant to be determined but whose interpretation is very clear. It is the local field at the vortex core since there  $\psi = 0$ , and so,  $h_3 = H'$ . In the absence of vortices the order parameter is constant and  $H' = 2\pi(\hbar q/mc)|\psi|^2$  since it must hold that  $h_3 = 0$  everywhere. We show that the above equations provide an

exact solution to Ampère's law and an approximate solution to the non-linear GL equation, and so, provided an easy and efficient method to search for the minimum of the free energy.

Ampère's law is exactly solved. To see it, just take the condition of Eq.(2.14) into the current, as given by Eq.(2.12) and Eq.(2.13). The Ampère's law, given by  $\partial_2 h_3 = 4\pi J_1/c$  and  $\partial_1 h_3 = -4\pi J_2/c$ , becomes  $\partial_2 h_3 = -(4\pi\hbar q/2mc)\partial_2|\psi|^2$  and  $\partial_1 h_3 = -(4\pi\hbar q/2mc)\partial_1|\psi|^2$ , respectively, since Eq.(2.15) holds. Then, one obtains that,

$$\vec{J} = \frac{\hbar q}{2m}\hat{x}_3 \times \vec{\partial}|\psi|^2. \quad (2.16)$$

The surface term, contained in the dual formulation of the kinetic energy, is given by Eq.(2.8).

$$\frac{\hbar}{q}(\partial_1 J_2 - \partial_2 J_1) = +\frac{\hbar^2}{2m}\vec{\partial}^2|\psi|^2. \quad (2.17)$$

The mathematical identity of Eq.(2.8), becomes,

$$\frac{|\vec{D}\psi|^2}{2m} = \left( H' - \frac{\hbar q}{mc}|\psi|^2 \right) \frac{\hbar q}{2mc}|\psi|^2 + \frac{\hbar^2}{4m}\vec{\partial}^2|\psi|^2, \quad (2.18)$$

once we have assumed that the first order equations are satisfied. The non-linear GL equation is approximately solved in the sense that its integrated version is exactly solved. This integrated version is obtained by multiplying the non-linear GL equation by  $\psi^*$ , and next integrating over the entire area  $\Sigma$  of the superconductor:

$$\int_{\Sigma} \frac{d^2x}{\Sigma} \left\{ \psi^* \frac{\vec{D}^2\psi}{2m} + \alpha(T)|\psi|^2 + \beta|\psi|^4 \right\} = 0. \quad (2.19)$$

Next, we transform this equation into an algebraic one whose usefulness is to fix the scale of the order parameter which has remained undefined when solving the

scale invariant Eq.(2.14). The first term of the integrated equation summed with its complex conjugate and divided by 2, can be expanded as follows,

$$\frac{1}{2} \left[ \psi^* \frac{\vec{D}^2 \psi}{2m} + \left( \frac{\vec{D}^2 \psi}{2m} \right)^* \psi \right] = -\frac{\hbar^2}{4m} \vec{\partial}^2 |\psi|^2 + \frac{|\vec{D}\psi|^2}{2m}. \quad (2.20)$$

Inserting Eq.(2.20) into the integrated equation, upon summing with its complex conjugate and dividing by 2, one obtains that,

$$\int_{\Sigma} \frac{d^2x}{\Sigma} \left\{ -\frac{\hbar^2}{4m} \vec{\partial}^2 |\psi|^2 + \frac{|\vec{D}\psi|^2}{2m} + \alpha(T) |\psi|^2 + \beta |\psi|^4 \right\} = 0. \quad (2.21)$$

The use of Eq.(2.18) turns the integrated equation into the following one.

$$\int_{\Sigma} \frac{d^2x}{\Sigma} \left\{ \left( \frac{H'}{2} \frac{\hbar q}{m c} + \alpha \right) |\psi|^2 - \left[ \pi \left( \frac{\hbar q}{m c} \right)^2 - \beta \right] |\psi|^4 \right\} = 0. \quad (2.22)$$

In summary Eq.(2.14), together with Eq.(2.22), fully determines the order parameter,  $\psi$ , and from Eq.(2.15) one obtains the local magnetic field,  $h_3$ .

### 2.3.1 The boundary conditions, the magnetization and the Gibbs free energy

There should be no current flowing out of the superconductor and the magnetic field must be continuous at the boundary. Here, we address the question on how to satisfy these boundary conditions in the context of the first order equations. The boundary conditions themselves are first order equations, as seen in Eq.(2.5) and Eq.(2.6), and so, their fulfilment is easily understood in the context of the second order equations. For instance, the derivative of the order parameter normal to the surface must vanish, according to Eq.(2.7), but this condition cannot be imposed on  $\psi$ , obtained through Eq.(2.14) because this is a first order equation itself and there is not enough free parameters in this solution. However, it is possible to satisfy Eq.(2.5)

simply by the requirement that the density  $|\psi|^2$  be constant at the boundary, which introduces a new parameter,  $c_0$ , fixed by the non-linear integrated GL equation, Eq.(2.22).

$$|\psi|^2 = c_0^2 \text{ for } \vec{x} \text{ at } \Upsilon, \text{ and,} \quad (2.23)$$

$$H' = H_a + 2\pi \frac{\hbar q}{mc} c_0^2. \quad (2.24)$$

Therefore, the constant  $H'$  is automatically fixed by  $c_0$  according to Eq.(2.15). The important point is that Eq.(2.23) is enough to guarantee that there is no current flowing outside the superconductor. This is just a direct consequence of Eq.(2.16). As  $|\psi|^2$  is constant along the border, there is no gradient tangential to it and only perpendicular to it, namely,  $\vec{\partial}|\psi|^2$  is normal to the surface, rendering  $\vec{J}$  always tangent to the surface.

The magnetization  $M_3$  is also directly obtained from the present formalism and easily shown to be paramagnetic in the absence of an applied external field. According to Eq.(2.15),

$$B_3 \equiv \int_{\Sigma} \frac{d^2x}{\Sigma} h_3 = H' - 4\pi\mu_B \int_{\Sigma} \frac{d^2x}{\Sigma} |\psi|^2, \quad (2.25)$$

given in units of the Bohr's magneton,  $\mu_B = \hbar q/2mc$ . Just take the thermodynamical relation  $B_3 = H_a + 4\pi M_3$  and Eq.(2.24) to obtain that,

$$M_3 = \mu_B \int_{\Sigma} \frac{d^2x}{\Sigma} (c_0^2 - |\psi|^2), \quad (2.26)$$

which means that the integral has the dimension of inverse of volume. In case of no applied external field, the order parameter is maximum at the boundary, namely, ( $|\psi|^2 \leq c_0^2$ ), and so the magnetization is paramagnetic,  $M_3 > 0$ .

Under the condition that the first order equations are satisfied, the Gibbs free

energy density of Eq.(2.1) becomes,

$$\begin{aligned} \Delta\mathcal{G} &= \int_{\Sigma} \frac{d^2x}{\Sigma} \left\{ \left( \alpha(T) + \frac{H_a \hbar q}{2 m c} \right) |\psi|^2 + \frac{1}{2} \left[ \beta - \pi \left( \frac{\hbar q}{m c} \right)^2 \right] |\psi|^4 \right\} \\ &+ \frac{(H' - H_a)^2}{8\pi} + \frac{\hbar^2}{4m} \oint_{\Upsilon} \frac{dl}{\Sigma} \hat{n} \cdot \vec{\partial} |\psi|^2. \end{aligned} \quad (2.27)$$

Two direct contributions of the boundary to the free energy, which are not present in A. Abrikosov's treatment of the GL theory [1], are the field energy due to  $H' \neq H_a$ , according to Eq.(2.24), and the perimetrical contribution of the normal gradient of  $|\psi|^2$ .

Near to the transition to the normal state the order parameter is weak, fact that allows for the expansion of the free energy in powers of  $\psi$ . From the present point of view this weakness also leads to the proposal of an iterative method to solve the first order equations. Firstly, one seeks a solution for  $\psi$  in Eq.(2.14) under a known external field  $H_a$  sufficiently near to the upper critical field line which sets the order parameter in the vicinity of the normal state transition. Any solution of Eq.(2.14), multiplied by a constant is also a solution and this constant is fixed by the integrated equation given by Eq.(2.22). Eq.(2.14) can be rewritten as,

$$\left[ \left( -i \frac{\partial}{\partial x_1} + \frac{\partial}{\partial x_2} \right) - \frac{2\pi}{\Phi_0} (A_1 + iA_2) \right] \psi = 0. \quad (2.28)$$

Let us introduce the complex notation,  $z \equiv x_1 + ix_2$ ,  $\bar{z} \equiv x_1 - ix_2$  into Eq.(2.28), and consider a constant external field,  $H_a$ , such that  $A_1 = -H_a x_2/2$  and  $A_2 = H_a x_1/2$ . In this case, the above equation becomes,

$$\frac{\partial \psi(z, \bar{z})}{\partial \bar{z}} = - \left( \frac{\pi H_a}{2\Phi_0} z \right) \psi(z, \bar{z}), \quad (2.29)$$

where  $\partial/\partial z = 1/2(\partial/\partial x_1 - i\partial/\partial x_2)$  and its complex conjugate is  $\partial/\partial \bar{z} = 1/2(\partial/\partial x_1 +$

$i\partial/\partial x_2$ ). The solution of Eq.(2.29) is promptly found to be,

$$\psi(z, \bar{z}) = f(z)e^{-\left(\frac{\pi H_a}{2\Phi_0}\right)z\bar{z}}, \quad (2.30)$$

where  $f(z)$  is *any* function of  $z$ . The local field is equal to  $H_a$  plus a correction proportional to  $|\psi|^2$  according to Eq.(2.15). Very close to the normal state one expect that this correction is small such that it suffices to solve Eq.(2.14) and feed the solution in Eq.(2.15) without any further recurrence, namely, a returning to Eq.(2.14) with a corrected  $\vec{A}$  associated to the local field  $h_3$ . Thus, the quest for a solution  $\psi(z, \bar{z})$  in a given geometry with cross sectional area  $\Sigma$  and boundary  $\Upsilon$  is reduced to the search of an analytical function  $f(z)$  that will render  $|\psi(z, \bar{z})|^2$  constant at the boundary  $\Upsilon$ . Assuming that at the boundary  $|\psi|^2 = c_0^2$ , this means that the analytical function  $f(z)$  must satisfy the condition  $|f(z)| = c_0 \exp\left(\frac{\pi H_a}{2\Phi_0}|z|^2\right)$ , where  $z$  belongs to the boundary. For a circular disk,  $|z|$  is automatically constant at the boundary, but in case of an arbitrary geometry this characteristic is no longer satisfied. In this chapter we will only consider the case that there is no external applied field,  $H_a = 0$ .

## 2.4 The dimensionless units

At this point, we find useful to switch to dimensionless units and rewrite all previous expressions in this fashion. As well known, the GL theory has only one coupling constant,  $\kappa = \lambda/\xi$ , the ratio between the London penetration length,  $\lambda = (mc^2/4\pi q^2\psi_0^2)^{1/2}$ , and the coherence length,  $\xi = (\hbar^2/2m|\alpha|)^{1/2}$ , respectively, where  $\psi_0 = (|\alpha|/\beta)^{1/2}$ . This renders this ratio temperature independent,  $\kappa = (\beta/2\pi)^{1/2} mc/\hbar q$  and only dependent on material parameter, for the usual assumption that  $\beta$  is a constant. Let us refer just in this paragraph to the dimensionless units by the prime notation. For instance, distance is measured in terms of the coherence

length such that  $\vec{x} = \xi \vec{x}'$ . The magnetic field is expressed in units of the upper critical field,  $\vec{h} = H_{c2} \vec{h}'$ ,  $H_{c2} = \sqrt{2} \kappa H_c = \Phi_0 / 2\pi \xi^2$ ,  $\Phi_0 = hc/q$ , where  $H_c = \Phi_0 / 2\pi \sqrt{2} \lambda \xi$  is the thermodynamical critical field. Then, the dimensionless vector potential is given by  $\vec{A} = H_{c2} \xi \vec{A}'$ , and the covariant derivative becomes  $D_j = \hbar D'_j / \xi$ ,  $D'_j \equiv \frac{1}{i} \partial'_j - A'_j$  since  $\partial_j = \partial'_j / \xi$ . Lastly, the dimensionless order parameter is obtained from  $\psi = \psi_0 \psi'$ . The order parameter value at the boundary is also defined dimensionless,  $c_0 = \psi_0 c'_0$ , and finally the dimensionless magnetization comes from  $M_3 = M'_3 H_{c2} / 8\pi \kappa^2$  since  $\psi_0^2 \mu_B = H_{c2} / 8\pi \kappa^2$ .

Hereafter, we drop the prime notation in all quantities, which means that they are all expressed in dimensionless units. The first order equations become,

$$D_+ \psi = 0, \text{ and,} \quad (2.31)$$

$$h_3 = H' - \frac{1}{2\kappa^2} |\psi|^2. \quad (2.32)$$

Once the order parameter and the local magnetic field satisfy the first order equations, the kinetic energy of Eq.(2.8) becomes,

$$|\vec{D}\psi|^2 = \left( H' - \frac{1}{\kappa^2} |\psi|^2 \right) |\psi|^2 + \frac{1}{2} \vec{\partial}^2 |\psi|^2. \quad (2.33)$$

The integrated equation, Eq.(2.22), in reduced units becomes,

$$\int_{\Sigma} \frac{d^2x}{\Sigma} \left[ (H' - 1) |\psi|^2 + \left( 1 - \frac{1}{2\kappa^2} \right) |\psi|^4 \right] = 0. \quad (2.34)$$

The Gibbs free energy density difference of Eq.(2.1) is in units of  $H_c^2 / 4\pi = |\alpha|^2 / \beta$ ,

given by,

$$\begin{aligned} \Delta\mathcal{G} &\equiv \frac{g-g_n}{|\alpha|^2/\beta} = \int_{\Sigma} \frac{d^2x}{\Sigma} \left\{ -|\psi|^2 + \frac{1}{2}|\psi|^4 + |\vec{D}\psi|^2 \right. \\ &\quad \left. + \kappa^2(h_3 - H_a)^2 \right\}. \end{aligned} \quad (2.35)$$

Similarly, Eq.(2.27), becomes

$$\begin{aligned} \Delta\mathcal{G} &= \int_{\Sigma} \frac{d^2x}{\Sigma} \left\{ -(1 - H_a)|\psi|^2 + \frac{1}{2} \left(1 - \frac{1}{2\kappa^2}\right) |\psi|^4 \right. \\ &\quad \left. + \frac{1}{2} \vec{\partial}^2 |\psi|^2 + \kappa^2 (H' - H_a)^2 \right\}. \end{aligned} \quad (2.36)$$

## 2.5 The vortex excited state and conformal mapping

In the absence of an applied field outside the superconductor,  $H_a = 0$ , and with the help of Eq.(2.34), the Gibbs free energy density of Eq.(2.36) becomes,

$$\Delta\mathcal{G} = \int_{\Sigma} \frac{d^2x}{\Sigma} \left\{ -\frac{1}{2} (1 + H') |\psi|^2 + \frac{1}{2} \vec{\partial}^2 |\psi|^2 + \kappa^2 H'^2 \right\}. \quad (2.37)$$

Then,  $H'$  follows directly from Eq.(2.24). Near to the normal state the order parameter is small enough such that iteration of the first order equations is not necessary. This means that the local magnetic field is small enough such that it can be dropped in Eq.(2.31) and directly obtained from Eq.(2.32). In this case, Eq.(2.31) and Eq.(2.32) are reduced to,

$$\partial_+ \psi = 0, \quad (2.38)$$

$$h_3 = \frac{c_0^2 - |\psi|^2}{2\kappa^2}. \quad (2.39)$$

The connection between vortex states and conformal mapping stems from Eq.(2.29), which simply becomes,

$$\frac{\partial\psi(z, \bar{z})}{\partial\bar{z}} = 0. \quad (2.40)$$

Expressing the order parameter as  $\psi \equiv \psi_R + i\psi_I$  in Eq.(2.38), one obtains that  $\partial_1\psi_R + \partial_2\psi_I = 0$  and  $\partial_2\psi_R - \partial_1\psi_I = 0$ , which are the well-known Cauchy-Riemann conditions for analyticity. We recall the so-called *Maximum Modulus Theorem* in Mathematics which says that for an analytical function  $\psi(z)$  at a given region  $\Sigma$ , the maximum of  $|\psi(z)|$  necessarily falls in its boundary  $\Upsilon$ . This theorem is useful because from it we know that the order parameter, constant at the boundary  $\Upsilon$ , indeed reaches its maximum value there, and therefore the magnetization is necessarily paramagnetic. The presence of vortices inside will only lead to the vanishing of the order parameter at points in its interior,  $\psi = 0$ , and still the maximum of  $|\psi|^2$  is at the boundary. This feature helps to establish fundamental differences between the finite boundary and the bulk superconductor, the latter understood as the case that only periodic solutions are sought. According to Liouville's theorem [52] any periodic analytical function  $\psi$  with zeros must also diverge, from which one draws the conclusion that the only possible physical solution is the constant one. In other words, it is not possible to find vortex solutions without the presence of an applied field in a unit cell with periodic boundary conditions. However they do exist for the long superconductor with a finite cross section. Thus, we conclude from the above discussion that the present method is general and applies for any number of vortices in any cross sectional geometry. As examples of our general method, we detail in this chapter two particular cases of a disk, namely, a vortex with vorticity  $L$  in its center and a vortex with vorticity one in any position inside the disk.

Let us define the integrals,

$$I_2 \equiv \frac{1}{c_0^2} \int_{\Sigma} \frac{d^2x}{\Sigma} |\psi|^2, \quad (2.41)$$

$$I_4 \equiv \frac{1}{c_0^4} \int_{\Sigma} \frac{d^2x}{\Sigma} |\psi|^4, \text{ and,} \quad (2.42)$$

$$I_{\Gamma} \equiv \frac{1}{c_0^2} \int_{\Sigma} \frac{d^2x}{\Sigma} \vec{\partial}^2 |\psi|^2. \quad (2.43)$$

From the integrated equation, Eq.(2.34) and the condition that the local magnetic field vanishes at the boundary, one obtains that,

$$c_0^2 = \left( \frac{1 - H'}{1 - 1/2 \kappa^2} \right) \frac{I_2}{I_4}, \quad (2.44)$$

$$H' = \frac{c_0^2}{2\kappa^2}. \quad (2.45)$$

Solving these equations for  $c_0$  and  $H'$ , we obtain that,

$$c_0^2 = \frac{2\kappa^2 I_2/I_4}{2\kappa^2 - 1 + I_2/I_4}, \quad (2.46)$$

$$H' = \frac{I_2/I_4}{2\kappa^2 - 1 + I_2/I_4}. \quad (2.47)$$

Notice that  $I_2 > I_4$  is indeed satisfied since the order parameter divided by  $c_0$  is always smaller than one inside the disk, and so, at each point the second power, Eq.(2.41), is larger than the fourth power, Eq.(2.42). The fact that  $I_2 > I_4$ , always render a solution for  $c_0$ . The difference of the free energy density given at Eq.(2.37) can be expressed in terms of  $c_0$  as,

$$\Delta \mathcal{G} = -\frac{1}{2}(I_2 - I_{\Gamma}) c_0^2 - \frac{1}{4\kappa^2}(I_2 - 1)c_0^4, \quad (2.48)$$

or in terms of  $H'$  as,

$$\Delta \mathcal{G} = -\kappa^2(I_2 - I_{\Gamma}) H' - \kappa^2(I_2 - 1)H'^2. \quad (2.49)$$

The magnetization given by Eq.(2.26) becomes  $M_3 = 2\kappa^2 H' - I_2 c_0^2$ , which yields,

$$M_3 = \frac{2\kappa^2 (1 - I_2) I_2 / I_4}{2\kappa^2 - 1 + I_2 / I_4}. \quad (2.50)$$

This interesting expression shows that the magnetization depends on the position of the vortices inside the superconductor, since  $I_2$  and  $I_4$  vary accordingly. In case of no vortices,  $I_2 = I_4 = 1$ , the magnetization vanishes. We also include the general expression for the magnetic field at the center of the vortex, as  $h_3(v) = H'$ :

$$h_3(v) = \frac{I_2 / I_4}{2\kappa^2 - 1 + I_2 / I_4}, \quad (2.51)$$

where  $v$  refers to the center of the vortex. We consider two particular examples of a thin long cylinder with radius  $R$ , namely, a vortex of arbitrary vorticity  $L$  at the center, and a vortex of a defined vorticity  $L = 1$  at arbitrary position. Through them we see the general aspects of the present theory such as the importance of the boundary term which makes the Gibbs energy explicitly dependent on  $R$ . Remarkably, the cooper pair density at the boundary determines the local magnetic field at the vortex core. There,  $\psi(v) = 0$  and so  $h_3(v) = c_0^2 / 2\kappa^2$  according to Eq.(2.32)

## 2.6 Long cylinder with a circular cross section

We find useful to apply our theory to Niobium [53, 46, 31], one of the favored materials to study the characteristics of vortex matter in superconductors and also used to construct nano-engineered superconductors [16]. All figures are expressed in reduced units and to retrieve the predicted values for Niobium we take the parameter values reported in Ref. [31], namely,  $\kappa = 2.1$  ( $\lambda(0) = 42$  nm,  $\xi(0) = 20$  nm). In particular, we choose the temperature of  $T = 7.7$  K which is close to the critical temperature,  $T_c = 9.3$  K, such that an order parameter approach is valid. Thus, for this temperature the local magnetic field, expressed in units of the upper critical

field, must be multiplied by  $H_{c2}(T = 7.7K) = 780$  Oe. Similarly, the magnetization must be multiplied by  $H_{c2}(T = 7.7K)/8\pi\kappa^2 = 7.0$  Oe.

### 2.6.1 Vorticity $L$ at the center

In this simple example we show that the EVS exists only in a special range of the radius and vorticity. The search for the order parameter in a disk cross section of radius  $R$  that satisfies Eq.(2.38), is reduced to find an analytical function that is constant at the perimeter of the disk. This is simply given by,

$$\psi = c_0 \left(\frac{z}{R}\right)^L = c_0 \left(\frac{r}{R}\right)^L e^{iL\theta}, \quad (2.52)$$

where  $c_0$  is the value of the order parameter at the boundary and  $L$  is an integer since the order parameter is assumed to be single-valued,  $\psi(\theta + 2\pi) = \psi(\theta)$ . In polar coordinates the order parameter is expressed in terms of  $r \equiv \sqrt{z\bar{z}}$ , and  $\tan \theta \equiv x_2/x_1$ . The fulfillment of  $|\psi| = c_0$  at the circle guarantees the confinement of the current to the superconductor's boundaries and  $\psi = 0$  at the center means that the solution has non-zero vorticity for  $L \neq 0$ . For  $L = 0$  there is no zero and so, describes the homogeneous ground state. Then, one can determine the integrals of Eqs.(2.41), (2.42) and (2.43), respectively.

$$I_2 = \frac{1}{L+1}, \quad (2.53)$$

$$I_4 = \frac{1}{2L+1}, \quad (2.54)$$

$$I_{\Gamma} = \frac{4L}{R^2}. \quad (2.55)$$

From Eq.(2.46) and Eq.(2.47), one obtains that,

$$c_0^2 = \frac{2\kappa^2(2L+1)}{2\kappa^2(L+1)+L}, \quad (2.56)$$

$$H' = \frac{(2L+1)}{2\kappa^2(L+1)+L}. \quad (2.57)$$

By inserting these expressions into the Gibbs free energy density, either Eq.(2.48) or Eq.(2.49), we obtain,

$$\begin{aligned} \Delta\mathcal{G} &= -\frac{1}{2} \left[ \frac{1}{L+1} - \frac{4L}{R^2} - \frac{L}{L+1} \frac{(2L+1)}{2\kappa^2(L+1)+L} \right] \\ &\times \frac{2\kappa^2(2L+1)}{2\kappa^2(L+1)+L}. \end{aligned} \quad (2.58)$$

The condition for the existence of the EVS,  $\Delta\mathcal{G} \leq 0$ , can only be achieved for a limited range of parameters  $R$  and  $\kappa$ . It means that the EVS exists for a given  $\kappa$  superconductor in case the radius is larger than a critical value, given by,

$$R_c = 2\sqrt{L(L+1) \cdot \frac{2\kappa^2(L+1)+L}{2\kappa^2(L+1)-2L^2}}. \quad (2.59)$$

In the limit  $\kappa \rightarrow \infty$ , the critical radius becomes  $R_c = 2\sqrt{L(L+1)}$ , and the Gibbs free energy for  $R > R_c$  becomes negative,  $\Delta\mathcal{G} \rightarrow [4L(L+1)-R^2](2L+1)/[2R^2(L+1)^2]$ .

The order parameter and the local magnetic field are given by,

$$\psi(r, \theta) = \sqrt{\frac{2\kappa^2(2L+1)}{2\kappa^2(L+1)+L}} \left(\frac{r}{R}\right)^L e^{iL\theta}, \quad (2.60)$$

$$h_3(r) = \frac{(2L+1)}{2\kappa^2(L+1)+L} \left[ 1 - \left(\frac{r}{R}\right)^{2L} \right]. \quad (2.61)$$

The paramagnetic magnetization and the field at the center of the vortex are given

by,

$$M_3 = \frac{L}{L+1} \frac{2\kappa^2(2L+1)}{2\kappa^2(L+1)+L}, \quad (2.62)$$

$$h_3(v) = \frac{(2L+1)}{2\kappa^2(L+1)+L}, \quad (2.63)$$

respectively.

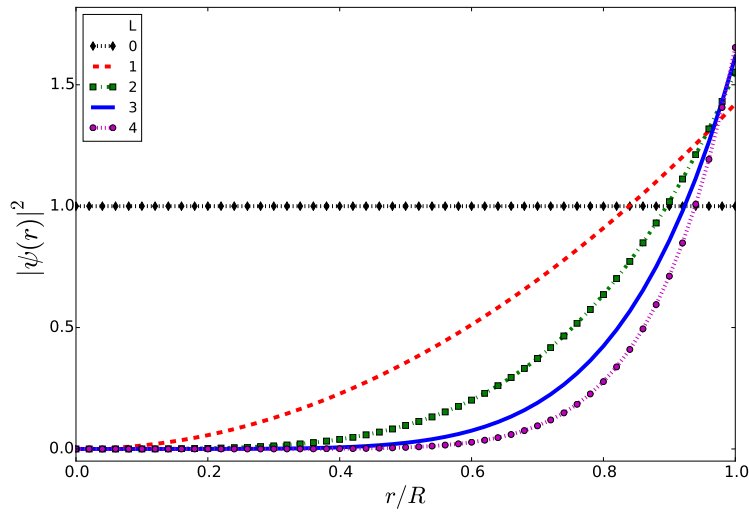


Figure 2.1: The superconducting density as a function of the relative distance to the cylinder's center for vorticity ranging from  $L = 0$  to  $L = 4$  in case of a vortex fixed at the center ( $\kappa = 2.1$ ).

Fig. 2.1 shows the superconducting density as a function of the distance to the center  $r$  for vorticity  $L = 0$  (the homogeneous state) to  $L = 4$ . The density  $|\psi|^2$  is obtained from Eq.(2.52) and  $c_0^2$  is given by Eq.(2.56). The superconducting density is maximum at the boundary, which implies in a paramagnetic effect, as previously shown. The superconducting density reaches  $c_0^2$  at the boundary and is a slow growing function of  $L$  for  $\kappa \geq 1/\sqrt{2}$ .

Fig. 2.2 depicts the local magnetic field versus the distance to the center, for vorticity ranging from  $L = 0$  to  $L = 4$ . This plot shows  $h_3(r)$  obtained from Eq.(2.39),

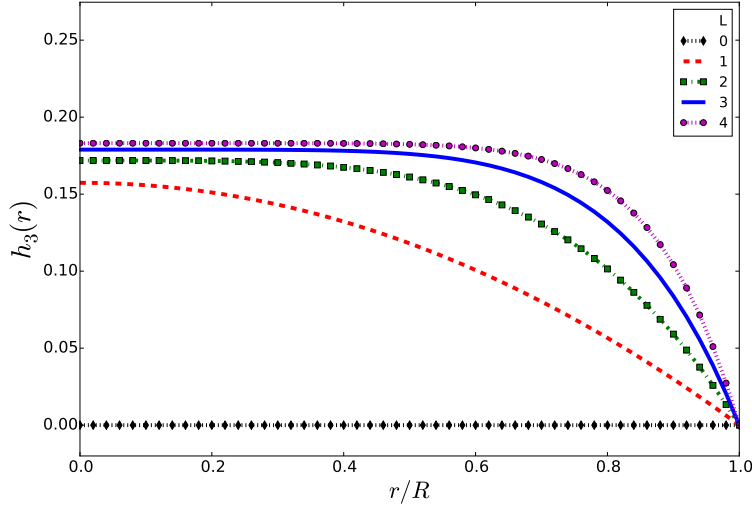


Figure 2.2: The local magnetic field as a function of the relative distance to the cylinder's center for vorticity ranging from  $L = 0$  to  $L = 4$  in case of a vortex fixed at the center ( $\kappa = 2.1$ ). To recover the Niobium values at the temperature of  $T = 7.7$  K the vertical axis must be multiplied by  $H_{c2}(T = 7.7 \text{ K}) = 780$  Oe

with  $c_0^2$  and  $|\psi|^2$  as described in Fig. 2.1. Notice that the field at the core  $h_3(v)$ , where  $v$  corresponds to  $r = 0$ , follows from Eq.(2.51). Thus, it depends on  $L$  through the integrals  $I_2$  and  $I_4$ , defined by Eq.(2.53) and Eq.(2.54). Interestingly, the magnetic field at the center of the vortex and the superconducting density at the boundary are directly related to each other, as previously pointed out. With the exception of the homogeneous state, which has no internal magnetic field, for all other states  $L \geq 1$  the local magnetic field reaches its maximum at the center and vanishes at the boundary, as expected. For  $L \geq 2$  the local field varies slowly from the center to the middle of the cylinder to then abruptly shows a strong decay.

The Gibbs free energy density as a function of the cylinder's radius is shown for different vorticities (from  $L = 0$  to  $L = 4$ ), in Fig. 2.3. This plot shows that the homogenous state  $L = 0$  is the absolute ground state with the minimum energy,  $\Delta\mathcal{G} = -0.5$ . Recall that our search is for the EVS, namely, for  $\Delta\mathcal{G} < 0$  otherwise  $\Delta\mathcal{G} > 0$  and the superconducting state can somehow decay into the normal state. For

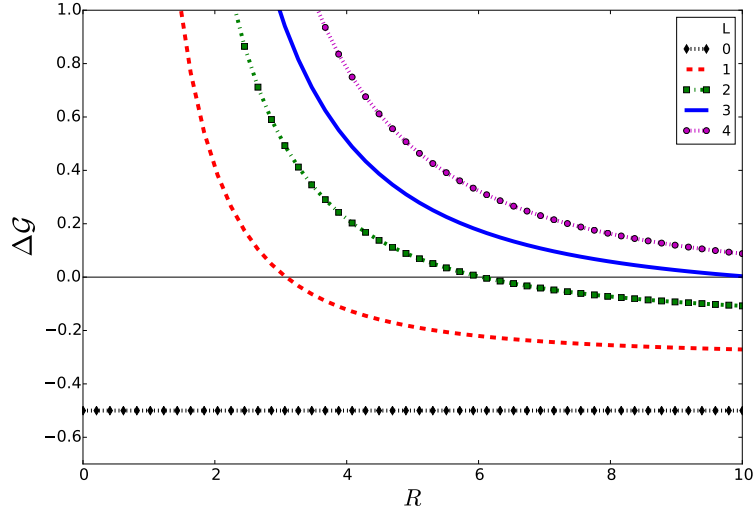


Figure 2.3: The Gibbs free energy difference between the superconducting and the normal states as a function of the cylinder's radius for vorticity ranging from  $L = 0$  to  $L = 4$  in case of a vortex fixed at the center ( $\kappa = 2.1$ ). The excited vortex state only exists in the negative range of this difference.

instance, the extreme value of this plot,  $R = 10$ , shows that the  $L = 0, 1, 2$  states are EVS whereas the  $L = 3, 4$  ones are not. The Gibbs free energy has the following values,  $\Delta\mathcal{G} = -0.27, -0.11, 0.003$  and  $0.09$  for  $L = 1, 2, 3, 4$ , respectively. The EVS exists for  $R > R_c$ ,  $R_c = 3.1, 6.0, 10.2, 17.3$  for  $L$  equal to  $1, 2, 3, 4$ , respectively.

### 2.6.2 Vorticity $L = 1$ at any position

The analytical function of  $z$  that describes the order parameter of a single vortex at any position  $0 \leq |a| \leq R$  inside a disk is given by,

$$\psi = c_0 \frac{\frac{z}{R} - \frac{a}{R}}{1 - \frac{z}{R} \frac{\bar{a}}{R}}, \quad (2.64)$$

where  $c_0$  is the order parameter value at the boundary. The coordinate  $z$  and the position  $a$  can be expressed in polar form,  $z = r e^{i\theta}$  and  $a = a_0 e^{i\alpha}$ , where we can

consider  $\alpha = 0$  without any loss of generality.

$$\psi = c_0 R \frac{r e^{i\theta} - a_0}{R^2 - a_0 r e^{i\theta}}. \quad (2.65)$$

The density of superconducting electrons is given by,

$$|\psi|^2 = |c_0|^2 \cdot R^2 \frac{r^2 + a_0^2 - 2 a_0 r \cos(\theta)}{R^4 + a_0^2 r^2 - 2 a_0 r R^2 \cos(\theta)}. \quad (2.66)$$

The integrals of Eqs.(2.41),(2.42) and (2.43) can be exactly obtained, as it is demonstrated in appendix B, and are given by,

$$I_2 = 2 - \frac{R^2}{a_0^2} - \left( \frac{R^2}{a_0^2} - 1 \right)^2 \ln \left( 1 - \frac{a_0^2}{R^2} \right), \quad (2.67)$$

$$I_4 = -4 \left( \frac{R}{a_0} \right)^4 + 6 \left( \frac{R}{a_0} \right)^2 - 1 - 4 \left( \frac{R}{a_0} \right)^2 \left[ \left( \frac{R}{a_0} \right)^2 - 1 \right]^2 \ln \left( 1 - \frac{a_0^2}{R^2} \right), \text{ and,} \quad (2.68)$$

$$I_\Upsilon = \frac{4}{R^2}. \quad (2.69)$$

Next, we take two special limits of these expressions. In the first one the vortex is just slightly displaced from the center, and the expressions of the previous section must be retrieved. This is the limit  $a_0 \rightarrow 0$ , but to obtain it, the following approximate expansion for the logarithm function must be introduced,  $\ln(1 - x^2) \approx -x^2 - x^4/2 - x^6/3 - x^8/4 - x^{10}/5 - x^{12}/6$ . Then, one obtains the needed approximated expressions for the integrals  $I_2$  and  $I_4$ , respectively,

$$I_2 \approx \frac{1}{2} + \frac{1}{3} \left( \frac{a_0}{R} \right)^2 + \frac{1}{12} \left( \frac{a_0}{R} \right)^4 + \frac{1}{30} \left( \frac{a_0}{R} \right)^6 + \frac{1}{60} \left( \frac{a_0}{R} \right)^8 - \frac{2}{15} \left( \frac{a_0}{R} \right)^{10} + \frac{1}{6} \left( \frac{a_0}{R} \right)^{12}, \quad (2.70)$$

$$I_4 \approx \frac{1}{3} + \frac{1}{3} \left( \frac{a_0}{R} \right)^2 + \frac{2}{15} \left( \frac{a_0}{R} \right)^4 + \frac{1}{15} \left( \frac{a_0}{R} \right)^6 - \frac{8}{15} \left( \frac{a_0}{R} \right)^8 + \frac{2}{3} \left( \frac{a_0}{R} \right)^{10}. \quad (2.71)$$

From these approximated expressions we can easily verify that  $I_2 = 1/2$ ,  $I_4 = 1/3$  and  $I_\Upsilon = 4/R^2$ , which are exactly the Eqs.(2.53), (2.54) and (2.55) for  $L = 1$ .

The other interesting limit is the vortex very near to the boundary of the cylinder. To treat it we change to the coordinate that express the distance of the vortex to the boundary, defined by  $y \equiv R - a_0$ . Inserting this new parameter into the order parameter we obtain the superconducting density which is given by,

$$|\psi|^2 = c_0^2 \frac{\left(\frac{y}{R}\right)^2 + \left(1 - \frac{y}{R}\right)^2 - 2\left(1 - \frac{y}{R}\right) \frac{r}{R} \cos(\theta)}{1 + \left(\frac{r}{R}\right)^2 \left(1 - \frac{y}{R}\right)^2 - 2\left(1 - \frac{y}{R}\right) \frac{r}{R} \cos(\theta)}. \quad (2.72)$$

The local magnetic field (Eq.(2.32)) takes into account the density given by Eq.(2.72). The expressions for  $c_0$  and  $H'$ , given by Eq.(2.46) and Eq.(2.47), respectively, are functions of  $I_2$  and  $I_4$ , which in terms of the coordinate  $y$  are given by,

$$I_2 = 2 - \left(1 - \frac{y}{R}\right)^{-2} - \left[\left(1 - \frac{y}{R}\right)^{-2} - 1\right]^2 \ln \left[1 - \left(1 - \frac{y}{R}\right)^2\right], \text{ and,} \quad (2.73)$$

$$I_4 = -4\left(1 - \frac{y}{R}\right)^{-4} + 6\left(1 - \frac{y}{R}\right)^{-2} - 1 - 4\left(1 - \frac{y}{R}\right)^{-2} \left[\left(1 - \frac{y}{R}\right)^{-2} - 1\right]^2 \ln \left[1 - \left(1 - \frac{y}{R}\right)^2\right]. \quad (2.74)$$

Similarly the Gibbs free energy density (Eq.(2.48) or Eq.(2.49)) is a function of Eq.(2.73) and Eq.(2.74), but also of Eq.(2.69), which renders it explicitly  $R$  dependent.

Very near to the boundary of the cylinder  $R \gg y$ , which means that the limit  $y \approx 0$  must be taken. Consider only the first order term in the expansion in  $y$  to obtain that  $I_2 \approx 1 - 2y/R$  and  $I_4 \approx 1 - 4y/R$ , and so,  $I_2/I_4 \approx 1 + 2y/R$ . Then, we

obtain that,

$$H' \approx \frac{1}{2\kappa^2} + \frac{1}{\kappa^2} \left(1 - \frac{1}{2\kappa^2}\right) \frac{y}{R}, \text{ and,} \quad (2.75)$$

$$c_0^2 \approx 1 + 2 \left(1 - \frac{1}{2\kappa^2}\right) \frac{y}{R}. \quad (2.76)$$

The paramagnetic magnetization becomes,

$$M_3 \approx 2 \frac{y}{R}. \quad (2.77)$$

The Gibbs free energy density is given by,

$$\Delta\mathcal{G} \approx -\frac{1}{2} \left(1 - \frac{4}{R^2}\right) + \left[ \frac{1}{\kappa^2} + \frac{4}{R^2} \left(1 - \frac{1}{2\kappa^2}\right) \right] \frac{y}{R}. \quad (2.78)$$

For  $R \rightarrow \infty$ ,  $c_0^2 = 1$ ,  $H' = 1/2\kappa^2$ ,  $M_3 = 0$  and  $\Delta\mathcal{G} = -1/2$ , which means that the homogenous state is recovered.

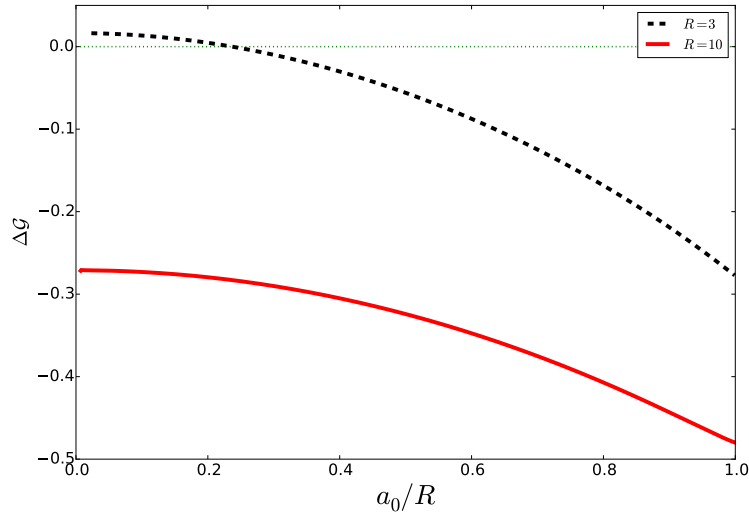


Figure 2.4: The Gibbs free energy difference between the superconducting and the normal states as a function of the vortex's position inside the cylinder for the case of vorticity one. Two radius of cylinders are considered ( $\kappa = 2.1$ ). The excited vortex state only exists in the negative range of this difference.

Fig. 2.4 shows the Gibbs free energy density as a function of the ratio  $a_0/R$ . The plotted curves are obtained from Eq.(2.48) with  $c_0^2$  given by Eq.(2.46) and the values of the integrals  $I_2$ ,  $I_4$  and  $I_\Upsilon$  given by Eqs.(2.67), (2.68) and (2.69), respectively. The two cases shown,  $R = 3$  and  $R = 10$ , demonstrate that the existence of EVS depends on the position of the vortex. In both cases the Gibbs free energy decreases monotonically from the center to the boundary of the cylinder. For  $R = 10$  the vortex in any position is in an EVS, since the Gibbs free energy is always negative, but this is not so for the  $R = 3$  cylinder. There, the Gibbs free energy is positive for  $a_0 < 0.24R$  such that only for  $a_0 > 0.24R$  there is an EVS. The Gibbs free energy is null for  $a_0 = 0.24R$  and decreases to reach the value  $\Delta\mathcal{G} = -0.27$  at the boundary.

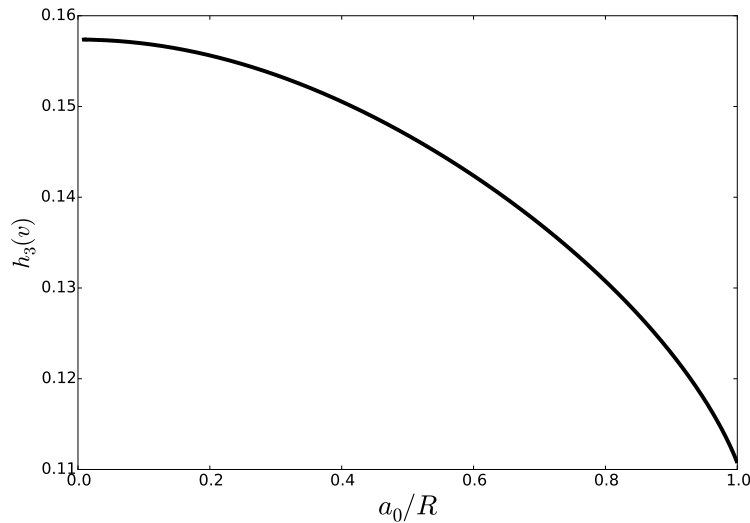


Figure 2.5: The magnetic field at the center of the vortex as a function of the position of the vortex inside the cylinder ( $\kappa = 2.1$ ). To recover the value for Niobium at the temperature of  $T = 7.7 K$  the vertical axis must be multiplied by  $H_{c2}(T = 7.7 K) = 780 Oe$ .

Fig. 2.5 illustrates how the local magnetic field at the vortex center varies as a function of the vortex position. This figure shows that this field  $h_3(v)$  depends on the ratio  $a_0/R$  according to Eq.(2.51). Thus, it only depends on the ratio  $I_2/I_4$ , defined by Eq.(2.67) and Eq.(2.68), respectively. The local field is maximum at the vortex center.

From this figure we verify that  $h_3(v)$  reaches a maximum when the vortex is at the center and slowly decreases when the vortex is positioned at the boundary. Fig. 2.5 is in agreement with Fig. 2.2 since  $h_3(0)$  for  $a_0 = 0$  corresponds to  $h_3(r = 0)$  for  $L = 1$ .

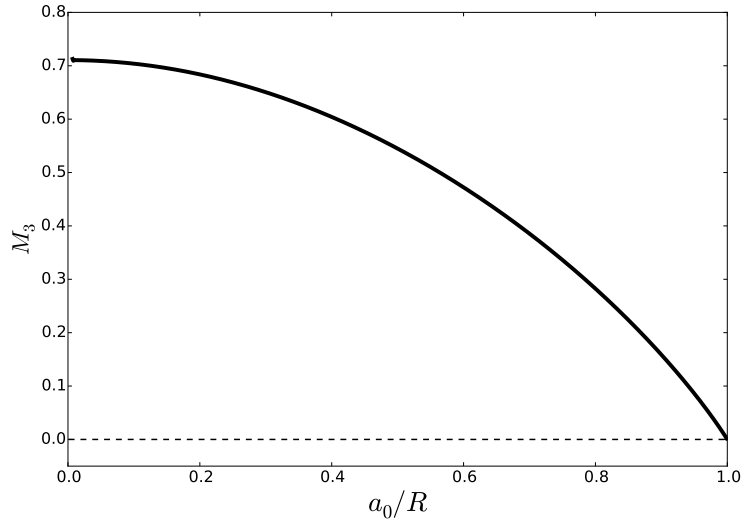


Figure 2.6: The magnetization as a function of the position of the vortex inside the cylinder ( $\kappa = 2.1$ ). To recover the value for Niobium for the temperature of  $T = 7.7 K$  the vertical axis must be multiplied by  $H_{c2}(T = 7.7 K)/8\pi\kappa^2 = 7.0 Oe$ .

Fig. 2.6 shows the paramagnetic magnetization as a function of the ratio  $a_0/R$  as obtained from Eq.(2.50). Interestingly, the magnetization depends on the position of the vortex, according to the integrals  $I_2$  and  $I_4$ , given by Eq.(2.67) and Eq.(2.68), respectively. The magnetization is stronger for the vortex near to the cylinder's center and weaker near to the cylinder border. For a vortex at the boundary,  $a_0 = R$ , the magnetization vanishes because  $I_2 = 1$ . This is consistent with the description of the exit of the vortex, although  $h_3(v)$  is not zero as can be seen in Fig. 2.5. The vortex next to the boundary means that the superconducting density is almost homogenous on the entire region of the cylinder and the integral  $I_2$  is almost equal to the unity what makes the magnetization goes to zero as can be seen from Eq.(2.50).

Finally, the three rows of Fig. 2.7 depict the vortex at three different positions,

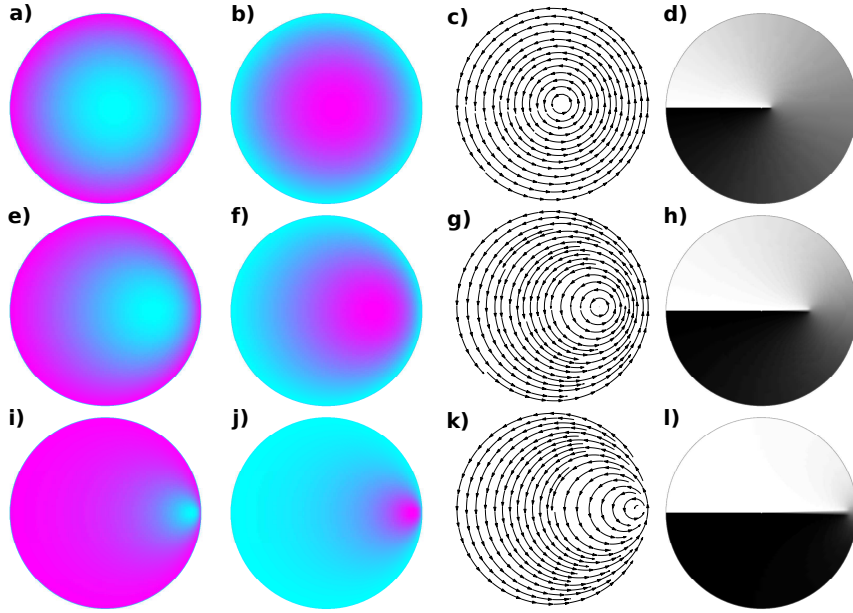


Figure 2.7: The superconducting density, the local magnetic field, the electric current density and the order parameter phase are depicted at three different positions of the vortex inside the cylinder,  $a_0/R = 0.1$  ((a) to (d)),  $0.5$  ((e) to (h)), and  $0.9$  ((i) to (l)). Figures (a), (e) and (i) display the density in (color on line) scheme ranging from low density (cyan) to high density (magenta). The (color on line) scheme is distinct for each of these three figures, as the density varies from zero at the center of the vortex to  $c_0^2$  at the boundary, whose value varies according to the position of the vortex inside the cylinder (see Eqs.(2.66), (2.46), (2.73) and (2.74)). The local magnetic field is shown in figures (b), (f) and (j), and the color scheme is distinct for each of these three figures. It ranges from the maximum at the center of the vortex (magenta), according to Eq.(2.32) and Eq.(2.51), to zero at the boundary (cyan). Figures (c), (g) and (k) show the vortex current around the vortex obtained from Eq.(2.16). Figures (d), (h) and (l) show the phase of the order parameter. The discontinuity line splitting the white to the black region shows the existence of a single vortex inside the cylinder.

$a_0/R = 0.1, 0.5$  and  $0.9$ , respectively. The columns correspond to the density, local magnetic field, current and phase, respectively. The density is obtained from Eq.(2.66) and Eq.(2.46), with the integrals of Eq.(2.73) and Eq.(2.74). Therefore, the density ranges from zero at the center of the vortex to the maximum value  $c_0^2$  at the boundary. The density is shown in Figs. 2.7(a), (e) and (i) in color (on line) scheme ranging from low density (cyan) to high density (magenta). The local magnetic field is obtained from Eq.(2.32) and ranges from the value given by Eq.(2.51) at the center of the vortex to zero at the boundary. Thus, the (color on line) scheme of Figs. 2.7(b),

(f) and (j) ranges from the maximum at the center of the vortex (magenta) to zero at the boundary (cyan). The vortex current is obtained from Eq.(2.16) and depicted in Figs. 2.7(c), (g) and (k). Notice that there is no current flowing out of the cylinder as the vortex moves towards the boundary, which is a general property guaranteed by the present formalism. Finally, Figs. 2.7(d), (h) and (l) show the phase of the order parameter, defined as  $\tan^{-1}(\psi_I/\psi_R)$ . The discontinuity, represented as a straight line that abruptly separates white to black, confirms the presence of a vortex in the cylinder.

## 2.7 Conclusion

In this chapter we defined the excited vortex state, which is a vortex state left inside the superconductor after the external applied field is switched off. The excited vortex state must have a free energy lower than the normal state otherwise the superconducting state collapses into the normal state. The excited vortex state is unstable in the sense that vortices must leave the superconductor since their presence is thermodynamically forbidden. However vortices are topologically stable as long as the superconducting state exists.

All our results stem directly from the first order equations used by A. A. Abrikosov to predict the vortex lattice. We discussed how the presence of a boundary to a non-superconducting region changes the results obtained by A. A. Abrikosov, gives an additional contribution to the Gibbs free energy density and renders the EVS solutions.

As a demonstration of the presented method, we obtained solutions for different angular momenta for the EVS with a vortex positioned in the cylinder's center. We found that there is a minimal radius for a cylinder to support such vortex states.

The order parameter, the local magnetic field, the magnetization and the Gibbs free energy density are calculated. Besides that, we obtained the vortex states for angular momentum  $L = 1$  with the vortex core positioned at different distances from the center. Then, we demonstrated that the states where the vortex are near the cylinder edge provides a lower free energy, which implies the instability of the EVS. We found a direct connection between the present problem and the theory of conformal mapping. We predicted values for the magnetization, which we showed to be intrinsically paramagnetic, in thin long wires of niobium.

# Chapter 3

## Vortex states in type *I* mesoscopic superconductors

In this chapter, we discuss the extension of the A. A. Abrikosov's classification of superconductors in type *I* and *II* and the need of a review of this classification in mesoscopic superconductors presenting a boundary to a non-superconducting region. We consider the first order equations approach, that is the same procedure used by A. A. Abrikosov when he proposed the existence of vortices in superconductors, to analyze the energy contributions due the boundary of a superconducting cylinder in a longitudinal magnetic field. We show the existence of vortex solutions in a type *I* superconducting cylinder immersed in a longitudinal magnetic field of intensity higher than the upper critical field  $H_{c2}$ .

### 3.1 Introduction

As it was introduced in chapter 1 and better discussed in chapter 2, in his seminal work A. A. Abrikosov [1] discovered vortices in type *II* superconductors through the GL theory. However, instead of solving the GL second order equations he solved the

so-called first order equations and then minimized the free energy to find the optimal vortex lattice. Here, we find that Abrikosov's original treatment of the GL theory also predicts vortex states in type *I* superconductors because of a negative surface energy caused by the external applied field. Therefore, the first order equation approach extended to the case that the superconductor has a border to a non-superconducting exterior region is studied here. For the sake of understanding we shall refer to type *I* and *II* superconductors according to the no border well-known definition. However, we prove here that this definition is outdated and must be reviewed.

Superconductors are classified by the ratio between the magnetic penetration depth  $\lambda$  and the coherence length  $\xi$ . According to the Ginzburg-Landau (GL) theory there are two types of superconductors, called *I* and *II*, whose properties are distinguished by the material parameter  $\kappa \equiv \lambda/\xi$  with respect to the critical value of  $\kappa_c = 1/\sqrt{2}$ . This division reflects the difference between the energy of an infinitely long interface occupied in one side by a superconductor and the other by the vacuum (normal region). According to the GL theory for special values of field and coupling, namely,  $H = H_c$  and  $\kappa_c$ , normal and superconducting regions can coexist with the same Gibbs free energy (zero difference between them). This is the so-called Bogomol'nyi critical point [15], originally derived in the context of high-energy physics. Nevertheless, the critical coupling  $\kappa_c$  was first pointed out by A.A. Abrikosov [1] in his study of the GL theory developed near  $H_{c2}$ . There, he shows that type *II* superconductors ( $\kappa > \kappa_c$ ) hosts vortices while type *I* superconductors ( $\kappa < \kappa_c$ ) does not. The vortices exist in the field range  $H \leq H_{c2}$  where the upper critical field obeys  $H_{c2}/H_c = \sqrt{2}\kappa$ , where  $H_c$  is the thermodynamic critical field.  $H_c \leq H_{c2}$  for  $\kappa > 1/\sqrt{2}$  and in the limit that  $\kappa \rightarrow 1/\sqrt{2}$ , we have that  $H_{c2} \rightarrow H_c$ , until these critical fields meet for  $\kappa = 1/\sqrt{2}$ . For the case  $\kappa < 1/\sqrt{2}$  ( $H_{c2} < H_c$ ) and these fields must be reinterpreted. In section 1.1 of the introductory chapter we started a discussion about the meaning of the critical fields and the critical values of

the GL parameter in type *I* and type *II* superconductors. Here, we continue that discussion in order to put in context the subject of the present chapter.

The widespread view is that for the type *I* superconductors only  $H_c$  has significance. The type *I* superconductor responds with shielding currents at the surface to the presence of an external applied field in order to cancel its presence inside. However, this purely Meissner phase collapses at a maximum field given by  $H_c$  in a first order transition. This contrasts with the disappearance of superconductivity in type *II* superconductors which is gradual and not abrupt, thus, through a second order transition. The density of vortices is such in  $H_{c2}$  that their normal cores touch each other and there is no more room for superconductivity. Nevertheless, according to M. Tinkham [140] and as noticed by many other authors [126, 49, 98, 96] long ago, the field  $H_{c2}$  exists in type *I* superconductors and has a physical interpretation. Consider a supercooling experiment where the sample is maintained at a fixed field  $H_a$  and the temperature is slowly lowered. The starting temperature is above the critical one ( $T > T_c$ ) such that the sample is in the normal state. Then, the temperature is lowered and the critical field line crossed in the diagram  $H$  versus  $T$ , at the temperature defined by  $H_a = H_c(T)$ . The sample is expected to abruptly become a superconductor at this crossing, but this is not so. The transition to superconductivity only takes place at a lower field  $H = H_{c2}(T)$ . This is because at a first order transition the effect of supercooling must be included, which means that a state of higher energy (the normal state), though unstable, remains and does not decay into the state of lower energy (the superconducting state) simply because there is an energy barrier separating both. This meta-stability disappears at  $H = H_{c2}(T)$  and for  $H < H_{c2}(T)$  the sample is in the superconducting state. We show here, that in the vicinity above  $H_{c2}(T)$  there are vortices in the type *I* superconductors.

Interestingly, surface superconductivity also exists for type *I* superconductor [49,

[98]. According to D. Saint-James and P. G. de Gennes [126] surface superconductivity arises above  $H_{c2}$  at a field defined by  $H_{c3} = 1.69H_{c2}$ . This expression can be written as  $H_{c3} = 1.69\sqrt{2}\kappa H_c = 2.37\kappa H_c$ . This defines the “special” value  $\kappa = 1/2.37 = 0.417$  and some authors proposed that type  $I$  superconductors are also split into two groups although this is disputed by others [154, 155]. M. Tinkham [140] pointed out that the field  $H_{c3}$ , and not  $H_{c2}$ , sets limit of supercooling in a type  $I$  superconductor. Since  $H_{c2} = \sqrt{2}\kappa H_c$  there are materials with  $\kappa$  between  $1/(1.69\sqrt{2})$  and  $1/\sqrt{2}$ , that is, in the range  $0.42 \leq \kappa \leq 0.707$  such that it holds that  $H_{c2} < H_c < H_{c3}$ . Therefore, for the materials within this range of  $\kappa$  the supercooling phase, expected to occur in the range  $(H_{c2}, H_c)$ , is absent since it is overshadowed by  $H_{c3}$ . These superconductors are defined as *type 1.5 superconductors* by M. Tinkham [140].

Interestingly, the metastability of the normal state under decreasing field down to a surface supercooling field  $H_{c3}$  became an experimental tool to determine the bulk parameter  $\kappa$  of several type  $I$  superconductors [126, 96, 13, 12], and coincides with the value obtained by using other experimental methods [82]. For instance, a technique of dividing a superconducting film into very many small squares allowed the observation of the supercooling field and it was found the presence of surface superconductivity in type  $I$  superconductors [13].

Several theoretical analysis of the GL theory are suggestive of the existence of vortices in type  $I$  superconductors [86, 95, 49]. Recently, single quantum vortices have been observed in type  $I$  superconducting Pb film by using scanning Hall probe microscopy [56, 57]. The importance of boundary conditions imposed on the order parameter by the geometrical confinement as well as surface barriers and demagnetizing effects was also pointed out in type  $I$  nanowires which shows the formation of a one-dimensional row of single-quantum vortices [45]. A phase of singly quantized vortices in type  $I$  superconductors has been found by G. R. Berdiyrov *et al.* [8] in a

mesoscopic superconductor rectangular prism (three-dimensional) with  $\kappa < 1/\sqrt{2}$ . Theoretical calculations made on the GL theory by I. G. de Oliveira [33] shows the presence of single quantized vortices above a certain critical field in case of a very long cylinder (two-dimensional) in case of a superconductor with  $\kappa = 1/\sqrt{2}$ . The latter two publications propose a phase diagram for mesoscopic superconductors unveiling the presence of quantized vortices. These numerical analysis give support to the present analytical results.

In summary, by using the same approach of A.A. Abrikosov, namely, by using the first order equations to solve the GL theory, but now extending it to include the presence of an external border, we show the existence of vortex states in type *I* superconductors for  $H > H_{c2}$ . The range of field that allows this state has an upper bound, namely, it is limited to a maximum field that can be taken as an  $H_{c3}$ , although it is not the state of P. G. de Gennes [32]. They have distinct physical properties although it is a negative surface energy created by the external applied magnetic field that sustains both. Nevertheless, the present vortex states live inside the superconductor, whereas P. G. de Gennes' only live in a rim surrounding the superconductor. The range of fields that guarantee the present states is dependent on the geometry and size of the sample, as discussed here.

It is well-known that a thin film made of a type *I* superconductor can turn into type *II*, regardless of any external boundary simply because the thickness of the film,  $d$ , modifies the existing London penetration length to create an effective one, the so-called Pearl screening length [120],  $\lambda_{eff} = 2\lambda^2/d$  such that  $\kappa_{eff} \equiv \lambda_{eff}/\xi$  is larger than  $1/\sqrt{2}$  [86, 25, 72]. To avoid such effect we think of very long cylinders with the applied field oriented along the major axis.

Recently, A. V. Vagov and co-workers [130, 144, 142, 143] have shown that

the standard GL approach can be regarded just as the lowest-order theory in a  $t = 1 - T/T_c$  expansion of the self-consistent gap equation from the Gorkov's equation. However, if next orders on  $t$  are included the energy associated with a surface between the superconducting and the normal phases is substantially modified. They proceeded to calculate the temperature dependence of  $\kappa_c$ , defined as the critical value of the GL parameter at which the surface energy becomes zero. Instead of a single point they find a critical parameter region where the energy is the same of the Bogomol'nyi point  $((\kappa; T) = (\kappa_c; T_c), H = H_c)$ . This topological degeneracy, lifted at  $T < T_c$ , is then the source of a wide diversity of unconventional phenomena in the critical interval of  $\kappa$  around  $\kappa_c$ . We remark that A. V. Vagov and co-workers do not include the effect of the external boundary whereas we do it although only in the tree level of the standard GL theory. It would be interesting to include the next order corrections in  $t$  in the present treatment thus go beyond the standard GL theory for the treatment of mesoscopic superconductors.

For the sake of completeness and in order to make the reading of the present chapter easier, we repeat some key expressions of the last chapter. Notice that the functions  $\tilde{\alpha}(t)$  and  $\tilde{\beta}(t)$  must be taken equal to one in order to retrieve the last chapter's theory. We also point out to a change in notation with respect to the previous chapter. The function  $\alpha(t)$  is positive defined below the critical temperature and not negative, as done in the previous chapter.

## 3.2 Ginzburg-Landau for type *I* superconductors

It is well-known that the thermodynamic critical field,  $H_c$ , of metals, which are type *I* superconductors, and the London penetration length, are best fitted by the

following expressions

$$H_c(t) = (1 - t^2)H_c(0), \quad (3.1)$$

$$\lambda(t) = \frac{1}{\sqrt{1 - t^4}}\lambda(0), \quad (3.2)$$

where  $t \equiv \frac{T}{T_c}$ ,  $H_c(0)$  and  $\lambda(0)$  are their zero temperature values. From it we determine the temperature behavior of some parameters. The coherence length follows from the expression  $H_c(t) = \Phi_0/2\pi\sqrt{2}\xi(t)\lambda(t)$  and by using the above expressions, one obtains that,

$$\xi(t) = \sqrt{\frac{1 + t^2}{1 - t^2}}\xi(0). \quad (3.3)$$

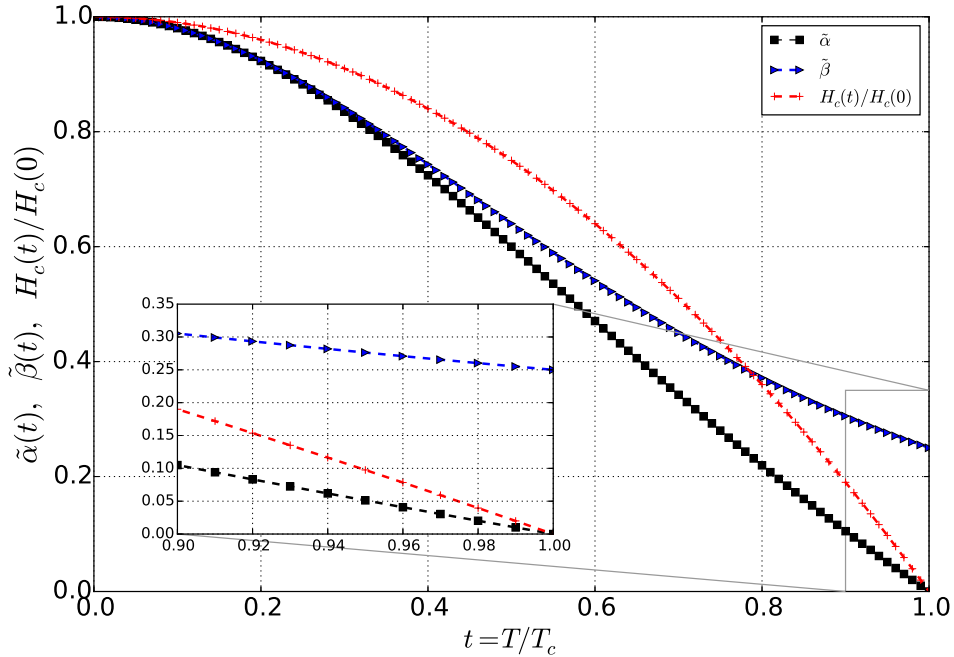


Figure 3.1: The critical field,  $H_c(t)/H_c(0)$  and the field above which vortex states can be found,  $H_{c2}(t)/H_{c2}(0) = \tilde{\alpha}(t)$ , are shown in reduced units. The condensate parameter,  $\tilde{\beta}(t)$ , is also displayed here.

According to the GL theory,  $\xi^2(t) = \hbar^2/2m\alpha(t)$ , and so,

$$\alpha(t) = \alpha_0 \tilde{\alpha}(t), \quad \tilde{\alpha}(t) \equiv \frac{1 - t^2}{1 + t^2}. \quad (3.4)$$

The critical field is related to the GL parameters as  $H_c^2(t)/4\pi = \alpha^2(t)/\beta(t)$ , which gives that,

$$\beta(t) = \beta_0 \tilde{\beta}(t), \quad \tilde{\beta}(t) \equiv \frac{1}{(1+t^2)^2}. \quad (3.5)$$

$\alpha_0$  and  $\beta_0$  are positive constants that correspond to the respective zero temperature values [140, 111]. Therefore, in this chapter we assume a different definition for the GL parameters,  $\alpha$  and  $\beta$ , of that given in the previous chapters, in order to best describe the temperature dependence of type *I* superconductors. Here, the temperature dependence of the mentioned parameters is given by the functions  $\tilde{\alpha}(t)$  and  $\tilde{\beta}(t)$  that are shown in Fig. 3.1. The upper critical field is  $H_{c2} = \Phi_0/2\pi\xi^2(t)$ , and so,

$$H_{c2}(t) = \frac{1-t^2}{1+t^2} H_{c2}(0) = \tilde{\alpha}(t) H_{c2}(0). \quad (3.6)$$

Next, we obtain the important relation between the upper critical field and the thermodynamic critical field at a given temperature. We have,

$$H_{c2}(t) = \frac{\sqrt{2}\kappa}{1+t^2} H_c(t). \quad (3.7)$$

It is well known that for mesoscopic superconductors the GL theory provides a good description for temperatures much lower than the critical temperature [37]. Therefore, we incorporate the above temperature behavior into the GL theory. We consider a very long superconductor submitted to an external constant magnetic field oriented along the major axis,  $\vec{H} = H_a \hat{x}_3$  such that effects of the top and the bottom are ignored and any cross sectional area, described by coordinates  $(x_1, x_2)$ , describes the physical properties of the superconductor. Therefore, the local magnetic field is perpendicular to this plane,  $h_3$ .

In this chapter we use the two-dimensional definition of the Gibbs free energy

density difference  $\Delta\mathcal{G} \equiv \mathcal{G}_S - \mathcal{G}_N$  given in section 2.2 from previous chapter, but we include the temperature dependence of the GL parameters  $\tilde{\alpha}(t)$  and  $\tilde{\beta}(t)$  defined above by Eq.(3.4) and Eq.(3.5). The Gibbs free energy density difference is given by

$$\Delta\mathcal{G} = \int_{\Sigma} \frac{d^2x}{\Sigma} \left\{ -\alpha(t)|\psi|^2 + \frac{\beta(t)}{2}|\psi|^4 + \frac{|\vec{D}\psi|^2}{2m} + \frac{(h_3 - H_a)^2}{8\pi} \right\}, \quad (3.8)$$

where the operator  $\vec{D} = D_1\hat{x}_1 + D_2\hat{x}_2$ , with  $D_j \equiv (\hbar/i)\partial_j - qA_j/c$ ,  $j = 1, 2$ , was defined in chapter 1, and is repeated here for completeness.

We introduce here the dimensionless units, which are zero temperature parameters, such that the explicit temperature dependence remains explicit in the theory. The notation is  $\xi_0 \equiv \xi(0)$ ,  $\lambda_0 \equiv \lambda(0)$  and  $\kappa \equiv \lambda_0/\xi_0$ . Hence, the penetration length,  $\lambda_0 = (mc^2/4\pi q^2\psi_0^2)^{1/2}$ , the coherence length,  $\xi_0 = (\hbar^2/2m\alpha_0)^{1/2}$ , and also  $\psi_0 = (\alpha_0/\beta_0)^{1/2}$  depend on  $\alpha_0$  and  $\beta_0$  which were previously defined. Hence, it holds that  $\kappa = (\beta_0/2\pi)^{1/2} mc/\hbar q$ . Let us refer just in this paragraph to the dimensionless units by the prime notation. For instance, distance is measured in terms of the coherence length such that  $\vec{x} = \xi_0\vec{x}'$ . The magnetic field is expressed in units of the upper critical field,  $\vec{h} = H_{c2}\vec{h}'$ ,  $H_{c2}(0) = \sqrt{2}\kappa H_c(0) = \Phi_0/2\pi\xi_0^2$ ,  $\Phi_0 = hc/q$ , where  $H_c(0) = \Phi_0/2\pi\sqrt{2}\lambda_0\xi_0$  is the thermodynamic critical field. Thus,  $H_{c2}(0) = \Phi_0/2\pi\xi_0^2$  is shortly called  $H_{c2}$ . Then, the dimensionless vector potential is given by  $\vec{A} = H_{c2}\xi_0\vec{A}'$ , and the covariant derivative becomes  $D_j = \hbar D'_j/\xi_0$ ,  $D'_j \equiv \frac{1}{i}\partial'_j - A'_j$  since  $\partial_j = \partial'_j/\xi_0$ . The current is defined by  $\vec{J} = (cH_{c2}/4\pi\xi_0)\vec{J}'$ . The dimensionless order parameter is obtained from  $\psi = \psi_0\psi'$ . Lastly, the dimensionless magnetization comes from  $M_3 = M'_3H_{c2}/8\pi\kappa^2$  since  $\psi_0^2\mu_B = H_{c2}/8\pi\kappa^2$ . Notice that any length, such as the radius of a disk is also scaled,  $R = \xi_0R'$ . Hereafter, we drop the prime notation though the dimensionless units are being used.

The Gibbs free energy difference in reduced units becomes,

$$\Delta\mathcal{G} = \int_{\Sigma} \frac{d^2x}{\Sigma} \left\{ -\tilde{\alpha}(t)|\psi|^2 + \frac{1}{2}\tilde{\beta}(t)|\psi|^4 + |\vec{D}\psi|^2 + \kappa^2 (h_3 - H_a)^2 \right\}, \quad (3.9)$$

and the Ginzburg-Landau (GL) equations are given by,

$$\vec{D}^2\psi - \tilde{\alpha}(t)\psi + \tilde{\beta}(t)|\psi|^2\psi = 0, \quad (3.10)$$

$$\vec{\nabla} \times \vec{h} = \vec{J}, \quad \vec{J} = \frac{1}{\kappa^2} \left( \psi^* \vec{D}\psi + c.c. \right). \quad (3.11)$$

The mathematical identity introduced in chapter 2 by Eq.(2.8) provides a dual view of the kinetic energy and is the gateway to introduce the first order equations. The dimensionless form of Eq.(2.8) is given by

$$|\vec{D}\psi|^2 = |D_+\psi|^2 + h_3|\psi|^2 + 2\kappa^2 (\partial_1 J_2 - \partial_2 J_1). \quad (3.12)$$

For a finite sample, boundary conditions must be imposed and they correspond to no current flowing out of the superconductor, as vacuum is assumed outside, and that the local field inside must be equal to the applied field outside. The former condition is automatically satisfied by imposing that the normal derivative of the order parameter vanishes. The perimeter of the cylinder and the cross section area are called  $\Upsilon$  and  $\Sigma$ , respectively, and  $\hat{n}$  is perpendicular outward to the boundary. The kinetic energy dual view displays a superficial (perimetric) term that stems from the current circulating in the boundary. For a bulk superconductor, where  $\Sigma \rightarrow \infty$ , this surface energy disappears because of periodic boundary conditions, as treated by A.A. Abrikosov [1]. However, in case of a finite cross section area,  $\Sigma$ , the current tangent to the boundary is important and in fact it is this surface (perimetric) term that sustains the onset of vortex states above the upper critical field.

The kinetic energy can be expressed as,

$$\int_{\Sigma} \frac{d^2x}{\Sigma} |\vec{D}\psi|^2 = \int_{\Sigma} \frac{d^2x}{\Sigma} [ |D_+\psi|^2 + h_3|\psi|^2 + 2\kappa^2 (\partial_1 J_2 - \partial_2 J_1) ], \quad (3.13)$$

and the current also acquires a new form given by

$$J_1 = \frac{1}{2\kappa^2} \{ (D_+\psi)^*\psi + \psi^*(D_+\psi) - \partial_2|\psi|^2 \}, \quad (3.14)$$

$$J_2 = \frac{1}{2\kappa^2} \{ i [(D_+\psi)^*\psi - \psi^*(D_+\psi)] + \partial_1|\psi|^2 \}. \quad (3.15)$$

The imposition of the first order equations

$$D_+\psi = 0, \quad (3.16)$$

$$h_3 = H' - \frac{1}{2\kappa^2}|\psi|^2, \quad (3.17)$$

solves exactly one of the GL equations, namely, Ampère's law, while the other, the non-linear GL equation, is only approximately solved. Hence, the first order equations provide an approximate solution of the second order GL equations, given by Eq.(3.10) and Eq.(3.11). Notice that the so far free parameter  $H'$  is important to adjust the local field to the external one at the boundary. Interestingly,  $H'$  is also the local field at the vortex core since there  $\psi = 0$ , and so,  $h_3 = H'$ . In possession of the solutions of the first order equations, one seeks among them the parameters that render the Gibbs free energy difference a minimum.

The condition of Eq.(3.16) inserted into the expressions for the kinetic energy and current density leads to simplified expressions. The superconducting current density becomes

$$\vec{J} = \frac{1}{2\kappa^2} \hat{x}_3 \times \vec{\partial} |\psi|^2. \quad (3.18)$$

The surface term is given by,

$$\partial_1 J_2 - \partial_2 J_1 = \frac{1}{2\kappa^2} \vec{\partial}^2 |\psi|^2, \quad (3.19)$$

once assumed that the first order equations are satisfied.

Remarkably, the first order equations provide an exact solution of an integrated version of the non-linear GL equation. This integrated version corresponds to the non-linear GL equation multiplied by  $\psi^*$ , and integrated over the entire area  $\Sigma$  of the superconductor:

$$\int_{\Sigma} \frac{d^2x}{\Sigma} \psi^* \left\{ \vec{D}^2 \psi - \tilde{\alpha}(t) \psi + \tilde{\beta}(t) |\psi|^2 \psi \right\} = 0. \quad (3.20)$$

This equation turns into an algebraic one by inclusion of the first order equations and use of the dual formulation of the kinetic energy:

$$\int_{\Sigma} \frac{d^2x}{\Sigma} \left\{ [H' - \tilde{\alpha}(t)] |\psi|^2 + \left[ \tilde{\beta}(t) - \frac{1}{2\kappa^2} \right] |\psi|^4 \right\} = 0. \quad (3.21)$$

Notice that this equation together with Eq.(3.16) fully determine the order parameter. Eq.(3.16) is scale invariant and so any solution multiplied by an arbitrary constant is also a solution. This remaining overall constant is fully fixed by the above integrated equation. Finally, it remains to determine the local field  $h_3$  and this is done through Eq.(3.17).

We consider the integrated equation a keystone to the classification of type *I* and *II* superconductors and in fact it is written in A.A. Abrikosov's original paper that led to the discovery of vortices for type *II* superconductors. Notice that it contains two integrals, namely, the average value of  $|\psi|^2$  and of  $|\psi|^4$  in space. These average values are positively defined, fact that restricts the multiplicative constants to have opposite signs in order that the overall sum vanishes. Indeed, the well known

vortex solutions of the type *II* superconductors correspond to negative and positive coefficients multiplying  $|\psi|^2$  ( $H' < \tilde{\alpha}(t)$ ) and  $|\psi|^4$  ( $\tilde{\beta}(t) > 1/2\kappa^2$ ), respectively. Here, we show that the opposite situation, of positive ( $H' > \tilde{\alpha}(t)$ ) and negative coefficients ( $\tilde{\beta}(t) < 1/2\kappa^2$ ), respectively, is also possible and these solutions correspond to vortices in type *I* superconductors. These two types of solutions of the integrated equation leads a new definition of type *I* and type *II* superconductors in case of the presence of a boundary without affecting the previous one that only works in case of no boundary. Notice that the above integrated equation contains the field  $H'$  instead of  $H_a$ .

The boundary conditions, namely, of no current flowing out of the superconductor and of a continuous magnetic field through the boundary, can be satisfied by a sole requirement on the first order equations solution: the density  $|\psi|^2$  must be constant along the boundary. Once  $|\psi|^2$  is constant along the border, its gradient component tangential to this border vanishes and only the component perpendicular to it remains. The fact that  $\vec{\partial}|\psi|^2$  is normal to the surface, renders  $\vec{J}$  always tangent to this surface according to Eq.(3.18). The continuity of the magnetic field is fixed by the constant  $H'$ , which becomes a function of  $c_0$  and  $H_a$ , according to Eq.(3.17). By its turn, the parameter  $c_0$  is fixed by the non-linear integrated GL equation, Eq.(3.21). One has,

$$|\psi|^2 = c_0^2 \text{ for } \vec{x} \text{ at } \Upsilon, \text{ and,} \quad (3.22)$$

$$H' = H_a + \frac{1}{2\kappa^2}c_0^2. \quad (3.23)$$

Thus, the field at the vortex core is larger than the applied field ( $H' > H_a$ ).

Hereafter, we introduce a second level of approximation to our approach, which is to work with an approximate solution of the first order equations. Since we are

looking for fields slightly above  $H_{c2}$ , the magnetic field inside the superconductor must be nearly constant and approximately given to the external field  $H_a$ . Recall the interpretation that upon supercooling at a temperature  $T$  one can cross the thermodynamic critical field  $H_c(t)$  down to  $H_{c2}(t)$  and remain in the normal state which means that the field is homogeneous and equal to the applied field  $H_a$ . Therefore, we take that  $A_1 = -H_a x_2/2$  and  $A_2 = H_a x_1/2$  into Eq.(3.16).

Next, we study two types of solutions inside a disk of radius  $R$ . The first one is a giant vortex of vorticity  $L$  at the center of the disk.

$$\psi = c_0 \left(\frac{r}{R}\right)^L e^{iL\theta} e^{-\frac{1}{4}H_a(r^2-R^2)}, \quad (3.24)$$

where  $L$  is a non zero integer. The second is a single vortex slightly displaced from the center of the disk by  $a_0$ ,

$$\psi = c_0 R \frac{r e^{i\theta} - a_0}{R^2 - a_0 r e^{i\theta}} e^{-\frac{1}{4}H_a(r^2-R^2)}. \quad (3.25)$$

Both solutions fulfill the requirement of being constant at the disk border, which means  $|\psi(R)|^2 = c_0^2$ .

### 3.3 The Bogomol'nyi equations and the first order equations

The Bogomol'nyi [15] equations solve the GL theory for the thermodynamic critical field  $H_a = H_c$  and critical coupling  $\kappa = \kappa_c$ . Hence, they hold in the parameter space  $(H_a, \kappa)$  at the coexistence line where the normal and the superconducting states have the same energy. We show here that the presence of an external boundary spoils the Bogomol'nyi [15] equations as solutions of the GL theory. This can be clearly

seen by using the dual formulation of the kinetic energy, as shown here. In case of the present GL theory with  $\tilde{\alpha}(t)$  and  $\tilde{\beta}(t)$  parameters, the Bogomol'nyi equations are associated to the following values of coupling and field,

$$H_a = \tilde{\alpha}(t), \quad (3.26)$$

$$\kappa = \frac{1}{\sqrt{2\tilde{\beta}(t)}}. \quad (3.27)$$

By introducing the dual view of the kinetic energy, the Gibbs free energy can be written as,

$$\begin{aligned} \Delta\mathcal{G} &= \int_{\Sigma} \frac{d^2x}{\Sigma} \left\{ (-\tilde{\alpha} + h_3) |\psi|^2 + \frac{1}{2} \tilde{\beta} |\psi|^4 + \kappa^2 (h_3 - H_a)^2 \right\} \\ &+ \int_{\Sigma} \frac{d^2x}{\Sigma} |D_+\psi|^2 + \frac{1}{2} \oint_{\Upsilon} \frac{dl}{\Sigma} \hat{n} \cdot \vec{\partial} |\psi|^2. \end{aligned} \quad (3.28)$$

We reexpress it in the following fashion,

$$\begin{aligned} \Delta\mathcal{G} &= \int_{\Sigma} \frac{d^2x}{\Sigma} \left\{ \kappa^2 \left[ (h_3 - H_a)^2 + 2(h_3 - \tilde{\alpha}) \left( \frac{|\psi|^2}{2\kappa^2} \right) + \tilde{\beta} (2\kappa^2) \left( \frac{|\psi|^2}{2\kappa^2} \right)^2 \right] \right\} \\ &+ \int_{\Sigma} \frac{d^2x}{\Sigma} |D_+\psi|^2 + \frac{1}{2} \oint_{\Upsilon} \frac{dl}{\Sigma} \hat{n} \cdot \vec{\partial} |\psi|^2. \end{aligned} \quad (3.29)$$

Notice that for the special values of coupling and field, given by Eq.(3.26) and Eq.(3.27) the Gibbs free energy becomes the sum of two positive terms, because each one of them is the square of a given quantity, plus the surface energy.

$$\Delta\mathcal{G} = \int_{\Sigma} \frac{d^2x}{\Sigma} \left\{ \kappa^2 \left( h_3 - H_a + \frac{|\psi|^2}{2\kappa^2} \right)^2 + |D_+\psi|^2 \right\} + \frac{1}{2} \oint_{\Upsilon} \frac{dl}{\Sigma} \hat{n} \cdot \vec{\partial} |\psi|^2. \quad (3.30)$$

However, only in case the surface term is absent the minimum of the Gibbs energy is zero and so, reached rendering each of the squares equal to zero. These are the

Bogomol'nyi equations

$$h_3 = \tilde{\alpha}(t) - \tilde{\beta}(t)|\psi|^2, \quad (3.31)$$

$$D_+\psi = 0. \quad (3.32)$$

The well-known Bogomol'nyi equations associated to the standard GL theory can be retrieved by taking  $\tilde{\alpha} = \tilde{\beta} = 1$ ,  $\kappa = 1/\sqrt{2}$  and  $H_a = 1$  ( $H_{c2} = H_c$ ).

However, the Bogomol'nyi equations only reach the minimum of the free energy in case of no surface energy, namely,  $\Delta\mathcal{G} = 0$ . For a finite area superconductor the presence of the above surface energy makes the Bogomol'nyi equations no longer be able to describe the minimum of the Gibbs free energy, since the Gibbs free energy difference becomes,

$$\Delta\mathcal{G} = \frac{1}{2} \oint_{\Gamma} \frac{dl}{\Sigma} \hat{n} \cdot \vec{\partial} |\psi|^2, \quad (3.33)$$

which means that one is away from the coexistence line between the superconductor and the normal state.

We stress the distinction between the Bogomol'nyi equations and what we call first order equations. Indeed, the Bogomol'nyi equations are first order equations though restricted to the parameter space associated to the coexistence line (where they solve exactly the no-boundary GL theory). The present first order equations (Eq.(3.16) and Eq.(3.17)) are applicable to any field and coupling, although they provide only approximate solutions even in the case of no boundaries. Next, we use an approximate solution for them (field inside the superconductor constant and equal to  $H_a$ ) to determine the range of field and coupling that allows for vortex solutions in the GL theory. For this, we introduce their solution into the GL free energy and study for the allowed parameter range. Once the order parameter and

the local magnetic field satisfy the first order equations, the kinetic energy becomes,

$$|\vec{D}\psi|^2 = \left( H' - \frac{1}{\kappa^2} |\psi|^2 \right) |\psi|^2 + \frac{1}{2} \vec{\partial}^2 |\psi|^2, \quad (3.34)$$

where Eq.(3.23) relates  $H'$  to the applied field  $H_a$ . The Gibbs free energy becomes,

$$\begin{aligned} \Delta\mathcal{G} &= \int_{\Sigma} \frac{d^2x}{\Sigma} \left\{ -(\tilde{\alpha}(t) - H_a) |\psi|^2 + \frac{1}{2} \left( \tilde{\beta}(t) - \frac{1}{2\kappa^2} \right) |\psi|^4 \right. \\ &\quad \left. + \frac{1}{2} \vec{\partial}^2 |\psi|^2 + \kappa^2 (H' - H_a)^2 \right\}. \end{aligned} \quad (3.35)$$

We obtain the corresponding equation to what we have obtained in Eq.(2.27) in section 2.3.1, with the temperature dependence of the GL parameters, and the two additional terms as compared to Abrikosov's Gibbs free energy [1], which are the field energy due to  $H' \neq H_a$  and the surface (perimetrical) contribution of the normal gradient of  $|\psi|^2$ .

### 3.4 The existence of vortex states above the field

#### $H_{c2}$

We formulate the general properties of the GL theory for  $H > H_{c2}$  in terms of the integrals defined in the previous chapter, Eqs.(2.41), (2.42), and (2.43), whose definition we repeat here for completeness

$$I_2 \equiv \frac{1}{c_0^2} \int_{\Sigma} \frac{d^2x}{\Sigma} |\psi|^2, \quad (3.36)$$

$$I_4 \equiv \frac{1}{c_0^4} \int_{\Sigma} \frac{d^2x}{\Sigma} |\psi|^4, \quad (3.37)$$

$$I_{\Gamma} \equiv \frac{1}{c_0^2} \oint_{\Gamma} \frac{dl}{\Sigma} \hat{n} \cdot \vec{\partial} |\psi|^2. \quad (3.38)$$

For instance, the magnetization  $M_3$ , as it was shown in chapter 2, is obtained from the thermodynamical relation  $B_3 = H_a + 4\pi M_3$  and  $B_3 \equiv \int_{\Sigma} \frac{d^2x}{\Sigma} h_3$ . Eq.(3.17) gives

that  $B_3 = H' - c_0^2 I_2 / (2\kappa^2)$ . Then, there are two expressions for  $B_3$  and by using Eq.(3.23) the magnetization is given by,

$$M_3 = \frac{1}{2} \frac{c_0^2}{2\kappa^2} (1 - I_2). \quad (3.39)$$

According to the above expression vortex states can either be diamagnetic ( $I_2 > 1$ ) or paramagnetic ( $I_2 < 1$ ).

The integrated equation in terms of the above integrals and of the constant  $c_0^2$  becomes,

$$(H' - \tilde{\alpha}(t)) c_0^2 I_2 + \left( \tilde{\beta}(t) - \frac{1}{2\kappa^2} \right) c_0^4 I_4 = 0. \quad (3.40)$$

Replacing  $H'$  by  $H_a$  through Eq.(3.23) gives that,

$$[H_a - \tilde{\alpha}(t)] I_2 c_0^2 + \left[ \left( \tilde{\beta}(t) - \frac{1}{2\kappa^2} \right) I_4 + \frac{1}{2\kappa^2} I_2 \right] c_0^4 = 0. \quad (3.41)$$

This leads to the determination of  $c_0^2$  in terms of known parameters

$$c_0^2 = \left\{ \frac{2\kappa^2 (H_a - \tilde{\alpha}(t))}{\left(1 - \tilde{\beta}(t)2\kappa^2\right) - \frac{I_2}{I_4}} \right\} \frac{I_2}{I_4}. \quad (3.42)$$

We only seek solutions here above the upper critical field, namely,  $H_a > H_{c2}$ , which is equivalent to have the following conditions.

$$H_a > \tilde{\alpha}(t), \quad (3.43)$$

$$1 - \tilde{\beta}(t)2\kappa^2 > I_2/I_4. \quad (3.44)$$

Both numerator and denominator must be positive in Eq.(3.42). The latter condition

can be casted as condition for the GL parameter

$$\kappa \leq \sqrt{\frac{1 - I_2/I_4}{\tilde{\beta}(t)}} \frac{1}{\sqrt{2}}. \quad (3.45)$$

Thus, we conclude that  $I_4 > I_2$  must hold in order that a GL parameter exists to sustain the present vortex states. The ratio  $I_4/I_2$  is obtained here for a giant vortex at the center and for a single vortex slightly displaced from the center.

The condition of a real solution for  $c_0^2$  is necessary but not enough as the superconducting state is characterized by a free energy lower than the normal state, which means,  $\Delta\mathcal{G} < 0$ . We introduce the integrated equation into the Gibbs free energy density to obtain that,

$$\Delta\mathcal{G} = \int_{\Sigma} \frac{d^2x}{\Sigma} \left\{ \frac{1}{2} (H_a - \tilde{\alpha}(t)) |\psi|^2 + \kappa^2 (H' - H_a)^2 + \frac{1}{2} \vec{\partial}^2 |\psi|^2 \right\}. \quad (3.46)$$

Solutions above the upper critical field,  $H_a > \tilde{\alpha}(t)$ , have the first term positive. Since the second is also positive the only possibility to revert the overall sign is that the surface energy, which corresponds to the last term, be negative. We write the Gibbs energy difference as a function of  $c_0^2$ ,

$$\Delta\mathcal{G} = \frac{1}{2} [(H_a - \tilde{\alpha}(t)) I_2 + I_{\Gamma}] c_0^2 + \frac{1}{4\kappa^2} c_0^4. \quad (3.47)$$

Notice that this equation can be expressed as,

$$\Delta\mathcal{G} = \frac{1}{2} c_0^2 \left\{ [(H_a - \tilde{\alpha}(t)) I_2 + I_{\Gamma}] + \frac{1}{2\kappa^2} c_0^2 \right\}. \quad (3.48)$$

Hence, at the line where the superconducting and the normal states coexist,  $\Delta\mathcal{G} = 0$ , which means that the constant  $c_0^2$  assumes a specific value, denoted by  $c_0'^2$ , whose

value is given by,

$$c_0^{\prime 2} = -2\kappa^2 [(H_a - \tilde{\alpha}(t)) I_2 + I_\Upsilon]. \quad (3.49)$$

From Eq.(3.49), it stems the condition,

$$H_a < \tilde{\alpha}(t) - \frac{I_\Upsilon}{I_2}. \quad (3.50)$$

The condition that  $c_0^{\prime 2} = c_0^2$  gives an equation to determine the  $H_{c3}$  field.

$$H_a = \tilde{\alpha}(t) - \frac{I_\Upsilon}{I_2} \frac{1}{\frac{1}{(1-\tilde{\beta}(t)2\kappa^2)I_4 - I_2} + 1}. \quad (3.51)$$

Notice that this is an implicit equation since  $I_\Upsilon$ ,  $I_2$  and  $I_4$  are also functions of the applied field  $H_a$ . Its solution should be obtained through an iterative method, that is,  $H_a$  is replaced by the attempted solution, firstly guessed as  $\tilde{\alpha}(t)$ , in the right side to obtain the field  $H_a$  in the left. The procedure is carried until convergence is reached. Since we expect that  $H_a \approx \tilde{\alpha}(t)$ , a single iteration should be enough. Therefore, one obtains that

$$H_{c3}(t) \approx \tilde{\alpha}(t) - \frac{I_\Upsilon}{I_2(\tilde{\alpha})} \frac{1}{\frac{1}{(1-\tilde{\beta}(t)2\kappa^2)I_4(\tilde{\alpha}) - I_2(\tilde{\alpha})} + 1}. \quad (3.52)$$

### 3.4.1 The existence of vortex states slightly above the field $H_{c2}$

Slightly above  $H_{c2}$  we can analytically prove the existence of the present vortex solutions which means to show that the conditions  $c_0^2 > 0$  and  $\Delta\mathcal{G} < 0$  are satisfied. We can write the applied magnetic field by defining the small parameter  $\epsilon$  such that,

$$H_a = (1 + \epsilon)\tilde{\alpha}(t), \quad \epsilon \ll 1. \quad (3.53)$$

Under this condition the order parameter becomes very small since  $c_0^2 \sim \epsilon$  and further simplifications can be introduced into the theory by neglecting terms of order  $\epsilon^2$  and higher. The Gibbs energy becomes,

$$\Delta\mathcal{G} = \frac{1}{2}I_{\Gamma}c_0^2 + O(\epsilon^2). \quad (3.54)$$

This shows that vortex states slightly above the upper critical field exist because the surface energy is negative,  $I_{\Gamma} < 0$ . In this case, one obtains that

$$c_0^2 = \epsilon \left\{ \frac{2\kappa^2\tilde{\alpha}(t)}{\left(1 - \tilde{\beta}(t)2\kappa^2\right) - \frac{I_2}{I_4}} \right\} \frac{I_2}{I_4} + O(\epsilon^2). \quad (3.55)$$

## 3.5 Vortex solutions

We focus on the two particular cases of vortices on the cylinder, namely, of a vortex with vorticity  $L$  in its center and of a single vortex near to the center of the cylinder. For both we define the magnetic flux  $\phi \equiv H_a R^2$  where  $R$  is the radius of the cylinder. Notice that this is not the flux through the cross section area,  $H_a \pi R^2$ .

### 3.5.1 Vortices at the center

Consider a giant vortex with vorticity  $L$  at the center, whose order parameter is given by Eq.(3.24). Thus, the superconducting density  $|\psi|^2$  and the density to the square power  $|\psi|^4$  are given by

$$|\psi|^2 = c_0^2 \left(\frac{r}{R}\right)^{2L} e^{-\frac{1}{2}H_a(r^2-R^2)}, \quad (3.56)$$

$$|\psi|^4 = c_0^4 \left(\frac{r}{R}\right)^{4L} e^{-H_a(r^2-R^2)}. \quad (3.57)$$

The integrals (3.36) and (3.37) become,

$$I_2 = e^{\frac{1}{2}\phi} \int_0^1 dx x^L e^{-\frac{1}{2}\phi x}, \quad (3.58)$$

$$I_4 = e^{\phi} \int_0^1 dx x^{2L} e^{-\phi x}. \quad (3.59)$$

They are solved to obtain that,

$$I_2 = L! \left(\frac{2}{\phi}\right)^{L+1} \left\{ e^{\frac{\phi}{2}} - \left[1 + P_L\left(\frac{\phi}{2}\right)\right] \right\}, \quad (3.60)$$

and

$$I_4 = (2L)! \left(\frac{1}{\phi}\right)^{2L+1} \left\{ e^{\phi} - [1 + P_{2L}(\phi)] \right\}, \quad (3.61)$$

where  $P_L(x)$  is a polynomial given by,

$$P_L(\alpha) = \sum_{m=1}^L \frac{\alpha^m}{m!}. \quad (3.62)$$

The surface integral leads to,

$$I_{\Upsilon} = \frac{2}{R} \frac{d}{dr} \left[ \left(\frac{r}{R}\right)^{2L} e^{-\frac{1}{2}H_a(r^2-R^2)} \right]_{r=R}, \quad (3.63)$$

whose final formula is

$$I_{\Upsilon} = \frac{2}{R^2} (2L - \phi). \quad (3.64)$$

Thus, the giant vortices are only possible for the case  $I_{\Upsilon} < 0$  which renders the condition  $\phi > 2L$ . Interestingly, this condition can be physically understood by the following argument. Firstly, we obtain the current circulating inside the cylinder from Eq.(3.18) and Eq.(3.56).

$$\vec{J} = \frac{1}{2\kappa^2} \hat{x}_3 \times \hat{r} \frac{d|\psi|^2}{dr} = \frac{1}{2\kappa^2} \frac{\hat{\phi}}{r} (2L - H_a r^2) |\psi|^2. \quad (3.65)$$

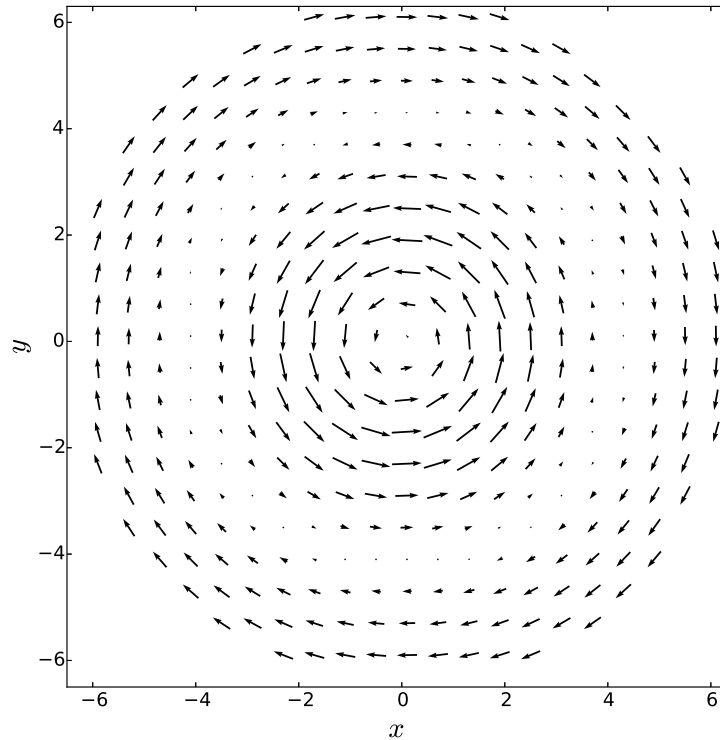


Figure 3.2: The current of a single vortex ( $L = 1$ ) at the center of the cylinder is shown here, as obtained from Eq.(3.65). The (paramagnetic) circulation around the vortex core prevails near the center but weakens towards the border and is overcome by the (diamagnetic) shielding currents. In between the current vanishes at  $\sqrt{2/H_a}$ , here taken as  $H_a = \tilde{\alpha}(0.9)$ . The radius of the cylinder, taken as  $R = 6.5$ , does not determine the radius of zero current.

The superconducting density  $|\psi|^2$  vanishes at the origin ( $|\psi|^2 \sim r^{2L}$  as  $r \rightarrow 0$ ) and reaches a maximum at  $r_0 \equiv \sqrt{2L/H_a}$  to then decrease from there on towards the border. Hence, the current circulates counterclockwise near the center, vanishes at  $r_0$  and then becomes clockwise. Interestingly, this current takes care of both the paramagnetic and diamagnetic contributions. As it was shown in Fig. 1.5 in chapter 1, the current near to the vortex core is of opposite sign with respect to the currents shielding the external field at the surface and they are both contained in this giant vortex solution. Notice that the critical radius  $r_0$  does not depend on

the radius  $R$  of the cylinder. Suppose that the field becomes intense enough such that the critical radius is at the border,  $r_0 = R$ . In this case, the shielding currents disappear and only the vortex current remains in the cylinder. Beyond this radius ( $r_0 > R$ ) the giant vortex state is no longer possible because the surface integral becomes positive,  $I_{\Gamma} > 0$ , according to Eq.(3.64). Fig. 3.2 pictorially depicts the current circulation around a single vortex at the center.

The ratio between the integrals is useful to know since it defines the parameter range where the solutions exist

$$\frac{I_4}{I_2} = \frac{(2L)!}{2^{L+1}L!} \frac{e^{\frac{\phi}{2}}}{\phi^L} \left\{ \frac{1 - [1 + P_{2L}(\phi)] e^{-\phi}}{1 - [1 + P_L(\frac{\phi}{2})] e^{-\frac{\phi}{2}}} \right\}. \quad (3.66)$$

In the limit of a very large flux  $\phi$  it is straightforward to check that  $I_4 > I_2$

$$\lim_{\phi \gg 1} \frac{I_4}{I_2} \rightarrow \frac{(2L)!}{2^{L+1}L!} \frac{e^{\frac{\phi}{2}}}{\phi^L}. \quad (3.67)$$

### 3.5.2 Magnetic flux piercing the superconducting cylinder

Next, we calculate the magnetic flux piercing the cylinder from the center to the radius determined by the maximum of the superconducting density which coincides with the value where the current density reverts the sense from positive (paramagnetic) to negative (diamagnetic), that is obtained by Eq.(3.65). The flux  $\Phi(\rho)$  as a function of an arbitrary radius denoted by  $\rho$  is defined by

$$\Phi(\rho) = \int_0^{2\pi} d\varphi \int_0^{\rho} h_3(r) r dr, \quad (3.68)$$

where the local magnetic field  $h_3(r)$  is given by Eq.(3.17).

Inserting the expression for  $h_3(r)$  in Eq.(3.68) we obtain

$$\Phi(\rho) = 2\pi \int_0^\rho \left[ H_a + \frac{c_0^2}{2\kappa^2} - \frac{c_0^2}{2\kappa^2} \left( \frac{r}{R} \right)^2 e^{H_a(R^2-r^2)/2} \right] r dr. \quad (3.69)$$

After a change of variables and simplifications, we perform the integration and obtain the following expression

$$\Phi(\rho) = \pi\rho^2 H_a + \pi\rho^2 \frac{c_0^2}{2\kappa^2} \left\{ 1 - \frac{R^2}{\rho^2} \left( \frac{2}{H_a R^2} \right)^{L+1} e^{H_a R^2/2} [\Gamma(L+1) - \gamma(L+1, H_a \rho^2/2)] \right\}, \quad (3.70)$$

where  $\Gamma(L+1)$  is the complete Gamma function and  $\gamma(L+1, H_a \rho^2/2)$  is the incomplete Gamma function.

From the obtained Eq.(3.70), we are able to know the flux due the local field to all extension of the cylinder for the angular momentum  $L = 1$ ,

$$\Phi(R) = \pi R^2 H_a + \pi R^2 \frac{c_0^2}{2\kappa^2} \left[ 1 + \left( \frac{2}{H_a R^2} \right)^2 \left( 1 + \frac{H_a R^2}{2} - e^{\frac{H_a R^2}{2}} \right) \right]. \quad (3.71)$$

We can also obtain the flux through the paramagnetic current area, which is the region starting at the center and delimited by the radius where the current density is null, namely,  $r_0 = \sqrt{2/H_a}$ ,

$$\Phi(r_0 = \sqrt{2/H_a}) = 2\pi + \frac{2\pi}{H_a} \frac{c_0^2}{2\kappa^2} \left[ 1 - 2(1 - 2e^{-1}) \frac{e^{\frac{H_a R^2}{2}}}{H_a R^2} \right]. \quad (3.72)$$

### 3.5.3 Results

We seek to determine the range of parameters that render the negative values for the Gibbs free energy density above  $H_{c2}$  for a single vortex state ( $L = 1$  in Eq.(3.24)) at the center of an Aluminum disk. Aluminum has the lowest GL parameter among metals,  $\kappa = 0.015$ . We focus here on the fixed temperature of  $T = 0.9T_c$ , which corresponds to  $\tilde{\alpha}(0.9) = 0.105$  and  $\tilde{\beta}(0.9) = 0.305$ . For this temperature  $2\kappa^2\tilde{\beta}(0.9) = 1.37 \cdot 10^{-4}$ , thus very small to the point that we can take  $1 - 2\kappa^2\tilde{\beta}(0.9) \approx 1.0$ . Then,  $c_0^2$  is positive upon the condition that  $I_2/I_4 \lesssim 1$  according to Eq.(3.42). The search for vortex solution for Aluminum in the range  $H > H_{c2} = \tilde{\alpha}(0.9)$  is focused on cylinders with the radii  $R = 6.0, 6.5, 7.0, 7.5$  and  $8.0$  under the magnetic field range  $H$  from  $\tilde{\alpha}(0.9)$  to  $1.8\tilde{\alpha}(0.9)$ .

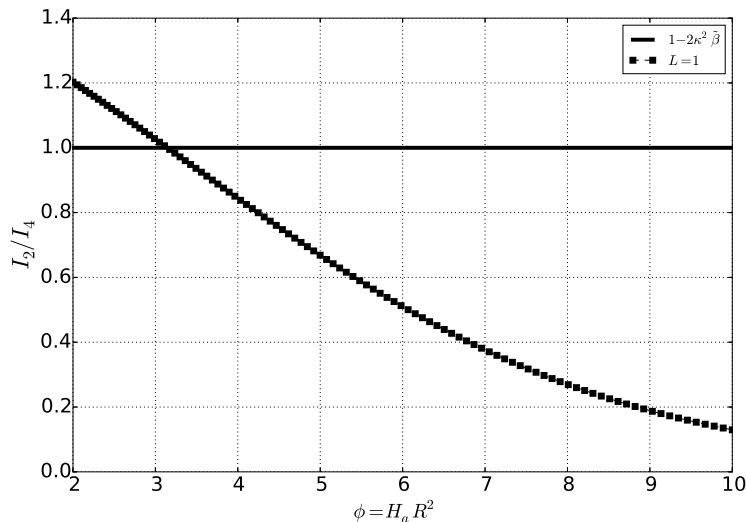


Figure 3.3: The line  $1 - 2\kappa^2\tilde{\beta}(0.9)$  and the ratio  $I_2/I_4$  are both shown ( $\kappa = 0.015$ ,  $t = 0.9$ ) here as a function of applied magnetic field. The ratio  $I_2/I_4$  only depends on  $\phi = H_a R^2$ .

Fig. 3.3 shows both the line  $1 - 2\kappa^2\tilde{\beta}(0.9)$  and the ratio  $I_2/I_4$  for  $L = 1$  as functions of  $\phi = H_a R^2$ . A more restrictive condition for the minimum radius than the

previous one is obtained. Recall that to have a negative surface integral,  $I_\Upsilon < 0$ , the condition  $H_a R^2 \geq 2$  must hold. Since the minimum applied field is  $H_{c2} = \tilde{\alpha}(0.9)$ , this condition becomes  $R \geq 4.36$ . Nevertheless, Fig. 3.3 shows a critical  $\phi = HR^2 \approx 3.12$  to have the condition  $I_2/I_4 \lesssim 1$  satisfied. For  $H_{c2} = \tilde{\alpha}(0.9)$  for this second condition that  $R > 5.45$  which then overwrites the first one.

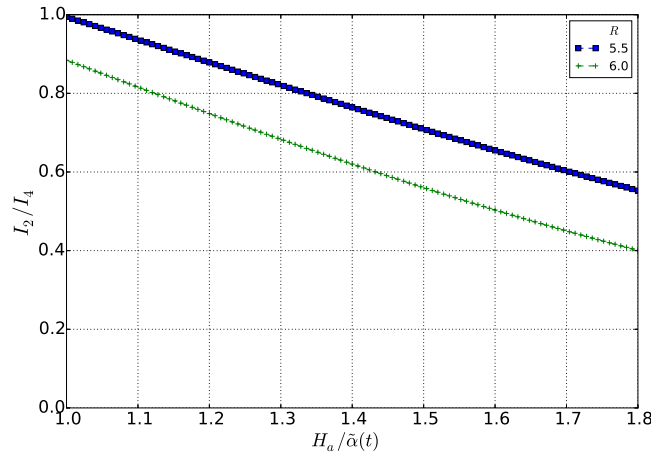


Figure 3.4: The line  $1 - 2\kappa^2\tilde{\beta}(0.9)$  and the ratio  $I_2/I_4$  ( $L = 1$ ) are shown ( $\kappa = 0.015$ ,  $t = 0.9$ ) for  $R = 5.5$  and  $R = 6.0$  as a function of the applied magnetic field.

We study two cylinders of radii  $R = 5.5$  and  $R = 6.0$  slightly above the critical value of  $R = 5.45$ . The ratio  $I_2/I_4$  is shown in Fig. 3.4 for these two radii in the studied range of magnetic field.

We find that the ratio falls below the line  $1 - 2\kappa^2\tilde{\beta}(0.9)$  and so, there are  $c_0^2$  values as shown in Fig. 3.5 as a function of the applied magnetic field.

The Gibbs free energy is shown in Fig. 3.6 for  $R = 5.5$  and  $R = 6.0$  in two ranges above the critical radius of  $R = 5.45$ . Indeed, the field range above  $\tilde{\alpha}(0.9)$  render the Gibbs energy smaller than zero for the cylinder  $R = 5.5$  is very small, as shown in the inset of Fig. 3.6. For  $R = 5.45$  this range collapses to zero.

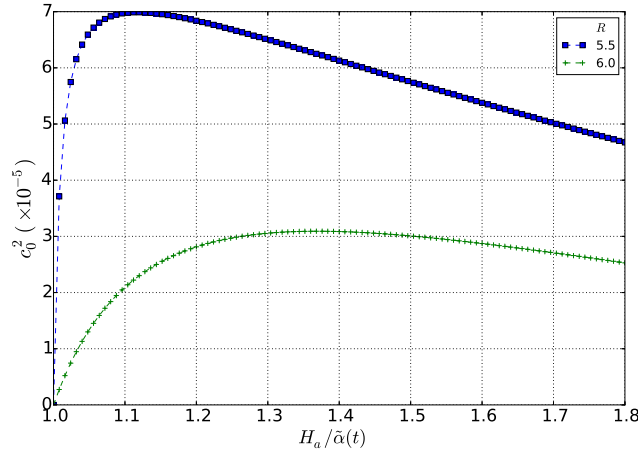


Figure 3.5: A single vortex at the center of the cylinder has its pair density at the surface shown ( $\kappa = 0.015$ ,  $t = 0.9$ ) for cylinder radii  $R = 5.5$  and  $R = 6.0$ .

Fig. 3.7 shows the ratio  $I_2/I_4$ , obtained from Eq.(3.66), for the selected set of radii and magnetic field range. This plot shows that the inequality  $I_2/I_4 \lesssim 1$  is always satisfied, and so, one can go ahead and search for a superconducting Gibbs energy below the normal state. Indeed, the coefficient  $c_0^2$  of Eq.(3.42) exist, as shown in Fig. 3.5 within the studied range of the applied field. We call the attention that according to Eq.(3.55) and Eq.(3.54) there is always this range although limited to the immediate neighborhood of  $H_{c2} = \tilde{\alpha}(t)$ .

The Gibbs energy density difference versus applied field is shown in Fig. 3.8 as obtained from Eq.(3.47). It takes into account the integrals Eq.(3.60), (3.64). The later describes the surface integral which must always be negative. The most interesting feature of Fig. 3.8 is to shown the existence of an optimal radius that features for  $R = 6.5$  the largest applied field windows (1.0 to 1.7)  $\tilde{\alpha}(0.9)$ . This means that as the radius enlarges from  $R = 6.0$  to 6.5 the applied field range, where the Gibbs energy density is negative, increases and once reached the maximum at  $R = 6.5$  it reduces again for  $R = 7.0$ . We also notice that for  $R = 6.5$  the Gibbs energy reaches its minimum value.

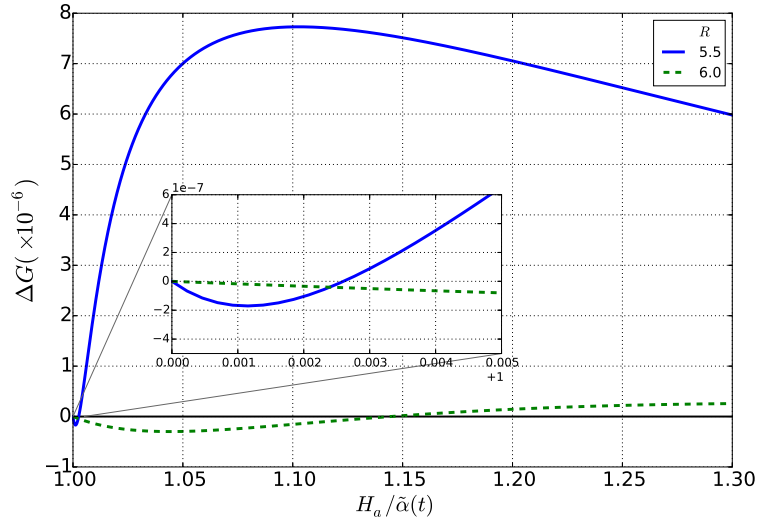


Figure 3.6: The difference in Gibbs energy between superconducting (one vortex at the center) and normal states is shown ( $\kappa = 0.015$ ,  $t = 0.9$ ) for cylinder radii  $R = 5.5$  and  $R = 6.0$  within a range of magnetic field shows that the negative range of the Gibbs energy difference is radically different for the two cylinders. The negative range for  $R = 5.5$  is shown in the vicinity of  $H_{c2} = \tilde{\alpha}(0.9)$  in the insertion.

The magnetization of such states follows from Eq.(3.39) and it requires the obtainment of  $I_2$  (Eq.(3.60)), which is shown in Fig. 3.9 versus the applied field range. The conclusion reached by this figure is that the state is diamagnetic in all its range. Notice that  $I_2$  has a monotonic growth with the field thus insensitive to the fact that the Gibbs energy difference flips sign at some field beyond which the vortex state no longer exists. Therefore, the magnetization beyond this field should be simply taken as equal to zero. Therefore, we conclude that the transition to the normal state is abrupt, therefore through a first order transition.

Fig. 3.10 shows that  $I_2 < 1$  for  $H_a < 1.128\tilde{\alpha}(0.9)$  which means a paramagnetic state, and for  $H_a > 1.128\tilde{\alpha}(0.9)$ ,  $I_2 > 1$ , therefore a diamagnetic state.

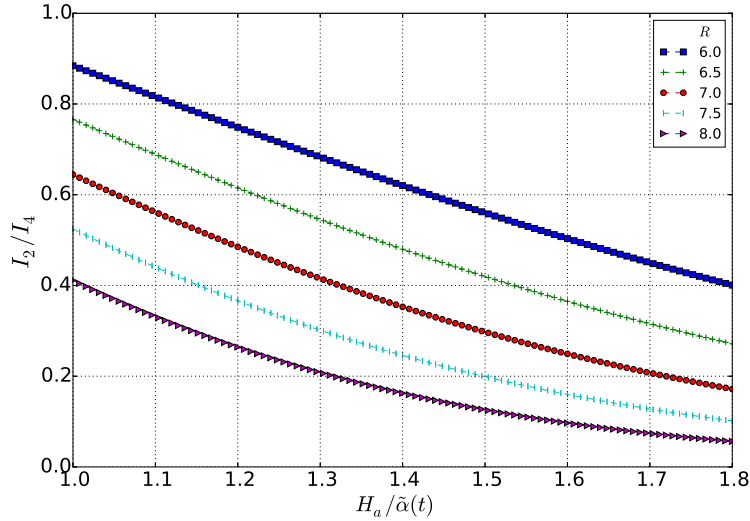


Figure 3.7: The line  $1 - 2\kappa^2\tilde{\beta}(0.9)$  and the ratio  $I_2/I_4$  ( $L = 1$ ) are shown here ( $\kappa = 0.015, t = 0.9$ ). The ratio is plotted for a selected set of cylinder radii and magnetic field range above the field range. The ratio must fall below the line in order that the single vortex state exist above  $H_{c2}$ .

### 3.5.4 Single vortex slightly displaced from the center

We address here the question whether the vortex state above the upper critical field is stable. For this, we concentrate on the single vortex ( $L = 1$ ) slightly displaced from the center by  $a_0$ . We shall find here that  $I_\gamma$  does not depend on  $a_0$ , hence the Gibbs energy  $\Delta\mathcal{G}$  (Eq.(3.54)) only depends on  $a_0$  through the ratio  $I_4/I_2$ , which is inside  $c_0^2$  and given by Eq.(3.55). Firstly, we notice such dependency of the ratio  $I_4/I_2$  is through the square,  $a_0^2$ , since  $I_4(a_0^2)$  and  $I_2(a_0^2)$ , fact that assures that the center is an equilibrium point. We want to show that  $\partial\Delta\mathcal{G}/\partial a_0 = 0$ , but it holds that  $\Delta\mathcal{G}(a_0^2)$ , then  $\partial\Delta\mathcal{G}/\partial a_0 = 2a_0\partial\Delta\mathcal{G}/\partial a_0^2$ , which vanishes for  $a_0 = 0$ . Next, it must be proven that this equilibrium is stable.

$$|\psi|^2 = c_0^2 R^2 \left( \frac{r^2 + a_0^2 - 2a_0 r \cos \theta}{R^4 + a_0^2 r^2 - 2a_0 r R^2 \cos \theta} \right) e^{-\frac{1}{2}H_a(r^2 - R^2)}, \quad (3.73)$$

$$|\psi|^4 = c_0^4 R^4 \left( \frac{r^2 + a_0^2 - 2a_0 r \cos \theta}{R^4 + a_0^2 r^2 - 2a_0 r R^2 \cos \theta} \right)^2 e^{-H_a(r^2 - R^2)}. \quad (3.74)$$

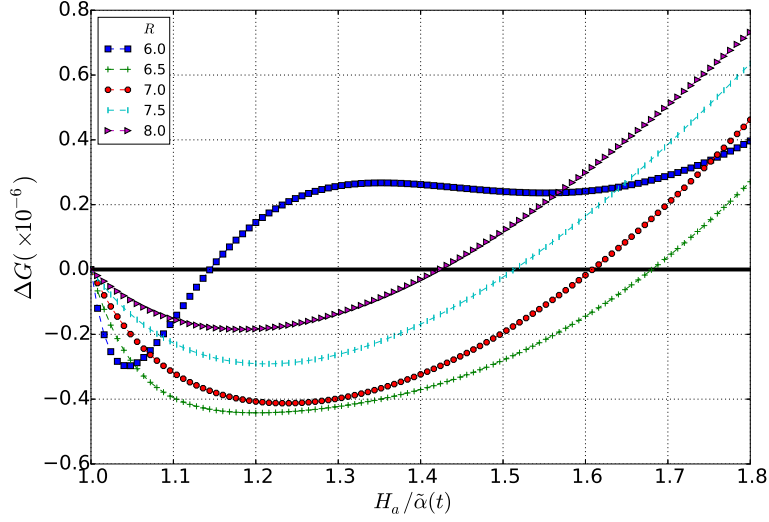


Figure 3.8: The difference in Gibbs energy between superconducting (one vortex at the center) and normal states is shown ( $\kappa = 0.015$ ,  $t = 0.9$ ) for a selected set of cylinder radii and magnetic field range above the field  $H_{c2} = \tilde{\alpha}(t)$ . The negative range is where the single vortex state can exist.

The integrals  $I_2$ ,  $I_4$  and  $I_\Upsilon$  are functions of  $a_0$ .

$$I_2 = \frac{1}{\pi} \int_0^R dr r f_2(r) e^{-\frac{1}{2}H_a(r^2-R^2)}, \quad (3.75)$$

$$f_2(r) = \int_0^{2\pi} d\theta \frac{r^2 + a_0^2 - 2a_0 r \cos(\theta)}{R^4 + a_0^2 r^2 - 2a_0 r R^2 \cos(\theta)}, \quad (3.76)$$

$$I_4 = \frac{R^2}{\pi} \int_0^R dr r f_4(r) e^{-H_a(r^2-R^2)}, \quad (3.77)$$

$$f_4(r) = \int_0^{2\pi} d\theta \frac{(r^2 + a_0^2 - 2a_0 r \cos(\theta))^2}{(R^4 + a_0^2 r^2 - 2a_0 r R^2 \cos(\theta))^2}, \quad (3.78)$$

$$I_\Upsilon = \frac{1}{\pi R} \int_0^{2\pi} d\theta \frac{\partial}{\partial r} \left[ f_\Upsilon(r, \theta) e^{-\frac{1}{2}H_a(r^2-R^2)} \right]_{r=R}, \quad (3.79)$$

$$f_\Upsilon(r, \theta) = R^2 \frac{r^2 + a_0^2 - 2a_0 r \cos(\theta)}{R^4 + a_0^2 r^2 - 2a_0 r R^2 \cos(\theta)}. \quad (3.80)$$

Eqs.(3.76), (3.78) and (3.80) have been previously defined in the appendix B as Eqs.(B.2), (B.4) and (B.6), respectively.

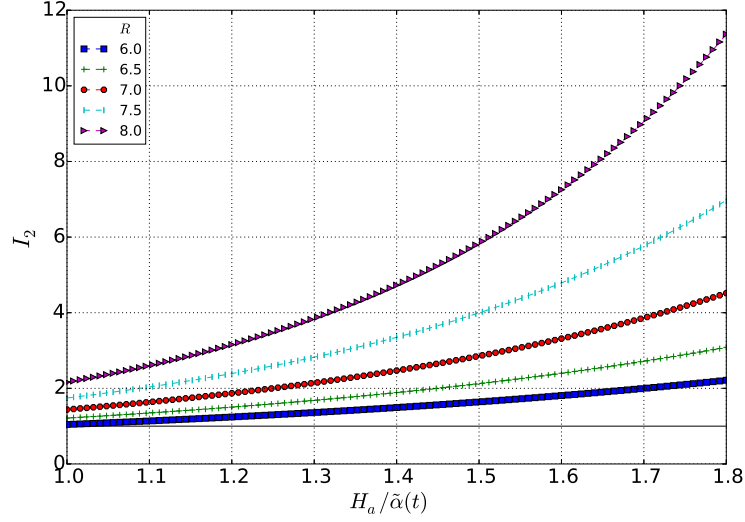


Figure 3.9:  $I_2$  is shown ( $\kappa = 0.015$ ,  $t = 0.9$ ) for selected set of cylinder radii and magnetic field range above the field  $H_{c2} = \tilde{\alpha}(t)$ . The states are diamagnetic since  $I_2 > 1$  in the whole field range for all radii.

The surface term can be written as,

$$I_\Upsilon = \frac{1}{\pi R} \int_0^{2\pi} d\theta \left[ \frac{\partial f_\Upsilon}{\partial r} - H_a R f_\Upsilon \right]_{r=R}. \quad (3.81)$$

Hence, we need to integrate,

$$\frac{\partial f_\Upsilon(R, \theta)}{\partial r} = \frac{2}{R} \frac{R^2 - a_0^2}{R^2 + a_0^2 - 2a_0 R^2 \cos \theta}, \quad (3.82)$$

$$f_\Upsilon(R, \theta) = 1. \quad (3.83)$$

By using the result for the integral, obtained before,

$$\int_0^{2\pi} dx \frac{1}{a + b \cos x} = \frac{2\pi}{(a^2 - b^2)^{1/2}}. \quad (3.84)$$

We finally reach that,

$$I_\Upsilon = \left( \frac{4}{R^2} - 2H_a \right), \quad (3.85)$$

which is the same result of Eq.(3.64) taken  $L = 1$ . We have just shown that the

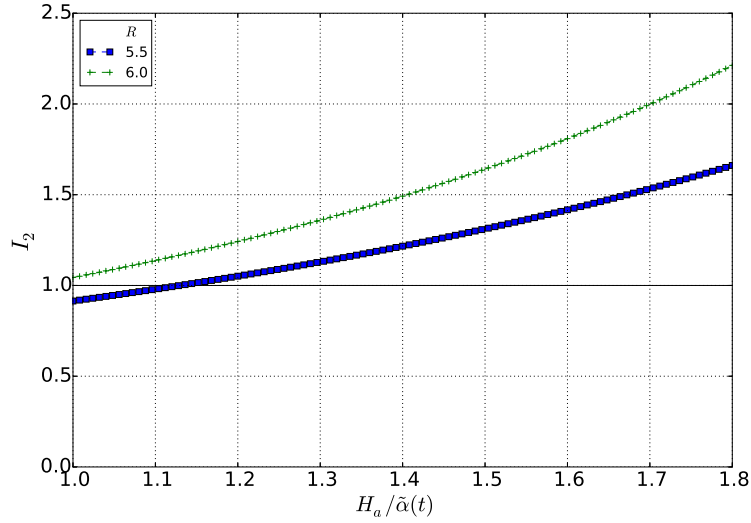


Figure 3.10:  $I_2$  is shown ( $\kappa = 0.015$ ,  $t = 0.9$ ) for cylinder radii  $R = 5.5$  and  $R = 6.0$  above the field  $H_{c2} = \tilde{\alpha}(t)$ . Notice that in the former case  $I_2 = 0$  for  $H_{c2} = 1.128\tilde{\alpha}(0.9)$ .

surface integral is independent of  $a_0$ .

The displacement from the center is small and so, we obtain that,

$$f_2(r) = \frac{2\pi}{R^2} \left\{ \left(\frac{r}{R}\right)^2 + \left(\frac{a_0}{R}\right)^2 \left[1 - \left(\frac{r}{R}\right)^2\right] \right\} + O\left(\frac{a_0}{R}\right)^4, \quad (3.86)$$

and

$$f_4(r) = \frac{2\pi}{R^4} \left\{ \left(\frac{r}{R}\right)^4 + \left(\frac{a_0}{R}\right)^2 \left[10\left(\frac{r}{R}\right)^2 - 8\left(\frac{r}{R}\right)^4 - 2\left(\frac{r}{R}\right)^6\right] \right\} + O\left(\frac{a_0}{R}\right)^4, \quad (3.87)$$

where  $O(a_0/R)^4$  represents terms of this order and higher which are abandoned.

The integrals become,

$$I_2 = e^{\frac{1}{2}\phi} \int_0^1 dx \left[ x + \left(\frac{a_0}{R}\right)^2 (1-x)^2 \right] e^{-\frac{1}{2}\phi x} + O\left(\frac{a_0}{R}\right)^4, \quad (3.88)$$

$$I_4 = e^{\phi} \int_0^1 dx \left[ x^2 + \left(\frac{a_0}{R}\right)^2 (10x - 8x^2 - 2x^3) \right] e^{-\phi x} + O\left(\frac{a_0}{R}\right)^4. \quad (3.89)$$

We calculate such integrals in the limit that  $\phi \gg 1$ . In this case, the exponential factor  $\exp(-\phi x)$  is expected to contribute only near to the origin, at  $x \approx 0$ . Therefore, only the lowest power of  $x$  contributes and according to Eq.(3.58) the dominant terms are given by,

$$I_2 \approx e^{\frac{1}{2}\phi} \int_0^1 dx \left[ x + \left(\frac{a_0}{R}\right)^2 \right] e^{-\frac{1}{2}\phi x} + O\left(\frac{a_0}{R}\right)^4, \quad (3.90)$$

$$I_4 \approx e^\phi \int_0^1 dx \left[ x^2 + \left(\frac{a_0}{R}\right)^2 (10x) \right] e^{-\phi x} + O\left(\frac{a_0}{R}\right)^4, \quad (3.91)$$

which render the results

$$I_2 \approx \frac{e^{\frac{1}{2}\phi}}{(\phi/2)^2} \left[ 1 + \left(\frac{a_0}{R}\right)^2 \frac{\phi}{2} \right] + O\left(\frac{a_0}{R}\right)^4, \quad (3.92)$$

$$I_4 \approx \frac{e^\phi}{(\phi)^3} \left[ 1 + \left(\frac{a_0}{R}\right)^2 5\phi \right] + O\left(\frac{a_0}{R}\right)^4. \quad (3.93)$$

At this point, we can address our relevant question concerning the behavior of  $I_4/I_2$  with respect to  $a_0^2$ . This is fundamental matter to determine the stability of the vortex solution. We find that,

$$\frac{I_4}{I_2} \approx \frac{e^{\frac{1}{2}\phi}}{2\phi} \left[ 1 + \frac{9}{2} \left(\frac{a_0}{R}\right)^2 \phi \right] + O\left(\frac{a_0}{R}\right)^4, \quad (3.94)$$

As the coefficient in front of  $(a_0/R)^2$  is positive the conclusion is that the ratio  $I_4/I_2$  increases with  $a_0^2$ . According to Eq.(3.55) and Eq.(3.54) the Gibbs energy decreases as the single vortex is displaced with respect to the center towards the edge of the disk. Therefore, the single vortex solution is stable by displacement from the center. A single vortex can exist at the center of a cylinder slightly above the upper critical field provided that  $\kappa$  satisfies Eq.(3.45). It remains to compare its Gibbs energy with other competitive states, such as the  $L = 2$  case and others.

### 3.6 Conclusion

We verified, through solutions of the first order equations, that the existence of a boundary in mesoscopic superconductors, in an applied uniform magnetic field, inserts a negative contribution that decreases the Gibbs free energy density. It is commonly accepted that only  $H_c$  has significance for the type  $I$  superconductors but we discussed here the role played by the  $H_{c2}$  and  $H_{c3}$  in mesoscopic superconductors of type  $I$ . We discussed the relation of the first order equations with the Bogomol'nyi equations that describes exactly the superconductivity at the critical magnetic field  $H_c$  for a material with the critical GL parameter  $\kappa_c = 1/\sqrt{2}$ . The main contribution of this chapter is the demonstration of the existence of vortex states in type  $I$  infinitely long superconductors for an applied field above the critical field  $H_{c2}$ . In addition to these results, we calculated the superconducting current density and verified that in the studied regime there is the coexistence of paramagnetic and diamagnetic currents inside the cylinder. These currents circulate in the same form as show in Fig. 1.5 that represents a configuration after the entrance of a vortex in a cylinder under the effect of a longitudinal applied magnetic field. Finally, we obtained the Gibbs free energy density as a function of the applied magnetic field for cylinders of different radii.

# Chapter 4

## Numerical methods

In this chapter we start the second part of the thesis that consists in the study of the interaction of a superconducting thin film in the presence of the magnetic field produced by magnetic elements near to it. These elements are magnetic dipoles that interact among themselves and set up in collective arrangements. The superconductor-magnetic hybrid systems are interesting because the stray field from these elements is not homogeneous and has positive and negative regions that locally affect the superconductor in different forms. Hence, the fact that the external magnetic field is not spatially homogeneous makes this chapter distinct from the previous ones where the field external to the cylinder, if any, is homogeneous. We consider the superconducting film thin enough that only the stray field component perpendicular to it is relevant as the tangent one is not able to influence in many properties such as the nucleation and arrangement of vortices in the superconductor.

In order to describe the behavior of the present hybrid systems a numerical treatment is adopted and its discussion is important with respect to the forthcoming chapters. In this chapter we focus on the description of the theoretical approaches important for the treatment of the superconducting film and of the magnetic elements. In the former we seek to solve the non-linear Ginzburg-Landau equation and determine the order parameter in the thin film, whereas in the latter

we determine the spatial distribution of the magnetic moments in space that leads to the external magnetic field that acts in the film. In case of the permalloy we discuss the interaction among its magnetic constituents that give rise to the magnetic vortex. These theoretical approaches enter our simulation method used to study the interaction of the superconducting thin film with a fixed array of permalloy.

## 4.1 Time-dependent Ginzburg-Landau equations

The state of a superconducting film interacting with an external applied field is fully described by the order parameter and the vector potential. Both are solutions of the GL equations, introduced in chapter 1 by Eq.(1.40) and Eq.(1.41). Nevertheless, this is true only in case that a time independent equilibrium state can be reached. As it was shown in chapter 2, these equilibrium solutions are a minimum of the Gibbs free energy density functional Eq.(2.1). However, it is possible a description of time dependent processes through the so-called time-dependent Ginzburg-Landau (TDGL) equations.

The TDGL equations were formulated by A. Schmid [128] and posteriorly they were derived from a microscopic treatment by L. P. Gor'kov and G. M. Éliashberg [68]. This formulation is a generalization of the time-independent GL equations that features the gauge invariance at all times. This extension is obtained from the assumption that the temporal derivative of the order parameter  $\psi$  is proportional to the variational derivative of the energy functional  $\Delta\mathcal{G}$  relative to the complex conjugate of the order parameter  $\bar{\psi}$ ,

$$-\Gamma \frac{\partial \psi}{\partial t} = \frac{\delta \mathcal{G}}{\delta \bar{\psi}} = \frac{\vec{D}^2 \psi}{2m} + \alpha \psi + \beta |\psi|^2 \psi, \quad (4.1)$$

where  $\Gamma$  is the diffusivity constant of the order parameter. The time requested to

stabilize  $\psi$ , that is, to bring it to the equilibrium, in case such equilibrium exists, is proportional to  $\Gamma$ . The GL parameters  $\alpha$  and  $\beta$  present the usual temperature dependence, and the operator  $\vec{D}$  is the two-dimensional covariant derivative whose components were defined as  $D_j \equiv (\hbar/i)\partial_j - qA_j/c$ , for  $j = 1, 2$  in chapter 1

However, the above equation (4.1) is not gauge invariant. In other words, this equation is not invariant under a gauge transformation,

$$\begin{aligned}\vec{A}(\vec{r}, t) &\rightarrow \vec{A}(\vec{r}, t) + \nabla\Lambda(\vec{r}, t), \\ V(\vec{r}, t) &\rightarrow V(\vec{r}, t) - \frac{1}{c} \frac{\partial\Lambda(\vec{r}, t)}{\partial t}, \\ \psi(\vec{r}, t) &\rightarrow \psi(\vec{r}, t)e^{iq\Lambda(\vec{r}, t)/\hbar c},\end{aligned}\tag{4.2}$$

where  $V(\vec{r}, t)$  is the electric potential. The time-dependent Ginzburg-Landau equation for  $\psi$ , which is gauge invariant, is given by,

$$-\Gamma \left( \frac{\partial\psi}{\partial t} + i\frac{q}{\hbar} V \psi \right) = \frac{\delta\mathcal{G}}{\delta\bar{\psi}} = \frac{\vec{D}^2\psi}{2m} + \alpha\psi + \beta|\psi|^2\psi.\tag{4.3}$$

To obtain the gauge invariant equation for the vector potential we consider the superconductor submitted to an applied electric current, such that the total current density is given by  $\vec{J}_T = \vec{J} + \vec{J}_n$ , where the current due to the normal electrons obeys the Ohm's law  $\vec{J}_n = \sigma\vec{E}$ , where  $\sigma$  is the electric conductivity. Expressing the electric field in terms of the electric potential and the vector potential  $\vec{E} = -\nabla V - (1/c)\partial\vec{A}/\partial t$ , we obtain the gauge invariant TDGL equation for  $\vec{A}$ ,

$$\sigma \left( \frac{\partial\vec{A}}{\partial t} + \nabla V \right) = \frac{q}{2m} \left[ (\vec{D}\bar{\psi})\psi + \bar{\psi}(\vec{D}\psi) \right] - \frac{c}{4\pi} \nabla \times \nabla \times \vec{A}.\tag{4.4}$$

To solve numerically the Eq.(4.3) and Eq.(4.4), we write them in a dimensionless

form. We also choose the special gauge where  $V(\vec{r}, t) = 0$ . Then, the equations become,

$$\frac{\partial \psi}{\partial t} = -\frac{1}{\eta} \left[ \vec{D}^2 \psi - \psi + |\psi|^2 \psi \right], \quad (4.5)$$

$$\frac{\partial \vec{A}}{\partial t} = \frac{1}{2} \left[ (\overline{\vec{D}\psi})\psi + \bar{\psi}(\vec{D}\psi) \right] - \kappa^2 \nabla \times \nabla \times \vec{A}, \quad (4.6)$$

where we have defined the following constants  $\eta \equiv (4\pi\lambda^2\sigma\alpha)/(c^2\Gamma)$ , with  $\kappa = \lambda/\xi$  the usual GL coupling constant. We use the dimensionless units given in chapter 2 and only repeated here for completeness: the order parameter is written in units of  $\psi_0 = (|\alpha|/\beta)^{1/2}$ , distance is measured in terms of the coherence length  $\xi$ , the magnetic field is expressed in units of the upper critical field  $H_{c2} = \sqrt{2}\kappa H_c = \Phi_0/2\pi\xi^2$ ,  $\Phi_0 = hc/q$ , where  $H_c = \Phi_0/2\pi\sqrt{2}\lambda\xi$  is the thermodynamical field. Then, the vector potential is given in units of  $H_{c2}\xi$ .

We stress here that we only consider the superconducting film in the presence of a fixed time independent external field created by the magnetic elements such that  $\partial\vec{A}/\partial t = 0$ . Although the external field is not homogeneous away from its sources, which are the magnetic elements, we have that  $\nabla \times \nabla \times \vec{A} = 0$ . Hence, the second equation reduces to the divergence of the superconducting current equal to zero, or  $\vec{\nabla} \cdot [(\overline{\vec{D}\psi})\psi + \bar{\psi}(\vec{D}\psi)] = 0$ . In summary we only solve Eq.(4.5) which is nothing but the equation that describes the relaxation to equilibrium. We will interpret our time dependent simulation as a search for the equilibrium solution. Notice that in the presence of an external applied current this equilibrium only exists until the spontaneous nucleation of vortex antivortex pairs begins to occur. This follows an increase in the current beyond its critical value. Beyond this point there is no equilibrium though there is an intermittent stationary state which consists on the periodic onset of vortex-antivortex pairs. We believe that the present treatment, namely, of just the time dependent equation for the order parameter at a time

independent field renders the present approach quantitatively approximate to the real solution of the TDGL equations in case that the current is larger than the critical. Nevertheless, it provides a qualitative description below because in this case there is an equilibrium state.

#### 4.1.1 Link variables method $U - \psi$

Our simulations are carried out on a spatially discretized version of Eq.(4.5). A detailed description of this method is given, for instance, by W. D. Gropp *et al.* [70]. In this method the superconducting region is represented by a Cartesian space grid of points and the equations are solved for these points on the grid. In order to write the equations (4.5) in a discrete form and to keep the gauge invariance, we define the auxiliary field

$$\mathcal{U}^x(x, y, t) = \exp\left(-i \int_{x_0}^x A^x(\nu, y, t) d\nu\right). \quad (4.7)$$

We explicitly perform the calculations for the  $x$ -component of the field since the  $y$ -component is analogously obtained. The definition of these fields allow us to establish the relation  $\partial_x \mathcal{U}^x = -i\mathcal{U}^x A^x$ . We calculate the derivative  $\partial_x (\mathcal{U}^x \psi)$  to get the expression,

$$\left(-i \frac{\partial}{\partial x} - A^x\right) \psi = -i\overline{\mathcal{U}^x} \frac{\partial}{\partial x} (\mathcal{U}^x \psi), \quad (4.8)$$

where the complex conjugate is represented by  $\overline{\mathcal{U}^x}$ , and the relation  $\overline{\mathcal{U}^x} \mathcal{U}^x = 1$  is valid. Deducing the Eq.(4.8) and organizing the terms, we obtain the kinetic term of the Eq.(4.5)  $(-i\partial_x - A^x)^2 \psi = -\overline{\mathcal{U}^x} \partial_x^2 (\mathcal{U}^x \psi)$ .

As a further step we define variables to be independent of a reference point but that they keep the information about the distance among the points given by  $a_x$ .

These variables are the so-called link variables, defined by

$$U^x(x, y, t) = \mathcal{U}^x(x + a_x y, t) \overline{\mathcal{U}}^x(x, y, t) = \exp \left( -i \int_x^{x+a_x} A^x(\xi, y, t) d\xi \right). \quad (4.9)$$

Once we have defined these variables, we obtain their discretized form from the relations  $\mathcal{U}_{i,j}^x = \prod_{k=1}^{i-1} U_{k,j}^x$  and  $\mathcal{U}_{i,j}^y = \prod_{k=1}^{j-1} U_{i,k}^y$ , where the variable  $U_{i,j}^x$  connect the points  $(i, j)$  and  $(i + 1, j)$  and the variable  $U_{i,j}^y$  connect the points  $(i, j)$  and  $(i, j + 1)$  in the grid. The link variables are related to the auxiliary fields, previously defined, by  $U_{i,j}^x = \overline{\mathcal{U}}_{i,j}^x \mathcal{U}_{i+1,j}^x$  and  $U_{i,j}^y = \overline{\mathcal{U}}_{i,j}^y \mathcal{U}_{i,j+1}^y$ .

In order to discretize the equations (4.5) we need to substitute the derivatives by a finite difference, which is done for a given function  $f(x)$  by  $(\partial_x f)_{i,j} \approx (f_{i+1,j} - f_{i,j})/a_x$  and  $(\partial_x^2 f)_{i,j} \approx (f_{i+1,j} - 2f_{i,j} + f_{i-1,j})/a_x^2$ , where  $a_x$  is the distance between two points in the  $x$  direction in the grid. When we write the spatial derivatives as finite differences and we insert the discrete link variables we obtain the TDGL for  $\psi$ ,

$$\begin{aligned} \eta \frac{\partial \psi_{i,j}}{\partial t} &= \frac{U_{i,j}^x \psi_{i+1,j} - 2\psi_{i,j} + \overline{U}_{i-1,j}^x \psi_{i-1,j}}{a_x^2} + \frac{U_{i,j}^y \psi_{i,j+1} - 2\psi_{i,j} + \overline{U}_{i,j-1}^y \psi_{i,j-1}}{a_y^2} + \\ &+ \psi_{i,j} - (\overline{\psi}_{i,j} \psi_{i,j}) \psi_{i,j}. \end{aligned} \quad (4.10)$$

To deduce the discrete equation for  $\vec{A}$ , we define the following variable

$$L_{i,j} = \exp(-i \phi_{i,j}) = \exp(-i \oint \vec{A} \cdot d\vec{l}) = U_{i,j}^x U_{i+1,j}^y \overline{U}_{i,j+1}^x \overline{U}_{i,j}^y, \quad (4.11)$$

where  $\phi_{i,j}$  is the magnetic flux in the point  $(i, j)$ .

Considering the mean value of the integral, we can simplify Eq.(4.11) for

$$L_{i,j} = \exp[-i a_x a_y B_z (x_i + \frac{a_x}{2}, y_i + \frac{a_y}{2})], \quad (4.12)$$

and we obtain the magnetic field on the central points of the grid as  $h_{i,j}^z \equiv B_z (x_i +$

$a_x/2, y_i + a_y/2) = i \ln(L_{i,j})/a_x a_y$ . We use this expression of the magnetic field to calculate the product  $L_{i,j} \bar{L}_{i,j-1} = \exp[-i a_x a_y (h_{i,j}^z - h_{i,j-1}^z)]$ . We expand the exponential in this last expression, we approximate its value in first order  $e^x \approx 1 + x$  and we consider the relation  $(h_{i,j}^z - h_{i,j-1}^z) \approx a_y \partial_y h_{i,j}^z$  to obtain the expression for the partial derivative of the magnetic field, given by,

$$\partial_y h_{i,j}^z \approx i \frac{(L_{i,j} \bar{L}_{i,j-1} - 1)}{a_x a_y^2}, \quad (4.13)$$

that is easily identified as the  $x$  component of the curl of the magnetic field  $(\nabla \times \nabla \times \vec{A})_x = (\nabla \times \vec{h})_x$ . The  $y$  component of the curl of the magnetic field is obtained in an analogous way.

In the following, we discretize the superconducting current terms, and for this purpose we use the auxiliary field  $\mathcal{U}$  and the relation (4.8):  $\bar{\psi}(\vec{D}\psi)_x \rightarrow \bar{\psi}_{i,j}(-i\partial_x - A^x)\psi_{i,j} = \bar{\psi}_{i,j}[-i\bar{\mathcal{U}}_{i,j}^x \partial_x(\mathcal{U}_{i,j}^x \psi_{i,j})]$ .

In this way, the  $x$  component of the superconducting current is written in terms of the link variables,

$$\frac{1}{2}[\bar{\psi}(\vec{D}\psi)_x + \psi(\overline{\vec{D}\psi})_x] = \frac{1}{a_x} \Im\{\bar{\psi}_{i,j} U_{i,j}^x \psi_{i+1,j}\}, \quad (4.14)$$

$$\frac{1}{2}[\bar{\psi}(\vec{D}\psi)_y + \psi(\overline{\vec{D}\psi})_y] = \frac{1}{a_y} \Im\{\bar{\psi}_{i,j} U_{i,j}^y \psi_{i,j+1}\}. \quad (4.15)$$

To calculate the time derivative of the  $x$  component of the vector potential we calculate the derivative of  $U^x$  in agreement with its definition in terms of the auxiliary field  $\mathcal{U}^x$

$$\frac{\partial}{\partial t}[\bar{\mathcal{U}}^x(x, y, t) \mathcal{U}(x + a_x, y, t)] = -i\bar{\mathcal{U}}^x(x, y, t) \mathcal{U}^x(x + a_x, y, t) \int_x^{x+a_x} d\xi \partial_t A^x(\xi, y, t). \quad (4.16)$$

We approximate the integral by its mean value  $\int_x^{x+a_x} d\xi \partial_t A^x(\xi, y, t) \approx a_x [\partial_t A^x(x +$

$a_x/2, y, t]$ ], and we obtain

$$\frac{\partial}{\partial t} \left( A^x \left( x_i + \frac{a_x}{2}, y_j, t \right) \right) = \frac{i}{a_x} \bar{U}_{i,j}^x \frac{\partial}{\partial t} U_{i,j}^x. \quad (4.17)$$

By using the discrete form of the  $x$  component of the superconducting current, the curl of the magnetic field and the time derivative of the vector potential (4.17), we write the discrete form for the TDGL for  $\vec{A}$ ,

$$\frac{\partial}{\partial t} U_{i,j}^x = -i U_{i,j}^x \Im \{ \bar{\psi}_{i,j} U_{i,j}^x \psi_{i+1,j} \} - \frac{\kappa^2}{a_y^2} U_{i,j}^x (L_{i,j} \bar{L}_{i,j-1} - 1). \quad (4.18)$$

For the  $y$  direction we obtain an analogous equation.

Once more, we recall that in the present study the superconducting thin film is subject to a time independent external field and the magnetic field resulting from circulating currents is ignored. Therefore, the above equation is not included in our study.

## 4.1.2 Boundary conditions

The hybrid system comprises a superconductor thin film and a parallel plane containing a periodic array of magnetic elements, such that the superconducting thin film responds accordingly and periodic boundary conditions must be imposed on the order parameter and on the vector potential. We choose the basic unit cell as a square. The appropriate boundary conditions for this situation were formulated by M. M. Doria *et al.* [42], and are given by

$$\vec{A}(\vec{r} + \vec{b}_i) = \vec{A}(\vec{r}) + \nabla \eta_i(\vec{r}), \quad (4.19)$$

$$\psi(\vec{r} + \vec{b}_i) = \psi(\vec{r}) e^{\frac{2\pi i}{\Phi_0} \eta_i(\vec{r})}, \quad (4.20)$$

where  $\vec{b}_i (i = 1, 2)$  are lattice vectors, and  $\eta_i$  is the gauge potential. These boundary conditions provide that  $\vec{A}$  and  $\psi$  are invariant under lattice translations for appropriate choice of the gauge potentials  $\eta_1$  and  $\eta_2$ . The stray field of the magnetic elements are localized in a limited region which is much smaller than the unit cell lateral side, which defines the square simulation area. The vector potential of the stray field decays away from the magnetic elements and becomes very small at the boundaries of the unit cell. The periodic boundary condition for the vector potential is relevant only for the situations where a uniform external field is applied and adds to the stray field of the magnetic elements. In this situation, we can choose the gauge which gives the vector potential for an uniform applied magnetic field  $H_a$  written as  $\vec{A} = xH_a\hat{y}$ . For this gauge choice the appropriate gauge potential to be considered in Eq.(4.19) is given by

$$\begin{aligned}\eta_x &= yH_aL_x, \\ \eta_y &= 0,\end{aligned}\tag{4.21}$$

where  $L_x$  and  $L_y$  are the sizes of the simulation area.

The boundary conditions in the  $x$  direction is given by

$$\begin{aligned}A_x(L_x, y) &= A_x(0, y), \\ A_y(L_x, y) &= A_x(0, y) + H_aL_x, \\ \psi(L_x, y) &= \psi(0, y)e^{\frac{2\pi i}{\Phi_0}H_aL_xy},\end{aligned}\tag{4.22}$$

and for the  $y$  direction we have

$$\begin{aligned}A_x(x, L_y) &= A_x(x, 0), \\ A_y(x, L_y) &= A_x(x, 0), \\ \psi(x, L_y) &= \psi(x, 0).\end{aligned}\tag{4.23}$$

The discrete version of these periodic boundary conditions for a grid of size  $N_x \times N_y$  is

$$\begin{aligned}
U_{N_x+1,j}^x &= U_{1,j}^x, & U_{i,N_y+1}^x &= U_{i,1}^x, \\
U_{N_x+1,j}^y &= U_{1,j}^y e^{-\frac{2\pi i n}{L_y}}, & U_{i,N_y+1}^y &= U_{i,1}^y, \\
\psi_{N_x+1,j} &= \psi_{1,j} e^{\frac{2\pi i n y}{L_y}}, & \psi_{i,N_y+1} &= \psi_{i,1},
\end{aligned} \tag{4.24}$$

where  $n$  is the number of flux quanta  $H_a L_x L_y / \Phi_0$ . Once we apply the Eq.(4.24) we obtain the necessary periodicity of the vector potential and the order parameter.

### 4.1.3 Ginzburg-Landau equation for the order parameter

In this section we detail the method used along the next chapters to obtain the time evolution of the order parameter in the superconducting thin film. The present description of this method is based on the PhD thesis of L. Komendová [83].

By considering that the vector potential does not change along the evolution of the superconducting system to the equilibrium configuration, we only need to solve the GL equation for the order parameter, given by,  $\vec{D}^2 \psi - \psi + |\psi|^2 \psi = 0$ . This equation is solved iteratively by assuming an initial solution  $\psi_0$ , describing the order parameter, that evolves to a state described by a function  $\psi$ , which is a solution in a further time step. We can iteratively improve an initial solution  $\psi_0$  by solving the equation

$$\varepsilon(\psi - \psi_0) = -(\vec{D}^2 \psi_0 - \psi_0 + |\psi_0|^2 \psi_0), \tag{4.25}$$

for the new order parameter  $\psi$  that becomes closer to the previous solution at each iterative step. This iterative procedure is carried out until we reach that  $\psi = \psi_0$  at

the end, and so,  $\vec{D}^2\psi_0 - \psi_0 + |\psi_0|^2\psi_0 = 0$ . Nevertheless, this iterative procedure is carried out in the discretized version of the equation. In a rectangular lattice, the order parameter is defined at each points  $(i, j)$  in the grid by  $\psi_{i,j}$ , and we introduce the link variables  $U_{i,j}^x$  described before in section (4.1.1). The iterative GL equation becomes

$$\begin{aligned} \varepsilon(\psi_{i,j} - \psi_{0;i,j}) &= \frac{U_{i,j}^x\psi_{0;i+1,j} - 2\psi_{0;i,j} + \bar{U}_{i-1,j}^x\psi_{0;i-1,j}}{a_x^2} \\ &+ \frac{U_{i,j}^y\psi_{0;i,j+1} - 2\psi_{0;i,j} + \bar{U}_{i,j-1}^y\psi_{0;i,j-1}}{a_y^2} \\ &+ \psi_{0;i,j} - (\bar{\psi}_{0;i,j}\psi_{0;i,j})\psi_{0;i,j}. \end{aligned} \quad (4.26)$$

It is important to notice that in the case that the time evolution of Eq.(4.10) is approximated by a simple Euler step,

$$\psi_{i,j}(t + \Delta t) = \psi_{i,j}(t) + \Delta t \frac{\partial \psi_{i,j}(t)}{\partial t} + \mathcal{O}(\Delta t^2), \quad (4.27)$$

we can neglect the terms  $\mathcal{O}(\Delta t^2)$  for an appropriate choice of a small time step  $\Delta t$ . Consequently, we can identify Eq.(4.10) with Eq.(4.26) once we make the following associations

$$\begin{aligned} \psi_{i,j}(t) &\rightarrow \psi_{0;i,j}, \\ \psi_{i,j}(t + \Delta t) &\rightarrow \psi_{i,j}, \\ \varepsilon &\rightarrow \frac{\eta}{\Delta t}. \end{aligned} \quad (4.28)$$

While  $\varepsilon$  is a parameter used to adjust the convergence of the relaxation process, the coefficient  $\eta$  is obtained from microscopic parameters in the TDGL equation. Hence, the iterative relaxation process used here to obtain the order parameter from Eq.(4.26) gives an equivalent solution to the TDGL equation (4.10) by means of the time derivative rendered by the single Euler step method.

In order to optimize the convergence we linearize the term  $(\bar{\psi}_{i,j}\psi_{i,j})\psi_{i,j}$  under the assumption that  $(\psi - \psi_0)$  is very small. Hence, we select the dominant contributions resulting in a linear expression for  $\psi$ . The non-linear term is linearized as follows,

$$\begin{aligned} |\psi|^2\psi &= \psi^2\bar{\psi} = [\psi_0 + (\psi - \psi_0)]^2[\bar{\psi}_0 + (\bar{\psi} - \bar{\psi}_0)] \\ &\approx |\psi_0|^2\psi_0 + 2|\psi_0|^2(\psi - \psi_0) + \psi_0^2(\bar{\psi} - \bar{\psi}_0) \\ &= 2|\psi_0|^2\psi - 2|\psi_0|^2\psi_0 + \psi_0^2\bar{\psi}. \end{aligned} \quad (4.29)$$

By inserting the expression (4.29) in the equation for the order parameter given by Eq.(4.26) and defining the notation  $U\psi_0$  to compactly represent the first two terms on the right hand side of the Eq.(4.26), we are able to obtain an equilibrium configuration for the order parameter under the effect of an external applied vector potential.

The final expression for the solution is obtained after the rearranging of Eq.(4.26) in an equation with a form where the terms multiplying  $\psi$  and  $\bar{\psi}$  are collected and written as coefficients  $C_1$  and  $C_2$ , respectively,

$$C_1\psi + C_2\bar{\psi} = C_3. \quad (4.30)$$

The coefficients are given in terms of the known old solution  $\psi_0$  by

$$C_1 = \varepsilon - 1 + \frac{4}{a^2} + 2|\psi_0|^2, \quad (4.31)$$

$$C_2 = \psi_0^2, \quad (4.32)$$

$$C_3 = U\psi_0 + \varepsilon\psi_0 + 2\psi_0|\psi_0|^2, \quad (4.33)$$

where we considered the same lattice parameter in both directions on the plane, namely,  $a = a_x = a_y$ .

From the above equation we can obtain an improved solution for the GL equation

given by

$$\psi = \frac{\overline{C_3}C_2 - C_3\overline{C_1}}{|C_2|^2 - |C_1|^2}. \quad (4.34)$$

In the iteration process, after each step, we calculate the difference between the new and old solutions, call it  $\Delta_\psi$ . When this difference is equal or smaller than a given value, usually  $\Delta_\psi \leq 10^{-5}$ , we consider that convergence has been reached and the system is in a stable or at least in a local meta stable state. It may happen that after a fixed number of steps,  $N_{steps} = 10^5$ , for example, the system is stabilized but has not yet satisfied the convergence criterion. This is interpreted by the presence of a shallow minimum with a very slow evolution towards the true minimum. Such cases demand analysis of results and maybe a posterior procedure to reach the ultimate minimum by changing parameters. The ultimate minimum, that is, the solution with the lowest energy, is accessible from different well defined initial states. We usually consider the following initial state cases, namely, (i) the superconducting state  $\psi \approx 1$ , (ii) the normal state  $\psi \approx 0$ , or (iii) a previous state obtained while sweeping up the magnetic field or other external parameter.

#### 4.1.4 Physical and numerical characteristics of the superconducting film

We consider a SC niobium (Nb) film with a typical critical temperature  $T_c = 6.8 K$ , coherence length at zero temperature  $\xi(0) = 10 nm$ , penetration depth  $\lambda(0) = 215 nm$  that are values found in experiments in thin films with thickness similar to the value that we have considered which is  $t_s = 10 nm$  [71]. The lateral size of the simulation region is chosen as  $L_x = L_y = 4 \mu m$ , as illustrated in Fig. 4.1. We suppose that the whole system is cooled to a temperature  $T = 6.2 K$  which gives the corresponding lengths  $\xi(6.2) = 33.3 nm$  and  $\lambda(6.2) = 723.7 nm$ . For the given values for the characteristic lengths of a superconductor we can calculate the Pearl penetration

length  $\lambda_{eff} \equiv 2\lambda^2/t_s = 104.7 \mu m$  and effective GL parameter  $\kappa_{eff} = 3145$ . Thus, it becomes clear that our simulation find experimental correspondence in the range of the high- $\kappa$  approximation that is characteristic for type *II* superconductors. From the presented values we verify that the effect of the small thickness for the film is to increase considerably the effective GL parameter that becomes much larger than the bulk value  $\kappa_{eff} \gg \kappa = \lambda(6.2)/\xi(6.2) = 21.5$ .

From the values obtained for  $\xi$  and  $\lambda_{eff}$  we can calculate the lower and upper critical fields for the superconducting film. The lower critical field is given by  $H_{c1} = \Phi_0 \ln(\kappa_{eff}) / (4\pi\lambda_{eff}^2) = 1.3 \times 10^{-3} G$  and the upper critical field is obtained from  $H_{c2} = \Phi_0 / (2\pi\xi^2) = 3.0 \times 10^3 G$ . We verify the large difference, that is characteristic of thin films, between the values of the critical fields.

For the numerical calculations it is considered a grid of  $400 \times 400$  points, where we use at least three grid points for one coherence length, which represent a square of  $120 \xi \times 120 \xi$  and thickness of  $0.3 \xi$ .

## 4.2 Micromagnetic simulations

We seek to explain here how a set of magnetic elements, which are microscopic magnetic dipoles, arrange themselves to yield configurations such as the magnetic vortex in a permalloy. This is a timely subject and many researchers have identified materials that hold magnetic vortex states which are promising candidates for nanometric storage data applications. Therefore, many different research groups have studied the internal structure of magnetic vortex [151], the annihilation dynamics of magnetic vortices and antivortices [76], the size and the shape of vortex in nanodisks as function of the applied magnetic field, material and geometry [20], the formation, properties and the stability of single vortices in magnetic nanodots [100], the dynamics of magnetic vortices driven by spin polarized currents in permalloy nanodisks [27] and even the exploration of three-dimensional nanomagnetism [50].

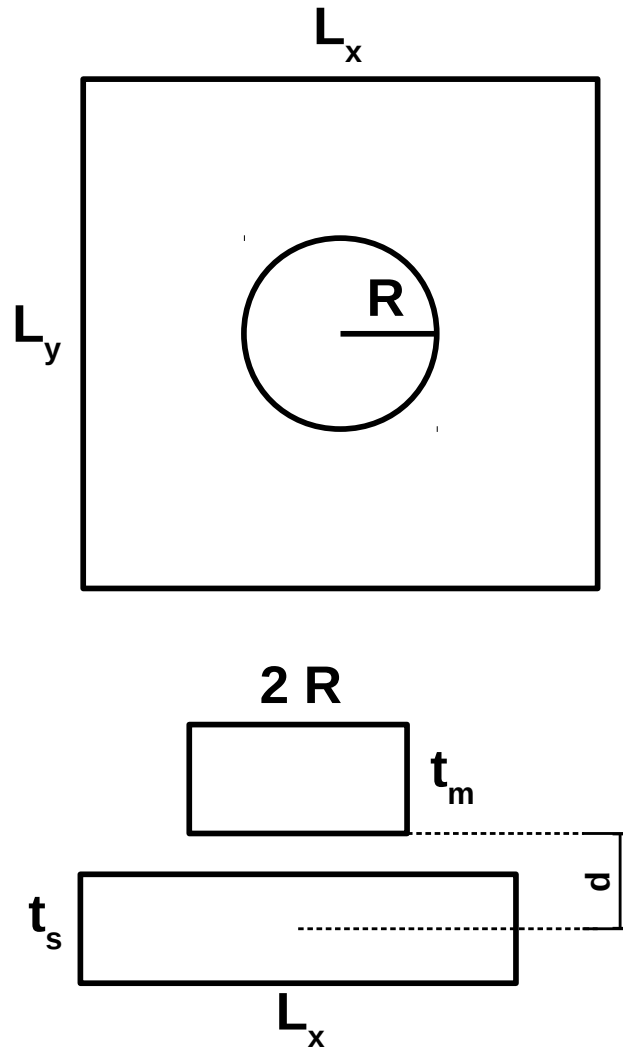


Figure 4.1: Representation of the superconducting simulation region of thickness  $t_s$ , sides  $L_x$  and  $L_y$ , and a ferromagnetic disk of thickness  $t_m$ , radius  $R$  and positioned at a distance  $d$  above the superconducting region.

The basic model to study the magnetic dynamics in materials is through the Landau-Lifshitz equation. Once dissipative effects are incorporated this equation becomes the Landau-Lifshitz-Gilbert equation. But first, we show some concepts involved in micromagnetic simulations and present the characteristics of our modelling and calculations performed on graphical cards. The derivation of the Landau-Lifshitz-Gilbert equation and the micromagnetism concepts presented in this section are mainly based on the Master's thesis of Rafaela de Medeiros de Souza [34].

The magnetism of systems in the scale of micrometer and nanometer are well

described by the micromagnetism that is the approach commonly used to investigate novel properties and to explain new phenomena observed in experiments. In this approach the atoms of the material are not considered separately but instead, the systems are modeled in lengths longer than the atomic scale. We present here the micromagnetic computational method used, for instance, to study properties of magnetic vortices [91, 77, 117] and skyrmions [127, 153, 51], by different softwares [148, 40]. Moreover we also discuss the energy and the local magnetic field of these magnetic systems.

### 4.2.1 Magnetic simulation cell

A nanometric volume of a magnetic material has its structure composed of a large number of atoms, which implies that the computational calculation to obtain the magnetic state of such structure is highly demanding if it is considered the interaction among individual atoms.

Fig. 4.2 illustrates the magnetic moments at the vertices and at the faces of a face-centered cubic crystalline (fcc) cell of lattice constant  $a_0$ . For example, a magnetic material with a crystal structure of type face-centered cubic with a lattice constant  $a_0$  has four atoms per unit cell. Hence, in a cubic volume  $v$  of side  $d$  the number of atoms in the volume is given by  $N_{at} = 4(d^3/a_0^3)$ . For a cubic volume of permalloy (Py), with side  $d = 5 \text{ nm}$  and lattice constant  $a_0 = 0.35 \text{ nm}$  [112], the number of atoms is  $N_{at} \approx 11.7 \cdot 10^3$ . It becomes clear that it is not efficient to calculate the magnetic configuration of a nanometric system which sides are of the order of  $100 \text{ nm}$ , for instance, considering the individual atoms. In order to optimize the computational calculations it is helpful the concept of simulation cell, that consists in a small cubic cell representing the atoms inside its volume, since the magnetization does not varies considerably.

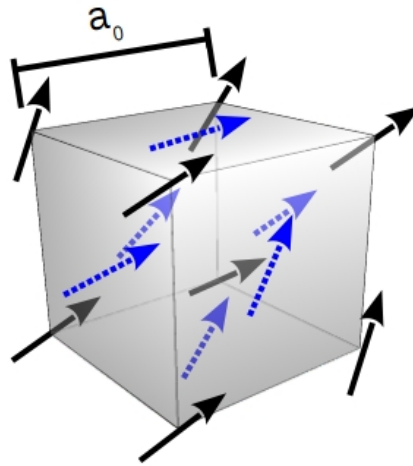


Figure 4.2: Representation of a face-centered cubic unit cell where the magnetic moments of the atoms at the vertices are shown as black arrows (continuous line) and the magnetic moments of the atoms at the faces are shown as blue arrows (dotted line).

In Fig. 4.3 it is shown a cubic simulation cell of side  $d$ , composed of several unit cells of side  $a_0$ . It is assumed that the simulation cell presents an effective magnetic moment that is equivalent to the sum of all the individual magnetic moments of the constitutive unit cells. When the magnetic configuration of a nanometric element is performed, the interaction among the effective magnetic moments of all simulation cells is calculated.

The side of the cubic simulation cell  $d$  is a parameter chosen in order to guarantee that the changing in the magnetic moments inside the volume is negligible. An important characteristic length for the magnetic systems is the exchange length  $l_{exc}$ , that is the larger distance where there is no considerably changes in the magnetization [11]. Therefore, the simulation cell size is chosen in such a way to be of the order of the exchange length of the material. The exchange length is defined by

$$l_{exc} = \sqrt{\frac{2A}{\mu_0 M_s^2}}, \quad (4.35)$$

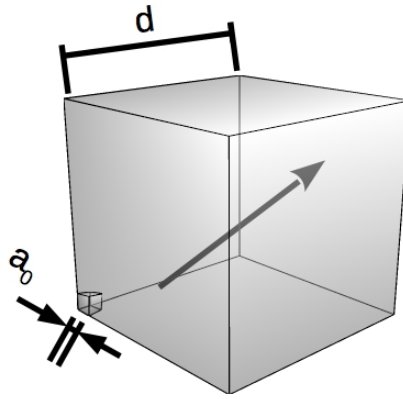


Figure 4.3: Representation of a simulation cell, of sides  $d$ , with an equivalent magnetic moment corresponding to the average of the magnetic moments of all crystalline cells, of sides  $a_0$ , which one of them is represented at the left frontal corner.

where  $A$  is the exchange stiffness,  $M_s$  is the saturation magnetization and  $\mu_0$  is the magnetic permeability of vacuum.

#### 4.2.2 Contributions to the magnetic energy

A given system is in a magnetic state which is the minimum of the magnetic energy . The equilibrium configuration is established when the energy reaches a minimum and this usually means that the magnetic moments are aligned to the effective local magnetic field. However, interaction among the magnetic moments can spoil this alignment.

The effective energy for a system composed by  $N$  atoms with magnetic moments  $\vec{\mu}_i$  and volume  $V$ , is given by the sum of the contributions of all atoms and is written

as

$$\begin{aligned}
E = & - J \sum_i \sum_j (\vec{\mu}_i \cdot \vec{\mu}_j) - \vec{H} \cdot M_s V \sum_i (\vec{\mu}_i) - \frac{KV}{2} \sum_i (\mu_i^z)^2 \\
& + \frac{M_s^2 V}{2} \sum_i \sum_j \left[ \frac{\vec{\mu}_i \cdot \vec{\mu}_j}{r_{ij}^3} - \frac{(\vec{\mu}_i \cdot \vec{r}_{ij})(\vec{\mu}_j \cdot \vec{r}_{ij})}{r_{ij}^5} \right], \tag{4.36}
\end{aligned}$$

where the first term represents the exchange energy related to the atom of magnetic moment  $\vec{\mu}_i$  and its first neighbor with magnetic moment  $\vec{\mu}_j$ , with  $J$  the exchange integral between both atoms; the Zeeman energy contribution is expressed in the term containing the external applied magnetic field  $\vec{H}_a$ ; the anisotropy contribution is included in the term proportional to the anisotropy constant of the material  $K$ ; and the last term is the magnetostatic energy, with  $r_{ij}$  the distance between the  $i$ -th and  $j$ -th atom.

Micromagnetism magnetic energy is calculated by considering the contributions of each magnetic cell as an effective energy for the group of atoms enclosed in that cell, where it is assumed that the quantities do not vary considerably. In the micromagnetic simulation it is considered that a cubic simulation cell of volume  $V_{cell}$  has a uniform magnetization of intensity  $M_s$ , whose direction is determined by the reduced magnetization vector  $\hat{m}$  with an effective magnetic moment  $\vec{\mu} = M_s V_{cell} \hat{m}$ .

The cartesian components of the reduced magnetization vector for a given cell can be written in terms of the polar and azimuthal angles  $\theta$  and  $\psi$ , respectively, as

$$\hat{m} = \frac{\vec{M}}{M_s} = \sin \theta \cos \psi \hat{x} + \sin \theta \sin \psi \hat{y} + \cos \theta \hat{z}. \tag{4.37}$$

This formulation for the reduced magnetization vector is extensively used for minimization procedures where the magnetization is continuous and can be considered as a function of the spatial coordinates by means of the dependence of the angles

$\theta(x, y, z)$  and  $\psi(x, y, z)$ . This formalism renders a micromagnetic energy density  $w$  for a magnet in an applied uniform magnetic field  $\vec{H}_a$  given by [87]

$$w = A(\nabla\hat{m})^2 - \mu_0 M_s \hat{m} \cdot \vec{H}_a - K(\hat{m} \cdot \hat{n})^2 - \frac{\mu_0 M_s}{2} \hat{m} \cdot \vec{H}_d, \quad (4.38)$$

where  $A$  is the exchange stiffness that is a constant for the material and is connected with the exchange energy,  $K$  is the uniaxial anisotropy constant,  $\hat{n}$  is a unitary vector that defines the anisotropy axis,  $\vec{H}_d$  is the demagnetizing field.

In order to determine the equilibrium state of a ferromagnet, together with the energy density we need to consider the Maxwell's equations for the demagnetizing field

$$\nabla \times \vec{H}_d = 0, \quad (4.39)$$

$$\nabla \cdot [\vec{H}_d + \mu_0 \vec{M}] = 0. \quad (4.40)$$

### Exchange contribution

The exchange interaction is responsible for the alignment of the magnetic moments in a material, which creates a magnetic order. This interactions is a quantic effect originated from the Coulomb interaction among electrons that are considered as point particles obeying the Pauli Exclusion Principle.

In terms of spin operators,  $\vec{S}_i$  and  $\vec{S}_j$ , and of the exchange integral  $J_{ij}$ , the exchange hamiltonian of an atom  $i$  with its neighbors is

$$H_i = - \sum_j J_{ij} \vec{S}_i \cdot \vec{S}_j, \quad (4.41)$$

where the exchange integral for a coulombian potential  $V(r)$ , is explicitly given by

$$J_{ij} = \int d\vec{r}_1 \int d\vec{r}_2 \bar{\psi}_i(\vec{r}_1) \psi_j(\vec{r}_2) V(r) \bar{\psi}_j(\vec{r}_1) \psi_i(\vec{r}_2). \quad (4.42)$$

In the case of isotropic interaction with the neighbors, the exchange integral is equal to  $J$  and the hamiltonian for a single atom  $i$  is simplified to  $H_i = -J \sum_j \vec{S}_i \cdot \vec{S}_j$  and thus, the hamiltonian for the whole system is  $H = -J/2 \sum_{i,j} \vec{S}_i \cdot \vec{S}_j$ . It can be shown [34] that the exchange stiffness constant  $A$  is proportional to the exchange integral, and it is also related to the magnetic spin moments of the atoms, the number of neighbors and the lattice constant  $a$  of a given crystalline structure. For example, for a bcc unitary cell the relation is  $A = 2JS^2/a$ .

### **Zeeman and demagnetizing contribution**

Contributions to the magnetic energy given by the external applied magnetic field  $\vec{H}_a$  and by the internal stray-field  $\vec{H}_d$  arises in the same form. While the external magnetic field interacting with the atomic magnetic dipoles in a material gives rise to the Zeeman energy in the energy density, the internal stray-field, also called demagnetizing field, that obey the Maxwell's equations (4.39) interacts with the atomic dipoles in order to contribute to the demagnetizing energy. Both contributions decreases the total magnetic energy when the magnetic moments are aligned with the effective local field. In micromagnetism the interaction of the fields  $\vec{H}_a$  and  $\vec{H}_d$  with the material is considered at the level of magnetic cells instead of atomic moments. Usually the external field is perpendicular to the disk plane  $\vec{H}_a = H_a \hat{z}$ , which gives a Zeeman energy contribution simplified as  $w_{Zeeman} = -\mu_0 M_s H_a \cos \theta$ . On the other hand, the demagnetizing term does not present a general simplification and needs to be considered in the form presented in Eq.(4.38).

### Magneto-crystalline anisotropy contribution

Anisotropy contribution is accounted for in this formalism by means of the energy density term given by  $w_K \equiv -K(\hat{m} \cdot \vec{n})^2$ .

The anisotropy axis is determined by the unit vector  $\hat{n}$ . We consider two orientations for the anisotropy axis  $\hat{n} = \hat{z}$  that corresponds to a unit vector perpendicular to the disk plane and an in-plane anisotropy axis given by  $\hat{n} = a\hat{x} + b\hat{y}$ , where  $a^2 + b^2 = 1$ . We should also consider two possibilities for the anisotropy constant  $K > 0$  and  $K < 0$ .

For an anisotropy axis perpendicular to the plane,  $\hat{n} = \hat{z}$ , we write the energy contribution as

$$w_K \equiv -K \cos^2 \theta. \quad (4.43)$$

For a positive anisotropy constant the minimum anisotropy contribution is given when the magnetization vector is parallel ( $\theta = 0$ ) or antiparallel ( $\theta = \pi$ ) to the anisotropy axis, and the system's energy is lowered by this negative contribution. For a negative anisotropy constant the minimum anisotropy contribution is given by the magnetization vector that lies in the plane  $xy$ , which is achieved by  $\theta = \pi/2$ , meaning the magnetization vector is perpendicular to the anisotropy axis and this energy term gives a null contribution in this particular case.

In-plane anisotropy is implemented by a preferential direction in the disk's plane, that is determined by a unit vector with angular distance  $\varphi_K$  from the  $x$  axis, which results  $\hat{n} = \cos \varphi_K \hat{x} + \sin \varphi_K \hat{y}$ . Therefore, the anisotropy energy density is given by

$$w_K = -K \sin^2 \theta \cos^2(\psi - \varphi_K), \quad (4.44)$$

which provides the most negative contribution for  $K$  positive, magnetic moments in the disk's plane  $\theta = \pi/2$  aligned parallel or anti-parallel with the anisotropy axis  $\psi = \varphi_K$  or  $\psi = \varphi_K + \pi$ . While the minimum contribution is a null term for negative

$K$ , magnetization perpendicular to the disk's plane  $\theta = 0, \pi$  or perpendicular to the anisotropy axis  $\psi = \varphi_K \pm \pi/2$ .

### 4.2.3 Micromagnetic simulations on GPU: MuMax3

In order to obtain the equilibrium magnetic state for the permalloy disks simulated in our calculations we used a GPU-accelerated micromagnetic simulation program called MuMax3 [148]. This is an open-source program that uses a finite-difference discretization method to calculate the space and time-dependent magnetization dynamics in nano to micro-sized ferromagnets. There are other commercial and open-source programs that use a similar technique. Some examples of open-source programs are OOMMF [40], that run on CPU and it was extensively used in research for the last decade, and MicroMagnum [43] that run on GPU. A similar commercial program is GpMagnet [93] that also run on GPU. As micromagnetic softwares that use finite-element technique we can list, e.g., NMag [54], Tetramag [80], MagPar [129] and FastMag [24]. These softwares demand more computing performance than the finite-difference methods, however they permit a more flexible geometric modeling.

We chose MuMax3 in reason that it is an open-source software that runs on graphical cards (GPU) presenting a higher performance when compared to other software that uses the CPU for processing the calculations, as for example, the widely known software OOMMF.

The first step to perform our simulations on MuMax3 is to define the geometry of the system to be studied. At this point, we define the shape of the magnetic element, the size, namely, the lateral lengths and the height. We also choose the number of grid points in which the system is divided, in order to obtain the best computing performance without lose information about the magnetic state. Each point on the three-dimensional grid works as a cubic simulation cell with an uniform magnetic moment whose direction is represented in terms of a reduced unitary magnetization

vector. Once we have chosen the shape and dimensions, we define the physical properties of material we are interested in study, as for example, the saturation magnetization, the exchange stiffness and the damping constant.

The further step is to select the solution method to perform the simulation according to what quantities one are interested to evaluate. In our case, we have interest in the magnetization configuration at the equilibrium state of the magnetic system that corresponds to the minimal energy state. The energy minimization is performed on MuMax3 by means of a function *relax()* that attempts to find the minimal energy of the system by monitoring the energy and torque evolution at different steps of the solution procedure in order to increase the performance. Once the minimal energy of the simulated system is achieved the simulation is concluded and the software provides a file containing the magnetization cartesian components of each simulation cell. That is the result we obtain from the software MuMax3.

#### **4.2.4 Physical and numerical characteristics of a permalloy disk**

In this section we present the physical properties of permalloy that is a ferromagnetic nickel-iron alloy. It can be prepared in different stoichiometries of nickel and iron but in this thesis we refer to the most used in experiments [63, 122, 147, 14] of permalloy-superconducting heterostructures, which is an alloy of 80% nickel and 20% iron ( $Ni_{80}Fe_{20}$ ).

Permalloy keeps its properties for temperature variations in the range considered for the cooling process which the niobium film needs to be submitted to achieve the superconducting state. Hence, we can consider that once the state of minimal energy is obtained for the permalloy disk with the application of magnetic field at a temperature above  $T_c$ , this magnetic equilibrium state is maintained in the disk after switch the field off and the system is cooled below  $T_c$ .

We choose the parameters for the permalloy disk as typical values often used in micromagnetic simulations [94, 79], for example, for permalloy disk and film respectively. We consider for the exchange stiffness  $A = 1.3 \times 10^{-11} \text{ J/m}$ , the damping constant  $\alpha = 0.01$  which correspond approximately to which is found experimentally for permalloy films  $\alpha = (0.0064 \pm 0.0002)$  by [112], for example. We fixed the saturation magnetization as  $M_s = 8.6 \times 10^5 \text{ A/m}$  which is a value commonly used in the literature [91, 114, 77, 117]. The exchange length, that gives the characteristic value for which the magnetization varies along the material, is calculated by Eq.(4.35) as  $l_{exc} = 5.3 \text{ nm}$ . The magnetic element we have chosen for our simulations is a disk with diameter  $D = 1 \text{ }\mu\text{m}$  and thickness  $t_m = 50 \text{ nm}$ . In order to calculate the magnetic equilibrium state we define a cubic lattice of  $N_x = 256 \times N_y = 256 \times N_z = 10$  points, corresponding to a cuboid of dimensions  $L_x = 1024 \text{ nm} \times L_y = 1024 \text{ nm} \times L_z = 50 \text{ nm}$ , in which interior the disk is modeled. Hence, the permalloy disk is composed of  $N \approx 491\,000$  cubic simulation cells of individual volume  $V_{cell} = 80 \text{ nm}^3$ , which renders a magnetic moment of  $\mu = M_s \times V_{cell} = 6.88 \times 10^{-20} \text{ Am}^2$ , for each cell, corresponding to approximately 7400  $\mu_B$ , where  $\mu_B$  is the Bohr magneton, a usual measure of magnetic moment as it was shown in chapter 2. At the end of the calculations, MuMax3 gives the direction of the magnetic moment of each simulation cell as cartesian components  $\mu_x, \mu_y, \mu_z$ .

In order to simulate the interaction of the permalloy disk with the superconducting film, we calculate the vector potential of the permalloy disk as a sum of the vector potential produced by each of the more than 490000 cubic simulation cells considered as infinitesimal magnetic dipoles holding an individual magnetic moment  $\mu = 6.88 \times 10^{-20} \text{ Am}^2$ . We insert the components  $A_x$  and  $A_y$  in the GL equation for the order parameter.

## 4.2.5 Landau-Lifshitz-Gilbert equation

The dynamic solutions obtained by MuMax3 are based on the evolution of the unitary reduced magnetization  $\hat{m}(\vec{r}, t)$ . It calculates the torque  $\vec{\tau} = \partial\hat{m}/\partial t$  by means of the Landau-Lifshitz-Gilbert theory, where the effective field  $\vec{H}_{eff}$  considers the contributions of all interactions presented in the energy density (4.38). Therefore, for completeness we include a discussion of this theory.

The general movement of magnetic moments, considering the damping, was first described in 1935, by L. Landau and E. Lifshitz [84], when they proposed an equation to describe the temporal evolution of a magnetic moment. The magnetization dynamics described by the Landau-Lifshitz equation can be formulated from a magnetic model analogous to the movement equations of a rigid body [4, 81]. That is the procedure we will follow here to present this equation. In classical mechanics, the torque  $\vec{\tau}$  on a rigid body is given by the temporal variation of the angular momentum  $\vec{J}$ .

$$\frac{d\vec{J}}{dt} = \vec{\tau}. \quad (4.45)$$

The torque produced by an external magnetic field  $\vec{H}_a$  on a particle of magnetic moment  $\vec{\mu}$  is related to the temporal variation of the angular momentum by

$$\frac{d\vec{J}}{dt} = \mu_0 \vec{\mu} \times \vec{H}_a, \quad (4.46)$$

where  $\mu_0 = 4\pi \times 10^{-7} \text{ H/m}$ , which characterizes the use of the SI system of units, that is extended for the calculations involving the magnetic elements in this chapter.

From quantum mechanics, it is known that the atomic magnetic moment is related to the total angular momentum by  $\vec{\mu} = -\gamma_e \vec{J}$ , where  $\gamma_e = g|q_e|/(2m_e)$  is the gyromagnetic ratio for the electron,  $q_e$  the electron charge,  $m_e$  the electron mass and

$g$  the Landè factor, given by

$$g = 1 + \frac{J(J+1) + S(S+1) - L(L+1)}{2J(J+1)}, \quad (4.47)$$

where  $L$  is the orbital angular momentum and  $S$  the spin angular momentum. For the particular case where the orbital angular momentum is null, the Landè factor is  $g = 2$ .

Substituting the expression for the angular magnetic moment of an electron in Eq.(4.46), this model describes the precession of the spin magnetic moment around the external applied field

$$\frac{d\vec{\mu}}{dt} = -\gamma\vec{\mu} \times \vec{H}_a, \quad (4.48)$$

where  $\gamma \equiv \gamma_e\mu_0$ .

Considering that the applied external magnetic field  $\vec{H}_a$  is uniformly distributed on space, it is possible to assume that all magnetic moments  $\vec{\mu}_i$  inside a given volume  $V$  are governed by the Eq.(4.48). Summing the contributions of all magnetic moments and dividing by the considered volume, and considering that the magnetization vector is defined by  $\vec{M} = \Sigma\vec{\mu}_i/V$ , it is obtained the equation for the gyromagnetic precession

$$\frac{d\vec{M}}{dt} = -\gamma\vec{M} \times \vec{H}_a. \quad (4.49)$$

The obtained equation describes the induced torque by any magnetic field, not only an external applied one. The effective field  $\vec{H}_{eff}$  includes all quantum and anisotropic effects. The dissipative process are introduced in the model by an extra term in the Landau-Lifshitz equation (4.49), which assumes that  $|\vec{M}| = constant$ . The damping process drives the magnetization to the effective magnetic field direction, which is an effect that minimizes the energy, since it aligns the magnetization with the effective field.

$$\frac{d\vec{M}}{dt} = -\gamma\vec{M} \times \vec{H}_{eff} - \frac{\lambda}{M_s}\vec{M} \times (\vec{M} \times \vec{H}_{eff}), \quad (4.50)$$

where  $\lambda$  is a characteristic constant of each material and  $M_s$  is the saturation magnetization.

The equation (4.50) describes the magnetization dynamics only for small damping, and for this reason it is not suitable to model some materials. In 1955, T. L. Gilbert and J. M. Kelley [61] proposed an additional term to the equation, that permitted to handle the strong damping presented by some materials. The proposed term considers the temporal variation of the magnetization vector and is given by

$$\frac{\alpha}{M_s} \left( \vec{M} \times \frac{d\vec{M}}{dt} \right), \quad (4.51)$$

where  $\alpha$  is the Gilbert damping parameter. By considering the term proposed by Gilbert, the Landau-Lifshitz equation becomes,

$$\frac{d\vec{M}}{dt} = -\gamma \vec{M} \times \vec{H}_{eff} + \frac{\alpha}{M_s} \left( \vec{M} \times \frac{d\vec{M}}{dt} \right). \quad (4.52)$$

After some algebraic manipulations and by use of vectorial identities, it is possible to show that the vector product involving the temporal derivative of the magnetization already includes the dissipative term and gives another term proportional to the temporal derivative

$$\vec{M} \times \frac{d\vec{M}}{dt} = -\gamma \vec{M} \times (\vec{M} \times \vec{H}_{eff}) - \alpha M_s \frac{d\vec{M}}{dt}. \quad (4.53)$$

Substituting Eq.(4.53) into Eq.(4.52), we obtain,

$$\frac{d\vec{M}}{dt} = -\gamma \vec{M} \times \vec{H}_{eff} + \frac{\alpha}{M_s} \left[ -\gamma \vec{M} \times (\vec{M} \times \vec{H}_{eff}) - \alpha M_s \frac{d\vec{M}}{dt} \right]. \quad (4.54)$$

The equation (4.54) can be rewritten in a reduced form that is more commonly found

in the literature [10, 148] as the Landau-Lifshitz-Gilbert equation

$$\frac{d\vec{m}}{dt} = -\frac{\gamma}{(1+\alpha^2)} \{ \vec{m} \times \vec{H}_{eff} + \alpha [\vec{m} \times (\vec{m} \times \vec{H}_{eff})] \}, \quad (4.55)$$

where the magnetization vector was divided by the saturation magnetization which defines the reduced magnetization  $\vec{m} \equiv \vec{M}/M_s$ .

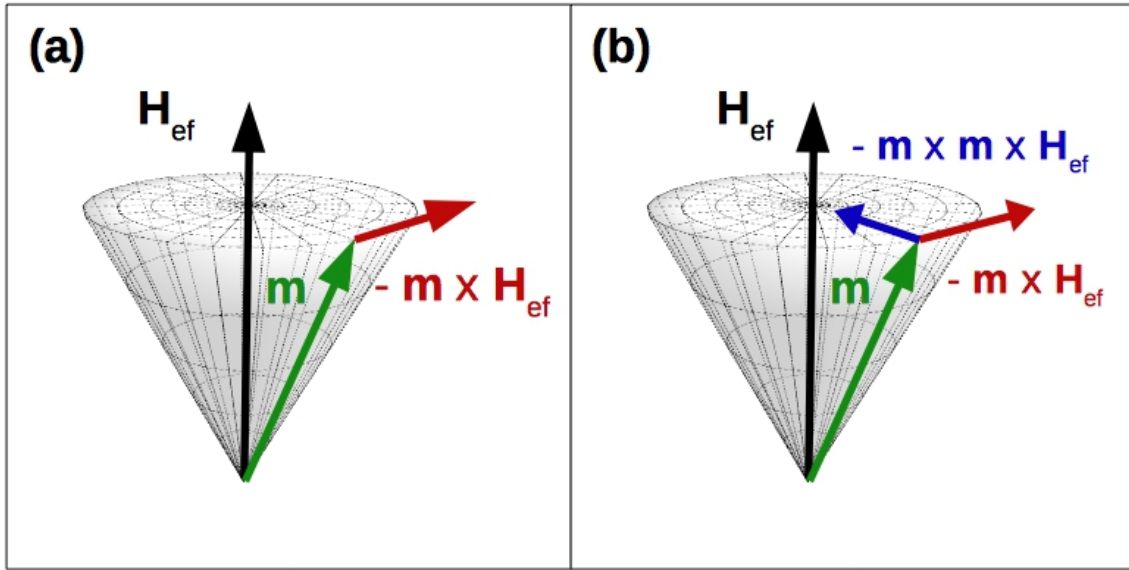


Figure 4.4: Representation of the magnetization vector that oscillates around the effective field in a cone (a) under the effect of the tangential term  $\vec{m} \times \vec{H}_{eff}$  and in a damped oscillation it tends to the alignment with the effective field (b) under the effect of the radial term  $\vec{m} \times \vec{m} \times \vec{H}_{eff}$ .

From the Landau-Lifshitz-Gilbert equation we can verify that in the absence of the damping term, that means  $\alpha = 0$ , the magnetic moment vector is only governed by the precession term. Thus, the magnetization vector rotates around the effective magnetic field  $\vec{H}_{eff}$ , as shown in Fig. 4.4. Considering the damping term included by Gilbert, the equation shows that the magnetization rotates around the local effective field in a damped movement, which tend to align the magnetization to the effective field in a precessional movement to the equilibrium state, where the system energy is a minimum.

# Chapter 5

## Rings of phase discontinuity

The effect of the permalloy disk's stray field on a superconducting film is studied in this chapter. Inside the permalloy disk there are magnetic dipole moments and the stray field is the superposition of the magnetic field of all dipoles. These dipole moments interact among themselves and how they are spatially oriented depends on this interaction. The magnetic vortex in the permalloy disk is the outcome of this interaction. However, we shall consider other arrangements whose orientation of the magnetic dipoles is fixed by hand. Nevertheless, they are useful to understand the onset of the phase discontinuity rings. We are specially interested on how the stray field interacts with the vortices on the superconducting film and how the superconducting phase is affected and modified by the magnetic system.

### 5.1 Introduction

In this chapter we address the properties of the phase of the superconducting state due to the presence of the permalloy disk. Remarkably, we find that it consists on a set of concentric rings of phase discontinuity. In order to gain understanding of this property, we briefly review the discussion introduced in chapter 1 about the

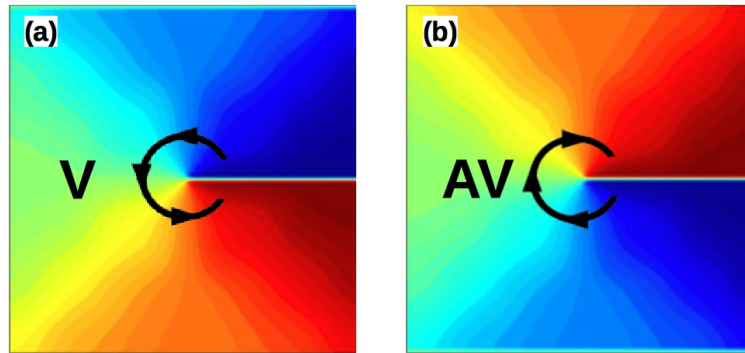


Figure 5.1: Superconducting phase of one single vortex (a) and one antivortex (b). The phase varies from  $\theta = 0$  (blue) to  $\theta = 2\pi$  (red).

phase of a single vortex state in a superconductor. This phase can be well represented by a hue ranging from blue (lowest value) to red (highest value) as can be seen in Fig. 5.1(a). In case of a single vortex, it smoothly changes the color from blue to red as the angle around the center of the vortex evolves counterclockwise from 0 to  $2\pi$ . The phase is the angle itself for a single vortex. There is a line that emerges from the center of the vortex and goes all the way to infinity, which characterizes the discontinuous jump of  $2\pi$ .

In case of an antivortex, as the illustrated in panel (b) of Fig. 5.1, the same discontinuity exists but the blue to red hue of the phase is observed in the clockwise sense. Therefore, in case of a pair vortex-antivortex this line of discontinuity reduces to a finite segment uniting the two centers, as it was illustrated in Fig. 1.4 of chapter 1.

At this point, we address the puzzling question on how should be the phase of the superconducting state without the presence of an applied external field. The immediate answer is that it should be constant everywhere. However, the example given below shows that there are other possible available configurations. We expect that they are all connected by a gauge transformation. Consider, for instance, a vortex and an antivortex on the top of each other such that they sum up to vanishing vorticity at all. The described state is not real since there is no magnetic field that could create this configuration in space. Nevertheless, assume that energy is given

to create this virtual pair that splits into a vortex and an antivortex. They move away from each other in opposite directions along a ring. Then, after a trip of half-circle they meet and cancel each other and return the energy given to create this pair to the environment. Although the initial and final configurations are of no vortices, a ring of phase discontinuity is left in the superconductor. Such process is observed in the corbino geometry under the presence of an external applied current. Surprisingly, we find that such rings of phase discontinuity are found under the permalloy disk, as shown here. To the best of our knowledge this kind of behavior in the superconducting phase has not been registered in the literature.

To best understand the association between the permalloy disk and the rings of phase discontinuity, we study in this chapter the effects of two other types of magnetic dot arrangements in the proximity of the superconducting film, namely, an annulus and several polygons of magnetic dipoles. The annulus corresponds to the permalloy disk removed of its center, thus removing the out-of-plane magnetic moments. The annulus solely possesses azimuthal in-plane arranged magnetic moments. The annulus can be thought as a sum of concentric rings of magnetic moments from a minimum to a maximum radius. The polygon corresponds to a selection of equidistant points (magnetic moments) sitting on a ring, all of them in-plane oriented and summing up to a zero magnetic moment. The annulus and polygon configurations are key elements to understand the onset of the rings of phase discontinuity as they both feature this property.

Our theoretical setup treats not just a single magnetic structure but a periodic array of them in proximity with an infinite superconducting thin film. We refer to such magnetic structures as magnetic dots which can be a permalloy disk with a magnetic vortex, an annulus or a polygon. Their constituents are the magnetic dipoles. The resulting stray field is also periodic and generates a non-uniform periodic

magnetic field that affects the superconductor. Depending on the physical properties and the magnetic state of the dots, the non-uniform magnetic field can generate pinning regions for vortices in the superconductor. Among the interesting questions associated to this problem is how superconducting vortices generated by an external field respond to the stray field in the presence of an external applied electric current. Therefore, one seeks to determine how effective is the permalloy disk as pinning center at a given magnetic state.

## 5.2 The Permalloy disk

Permalloy disks hold a variety of magnetic states depending on intrinsic internal parameters and the shape and size of the disk. Defining fixed values for the exchange stiffness  $A$  and saturation magnetization  $M_s$  and varying the perpendicular anisotropy parameter  $K$  is a procedure to find distinct magnetic states in permalloy disks by micromagnetic simulations, as were reported by E. R. P. Novais *et al.* [114], for instance. They also analyzed the behavior of elliptical nanodots, in zero perpendicular anisotropy, when the thickness and the semiaxis were varied. They found magnetic states as single domain, perpendicular or parallel to the disk's plane, vortex in the plane or with a perpendicular component to the plane.

Permalloy disks with dimensions in the range of  $D \simeq 10^{-6} \text{ m}$  (diameter) and  $t_m \simeq 10^{-8} \text{ m}$  (thickness) are a type of magnetic systems that admit a stable magnetic vortex as the equilibrium state. These vortex states have been observed and analyzed by magnetic force microscope [132, 156] and atomic force microscope [152, 97], for example. In this state the microscopic magnetic moments in the permalloy disk are basically divided into two kinds, as illustrated in Fig. 5.2. At the center of the disk the magnetic moments have an out-of-plane orientation, that is shown in blue in the inset of Fig. 5.2, and outside this center they have an in-plane curling orientation

with an azimuthal sense, either clockwise or counterclockwise. In Fig. 5.2 these in-plane magnetic moments are shown in red. The stray field of the magnetic vortex state has a pronounced peak well localized at the disk's center and vanishes elsewhere. The localized stray field can be strong enough to create pinning regions for vortices in the superconducting film [22, 97]. Nevertheless, the permalloy disk can be driven out from the vortex magnetic state to an uniform magnetization state by applying an in-plane magnetic field, see for instance [131, 109]. This characteristic of the permalloy disks gives the possibility to produce tunable pinning centers in the SC film.

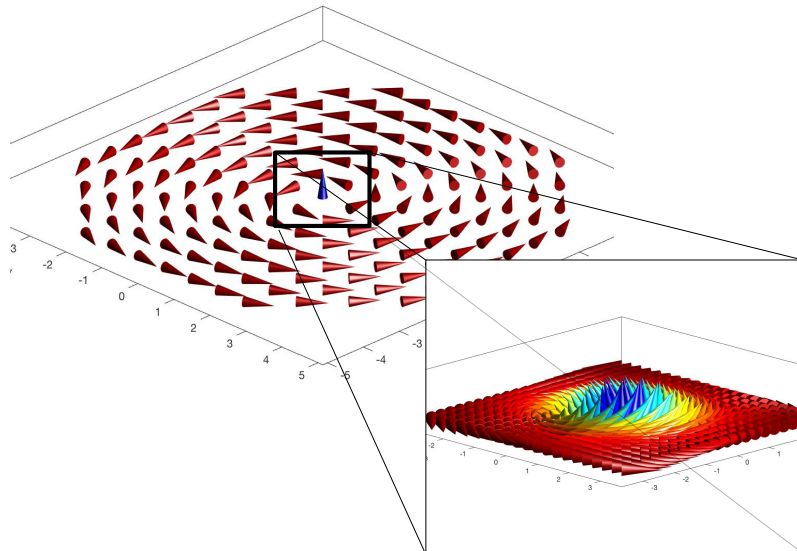


Figure 5.2: Representation of the magnetic moments of a permalloy disk in a magnetic vortex state. The magnetic moments outside the center are in an in-plane azimuthal arrangement (red) and at the center they present an out-of-plane orientation (blue), as shown in the inset.

Since we explore here magnetic arrangements other than the permalloy field, we often will refer to them as magnetic dots. We refer to any magnetic material considered in this thesis as ferromagnet.

The system made of magnetic dots on the top (or below) of a superconductor has been extensively studied in the past both from the theoretical and experimental point of views [145, 85, 35, 26, 64, 133]. The simplest description of a magnetic dot

is through a magnetic dipole, and its proximity to the superconducting film gives rise to vortex and antivortex configurations [124, 106, 21, 108, 102, 104, 123]. A magnetic dipole inside a superconductor produces inner vortex lines [41]. The presence of magnetic dots below a superconducting film produces interesting effects on the upper critical field since the internal field can either add or subtract the applied field [146].

To attain our theoretical objectives we first obtain the magnetic state of a circular permalloy disk through the software package called Mumax3 [148], as discussed in section 4.2.3 of chapter 4. In our simulations we define the geometric parameters of the circular disk and the internal parameters: saturation magnetization  $M_s$ , exchange stiffness  $A$  and damping constant  $\alpha$ . Mumax3 seeks the minimum of the total magnetic energy by considering the internal stray field and the interaction among the magnetic cells.

After the evolution of the minimization procedure, when the total magnetic energy reaches a significant low level, Mumax3 starts to monitor the temporal evolution of the reduced magnetization magnitude. This two-steps process is repeated until the desired accuracy is verified.

Once a stable state is reached, the local magnetization is obtained, which means that the orientation and strength of the magnetic dipole moments distributed inside the disk become known. Hence, the individual magnetic dipoles are oriented in different directions determined by the condition of a minimal energy state. This is explained in details in chapter 4. Nevertheless, to obtain the external stray field generated by this distribution of magnetic dipoles another step is necessary which corresponds to determine the vector potential in space. This must be done in order to apply the Ginzburg-Landau theory and describe the effects of this stray field into the superconducting film. Once in possession of the permalloy disk vector potential field in space, we seek to obtain the superconducting density, phase and current density in the thin film by minimizing the Ginzburg-Landau energy functional as

discussed in section 4.1.3.

The major features of the magnetic vortex state in the permalloy disk are discussed below. The permalloy disk is split into two regions, its center which forms a core and an annulus around this core. At the center of the disk the magnetic moments point out of the plane and produce a narrowly peaked stray field along the disk's axis. In the annulus the magnetic moments are in-plane and point in the azimuthal direction. Thus, they can be regarded as arranged in rings. Interestingly, the rings do not yield any stray field, as discussed below. This is because a ring of magnetic moments is basically a coil wrapped around a torus [125], namely, a toroid. To understand this, consider the solenoid which is a long straight coil of wire that generates a nearly uniform magnetic field in its interior and zero outside. If we curb the solenoid into itself to become a toroid, the magnetic field remains perfectly confined to its interior and vanishes outside, as found through Ampère's.

Now each current loop in this toroid can be regarded as a magnetic dipole with moment  $m = IA$ , where  $I$  is the circulating current in the toroid and  $A$  the cross section area of the loop. Hence, the total magnetic field due to a ring of magnetic dipoles is that of a toroid and so, it is expected to be confined to the internal cross section area  $A$ . Nevertheless, we find that the stray field of the ring produces an interesting effect on the superconducting film. The same holds for the annulus, which can be regarded as a sum of rings, and also for the permalloy disk, which excluded of its core becomes an annulus. This discussion is the central topic of this chapter.

Some extra assumptions are added to the Ginzburg-Landau analysis concerning the description of the superconducting film. For an infinite superconducting film of thickness  $d$ , we assume  $d < \xi$  which means that the order parameter does not change significantly along the film's thickness and then it only depends on the planar coordinates  $\psi = \psi(x, y)$ . A second assumption is that  $d \ll \lambda$  which gives rise to

an effective penetration length that is defined as the Pearl length  $\lambda_{eff} \equiv 2\lambda^2/d$  and has the physical meaning that an external magnetic field penetrates perpendicularly the film without the Meissner shielding, namely, there are no changes of its behavior compared to the empty space, which means that  $\vec{A} = \vec{A}_{ext}$ . If the effective Ginzburg-Landau parameter  $\kappa_{eff} = \lambda_{eff}/\xi \gg 1$ , we can neglect the contribution of the superconducting current  $\vec{J} = (q/2m (\psi^* \vec{D}\psi + c.c.))$  given by Eq.(2.4) to the second GL equation  $\vec{\nabla} \times \vec{h} = (4\pi/c)\vec{J}$  shown in Eq.(2.3). The vector potential in space is the sum of the vector potential of each magnetic cell that composes the permalloy disk or any magnetic dot. In order to calculate the vector potential produced by our magnetic disk we consider the superposition of the vector potential produced by all the magnetic moments inside the disk. We consider a dielectric layer separating the film of the permalloy disk. Then, the interaction between the two parts is done only by means of the stray field and we avoid the proximity effect that would promote the interchange of superconducting Cooper pairs of the film and metallic electrons of the dot. We only take into consideration the magnetic field component that is perpendicular to the film.

### 5.2.1 Physical parameters

The magnetic state of the permalloy disk is obtained by minimizing the magnetic energy by choosing the internal parameters, such as the given in section 4.2.4: exchange stiffness  $A = 1.3 \times 10^{-11} J/m$ , the damping constant  $\alpha = 0.01$ , saturation magnetization  $M_s = 8.6 \times 10^5 A/m$ ; and for the geometry which we have chosen a circular disk with diameter  $D = 1 \mu m$  and thickness  $t_m = 50 nm$ . In order to compare with the superconducting film we express the dimensions of the disk in terms of the coherence length  $\xi = 33.3 nm$ , which give us  $D = 15 \xi$  and  $t_m = 1.5 \xi$ . The magnetic state of the disk is simulated inside a cubic box of dimensions  $1024 \times 1024 \times 50 nm^3$  divided in  $256 \times 256 \times 10$  grid points, which results in a disk composed of approximately

491000 cubic simulation cells of volume  $V_{cell} = 80 \text{ nm}^3$  each. For these parameters, in the absence of uniform external field, the equilibrium state of our permalloy disk is the magnetic vortex state.

## 5.2.2 Vector potential of a permalloy disk

Results obtained from the micromagnetic simulations performed on MuMax3 permit us to calculate the vector potential generated by the permalloy disk by considering the contribution of each of its magnetic moments and summing them up.

The vector potential of an individual magnetic dipole moment is given by

$$\vec{A} = \frac{\vec{\mu}_{dip} \times (\vec{r} - \vec{r}_{dip})}{|\vec{r} - \vec{r}_{dip}|^3}, \quad (5.1)$$

where  $\vec{r}$  is the coordinate vector of the observation point and  $\vec{r}_{dip}$  gives the position of the magnetic dipole moment with orientation  $\vec{\mu}_{dip}$ . We calculate the magnetic dipole moment as  $\mu_{dip} = M_s V_{cell} = 6.88 \times 10^{-20} \text{ Am}^2$ .

The vector potential of a magnetic disk at a point of observation determined by  $\vec{r}$  is written as

$$\vec{A}(\vec{r}) = \sum_{i=1}^N \frac{\vec{\mu}_i \times (\vec{r} - \vec{r}_i)}{|\vec{r} - \vec{r}_i|^3}, \quad (5.2)$$

where  $N$  is the total number of magnetic dipoles contained inside the permalloy disk. The distance between each magnetic dipole and the superconducting film is considered in the calculation of the vector potential.

The superconducting region of our system is a film of thickness  $t_s = 0.3 \xi$  and infinitely long, what is simulated by the imposition of periodic boundary conditions on a finite region of lateral sizes  $L_x \times L_y = 120 \xi \times 120 \xi$ . The middle plane of the superconducting film defines the  $xy$ -plane, which means that the niobium film

occupies the space between the planes  $z = -t_s/2$  and  $z = t_s/2$ . We assume that only the perpendicular component of the magnetic field affects the superconducting film. Moreover, we consider that this field does not vary considerably along the superconducting thickness. Then, the average value inside the film must be considered. For this reason, we integrate the vector potential of each magnetic cell in the  $z$  direction along the film thickness by the integral

$$\langle \vec{A}_i(x, y) \rangle_z = \frac{1}{t_s} \int_{-t_s/2}^{+t_s/2} \frac{\vec{\mu}_i \times (\vec{r} - \vec{r}_i)}{|\vec{r} - \vec{r}_i|^3} dz, \quad (5.3)$$

and we obtain the following expression for the  $A_x$  and  $A_y$  components

$$\begin{aligned} \langle A_x \rangle_z(x, y) &= \frac{1}{t_s(\bar{x}^2 + \bar{y}^2 + (\bar{z} - t_s/2)^2)^{1/2}} \left\{ \mu_y + \mu_z \left[ \frac{\bar{y}(\bar{z} - t_s/2)}{\bar{x}^2 + \bar{y}^2} \right] \right\} \\ &\quad - \frac{1}{t_s(\bar{x}^2 + \bar{y}^2 + (\bar{z} + t_s/2)^2)^{1/2}} \left\{ \mu_y + \mu_z \left[ \frac{\bar{y}(\bar{z} + t_s/2)}{\bar{x}^2 + \bar{y}^2} \right] \right\}, \\ \langle A_y \rangle_z(x, y) &= \frac{1}{t_s(\bar{x}^2 + \bar{y}^2 + (\bar{z} - t_s/2)^2)^{1/2}} \left\{ \mu_x + \mu_z \left[ \frac{\bar{x}(\bar{z} - t_s/2)}{\bar{x}^2 + \bar{y}^2} \right] \right\} \\ &\quad - \frac{1}{t_s(\bar{x}^2 + \bar{y}^2 + (\bar{z} + t_s/2)^2)^{1/2}} \left\{ \mu_x + \mu_z \left[ \frac{\bar{x}(\bar{z} + t_s/2)}{\bar{x}^2 + \bar{y}^2} \right] \right\}, \end{aligned} \quad (5.4)$$

where  $\bar{x} = x - x_m$ ,  $\bar{y} = y - y_m$ ,  $\bar{z} = z - z_m$  and the brackets  $\langle \rangle_z$  means the average over the superconductor thickness.

It is considered a layer with thickness  $t_{ins}$  of an insulator separating the superconducting film and the permalloy disk. Therefore, the distance between the middle plane of the niobium film, that corresponds to the plane  $z = 0$ , to the base of the disk positioned above the film is defined as  $d = t_s/2 + t_{ins}$ , where  $t_{ins}$  assume different values along our simulations.

In order to calculate any possible vortex configuration, the obtained vector

potential components  $A_x$  and  $A_y$  are inserted into the two-dimensional GL equation for the order parameter, introduced in chapter 1 by Eq.(1.40) and given below in its dimensionless form

$$-(\nabla - i\vec{A})^2\psi - \psi + |\psi|^2\psi = 0, \quad (5.5)$$

for completeness of this chapter. As described in chapter 4, we solve this equation by means of a relaxation iterative process on a cartesian grid.

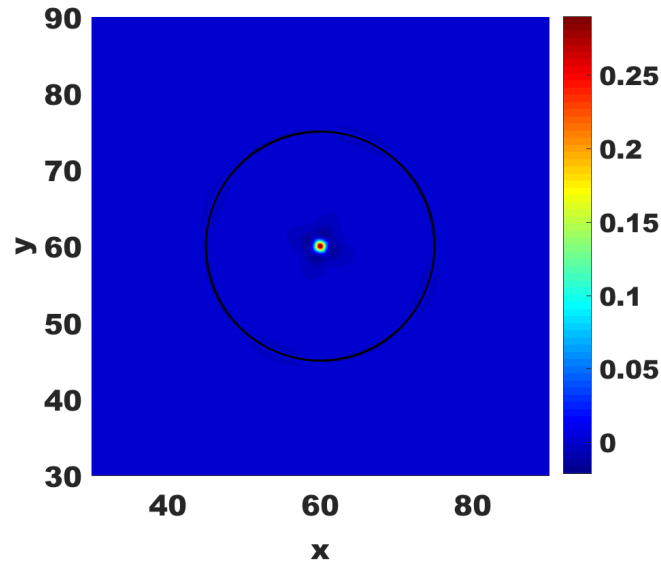


Figure 5.3: Perpendicular component of the permalloy disk's stray field. The disk is positioned at a distance  $d = 0.3 \xi$  above the middle plane of the niobium film. The values shown in the colorbar are in units of  $H_{c2}$ .

The perpendicular component of the disk's stray field is calculated numerically as the curl of the vector potential  $B_z = \nabla \times \vec{A} = \partial_x A_y - \partial_y A_x$ . The resulting perpendicular magnetic field is shown in Fig. 5.3. The field shows the typical form that characterizes a magnetic vortex, namely, a peak in the center of the disk which position is represented in the figure by the black circumference. A region of negative field is observed around the positive peak produced by the magnetic vortex in the disk. The minimum value of the field in this region is  $B_z^{min} = -0.021 H_{c2}$  while the maximum value reached in the central peak is  $B_z^{max} = 0.290 H_{c2}$ . The lower critical field of our niobium thin film was found in section 4.1.4 as  $H_{c1} = 0.4 \times 10^{-6} H_{c2}$ .

Thus, the intensity of the permalloy field in the center of the disk  $B_z^{max} = 0.290 H_{c2}$  is much more intense than the lower critical field which gives the measure for the vortex nucleation in the case of an uniform applied field. Another comparison we can consider is related to the uniform field  $H_a$  that is necessary to hold one quantum flux in simulation unitary cell. The total magnetic flux  $\Phi$  in a given area  $L_x L_y$  is  $\Phi = H_a L_x L_y$ . Writing the field in terms of  $H_{c2}$  and the lengths in terms of  $\xi$  we simply have  $\Phi/\Phi_0 = h_a l_x l_y / 2\pi$ , where  $h_a$ ,  $l_x$  and  $l_y$  are dimensionless values, and  $\Phi_0$  is the quantum flux. The necessary applied field to maintain a flux  $\Phi/\Phi_0 = 1$  in the considered area is  $H_a = 0.4 \times 10^{-3} H_{c2}$ , which is a small value compared to the maximum of the disk's stray field but it would be an uniform field on the whole superconducting area.

### 5.2.3 Superconducting density and phase

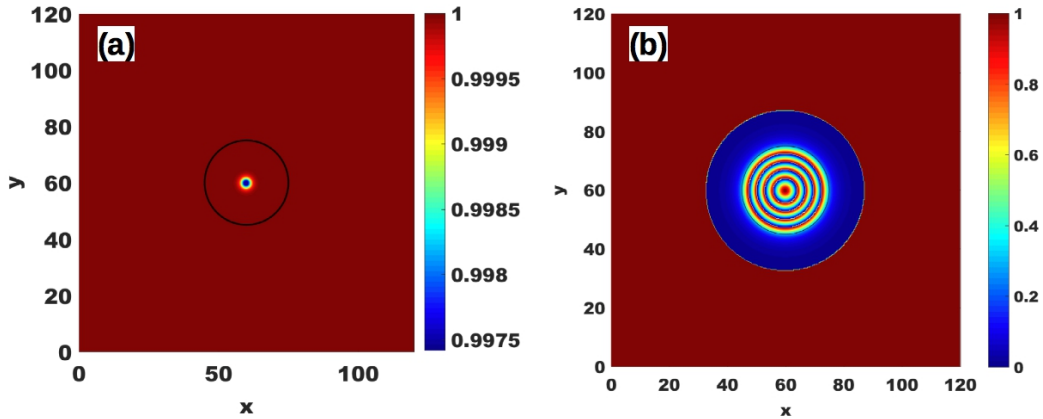


Figure 5.4: Superconducting density (a) and phase (b) of the niobium film under the effect of the permalloy disk's stray field. The disk is positioned at a distance  $d = 0.3 \xi$  above the middle plane of the niobium film.

Fig. 5.4(a) shows the superconducting density under the effect of the permalloy disk stray field. Only a small suppression of the superconducting density is observed at the center of the figure in the region affected by the intense peak of the disk field. The superconducting density decreases from the constant maximal value maintained in almost the whole region to the minimal value  $|\psi|^2 = 0.9975$  at the center.

We consider that the vortex nucleation in the region of maximum field does not happen because this stray field, even presenting a value much higher than  $H_{c1}$  at the peak, is localized in a region approximately circular of radius  $\approx 0.75 \xi$ , in other words, the stray field affects a region smaller than the size of a superconducting vortex and in a non-homogenous form. Although the superconducting density is weakly affected by the non-homogeneous stray field of the permalloy disk, the superconducting phase presents a great change as can be seen in panel (b) of the Fig. 5.4. The rings of phase discontinuity arises in the presence of the permalloy disk.

Here, we are focussed on the effects on the phase of the superconducting state which seems to come from the annulus of the permalloy disk. To confirm this we study next the effect of a theoretical annulus of magnetic moments on the film.

### 5.3 Magnetic annulus

In this section we analyse the interaction of the infinite superconducting thin film with a magnetic annulus, in an azimuthal magnetic state, positioned at a distance  $d$  above the film. As it was commented along the text and is shown in Fig. 5.5, a magnetic annulus is a perforated disk that we consider here as a model to investigate the effect of the azimuthal magnetic moments of the permalloy disk. To follow this idea we consider the dimensions and the magnetic properties of the annulus as the same as the permalloy disk which were presented in section 4.2.4 and we summarize here to provide completeness to this section. The thickness is  $t_m = 50 \text{ nm}$ , with an external radius  $R = 500 \text{ nm}$  and an internal radius  $r = 25 \text{ nm}$  that corresponds to a typical value for the magnetic vortex core found in the minimal energy state in permalloy disks. In reason of the hole at the center, the annulus has less magnetic cells than the disk. The annulus is divided in few more than  $N = 489000$  magnetic cells of volume  $V = 80 \text{ nm}^3$ . Each of them carrying a constant magnetic moment

$$\mu = 6.88 \times 10^{-20} \text{ Am}^2.$$

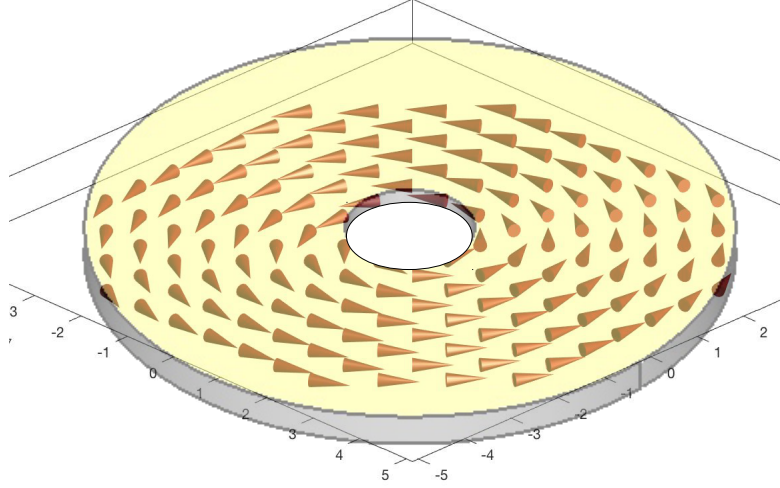


Figure 5.5: Representation of the arrangement of the magnetic moments inside the magnetic annulus, which is equivalent to a permalloy perforated disk without the out-of-plane magnetic moments at the center. In the annulus all the magnetic moments are in the in-plane azimuthal arrangement.

### 5.3.1 Vector Potential of a magnetic cell

From the Eq.(5.1) we can write the vector potential of a cell with magnetization vector  $\vec{M} = M_s \hat{m}$  where the reduced magnetization vector introduced in chapter 4 has the direction defined by the angles  $\theta, \psi$  and is given by  $\hat{m} = (\sin \theta \cos \psi) \hat{x} + (\sin \theta \sin \psi) \hat{y} + (\cos \theta) \hat{z}$ .

$$\begin{aligned} \vec{A} &= \frac{\mu}{|\vec{r} - \vec{r}_m|^3} \{ (\bar{z} \sin \theta \sin \psi - \bar{y} \cos \theta) \hat{x} \\ &+ (\bar{x} \cos \theta - \bar{z} \sin \theta \cos \psi) \hat{y} \\ &+ [\sin \theta (\bar{y} \cos \psi - \bar{x} \sin \psi) \hat{z}] \}, \end{aligned} \quad (5.6)$$

where  $\bar{x} = x - x_m, \bar{y} = y - y_m, \bar{z} = z - z_m$ , the position of the magnetic cell is given by  $\vec{r}_m = x_m \hat{x} + y_m \hat{y} + z_m \hat{z}$ .

If the cell has only an in-plane component of the magnetization we set  $\theta = \pi/2$

in Eq.(5.6) and  $\psi$  is the angle of the magnetic moment with the  $x$  axis. The vector potential is then given by

$$\vec{A} = \frac{\mu}{|\vec{r} - \vec{r}_m|^3} [\bar{z} \sin \psi \hat{x} - \bar{z} \cos \psi \hat{y} + (\bar{y} \cos \psi - \bar{x} \sin \psi) \hat{z}]. \quad (5.7)$$

In order to use the Eq.(5.7) to represent the magnetic moments of a cell of the magnetic annulus, we define the relation  $\psi = \varphi_m + \pi/2$ , where  $\varphi_m = \arctan(y_m/x_m)$  is the angle, with respect to the  $x$  axis, of the position of one determined magnetic moment. Any magnetic moment has its azimuthal direction defined by a vector tangent to a circle of radius  $\rho_m = \sqrt{x_m^2 + y_m^2}$ . By considering this definition, the vector potential given in Eq.(5.7) is simplified to give us the planar components

$$A_x = \frac{\mu \bar{z}}{(\bar{x}^2 + \bar{y}^2 + \bar{z}^2)^{3/2}} \cos \varphi_m \hat{x}, \quad (5.8)$$

$$A_y = -\frac{\mu \bar{z}}{(\bar{x}^2 + \bar{y}^2 + \bar{z}^2)^{3/2}} \sin \varphi_m \hat{y}. \quad (5.9)$$

The  $A_z$  component is ignored because it only yields a magnetic field contribution along the film thickness and we are interested in the perpendicular component. In the same way as it was done for the permalloy disk, we insert the calculated  $A_x$  and  $A_y$  components in the GL equation for the order parameter to obtain the solution of minimal energy.

The Eq.(5.8) and Eq.(5.9) correspond to the vector potential of a single magnetic dipole inside the annulus. In order to obtain the vector potential produced by the entire annulus, we adopt the same procedure described for the permalloy disk. We consider the integration along the  $z$  coordinate of the Eq.(5.8) and Eq.(5.9), obtaining the average for the vector potential components  $\langle A_x \rangle_z$  and  $\langle A_y \rangle_z$  of a single magnetic dipole. The vector potential produced by the annulus is obtained by the summation over all magnetic dipoles inside the annulus volume.

### 5.3.2 Superconducting density and phase

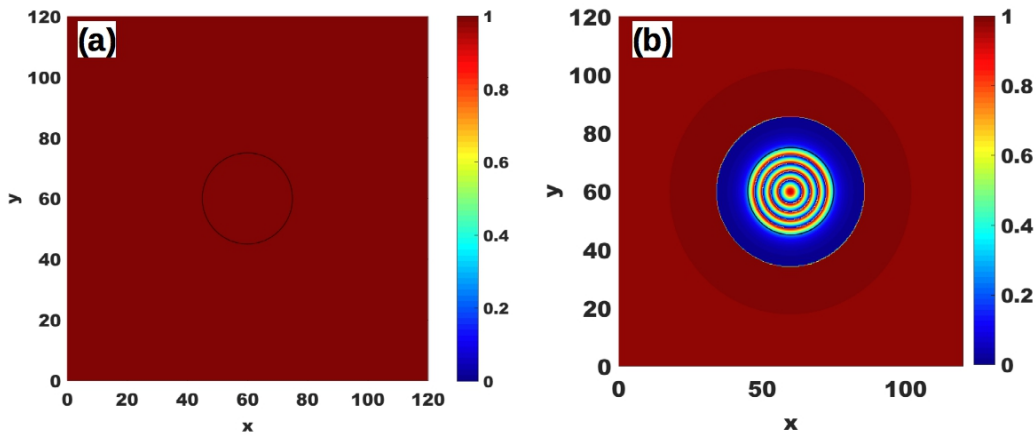


Figure 5.6: Superconducting density (a) and phase (b) at the equilibrium state for the SC film under the magnetic annulus, which position is indicated by the black solid circumference in the center.

The obtained solution for the superconducting density under the effect of the magnetic annulus is shown in Fig. 5.6. Although the stray field of the annulus does not change the superconducting density, it is noticeable that the presence of the annulus causes a distinct effect on the superconducting phase, which consists on the generation of rings of phase discontinuity.

Comparison between the superconducting phases for the permalloy disk and annulus shown, respectively, in Fig. 5.4(b) and Fig. 5.6(b), permits us to conclude that are the in-plane magnetic moments in the permalloy disk that produces the discontinuity rings in the phase. The only difference in the superconducting density for both cases is the small suppression in the center of the superconducting region that is caused by the out-of-plane moments in the permalloy disk.

In search of the origin of the rings of phase discontinuity, we simplify our system in one more level. Next, we study polygons of magnetic moments, in an azimuthal arrangement, which can be added to form an annulus.

## 5.4 Polygons of magnetic dipoles

In this section we analyse the influence of the stray field of a polygon of magnetic dipoles on a superconducting film. We consider different numbers of magnetic dipoles in a specific arrangement that we will define posteriorly. The stray field of the individual magnetic dipoles acts collectively in such a way to produce interesting effects on the superconducting density, phase and current. In order to observe the effect of the magnetic dipoles stray field, we calculate the vector potential for the polygon of magnetic dipoles. In possession of the vector potential due to the magnetic system we solve the GL equation for the order parameter and calculate the superconducting current.

We consider the superconducting film with similar parameters to the given in the previous sections, that we summarize below. We take a niobium thin film, which infinite characteristic is simulated in a square region where periodic boundary conditions are applied on the sides of length  $L_x = 120 \xi$  and  $L_y = 120 \xi$ . The order parameter is assumed to be constant along the thickness that measures  $t_s = 0.3 \xi$ , as in the previous systems. The middle of the superconducting film thickness defines the plane  $z = 0$ .

We consider an even number of magnetic dipoles positioned in the same plane  $z = z_{dip} = 3.2 \xi$  which implies that the distance,  $d$ , between the surface's film and the dipoles is  $d = z_{dip} - t_s/2 = 3.05 \xi$ . On this plane, the in-plane magnetic dipoles are arranged in an azimuthal configuration related to a reference circumference of radius  $R = 15 \xi$  which center coincides with the center of the square superconducting region. The position of one magnetic dipole is defined by the vector  $\vec{r}_{dip} = x_{dip} \hat{x} + y_{dip} \hat{y} + z_{dip} \hat{z}$ . We consider the coordinate system range is from 0 to 120 in  $x$  and  $y$  directions and the reference circumference has its center at point  $\vec{r}_0 = (L_x/2) \hat{x} + (L_y/2) \hat{y}$ . Thus, the coordinate of each magnetic dipole is defined by

the relations  $x_{dip} = L_x/2 + R \cos \varphi_{dip}$  and  $y_{dip} = L_y/2 + R \sin \varphi_{dip}$ , where  $\varphi_{dip}$  is the angle between the position of the dipole and the  $x$  axis.

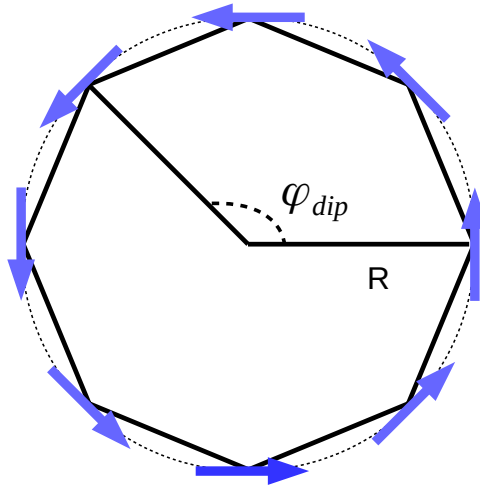


Figure 5.7: Octagon of magnetic dipoles inscribed in a circumference of radius  $R$ . The position of each dipole is determined by the angle  $\varphi_{dip}$

As an example of arrangement of the dipoles in a polygon, it is shown in Fig. 5.7 an illustration of the octagon of magnetic dipoles inscribed in a circumference of radius  $R$ . Each magnetic dipole occupies a position fixed by the angle  $\varphi_{dip}$  between the dipole and  $x$ -axis. The square and the hexadecagon are obtained by a similar arrangement.

The magnetic dipole moment is expressed as  $\vec{\mu} = \mu_{dip}(-\sin \varphi_{dip} \hat{x} + \cos \varphi_{dip} \hat{y})$ , where  $\mu_{dip}$  is in units of  $\mu_{GL} \equiv H_{c2} \xi^3$ . We fixed the magnetic moment for each dipole as  $\mu_{dip} = 16 \mu_{GL}$ , after perform simulations for different values for the magnetic moment and distance to the superconducting film. The distance to the superconducting film and the value for the magnetic moment are particular choices to illustrate the properties of the azimuthal arrangement in our system. For effect of comparison, G. Carneiro in Ref. [23] considers the magnetic moment  $\mu_{dip} = 5.3 \mu_{GL}$  for in-plane magnetic dipoles in an array positioned above a superconducting film at a distance

$d = 2 \xi$ . While J. Piña *et al.* in Ref. [123] considered an array of dipoles with magnetic moment perpendicular to a superconducting film at distances varying from  $d = 2 \xi$  to  $d = 6.5 \xi$  and magnetic moments varying from  $\mu = 0$  to  $\mu = 180 \mu_{GL}$ . In these works it is observed the nucleation of vortices and antivortices in the superconductor in distinct configurations depending on these two parameters  $d$  and  $\mu$ .

### 5.4.1 Vector Potential of a polygon of magnetic dipoles

To calculate the vector potential for the polygon of magnetic dipoles we perform the same procedures described for the permalloy disk and the annulus. We consider the general expression for the vector potential of a single magnetic dipole given by Eq.(5.1). Inserting the magnetic dipole moment  $\vec{\mu} = \mu_{dip}(-\sin \varphi_{dip} \hat{x} + \cos \varphi_{dip} \hat{y})$  we obtain expressions for  $A_x$  and  $A_y$  with the same form of Eq.(5.8) and Eq.(5.9), however, in the polygon case the coordinate  $z_{dip}$  assumes only one value.

The vector potential of a single magnetic dipole is given by the well known expression

$$\vec{A}(\vec{r}) = \frac{\vec{\mu} \times (\vec{r} - \vec{r}_{dip})}{|\vec{r} - \vec{r}_{dip}|^3}. \quad (5.10)$$

By inserting the expression for the magnetic dipole moment into Eq.(5.10), it simplifies to

$$\vec{A} = \frac{\mu_{dip}}{(\bar{x}^2 + \bar{y}^2 + \bar{z}^2)^{3/2}} [\bar{z} \cos \varphi_{dip} \hat{x} + \bar{z} \sin \varphi_{dip} \hat{y}], \quad (5.11)$$

where  $\bar{x} = x - x_{dip}$ ,  $\bar{y} = y - y_{dip}$ ,  $\bar{z} = z - z_{dip}$ .

For an array of  $N_d$  dipoles placed on the vertices of a polygon the resulting vector potential is just the superposition of the one-dipole vector potential. The position of each dipole can be seen as if it was determined by the condition that the angular

distance between two neighbors is equal. In this way, the angle related to the position of a dipole is determined by  $\varphi_{dip,n} = 2\pi n/N_d$ , where  $n = 1 - N_d$ . We perform the integration of the vector potential along the thickness of the superconducting film, and then, we take the vector potential superposition of all magnetic dipoles in the polygon.

Our solution method is the iterative procedure that is explained in details in section 4.1.3. In this method the solution for the superconducting order parameter is obtained through a relaxation process, by considering the external influences by means of the vector potential, to a state of lower free energy. The initial state of all simulations in this section is the normal one, where the order parameter is  $\psi \approx 0$  over all the superconducting area. We are able to follow the evolution of the order parameter, and other significant quantities, along all the steps of the relaxation to the ground state. In our calculations, we seek a stable solution through a maximum of  $10^5$  iterative steps. After this number of steps we consider that we have achieved a stable or meta-stable solution. Usually, for a given array of parameters, the solution converges for some thousands of steps (5000 – 10000 steps) in the relaxation process.

#### 5.4.2 Square - 4 magnetic dipoles

The first polygon of magnetic dipoles we analyze consists of four dipoles on the vertices of a square inscribed in a circumference of radius  $R = 15 \xi$ . The circumference is centralized in the superconducting region. The magnetic dipoles are fixed at angles  $\varphi_{dip} = \pi/2, \pi, 3\pi/2, 2\pi$ . The magnetic moments are oriented in an azimuthal configuration in the counterclockwise sense.

We use the calculated vector potential, produced by the square of magnetic dipoles to numerically solve the GL equation, as described in section 4.1.3. We obtain the superconducting density and phase, which permit us to calculate the superconducting

current density. Below, are shown some figures of the superconducting density, phase and current density at different steps after the beginning of the iteration procedure, and in the equilibrium state for the superconducting film under the effect of the square of dipoles. In this way, we intend to illustrate how the superconducting phase is affected by the square of dipoles.

In the case of only four dipoles above the superconducting film, we obtain a stable solution after some few thousands of steps in the relaxation procedure. We analyse the results for two intermediate states that were obtained for some steps after the beginning of the iteration process, and the configuration obtained at the equilibrium state.

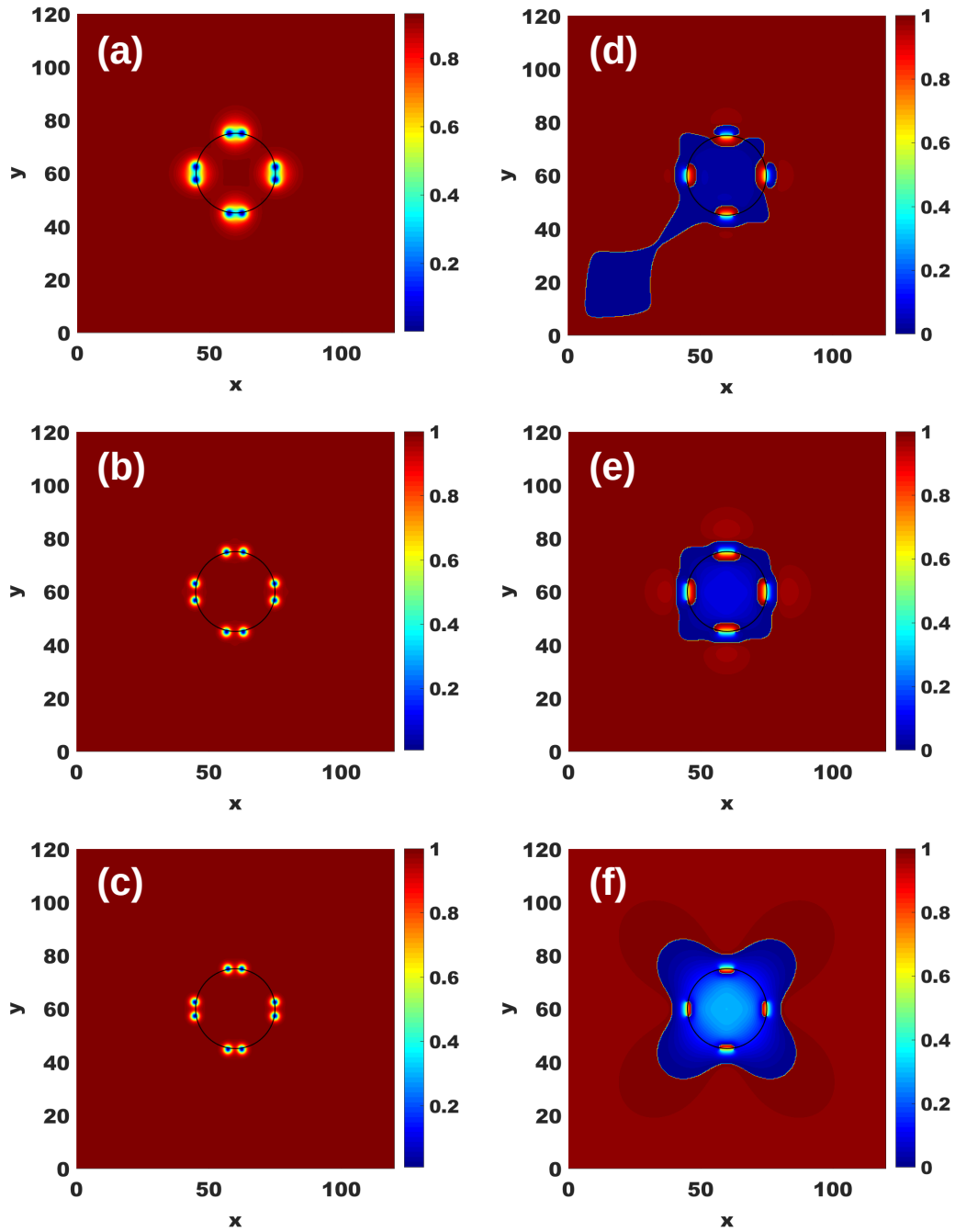


Figure 5.8: Superconducting density  $|\psi|^2$  (*a, b, c*) and phase  $\theta$  (*d, e, f*). Each row represents a different state, where it is shown two intermediate states (*a, d*), (*b, e*) and the equilibrium one (*c, f*). The phase varies from  $\theta/2\pi = 0$  and  $\theta/2\pi = 1$ .

In Fig. 5.8, in first column it is shown the superconducting density ( $a, b, c$ ) and in the second one the phase ( $d, e, f$ ) corresponding to states taken from the relaxation process at 4 iterations after the simulation beginning ( $a, d$ ), 44 iterations ( $b, e$ ) and at the equilibrium state ( $c, f$ ) obtained at the end of the simulation. The first row shows a state just after the beginning in the normal state where  $\psi \approx 0$ . At this step, the superconductivity has nucleated in almost the whole region in a uniform way. In the colorbar of panel ( $a$ ) it is possible to see that the red region corresponds to  $|\psi|^2 \approx 1$ . The density is null in blue regions ( $|\psi|^2 = 0$ ) below the dipoles due the presence of the dipoles magnetic field. It is seen one pair of points of zero density below each dipole which corresponds to a VAV pair as can be confirmed by the phase shown in panel ( $d$ ). It is seen, below each dipole, a small curved segment that corresponds to a bound VAV pair. As it was discussed in details in section 1.1, the VAV pair presents a phase corresponding to a curved segment with a hue from blue to red around each extremity but in opposite sense. We identify the continuous hue, around an extremity of one of these curved segments, from blue  $\theta/2\pi = 0$  to red  $\theta/2\pi = 1$  in the counterclockwise sense as a vortex and in the clockwise sense as an antivortex.

The second intermediate state ( $b, e$ ) shown in Fig. 5.8 presents the vortices and antivortices completely separated as can be seen in the superconducting density ( $b$ ). The phase shown in panel ( $e$ ) presents a more uniform distribution. By the definition of the vortex (antivortex) based on the variation of the hue, it can be verified that below each positive pole there is an antivortex and below the negative pole there is a vortex.

Although the superconducting density of the equilibrium state ( $c, f$ ) obtained at the end of the relaxation is not much different from the previous intermediate state, the phase shows a great change. The curved segments characterizing the VAV pairs are smaller at this state and there is a symmetric four-fold form of the

phase around the region affected by the square of dipoles. We verify that for this arrangement of dipoles, namely, the square of dipoles, the state of lower energy admits the coexistence of vortices and antivortices in the superconducting film.

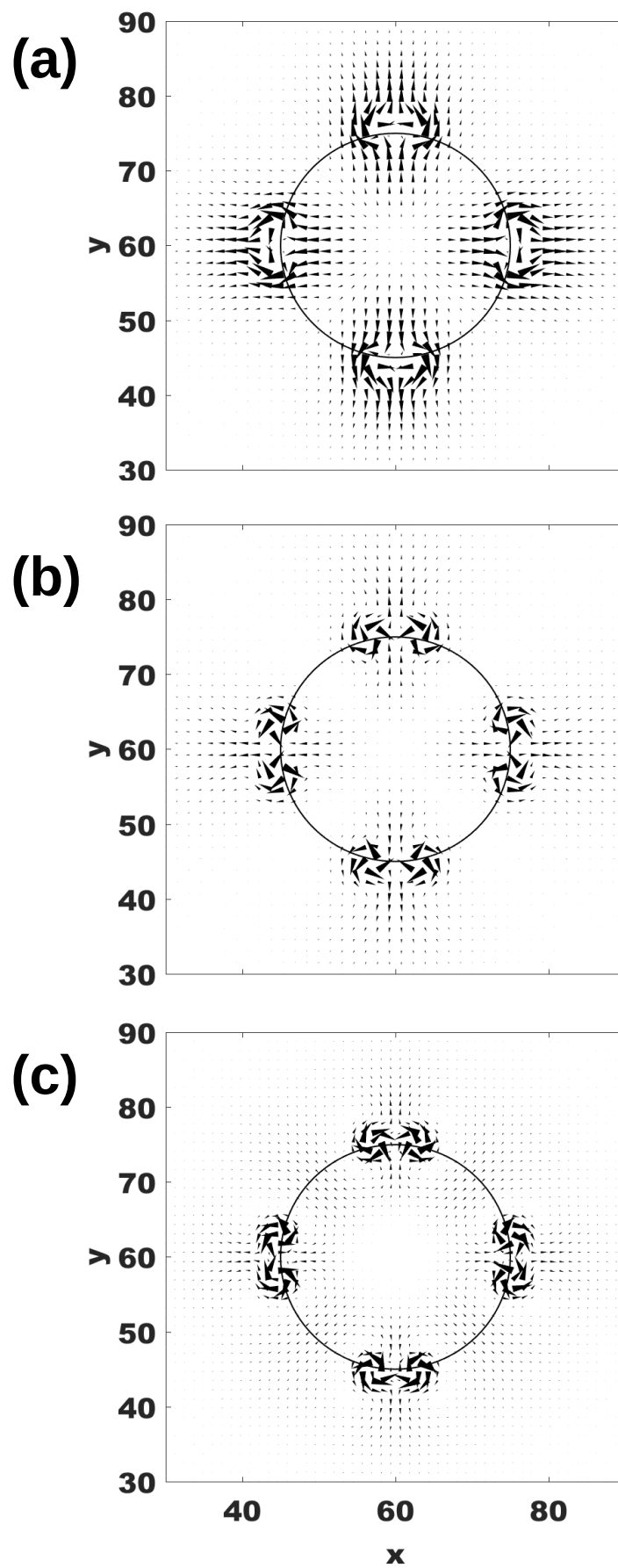


Figure 5.9: Superconducting current density corresponding to the three states shown in Fig. 5.8.

In Fig. 5.9, we show the superconducting current density focusing on the central region of the simulation area because we are interested on the behavior of the current in the area under influence of the magnetic field of the dipoles. The current is too weak or even null in the regions that are distant from the magnetic dipoles and the superconducting state is uniform. Because that, we adjust the spacement and the scale of the arrows in the graph in order to present the best visualization in the area close to the dipoles. Here, panel (a) corresponds to the first intermediate state shown in Fig. 5.8(a, d). At this step of the relaxation process the current flows predominantly in a radial direction from the center of the figure to the borders. Below the region closer the magnetic dipoles the current flows in a curved path indicating the beginning of a circulation.

Panel (b) of Fig. 5.9 correponds to the second intermediate state shown in Fig. 5.8(b, e) and panel (c) to the equilibrium state. The current density in these two states are very similar in behavior, mainly presenting changes in intensity which is not measurable by our graphs since we adjust the scale for the best visualization. It is seen that the current above the positive pole circulates in clockwise sense while in the negative pole the current flows in the counterclockwise direction. It can be observed that there is a small current flux (compared to the circulating current around the poles) in between the positive and negative poles of the same magnetic dipole and between two adjacent dipoles.

### 5.4.3 Octagon - 8 magnetic dipoles

In the same form as made for the square of dipoles, here we consider a set of magnetic dipoles positioned at the vertices of an octagon inscribed in a reference circumference, at the center of the superconducting area, with the radius of equal value to the annulus and disk which is  $R = 15 \xi$ . Hence, the magnetic moments are

fixed in an azimuthal orientation at angles  $\phi_{dip} = \pi/4, \pi/2, 3\pi/4, \pi, 5\pi/4, 3\pi/2, 7\pi/4$  and  $2\pi$ . The vector potential of the octagon is calculated and inserted into the GL equation that is numerically solved to obtain the order parameter of the equilibrium state.

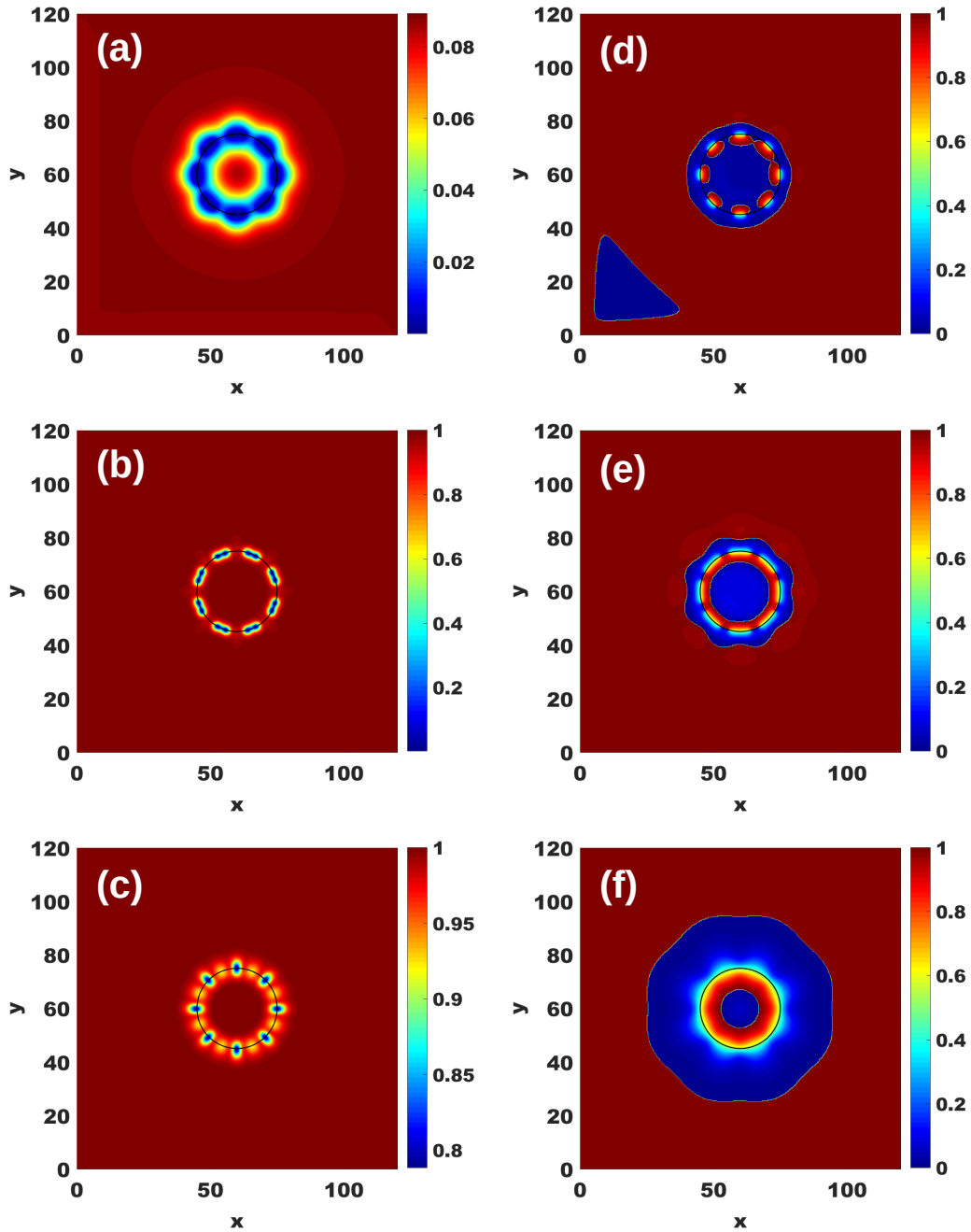


Figure 5.10: Superconducting density (*a, b, c*) and phase (*d, e, f*) for two intermediate states (*a, d*) and (*b, e*) of the relaxation process which results in the equilibrium state (*c, f*). The phase varies from  $\theta/2\pi = 0$  and  $\theta/2\pi = 1$ .

In Fig. 5.10(a) we show the superconducting density at two iterative steps after the beginning of the relaxation from a uniform normal state with  $|\psi|^2 \approx 0$  over all the region. In this state (a, d), it is seen that the superconducting state is weakly developed since the density shown in panel (a) varies between  $|\psi|^2 = 0$  below the magnetic dipoles and reaches the maximum value  $|\psi|^2 \approx 0.085$  in the more distant regions. The density shows some elongated regions where the superconductivity is maximal but it is not clear the existence of vortices or antivortices. Their existence is observed in panel (b) where the phase shows the characteristic set of curved segments associated to bound VAV pairs. It is seen that some segments have their two extremities below the same dipole while others segments presents one extremity below different magnetic dipole indicating the bounding between vortices and antivortices generated by different dipoles.

A snapshot of a second intermediate state, taken at 20 iterative steps after the beginning of the simulation is characterized by the density (b) and phase (e). This state has already evolved to a more uniform configuration with  $|\psi|^2 = 1$  over almost the whole superconducting region. It is seen eight elongated regions which each of them have two points of maximal suppression where  $|\psi|^2 = 0$ . Interestingly, these regions of suppression occurs below the reference circumference but between two adjacent magnetic dipoles. From panel (e) that shows the superconducting phase, it is observed the existence of a closed curve forming a blue circle at the center of the figure. It is the first evidence of connection between the rings of phase discontinuity and the azimuthal arrangement of magnetic dipoles. It is also shown eight small curved segments in the regions between two adjacent dipoles corresponding to the pairs of suppression regions visible in the density graph (b).

Finally, in the lower row of Fig. 5.10 the equilibrium state is shown. In panel (c) it is clear that there is not the presence of vortex (antivortex) anymore. It is

only visible eight regions of superconductivity suppression, reaching a minimal value  $|\psi|^2 \approx 0.8$ , below each dipole and other regions of smaller suppression  $|\psi|^2 \approx 0.9$  between adjacent dipoles. The phase shown in panel (*f*) does not show any curved segment. Indeed, it is only seen a closed circular curve at the center and another closed curve, similar to a rounded octagon, outside the region affected by the octagon of dipoles.

We interpret the process shown in these snapshots of the relaxation as the attraction of a vortex generated below one given dipole by an antivortex generated below a neighbor dipole. The pair under this interaction become closer until their collapse and annihilation. The effect in the phase is the connection of the line segment extremities corresponding to a vortex to the other extremities that determines an antivortex.

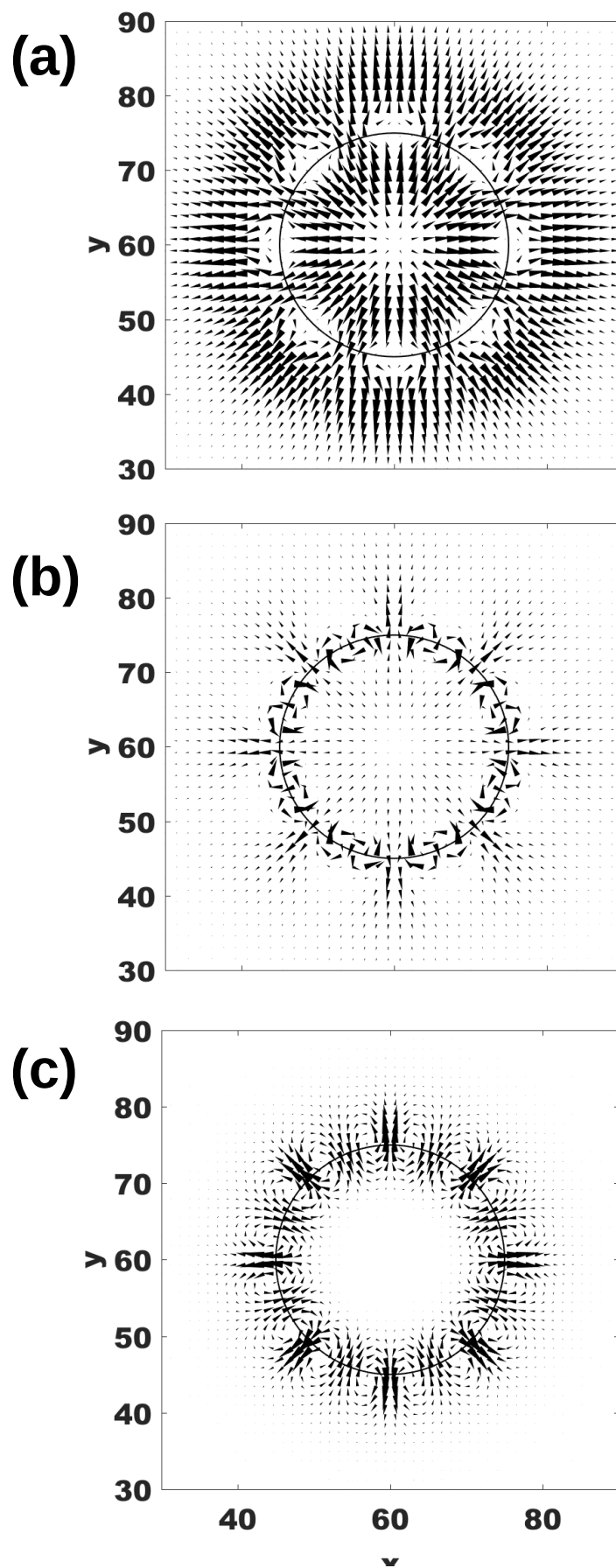


Figure 5.11: Superconducting current corresponding to the three states shown in Fig. 5.10.

In Fig. 5.11(*a*) we present the current density (*a*), (*b*) and (*c*) for the three states (*a, d*), (*b, e*) and (*c, f*), respectively, in Fig. 5.10. As commented before, these graphs are intended to illustrate the dominant behavior of the current density, since the scale of the arrows are adjusted to the best visualization of each state. Therefore, the intensity of the current density changes significantly among the three shown panels what does not permit us to compare the intensity of different states but only on different regions in a graph for a determined state. In panel (*a*), the current corresponding to the first intermediate state Fig. 5.10(*a, d*) presents a radial flow from the center to the area external to the octagon of dipoles with regions of null current below the dipoles. These regions correspond to the vortices (antivortices) cores.

The second intermediate state Fig. 5.10(*b, e*) presents a current density more localized in the dipoles regions as can be seen in Fig. 5.11(*b*). It is observed a radial current still flowing from the center to the external regions below the dipoles but between the dipoles the predominant behavior is the circulating flow due the vortex (antivortex) localized on these regions.

In panel (*c*) of Fig. 5.11, it is shown a superconducting current density concentrated below the octagon of dipoles. Exactly below each dipole, the current presents an outwardly radial flow with a higher intensity compared the current flowing inward in the region between the dipoles. This current flow is responsible for the superconducting suppression observed in Fig. 5.10(*c*).

In conclusion, for the octagon of dipoles with the chosen magnetic moment value, the coexistence of static vortices and antivortices is not favorable. The vortex below the negative pole of a given dipole is attracted and annihilate with the antivortex below the positive pole of an adjacent magnetic dipole. The resulting equilibrium

state presents superconductivity with suppressed regions formed under the action of induced currents generated by the stray field. These currents are Meissner currents since the current flows oppositely to those of a vortex (antivortex) below the dipole as can be seen in comparison with the square of dipoles in Fig. 5.9(c). Hence, the induced current in the octagon equilibrium state shields the film from the penetration of magnetic field.

#### 5.4.4 Hexadecagon - 16 magnetic dipoles

In this section we present the results for an array of sixteen dipoles positioned on the vertices of the hexadecagon inscribed in a circumference of radius  $R = 15 \xi$ . The hexadecagon is in the center of the simulation region and as before the magnetic dipoles are arranged in the azimuthal configuration at angles defined by the relation  $\varphi_{dip,n} = \pi n/8$ , where  $n = 1, \dots, 16$ . As it was done for the previous polygons, here we consider two intermediate states and the equilibrium configuration.

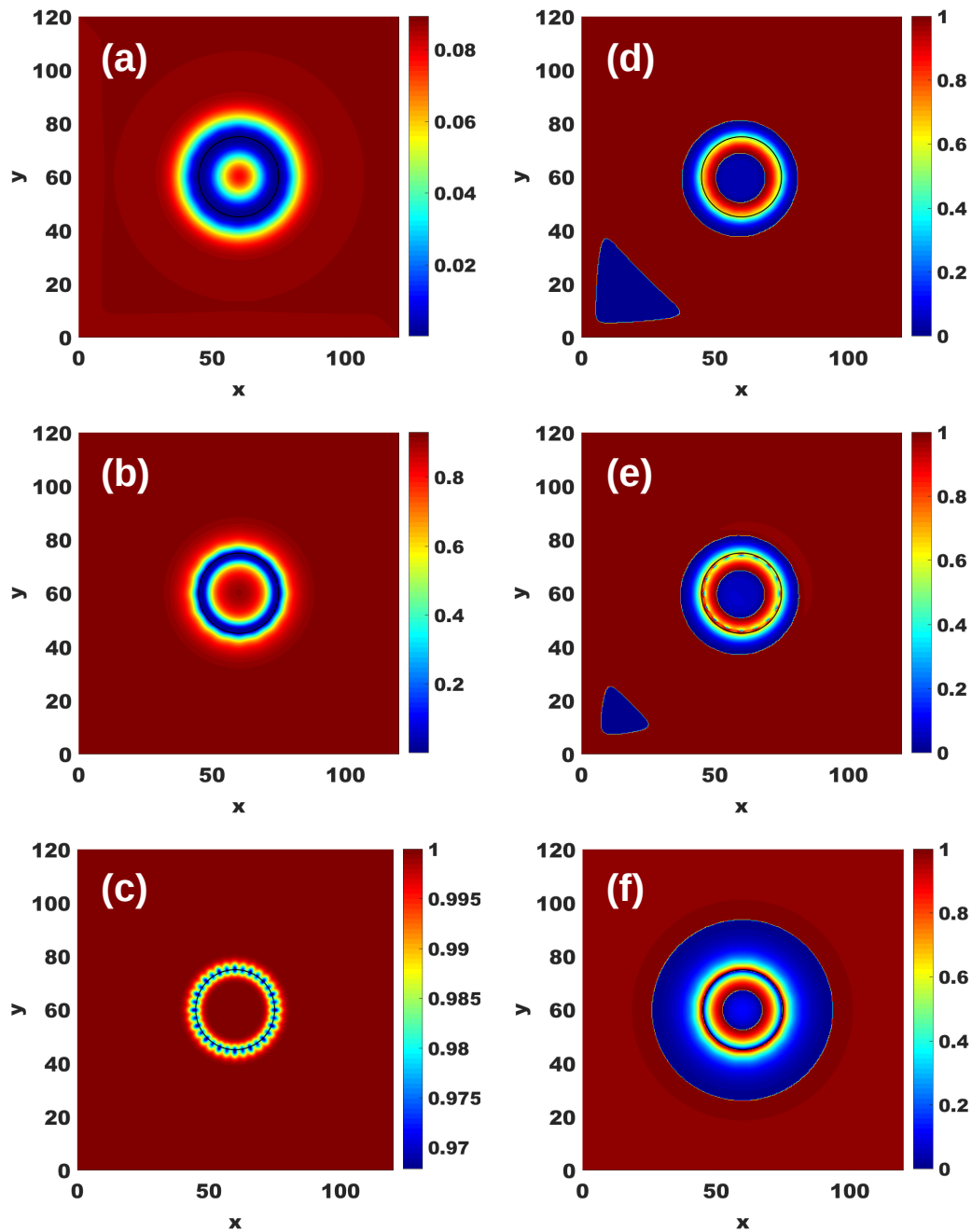


Figure 5.12: Superconducting density ( $a, b, c$ ) and phase ( $d, e, f$ ) for two intermediate states ( $a, d$ ) and ( $b, e$ ) of the relaxation process and the final equilibrium state ( $c, f$ ).

In Fig. 5.12 it is shown the superconducting density ( $a, b, c$ ) and phase ( $d, e, f$ ). The state ( $a, d$ ) corresponds to the second iterative step after the beginning of the relaxation from the uniform normal state  $|\psi|^2 \approx 0$ . At this stage of the relaxation the superconductivity has just started the nucleation. It is observed in panel ( $a$ ) that the density has maximal value  $|\psi|^2 \approx 0.085$ . Moreover, it is formed a ring presenting the maximal suppression of the order parameter just below the region of the hexadecagon. In panel ( $b$ ), it is shown the superconducting phase that presents an internal blue circle separated by a discontinuity line of a radial hue from red to blue which corresponds to a phase change from  $\theta/2\pi = 1$  to  $\theta/2\pi = 0$ .

The second intermediate state for the hexadecagon system shows a superconducting density, in Fig. 5.12( $b$ ), almost uniform  $|\psi|^2 \approx 1$  over the whole area with a ring of complete suppression below the hexadecagon. The phase shown in panel ( $e$ ) presents an interesting detail. The general distribution is the same of the previous state, however, it is seen a group of small disturbances over the region that presented a continuous hue in the previous state. The mentioned disturbances in the phase are localized exactly below each dipole of the hexadecagon what make us to interpret these disturbances as vortices and antivortices that nucleate below the respective poles as in the previous polygons. But since for the hexadecagon the dipoles are very close to each other, the nucleated vortex (antivortex) below a given dipoles mutually attract the antivortex (vortex) of a neighbor dipole, and finally they annihilate themselves generating the shown disturbances in the superconducting phase.

At the end of the relaxation process we obtain the equilibrium state whose superconducting density and phase are respectively shown in panels ( $c$ ) and ( $f$ ) of Fig. 5.12. It is interesting to notice that we considered the interaction of sixteen dipoles with the superconducting film but it is seen thirty two well defined regions of a weak suppression of the superconductivity  $|\psi|^2 \approx 0.97$  around the hexadecagon of dipoles. In the superconducting phase, shown in panel ( $f$ ), it can be identified three

concentric regions, where the smaller one is a blue circle  $\theta/2\pi \approx 0$  delimited by a discontinuity circumference where a jump in the phase takes place. The intermediary region is a ring presenting a hue from  $\theta/2\pi = 1$  to a more external discontinuity circumference where the phase is  $\theta/2\pi = 0$  in the internal region and jumps to  $\theta/2\pi = 1$  in the external side of the described ring. It is observed that the second discontinuity circumference is positioned exactly below the circumference that delimits the hexadecagon. The more external concentric region is a second ring of phase variation that is limited by a large external circumference discontinuity separating the region affected by the hexadecagon of the remained superconducting region that presents a uniform phase.

Another important information shown in the hexadecagon concerns the radial gradient of the phase. near to the region where the phase varies rapidly in contrast with the other regions. This intense radial phase gradient we consider to be connected to the radial current density, as observed for all polygons.

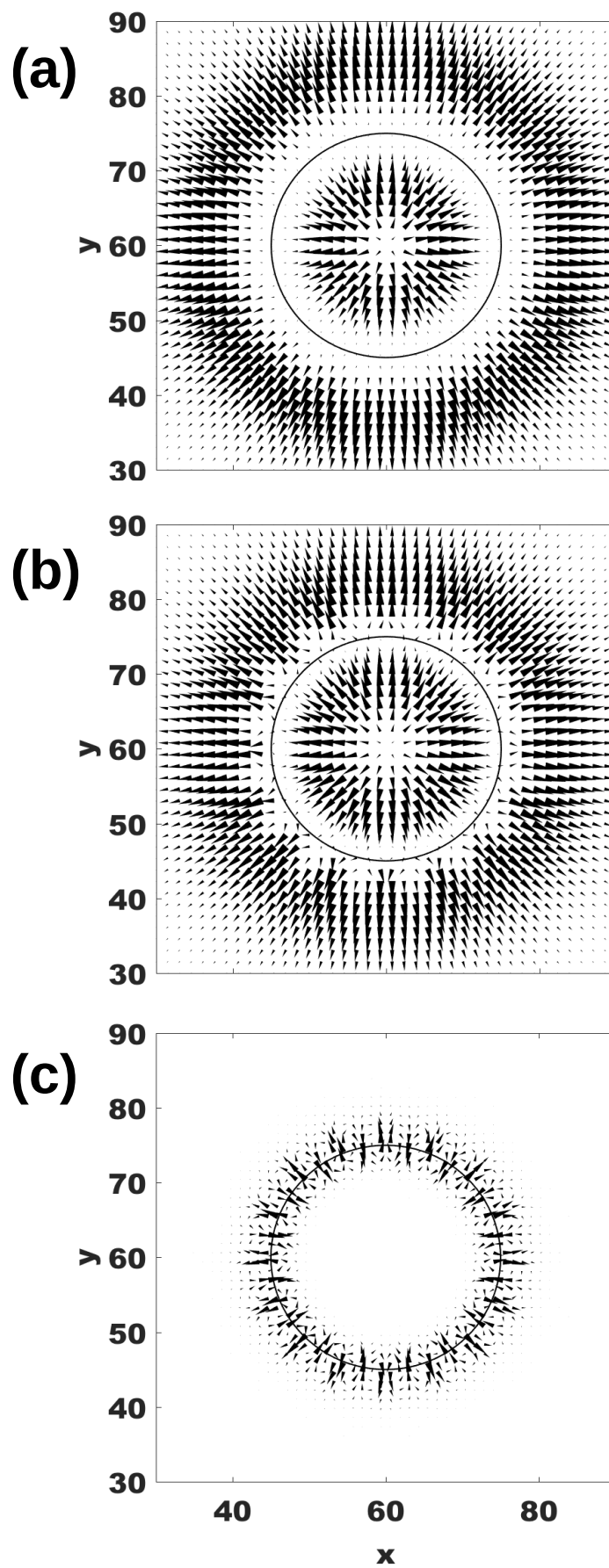


Figure 5.13: Superconducting current corresponding to the three states analyzed in Fig. 5.12.

The superconducting current density for the three considered states obtained in our relaxation for the hexadecagon is presented in Fig. 5.13. Panels (a) and (b) correspond to the first and second intermediate states shown in Fig. 5.12(a, d) and Fig. 5.12(b, e) respectively. For the hexadecagon, the current density shown in Fig. 5.13 does not give too much information. Since, the dipoles are very closer the current flow is very localized and the arrow plot is not suitable to analyze the behavior at the necessary scale, but we extract some general considerations from this figure. In first place, it is seen a predominant radial flow of the current density for the intermediate states at the beginning of the relaxation, panels (a) and (b). The current flow is from the center to the external areas, excluding the region below the dipoles, where the current density presents a minimum. We need to remember that the arrow are adjusted to improve the visualization. For both discussed intermediate states the intensity of the current is very small and it is not related to any effect observed in the previous discussion. In panel (c), the current density for the equilibrium state is shown, presenting the already characteristic circulating behavior around the position below the dipoles. As before, we identify these current circulation as Meissner currents since the circulation above each pole of the magnets creates a magnetic field that tends to oppose the local stray field of the dipole.

## 5.5 Conclusion

In this chapter, we presented the effect of a permalloy disk above a superconducting thin film. The permalloy disk does not produce the nucleation of isolated vortices in the film because the stray field generated by its magnetic state is very narrow, affecting only a restricted region of the superconducting film. The disk stray field presents a predominantly positive magnetic field in a circular area of radius  $r_{core} \approx 30 \text{ nm}$ , that is small when compared to the size of the disk. Since we consider an infinite superconducting film, the total magnetic flux must be zero over the superconducting region. Hence, in the absence of regions with a negative stray field, close to the

magnetic disk, it becomes energetically unfavorable the nucleation of vortices and antivortices.

Although the stray field does not produce significant effects on the superconducting density, we observed a distinct behavior in the superconducting phase. The presence of the permalloy disk produces the appearance of rings of phase discontinuity in the phase.

In order to investigate the mentioned effect on the phase, we constructed a permalloy annulus that is characterized by the magnetic moments in the same arrangement as that of a permalloy disk excluded from its out-of-plane core. The results obtained from the permalloy annulus showed us that it is, indeed, the in-plane magnetic moments present in the disk and the annulus that produces the rings of phase discontinuity in the superconducting film.

As a further step to obtain a better understanding of the mentioned phenomenon we constructed a model with some few in-plane magnetic dipoles, that were called, polygon of dipoles.

From the results presented in the analysis of the superconducting film with the polygon of dipoles, namely, the square, the octagon and the hexadecagon, we can conclude that for a small number of dipoles, the distance among them is sufficient to permit that the perpendicular component of the stray field be strong enough to create vortices and antivortices below the dipoles.

We observed the pinning of the vortices below the negative poles and the antivortices below the positive poles at the equilibrium state for the square of dipoles. For the octagon of dipoles, we verified that the distance between two neighbors dipoles decreases, and therefore the vortices nucleated below a given dipole mutually attract the antivortices of an adjacent dipole and they annihilate themselves, resulting in a state of localized superconductivity suppression caused by the circulating currents

around the poles at the equilibrium.

For the hexadecagon of dipoles, we observed an indication of what could be considered the nucleation of VAV pairs but only a locally suppressed order parameter is objectively seen since the beginning of the relaxation process.

We concluded that the observed density suppression is caused by the Meissner currents circulating below the poles of the magnetic dipoles. In reason of the circulation of these currents there is a local radial current density below the polygons that we argue to be related to the phase gradient maximum and be the reason for the existence of the rings of discontinuities in the superconducting phase.

We argue that the in-plane magnetic moments inside permalloy disk produces the same effects as the polygons of dipoles, which is the nucleation of VAV pairs that annihilates among them.

Assuming that the dipoles inside the disk induces a radial Meissner current as the polygons does, the overall effect can be compared to the “Gedankenexperiment” discussed in chapter 1 and the nucleation of VAV pairs in a corbino disk that was already studied in [73].

As a form to verify the relation of the discontinuities rings in the phase with the nucleation of VAV pairs, we consider the possibility of stimulate the VAV pairs nucleation by an applied current density. That is the main topic of the next chapter.

# Chapter 6

## Nucleation of vortex-antivortex pairs near to an array of defects

In this chapter we analyze the nucleation of vortex-antivortex (VAV) pairs in a superconducting thin film in the presence of an array of disks that can be either magnetic dots or regions of a  $T_c$  suppressed superconductor. In the latter case the Cooper pair density is reduced inside the disk to 25% of its external value. We treat this case to reach better understanding of the array of permalloy disks, which is our main objective. The appearance of VAV pairs is stimulated by an external applied current density in both cases.

### 6.1 Introduction

Firstly, we discuss the local suppression of superconductivity inside an array of encrusted disks in an infinite superconducting film. The Cooper pair density is lowered through the proximity effect between the superconducting (film) and the normal (disk) region [78, 55, 118]. Next, we study the magnetic dots whose constituents are magnetic moments. The theoretical model of the magnetic annulus has been defined in chapter 5, and corresponds to a perforated disk with external

radius  $R$ , internal radius  $r$ , such that all the magnetic moments that constitutes the annulus are in the azimuthal direction, as defined in section 5.3. We obtain the total magnetization of the annulus simply by summing all the contributions of its microscopic magnetic moment dipoles. Distinctively, the permalloy disk of radius  $R$  has its local magnetization obtained from micromagnetic simulations performed with the software Mumax3 [148], and so, it is a resulting equilibrium solution of a free energy minimization procedure. The magnetic dot systems (permalloy, annulus) we think of them as positioned above and separated of the superconducting film by an insulating layer of thickness  $d$  in order to avoid the transference of electrons between both systems.

The interaction between magnetic and superconducting subsystems (S/F) is only through the inhomogeneous periodic stray field that yields localized regions of positive and negative magnetic field, perpendicularly to the film. In consequence of these perpendicular localized stray field, there is the generation of Meissner currents in the film in order to oppose the penetrating field. We apply an external uniform dc current across the length of one side of the film. This current added to the blocking localized currents sum their intensity in some regions and decreased in others, and this is the reason for the nucleation of vortices and antivortices in the superconducting film. Similarly to the previous chapter no counter action is considered, namely, these supercurrents do not modify the magnetic moment arrangement of the permalloy and of the annulus. We do not apply an external uniform magnetic field in a region of suppressed superconductivity, as it was done by M. Ghinovker *et al.* [59, 60], or in a superconducting film under the effect of the stray field of a magnetic dipole array as it was investigated by C. L. S. Lima and C. C. de Souza Silva [89], for example.

In both cases studied here, the total magnetic flux is zero at the very beginning, and so, remains zero when the external current is applied. The quantization of flux imposes, when the effects of the disks are strong enough to induce the nucleation, that they must occur in pairs of vortices and antivortices, in order to maintain the total

magnetic flux through the film equals to zero. Moreover, there are regions where the total current in the film is stronger than the depairing (or Ginzburg-Landau) current density  $J_{GL} = c\Phi_0/(12\sqrt{3}\pi^2\lambda^2\xi) = \sqrt{2}cH_c/(6\pi\sqrt{3}\lambda)$  [140], giving rise to normal regions, which are areas where the order parameter is strongly suppressed. These areas become candidates for the nucleation of vortices and antivortices since there the order parameter ought to vanish. The orientation of the current flow around these normal spots will favor the nucleation either of a vortex or an antivortex [23, 101, 74]. For systems containing a localized region where superconductivity is suppressed, we know from previous works that when this suppression is a result of an obstacle, like a hole [23] or a turn at some angle [28, 29], in the path of the current flow there is the effect of current crowding [9, 2] that generates areas, in the vicinity of the obstacle, with positive and negative field. At some increased value of the applied current vortices and antivortices are generated at these areas of positive or negative flux. We analyze here how the applied current stimulate the nucleation of VAV pairs in the case in which the order parameter is only partially suppressed by the proximity effect with a metallic disk. In the literature it has been considered the effect of magnetic and intrinsic defects in superconductors in reason of the importance to determine the parameters that can control the formation and stabilization of VAV pairs [103, 124] as well the varied phase configurations that can emerge from the systems where the vortices coexist with the antivortices [105, 103, 109]. In case of an intrinsic defect, e. g., an array of holes [23] or columnar defects [101], in the superconducting film it is explained in the literature the process that leads to the nucleation of VAV pairs.

In this thesis we find that novel features emerge from the systems containing the ferromagnets. Even though the perpendicular component of the ferromagnets (annulus/disk) stray field  $h_z$  is very weak and it is not enough to nucleate vortices (antivortices), the stray field is sufficient to create localized Meissner currents which combined with an external current can generate VAV pairs. As shown in section 5.3, another effect of the annulus on the superconductor is the formation of concentric

circles in the superconducting phase in reason of the curling of the magnetic moments that form the azimuthal magnetic state in the annulus/disk. We analyze the formation of these circles in the phase seeking to correlate them with the VAV pairs formation.

Our main objective in this chapter is to analyze the nucleation of VAV pairs as a function of the applied current for the superconducting film with the circular encrusted region of suppression of the order parameter and the film underneath the ferromagnets: annulus and disk. We want to correlate the nucleation of VAV pairs through a controlled given parameter. In case of the encrusted circular regions, the order parameter can be suppressed with different intensities. For the magnetic systems the generation of VAV pairs is studied in terms of the distance  $d$  between the film and the annulus (disk).

In all three cases we consider that the disks in the array are far apart ( $l_{disk} \gg R \gg \xi$ ), where  $l_{disk}$  is the distance among the disks. This allows us to perform the simulations by considering only one disk per simulation area. In all three cases we solve the Ginzburg-Landau equation for the order parameter iteratively in a unit cell, which consists on a square area, with the disk at the center under periodic boundary conditions with the appropriate gauge choice, as it was explained in details in section 4.1.2. Our numerical procedure simulates the cooling down process starting from the normal state, where the order parameter is zero, to reach a temperature  $T = 6.2 K$  in the presence of the stray field for the annulus and disk.

The applied dc current is uniform,  $I$ , and flows along the  $x$ -direction of the film. By considering the current across the simulation area of cross section  $t_s L_y$ , we can define the applied current density as  $\vec{J}_a = I/(t_s L_y) \hat{x}$ . The dc applied current is implemented in our formalism by the addition of a constant contribution to the applied vector potential, as it is done by M. V. Milošević and F. M. Peeters in Refs. [102, 107], for example. We can better understand this procedure when we consider that the

total current in the film is the sum of the applied  $\vec{J}_a$  and the superconducting  $\vec{J}$  current density  $\vec{J}_T = \vec{J}_a + \vec{J}$ , where we remember that  $\vec{J} = (\hbar q |\psi|^2 / m) [\nabla \theta - (2\pi / \Phi_0) \vec{A}]$ . Away from the center of the superconducting square, the order parameter and the superconducting phase are spatially uniform,  $\psi \rightarrow \psi_0 = \sqrt{|\alpha| / \beta}$ , and this gives for the superconducting current density  $\vec{J} = -(c / 4\pi \lambda^2) \vec{A}$ , which corresponds to the London limit. For the numerical calculations the vector potential is written in units of  $H_{c2} \xi$  and we obtain the dimensionless superconducting current density  $\vec{J} / j_0 = -\vec{A}$ , where  $j_0 \equiv c H_{c2} \xi / 4\pi \lambda^2$ . Similarly to the superconducting current, the applied current is written as  $\vec{J}_a / j_0 = -\vec{A}_a$ . The total current density at the border of the superconducting square has only the contribution of the applied current  $\vec{J}_T = \vec{A}_a$ , since the vector potential generated by the magnetic disk vanishes away from the source.

The intensity of the applied current density  $j_a = |\vec{J}_a|$  can be compared with the depairing current density,  $j_{GL}$ , in order to establish the range of variation of the applied current in our systems. In units of  $j_0$ , the depairing current density is  $j_{GL} / j_0 = 2 / (3\sqrt{3}) = 0.385$ . Then, we consider the applied current in the range  $0 < j_a < 0.35$ , in our simulations.

## 6.2 Encrusted disks with local suppression of the order parameter

We envision a periodic array of disks where the order parameter  $\psi$  within these disks is just a fraction of the maximum reached outside the disks. We think of as a consequence of the proximity effect [30]. In superconductor-ferromagnet (S/F) interfaces the order parameter decays with a damped oscillatory behavior inside the ferromagnet [138, 3]. One can think of two superconductors with different critical temperatures ( $T_{cn}$  and  $T_{cs}$ ) that obey the conditions  $T_{cs} > T_{cn}$  and  $T_{cs} - T_{cn} \ll T_{cn}$ .

As a consequence of the proximity effect in the interface between the encrusted disk and the film, the superconducting film S has a localized suppression of the order parameter in the region in contact with the disk N.

We consider an array of disks with a radius  $R = 15 \xi$ . The infinitely periodic thin film has its unit cell simulated as a square of side  $L_x = L_y = 120 \xi$  with periodic boundary conditions. In our simulations we solve the Ginzburg-Landau equation for the order parameter iteratively, as explained in details in section 4.1.3. Along the iterative process, the suppression over the disk is kept fixed by an appropriate numerical parameter in order that the chosen maximum superconducting density at the center of this region be  $|\psi|^2 = 0.25$ . At zero applied current, the superconducting density is constant,  $|\psi|^2 = 1$ , outside the suppression region but it decays continuously at the outer rim delimited by the disk's radius and reach the fixed value  $|\psi|^2 = 0.25$  at the center of the suppression region.

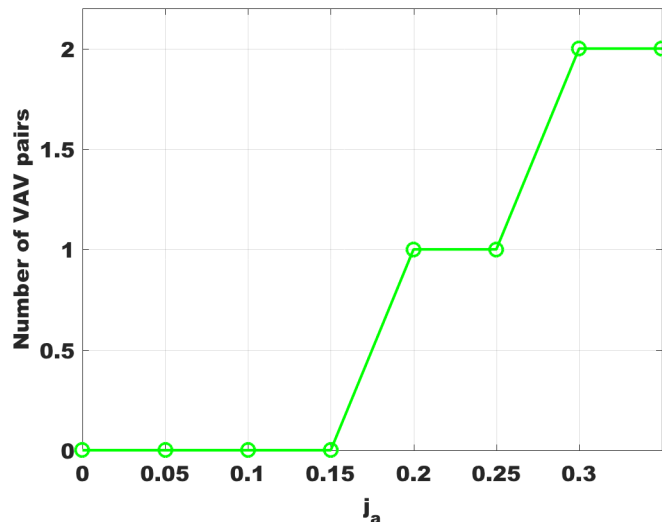


Figure 6.1: Number of VAV pairs, generated inside the region of suppressed superconductivity, as a function of the applied current.

The nucleation of VAV pairs starts in our system upon the presence of an uniform applied current density  $\vec{J}_a = j_a \hat{x}$ . Fig. 6.1 shows the number of VAV pairs that nucle-

ates in the suppression region as a function of the applied current. It is shown that for applied currents of value smaller than  $j_a = 0.15 j_0$  there are not the nucleation of VAV pairs in the suppression region. When the applied current is from  $j_a = 0.20 j_0$  to  $j_a = 0.25 j_0$  we observe that only one VAV pair is created in the film. Finally, for our final range of applied currents that goes from  $j_a = 0.30 j_0$  to  $j_a = 0.35 j_0$  we can identify the generation of two VAV pairs. From these results we see the characterization of three different regimes consisting of absence of VAV pairs, or nucleation of one and two VAV pairs depending on the intensity of the applied current.

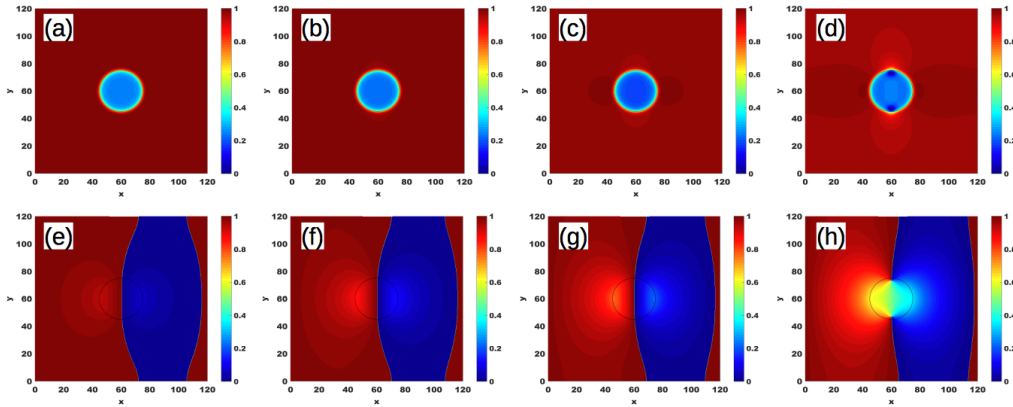


Figure 6.2: Superconducting density (upper row) and phase (lower row) for different values of applied current  $j_a$  in each column. The values of the current are as follows:  $j_a = 0.05 j_0$  for panels (a) and (e),  $j_a = 0.10 j_0$  for panels (b) and (f),  $j_a = 0.15 j_0$  for panels (c) and (g),  $j_a = 0.20 j_0$  for panels (d) and (h). For the superconducting density: dark red (blue) corresponds to  $|\psi|^2 = 1$  ( $|\psi|^2 = 0$ ), while for the phase: dark red (blue) relates to  $\theta = 2\pi$  ( $\theta = 0$ ).

Fig. 6.2 shows a sequence of equilibrium states obtained for increased values of the applied current from  $j_a = 0.05 j_0$  to  $j_a = 0.15 j_0$ . From the figure, we notice that the stronger current implies in a gradual variation of the superconducting density around the suppression region characterized by dark areas on the imaginary horizontal line that divides the figure in the middle horizontally ( $y = 60 \xi$ ), and light areas on the imaginary vertical line that divides the figure in the middle vertically ( $x = 60 \xi$ ), as can be seen in panels (a), (b), (c) for the density. We also observe a small variation of the superconducting phase as shown in panels (e), (f), (g). For

$j_a = 0.20 j_0$  it is possible to notice two well defined regions, shown on panel (d) as two dark blue spots on the north and south poles of the disk, where the superconducting density goes to zero inside the region of suppression characterizing the existence of vortices. Indeed, as can be verified in the phase, at this value of applied current density there is a VAV pair positioned close to the edge of the suppression region where the current is maximum. At this current it is possible to observe the nucleation of a VAV pair inside the suppression region but we verify that the pair does not leave this region, characterizing the pinning of the VAV pair.

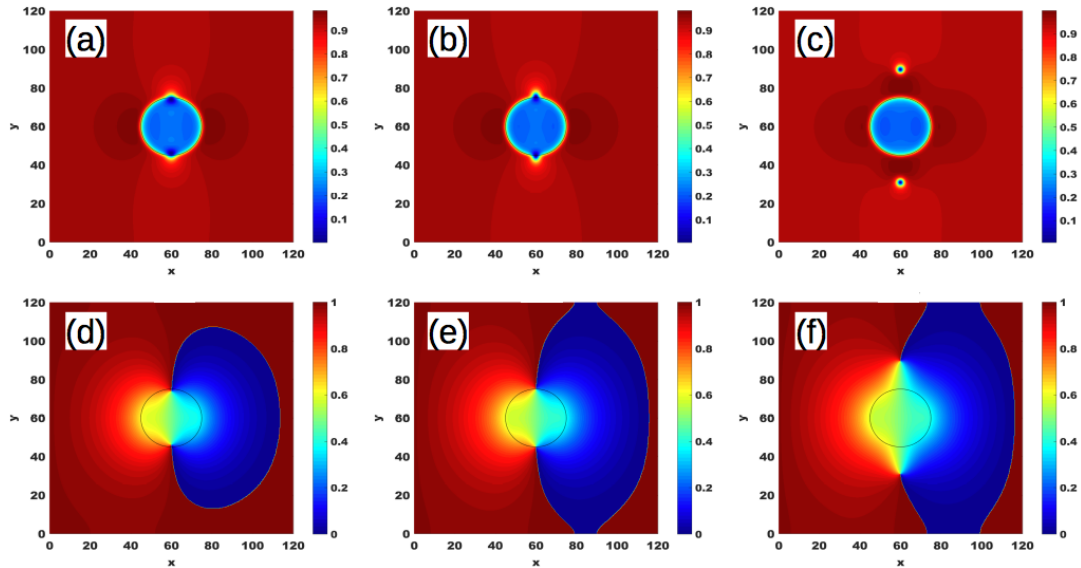


Figure 6.3: Superconducting density (upper row) and phase (lower row) for applied current  $j_a = 0.25 j_0$ . Each column presents the density and phase for a different state obtained from the relaxation process. For the superconducting density: dark red (blue) corresponds to  $|\psi|^2 = 1$  ( $|\psi|^2 = 0$ ), while for the phase: dark red (blue) relates to  $\theta = 2\pi$  ( $\theta = 0$ ).

Fig. 6.3 shows the superconducting density in panels (a), (b), (c) and the phase in panels (d), (e), (f), respectively, for three intermediate states (each column presents one state) obtained for an applied current  $j_a = 0.25 j_0$ . We observe that for this value of current it is energetically more favorable that the VAV pair leaves the confinement inside the disk and move outwards to the edges of the unit cell. Notice that the

nucleated VAV pair leaves the disk region in search of a lower energy state which is never reached because once the VAV pair is far away the center, a new VAV pair should nucleate. We are in the presence of an intermittent periodic phenomena which is out of reach of our relaxation equations. Those are only able to reach a stable minimum configuration. In case this one does not exist, we should halt the simulations and content ourselves with the nucleation of the VAV pair and not with the dynamics beyond this nucleation. After this step in our simulation, the system is not in equilibrium anymore, and our adopted method of solution is not appropriate beyond this point.

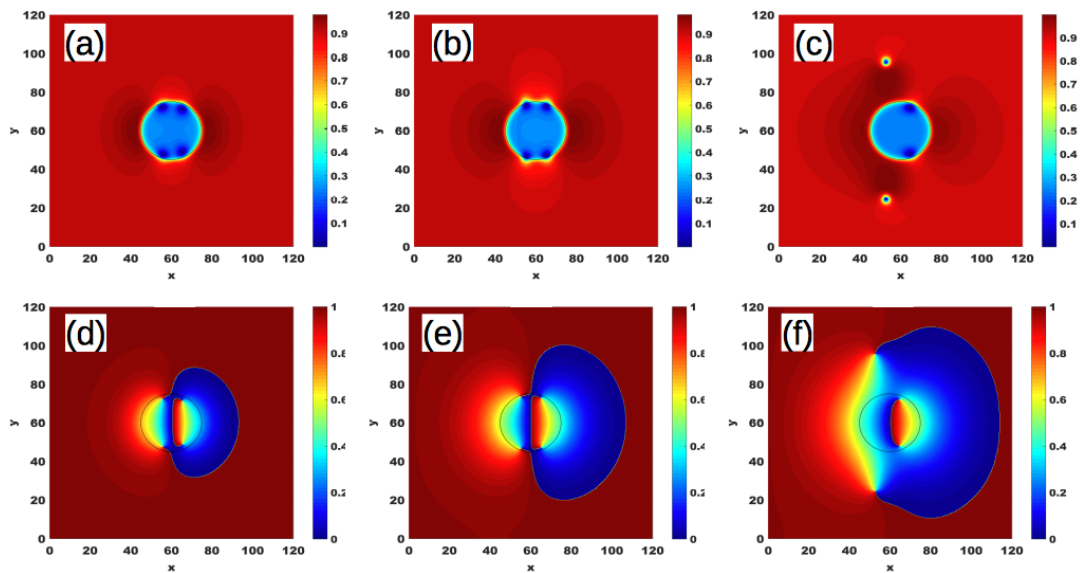


Figure 6.4: Superconducting density (upper row) and phase (lower row) for applied current  $j_a = 0.30 j_0$ . Three stages of the relaxation process are presented in the sequence of columns. For the superconducting density: dark red (blue) corresponds to  $|\psi|^2 = 1$  ( $|\psi|^2 = 0$ ), while for the phase: dark red (blue) relates to  $\theta = 2\pi$  ( $\theta = 0$ ).

Interestingly, in Fig. 6.4 where the external current is  $j_a = 0.30 j_0$ , we notice the formation of two VAV pairs inside the central circle. For the states  $(a, d)$  and  $(b, e)$ , which superconducting density are shown in panels  $(a)$  and  $(b)$ , it is seen that both pairs move to the edge of the suppression region but only one pair leaves the central region as can be seen in panel  $(c)$ .

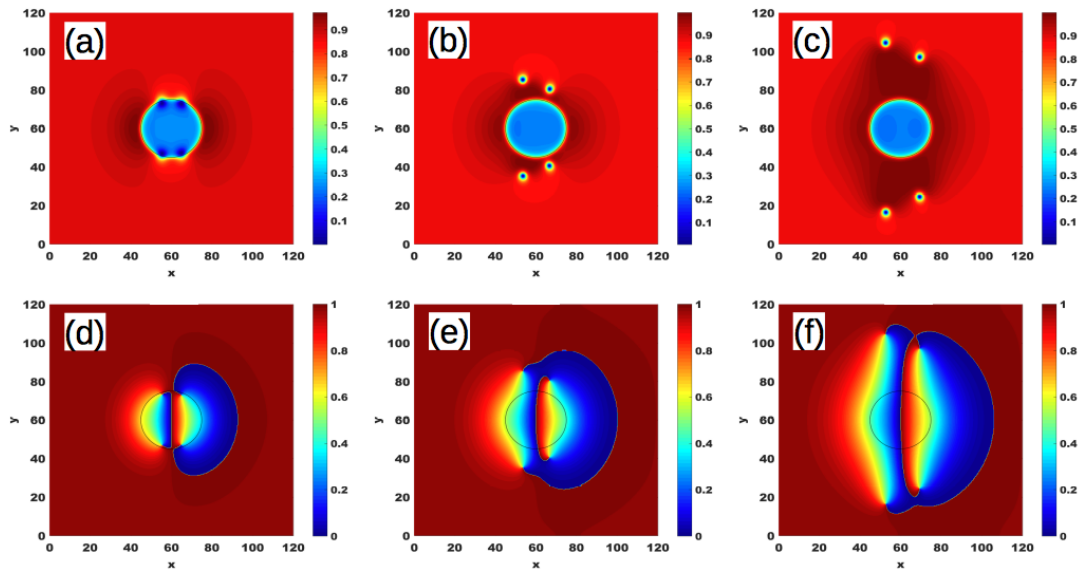


Figure 6.5: Superconducting density (upper row) and phase (lower row) for applied current  $j_a = 0.35 j_0$ . Each column correspond to a distinct state obtained from the iterative procedure. For the superconducting density: dark red (blue) corresponds to  $|\psi|^2 = 1$  ( $|\psi|^2 = 0$ ), while for the phase: dark red (blue) relates to  $\theta = 2\pi$  ( $\theta = 0$ ).

Finally, at the applied current of value  $j_a = 0.35 j_0$ , shown in Fig. 6.5, we observe, in state (a, d) that two VAV pairs nucleated inside the suppression region are close to the edge in a similar form of the observed for current  $j_a = 0.30 j_0$ . At state (b, e) the VAV pairs have crossed the rim of the suppression region simultaneously, and in the sequence, the state (c, f) shows that the VAV pairs tend to move away of the center.

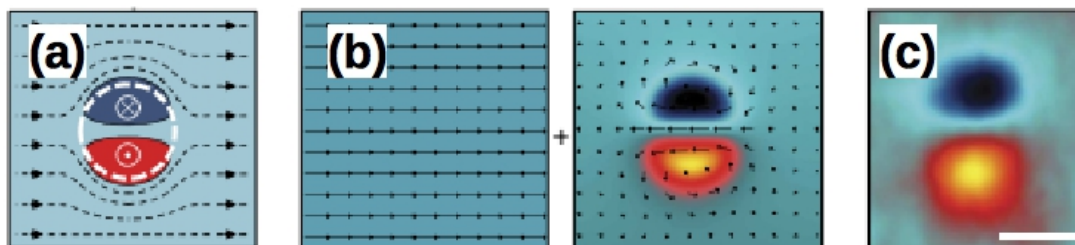


Figure 6.6: Figure adapted from Ref. [58]. The bounded VAV pair in panel (a) results of the superposition of a uniform current with two opposite sense current loops as shown in (b). Panel (c) shows the vortex dipole observed by J. Y. Ge *et al.* The red (blue) region corresponds to a region of positive (negative) magnetic field.

Our results are in agreement with the experimental observation, reported by J. Y. Ge *et al.* [58], of bound vortex dipoles induced by Meissner current, at pinning centers that were randomly created during the sample preparation. In their work it is verified, experimentally and in simulations, the formation of a bound vortex-antivortex pair inside a pinning center due to Meissner currents flowing in a Pb film that is submitted to a perpendicular uniform magnetic field. In our case there is no applied field but there is a controllable uniform current that produces an analogous effect to the Meissner current in their work. The current flowing around the pinning center, which is a region of suppressed superconductivity, generates two half-loops of opposite current sense, producing the VAV pair, as illustrated in Fig. 6.6 adapted from the discussed article. In our results for the circular region of suppression we observed that increasing the applied current implies in the generation of an increasing number of VAV pairs. The authors of the discussed work also found that in some pinning centers there is the generation of more than one VAV pair forming vortex clusters that are seen as elongated regions where the measured perpendicular magnetic field is not null.

### 6.3 Annulus and the superconducting film

We study the nucleation of VAV pairs induced by an applied current, by considering the effect of a magnetic annulus positioned at three different heights above the superconducting film, namely,  $d/\xi = 0.3, 0.6, 0.9$ . For the sake of easy understanding we briefly review the characteristics of the magnetic annulus, reported in section 5.3: the external and internal radii are  $R = 500 \text{ nm}$  and  $r = 25 \text{ nm}$ , respectively, the thickness is  $t_m = 50 \text{ nm}$ ; the parameters used in the numerical simulations are  $N \approx 489000$  magnetic cubic cells of individual volume  $V_{cell} = 80 \text{ nm}^3$  and uniform magnetization  $M_s = 8.6 \cdot 10^5 \text{ A/m}$  that are typical parameters to describe permalloy nanostructures. By considering the informed values we obtain for the magnetic moment of the annulus,  $\mu = 6.88 \times 10^{-20} \text{ Am}^2$ .

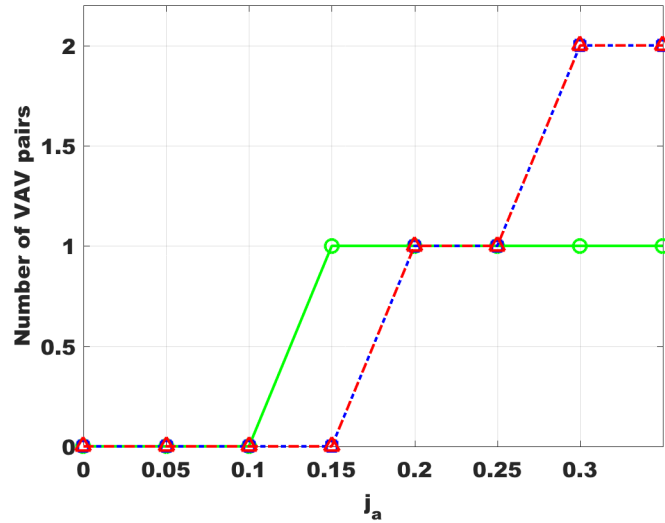


Figure 6.7: Number of VAV pairs generated by a magnetic annulus positioned above the film. The distance  $d = 0.3 \xi$ ,  $d = 0.6 \xi$  and  $d = 0.9 \xi$  are shown respectively by the green line with circles, the blue dashed line with squares and the red line with triangles.

Fig. 6.7 shows a graph that contains the information concerning the number of VAV pairs generated for the three informed distances  $d$ . The green line with circles represents the results for the annulus at distance  $d = 0.3 \xi$ , the blue line with squares shows the behavior of our system when the annulus is at  $d = 0.6 \xi$  and finally the results for distance  $d = 0.9 \xi$  are shown by the red line with triangles. From this figure one concludes that increasing  $d$ , the distance between the annulus and the superconducting film, the applied current must also increase in order to generate VAV pairs in the film. Interestingly, we also notice that the highest  $d$  has the maximal onset of VAV pairs. Still considering the Fig. 6.7 we see that for the distance  $d = 0.3 \xi$  and current from  $j_a = 0.05 j_0$  to  $j_a = 0.10 j_0$  there is no formation of VAV pairs. Increasing the applied current from  $j_a = 0.15 j_0$  to  $j_a = 0.35 j_0$  brings the nucleation of only one VAV pair in the region under the magnetic annulus. For both distances  $d = 0.6 \xi$  and  $d = 0.9 \xi$ , the number of the generated VAV pairs remains the same for the considered values of applied current. However, as we show

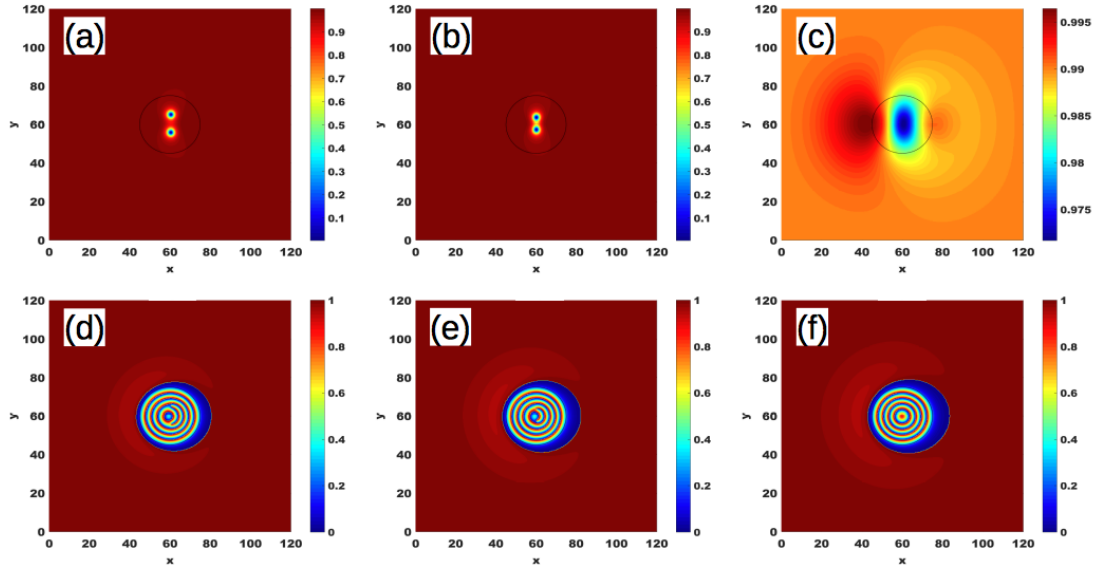


Figure 6.8: Superconducting density (upper row) and phase (lower row) for applied current  $j_a = 0.10 j_0$  and distance  $d = 0.3 \xi$ . The sequence of states shown in columns  $(a, d)$ ,  $(b, e)$  and  $(c, f)$ , respectively, present stages of the relaxation process where a nucleated VAV pair annihilates at the center under the annulus.

in the next figures, the behavior of our system is slightly different between these two cases.

### Annulus at a distance $d = 0.3 \xi$ above the SC film

Fig. 6.8 shows a sequence of three snapshots of the relaxation process where it is presented three states  $(a, d)$ ,  $(b, e)$  and  $(c, f)$  that allow us to observe the formation of a VAV pair, but with the special feature that the vortex and the antivortex attract each other and do not leave the disk to finally annihilate themselves under the center of the annulus. Therefore, this process does not count as a nucleation of a VAV pair in our previous analysis shown in Fig. 6.7, namely, and so, it enters as a zero VAV pair for the corresponding applied current. We only considered as non zero VAV pairs those which leave the circle defined by the magnetic annulus. It can be noticed that in panels  $(a, b)$  the range of the superconducting density varies from  $|\psi|^2 = 0$  (blue) at the center of the vortex (antivortex) to  $|\psi|^2 = 1$  (red) on the

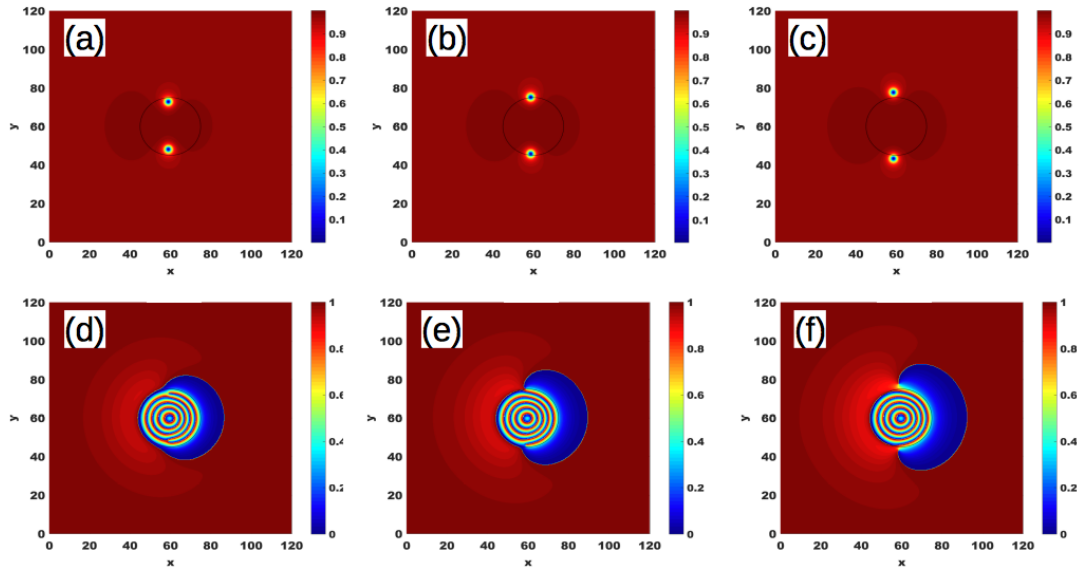


Figure 6.9: Superconducting density (upper row) and phase (lower row) with applied current  $j_a = 0.15 j_0$  and annulus at a distance  $d = 0.3 \xi$  above the SC film.

uniform regions, while in panel (c) the range of the superconducting density varies from  $|\psi|^2 \approx 0.975$  (blue) to  $|\psi|^2 \approx 1$  (red), which means that in the latter case there is only a local suppression of the superconducting density.

For current values ranging from  $j_a = 0.15 j_0$  up to  $j_a = 0.35 j_0$ , there is the formation of only one VAV pair under the annulus positioned at a distance of  $d = 0.3 \xi$  above the superconducting film. In Fig. 6.9 it is shown three intermediate states for applied current  $j_a = 0.15 j_0$ .

In this figure, one can observe that the number of concentric circles in the phase graph, in the region under the annulus, increases from 4 in panel (d) to 5 in panel (f).

### Annulus at a distance $d = 0.6$ above the SC film

Fig. 6.10 shows some intermediate states which are screen shots of the relaxation process for a magnetic annulus positioned at  $d = 0.6 \xi$  above the film and with an applied current  $j_a = 0.15 j_0$ . The superconducting density and phase are shown in

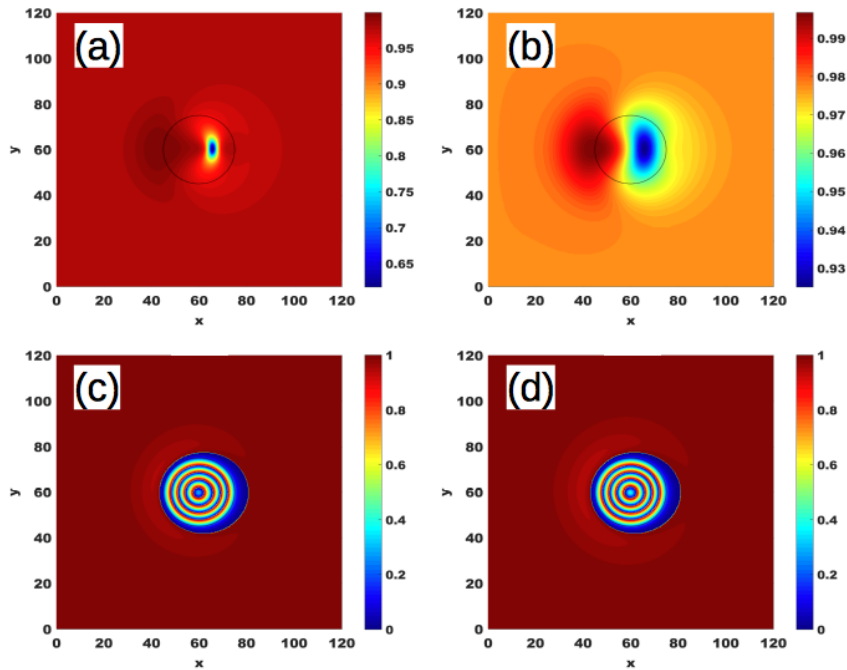


Figure 6.10: Superconducting density (upper row) and phase (lower row) with applied current  $j_a = 0.15 j_0$  and annulus at a distance  $d = 0.6 \xi$  above the SC film.

panels (a) and (c), respectively, and correspond to states preceding the annihilation of a VAV pair. In the second column, we have a state, whose density and phase are shown, respectively, in panels (b) and (d), subsequent to the annihilation of a VAV pair.

Fig. 6.11 displays in columns the superconductivity density and the corresponding phase in a sequence of intermediate states where the generated VAV pair leaves the region under the magnetic annulus. Here, similarly to the previous result, it is also possible to observe that the number of concentric circles of phase discontinuity increases from 4, when the VAV pair is below the annulus, to 5, when the pair leaves the region under the annulus.

Fig. 6.12 corresponds to the applied current  $j_a = 0.30 j_0$  for the same distance  $d = 0.6 \xi$  between the annulus and the film. On this figure we observe a sequence of states where it is possible to verify the formation of two VAV pairs under the annulus.

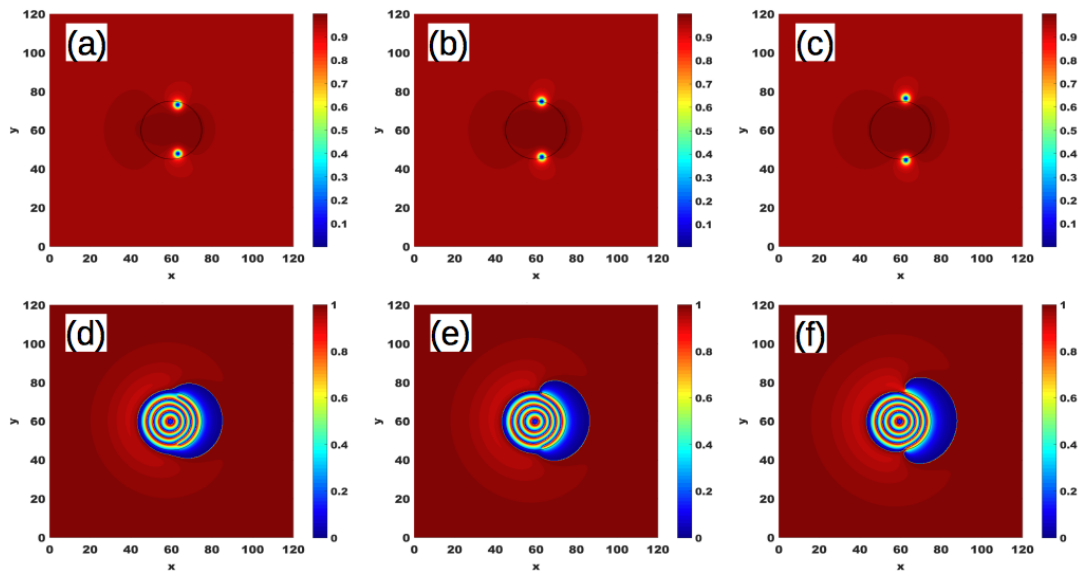


Figure 6.11: Superconducting density (upper row) and phase (lower row) with applied current  $j_a = 0.20 j_0$  and annulus at a distance  $d = 0.6 \xi$  above the SC film.

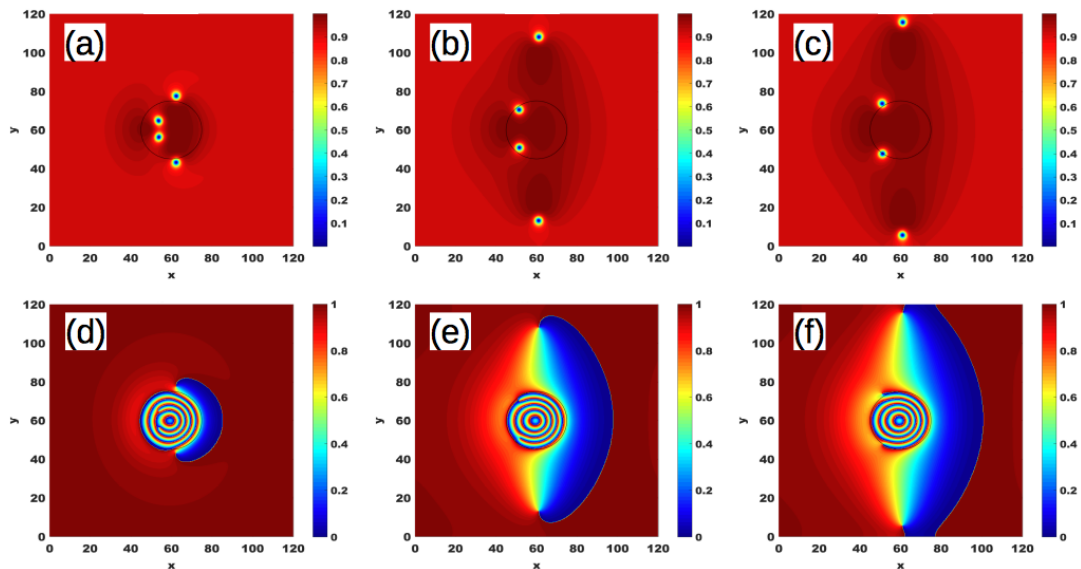


Figure 6.12: Superconducting density (upper row) and phase (lower row) with applied current  $j_a = 0.30 j_0$  and annulus at a distance  $d = 0.6 \xi$  above the SC film.

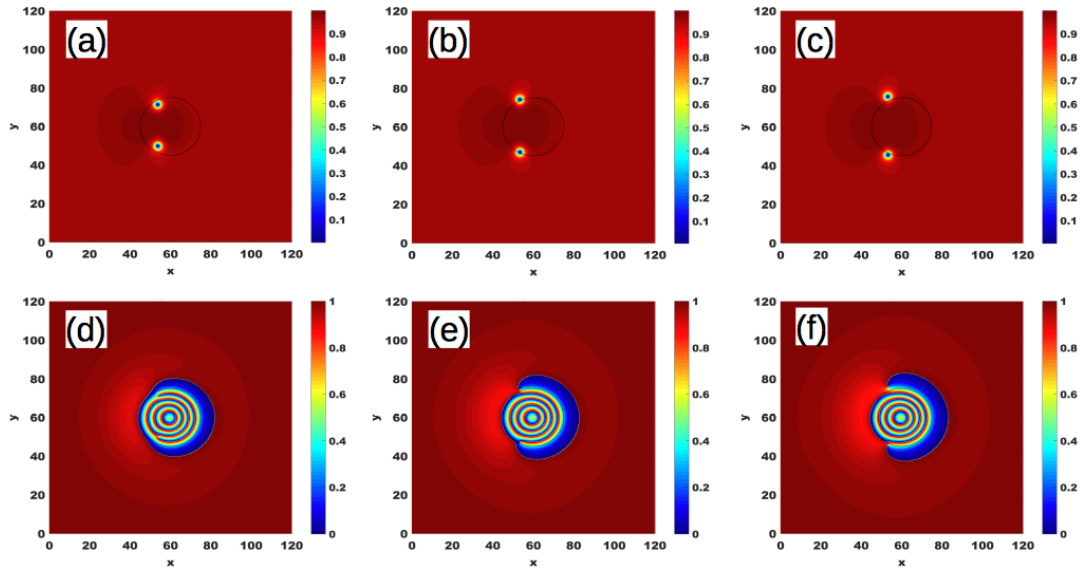


Figure 6.13: Superconducting density (upper row) and phase (lower row) with applied current  $j_a = 0.20 j_0$  and annulus at a distance  $d = 0.9 \xi$  above the SC film.

Even though the VAV pairs are formed closely to each other, we observe that one VAV pair leaves firstly and next the second pair also leaves the disk. For this case, we can count three closed circles of phase discontinuity in the central region and one opened line that form a spiral, for the state shown in panel (d). In panel (f), we can verify that the number of closed circles under the annulus is four. Thus, we can conclude that after the generation and the departure of one VAV pair from the annulus, there is the increasing in the number of discontinuity phase circles that can be seen in the phase diagrams. Increasing the current to  $j_a = 0.35 j_0$  we observe a similar behavior of the system.

### Annulus at a distance $d = 0.9$ above the SC film

The next sequence of figures are related to the third value for the distance between the annulus and the film, that is,  $d = 0.9 \xi$ . In this case, we observe that the nucleation of VAV pairs is only favorable for values of applied current higher than  $j_a = 0.15 j_0$ . Fig. 6.13 shows a sequence of states where there is a VAV pair formed

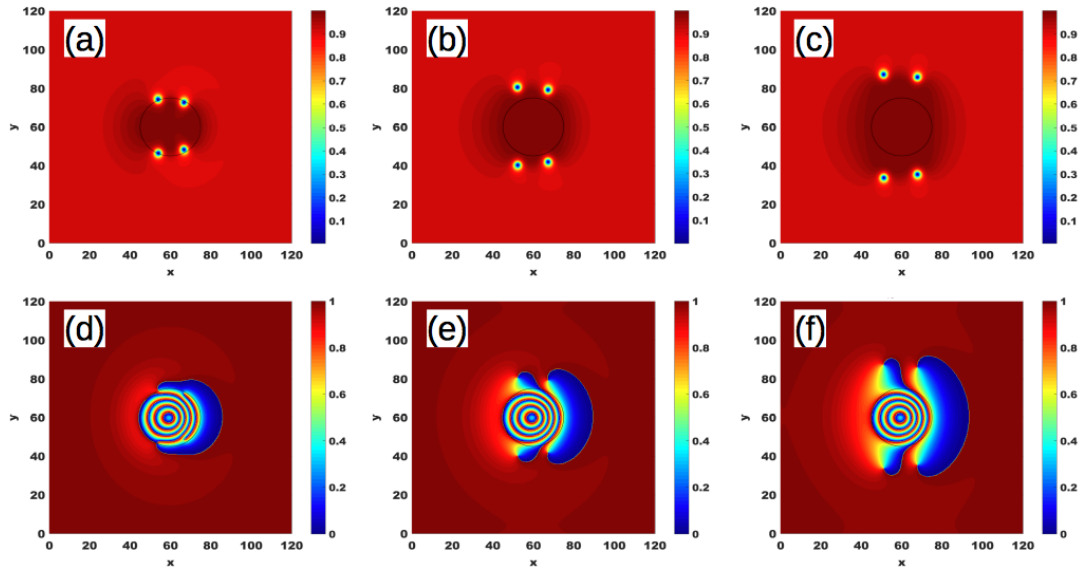


Figure 6.14: Superconducting density (upper row) and phase (lower row) with applied current  $j_a = 0.30 j_0$  and annulus at a distance  $d = 0.9 \xi$  above the SC film.

at the center, under the annulus. Thus, the force generated by the applied current on the VAV pair is stronger than the attraction between the vortex and the antivortex. Thus, it is energetically more favorable that the VAV move away from the center, separating themselves as the relaxation process continues. The same behavior is observed if we increase the intensity of the applied currents to values larger than  $j_a = 0.30 j_0$ .

For the current ranging from  $j_a = 0.30 j_0$  to  $j_a = 0.35 j_0$  the simultaneous formation of two VAV pairs is observed, as shown in Fig. 6.14. We notice the distinction of these illustrated sequence of states from the states shown in Fig. 6.12 with distance  $d = 0.6 \xi$ , where the formation of two VAV pairs is such that each pair moves individually to the edges of unit cell. Here, we clearly see that the strong applied current forces both pairs to simultaneously leave the disk.

Finally, Fig. 6.15 shows the strength of the perpendicular component of the stray field of the magnetic annulus at the three considered distances  $d = 0.3 \xi$ , panels (a),

$d = 0.6 \xi$ , panels (b) and  $d = 0.9 \xi$ , panels (c). It is observed that increasing the height of the annulus with respect to the film, the magnetic field intensity decreases considerably but there is no significant change in its spatial distribution. The stray field presents its highest intensity on localized regions around the external radius of the annulus where it reaches both positive and negative values at some spots. These spots of more intense magnetic field are a consequence of the magnetic dipoles, that composes the cells of the annulus, positioned on a square grid. We recall that we describe the disks on a square lattice. Therefore, the external side of the disk is approximated by a discrete number of finite size steps due to the square lattice. This effect tends to diminish as we increase the number of grid points on the lattice. However, the increasing of the number of cell points is limited by the computational time consumption. It is seen that the localized regions present a rotational symmetry of 90 degrees, which should be attribute to the cause just explained, namely, of a square grid where the dipoles are positioned.

## 6.4 Permalloy disk and the superconducting film

In this section the nucleation of VAV pairs in a superconducting film is considered under the effect of the stray field of a permalloy disk positioned at three different chosen distances, namely,  $d/\xi = 0.3, 0.6, 0.9$ . The permalloy disk has the same

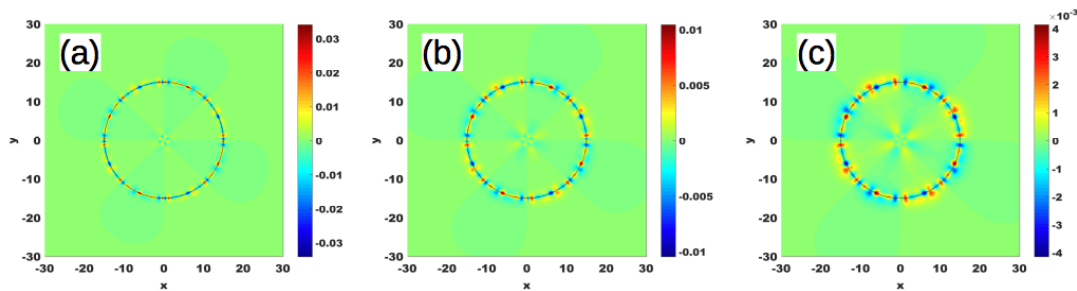


Figure 6.15: Perpendicular component  $h_z$  of the disk's stray field without any applied current  $j_a = 0$ . The annulus are positioned at distances  $d/\xi = 0.3, 0.6, 0.9$

dimensions and properties of our previous sections, which are the same of the defined magnetic annulus, but with the difference that the magnetic state is obtained by energy minimization by means of micromagnetic simulations. The state of minimal energy corresponds to a magnetic vortex state where the magnetic moments are in a head-to-tail arrangement as discussed in the definition of the annulus. This holds for out of the core magnetic moments, but inside the core the permalloy also has the out-of-plane magnetic moments at the center, what characterizes the sharp peak in the perpendicular component of the magnetization.

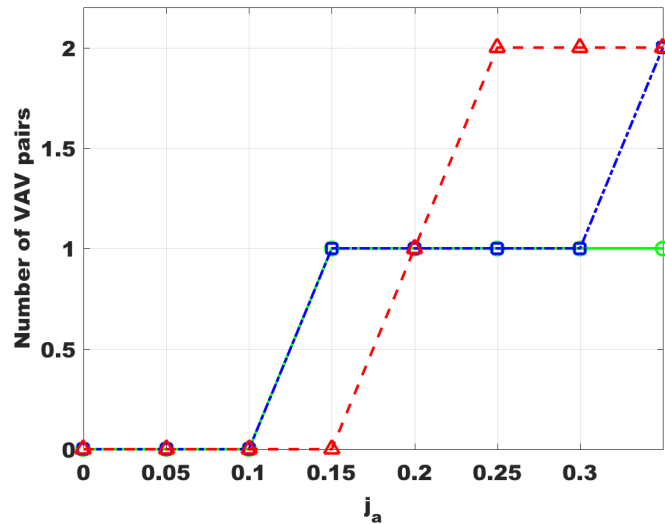


Figure 6.16: Number of VAV pairs generated by a permalloy disk positioned above the film. The distance  $d = 0.3 \xi$ ,  $d = 0.6 \xi$  and  $d = 0.9 \xi$  are shown respectively by the green line with circles, the blue dashed line with squares and the red line with triangles.

Fig. 6.16 shows the number of VAV pairs generated in the film as a function of the applied current. It is interesting to compare the present results with those obtained for the annulus. Firstly, for the distance  $d = 0.3 \xi$  the two systems present the same behavior, namely, there is no VAV pair for current smaller than  $j_a = 0.10 j_0$  and for values greater than  $j_a = 0.15 j_0$  to the end of our range, there is the formation of only one VAV pair. However, noticeable differences arise for the two other cases,

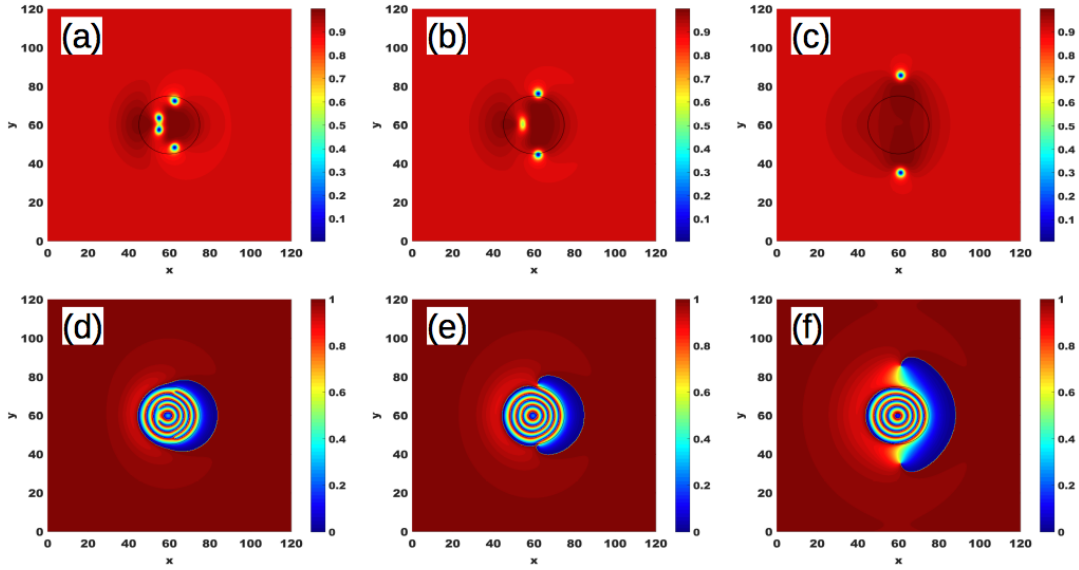


Figure 6.17: Superconducting density (upper row) and phase (lower row) with applied current  $j_a = 0.30 j_0$  and disk at a distance  $d = 0.6 \xi$  above the SC film.

namely,  $d = 0.6 \xi$  and  $d = 0.9 \xi$ .

For  $d = 0.6 \xi$ , and for an applied current in the range  $j_a < 0.1 j_0$  there is no formation of VAV pairs. For  $0.15 < j_a/j_0 < 0.30$  there is the nucleation of only one VAV pair, and for  $j_a > 0.35 j_0$ , two VAV pairs are formed under the permalloy disk. For the last case analyzed here, the system with  $d = 0.9 \xi$  also presents the three regimes but with different ranges of applied current delimiting the behavior changing. There is no nucleation of VAV pairs for currents smaller than  $j_a = 0.15 j_0$ . For  $j_a = 0.20 j_0$  there is only one VAV pair leaving the region under the effect of the permalloy disk. And for  $j_a > 0.25 j_0$  there is the formation of two VAV pairs.

In summary the obtained results for the permalloy disk are similar to the results for the magnetic annulus. Thus, we present here only a few detailed snapshots of the relaxation process for the permalloy disk. For  $d = 0.3 \xi$  there is the nucleation of only one VAV pair and all the results are analogous to the magnetic annulus system. In the intermediary distance  $d = 0.6 \xi$  we observe an interesting effect for the applied

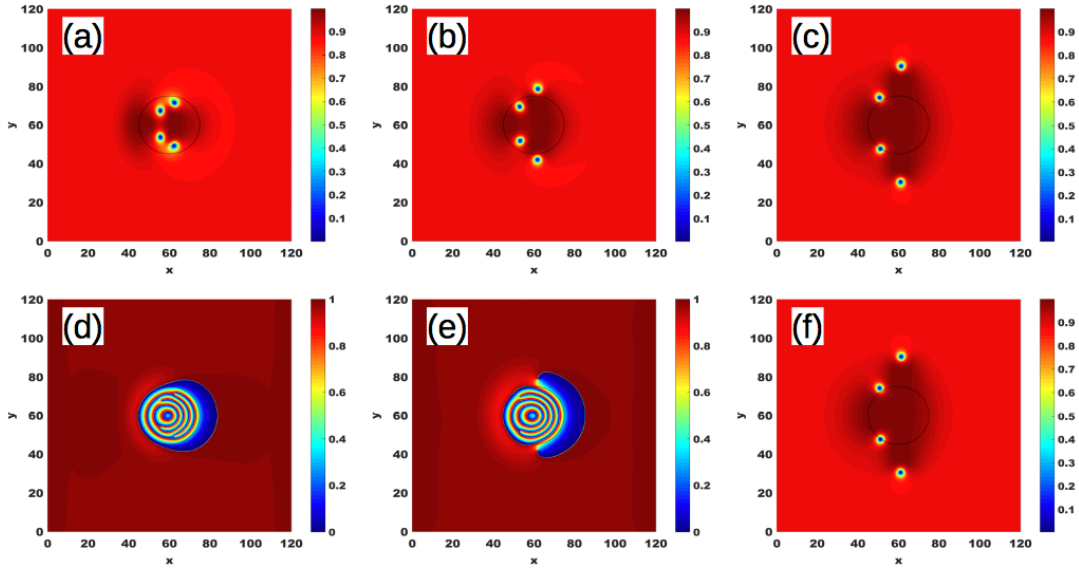


Figure 6.18: Superconducting density (upper row) and phase (lower row) with applied current  $j_a = 0.35 j_0$  and disk at a distance  $d = 0.6 \xi$  above the SC film.

current  $j_a = 0.30 j_0$ . Fig. 6.17 reports the formation of two VAV pairs. One of them is formed close to the edge, and the other below the central region, of the permalloy disk. We observe in panels (a, d) that the vortex and the antivortex of the central pair attracts each other until the annihilation shown in panels (b, e). Differently, the more external VAV pair is dragged apart and leaves the region under the disk as can be seen in panels (c, f).

Increasing the applied current, the resulting behavior of the superconducting film is completely analogous to the magnetic annulus case. For this considered distance, at an applied current  $j_a = 0.35 j_0$  there is the nucleation of two VAV pairs but they leave the center of the superconducting region separately, as can be seen in Fig. 6.18.

For the higher height of the permalloy disk  $d = 0.9 \xi$ , we verify that for currents more intense than  $j_a = 0.25 j_0$  there is always the nucleation of two VAV pairs and they leave the region under influence of the permalloy disk simultaneously, as shown in Fig. 6.19.

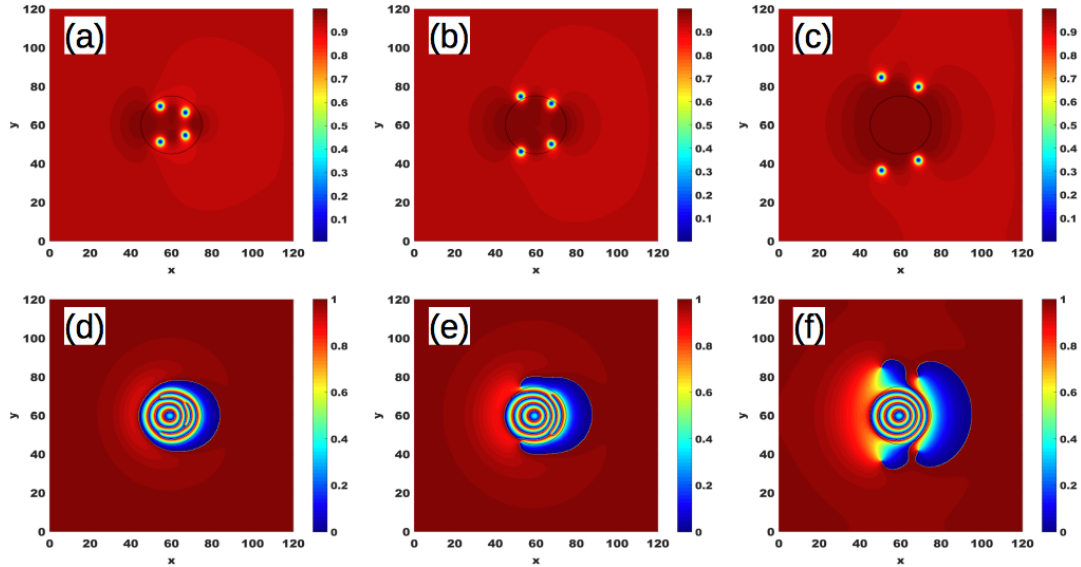


Figure 6.19: Superconducting density (upper row) and phase (lower row) with applied current  $j_a = 0.25 j_0$  and disk at a distance  $d = 0.9 \xi$  above the SC film.

## 6.5 Conclusion

In this chapter we have analyzed the nucleation process of VAV pairs in systems composed of a superconducting thin film interacting with an array of disks. Firstly, we studied non magnetic encrusted disks such that the order parameter is suppressed there. In this presented system the order parameter inside the region of the encrusted disks is fixed to be a fraction of its value outside. Next, we have studied two systems of magnetic dots, namely, the annulus and the permalloy disk, the former being the latter removed of its core. We find that the nucleation of VAV pairs is stimulated by an applied current density.

The VAV pairs, nucleated at the center of the suppression region, move towards the edges of the disk (north and south poles) perpendicularly to the applied current. At these poles there is a local increase of the current density. We found two types of states depending on the value of the applied current. The first type are equilibrium

states, such that the VAV pair remain pinned at the poles, and the second type are non-equilibrium states where the VAV pair leaves the disks and moves away from it. This is an intermittent state with the periodic onset of VAV pairs. Hence, this state can be regarded as stationary but not as an equilibrium state because the time evolution continues through a sequence of states showing that the VAV pairs leave the suppression region.

For the magnetic systems, namely, the annulus and the permalloy disks, there are two contributions to the current density, namely, the external applied current  $\vec{J}_a$  and the superconducting current  $\vec{J}$ , that add up in each point of space,  $\vec{J}_T = \vec{J} + \vec{J}_a$ . The nucleation of VAV pairs occurs where this total current density, exceeds the depairing current [23]. This is because in such a situation the order parameter drops to zero thus creating the optimal situation of the onset of vortices.

Our simulation takes as initial state the film in the normal state,  $\psi \approx 0$ . Then, these systems evolve to their final equilibrium states where the superconducting density is inhomogeneous. During the relaxation process, the superconducting current  $\vec{J}$  is predominantly made of Meissner currents and is localized on the regions where the annulus/disk stray field is more intense. In the annulus system, as we explained, the stray field presents regions of positive and negative values around the outer radius as result of the square grid used to model the disk. Differently, for the disk system in the magnetic vortex state, the pronounced peak of the magnetic field  $h_z$  is at the center.

# Chapter 7

## Summary

The main results obtained in this thesis are summarized here and also some possible extensions for future research are presented.

The first part of this thesis is based on A. A. Abrikosov's treatment of the Ginzburg-Landau theory which has led him to the classification of superconductors in type I and II and to the discovery of vortices in bulk for type II superconductors. This is the so-called first order equations formalism that we extended here to the case of a superconductor with an external boundary to a non-superconducting insulating region. It applies to a infinitely long superconductor such that any cross section perpendicular to the applied field contains the same physical properties. For instance we find that in case of no applied field the bulk superconductor (no boundary) cannot sustain vortices, the boundary allows their presence, although, their lowest Gibbs free energy is at the boundary when they leave the superconductor. In this case we reduce the problem of obtaining vortex solution to the discovery of analytical functions in the complex plane such that their modulus is constant in the boundary. Following this formalism, we studied infinitely long superconducting cylinder with radius in the mesoscopic range.

In chapter 2, we address the situation faced by a superconductor in case the

external magnetic field is switched off and vortices although topologically stable form a collective state which is unstable and can only remain inside the superconductor under the presence of external pinning. We believe that there will be physical consequences depending if the vortex state has energy below or above the normal state. In case a vortex state, although unstable, can have its Gibbs energy below that of the normal state we denominate it an excited vortex state - EVS. We reported that a cylinder must have a minimal radius to hold the EVS. We also obtained analytical expressions to the order parameter, the local magnetic field and the magnetization, which we verified to be intrinsically paramagnetic, in long wires made of niobium. The results related to the EVS were published in Ref. [66]. We found that the theory of conformal mapping could be used to explore the application of the first order equations in two-dimensional superconductors with different cross section geometries. Obviously the EVS can only exist below the critical temperature.

In chapter 3 we consider a superconductor with an external boundary still within the first order equations formalism. For the bulk superconductors (no boundaries) A.A. Abrikosov shows that superconductivity can only exist below the upper critical field  $H_{c2}$ , which in a diagram applied field versus temperature corresponds to a straight line. In case of the choice of Ginzburg-Landau parameters specially fitted to describe a type I superconductor, as discussed in this chapter, this line is no longer straight. We show here that the presence of a boundary allows for vortex states above the upper critical field provided that its coupling  $\kappa$  is below a certain threshold. Remarkably this implies in a revision of the critical coupling that separates type *I* to type *II* superconductor. We carry this task here partially by determining the magnetic field range and radius that a mesoscopic cylindrical superconductors, can sustain a single vortex in its center, namely, with a Gibbs free energy density lower than the normal state. Essentially we have demonstrated that the finite boundary yields a negative surface energy contribution able to sustain vortex solutions even for a type *I* superconducting cylinder immersed in a magnetic field above the upper critical field.

The second part of this thesis concerns superconductor-ferromagnetic heterostructures where the stray field from the magnetic part is not homogeneous and presents positive and negative regions that locally affect the superconductor in different forms. We used the non-linear Ginzburg-Landau equation to numerically treat the interaction of the superconducting thin films with an array of magnetic dots.

We apply a numerical procedure, based on the software MuMax3, to determine the magnetic state of permalloy and find the magnetic vortex. The effects of the stray field produced by this magnetic vortex on the superconducting film is then considered. Our numerical algorithm allows for the general study of the interaction of a superconducting film with magnetic dots of different shapes in any magnetic state. The total vector potential of such a magnetic state as the superposition of thousands of magnetic dipoles in arbitrary orientation. Hence we have a powerful tool to investigate how the superconductivity is locally affected by magnetic textures which could be compared with recent experiments as is the case of magnetic vortex in permalloy disks.

In chapter 5 we observe a novel effect on the superconducting phase due to the presence of the permalloy disk's stray field. This is the appearance of rings of phase discontinuity in the phase. In order to investigate the mentioned effect on the phase, we constructed simplified models characterized by the magnetic moments in the same arrangement as that of a permalloy disk excluded from its out-of-plane core. We considered two systems: a permalloy annulus and polygons of magnetic dipoles. The results obtained for the permalloy annulus shows that the in-plane magnetic moments are responsible for the rings of phase discontinuity in the superconducting film as they also arise both for the annulus and polygons.

From the results presented in the analysis of the superconducting film with the polygon of dipoles, namely, the square, the octagon and the hexadecagon, we verified that for the square of dipoles, the distance among them is sufficient to permit that the perpendicular component of the stray field be strong enough to create coexisting vortices and antivortices below the dipoles. For the octagon and the hexadecagon, we observed a local suppression of the superconducting density that is caused by the Meissner currents circulating below the poles of the magnetic dipoles. We argue that the in-plane magnetic moments inside permalloy disk produce the same effects as the polygons of dipoles, which is the nucleation of VAV pairs that annihilates among them, leaving a suppression of the order parameter. Although, this process of VAV pairs annihilation with a resulting suppression is not observed in our simulations for the permalloy disk we interpret the rings of phase discontinuity as a track record. The nucleation and annihilation of VAV pairs can be compared to the “Gedankenexperiment” discussed in the chapter 1 and the nucleation of VAV pairs in a corbino disk that was already studied [73]. As a form to verify the relation of the discontinuities rings in the phase with the nucleation of VAV pairs, we considered the possibility to stimulate the VAV pairs nucleation by an applied current density.

In chapter 6 we study the nucleation of vortex-antivortex (VAV) pairs through the application of a current density. To gain understanding about the onset of VAV pairs we also studied the system consisting of a superconducting film with encrusted non magnetic disks. These encrusted disks are regions where the superconducting density is suppressed to 25 % of its maximal value. We obtained the nucleation of VAV pairs that move, perpendicularly to the applied current, towards the edges of the circular region of suppression. We found equilibrium and also stationary intermittent states. In the former the VAV pair remain pinned at the extremities of the disk. For the latter the time process evolves through a sequence of periodic states where the VAV pairs leave the suppression region. We found similarities of our results with a recent

experimental realization of bound vortex dipoles induced by Meissner currents [58].

For the system consisting of a superconducting film and the magnetic dots, namely the annulus and permalloy disks, we analyzed the nucleation of VAV pairs in terms of the external applied current and the distance of the annulus/disk to the superconducting film. As expected, we observed the nucleation of the VAV pairs below the annulus and the disk. From snapshots of the relaxation process, we confirmed the connection between the rings of phase discontinuity with VAV pairs nucleating and subsequently annihilating themselves below the annulus/disk. When the current is intense enough it produces a Lorentz force that can separate a VAV pair, as it was described in section 1.4.1.

From the exposed along this section we consider that there are different possibilities to be explored as a sequence of the research started in this thesis. The most direct realizations would be the study of equilibrium configuration of vortex states (one single vortex with angular momentum  $L > 1$  or multiple vortices) in a type  $I$  superconductor through the first order equations formalism; and the analysis of the VAV pair nucleation in a superconducting film in the vicinity of a lattice of permalloy disks by means of the TDGL equations.

# Bibliography

- [1] ABRIKOSOV, A. A. *Sov. Phys. JETP* 5 (1957), 1174–1178. 2, 27, 31, 35, 55, 56, 64, 71
- [2] ADAMI, O.-A., CERBU, D., CABOSART, D., MOTTA, M., CUPPENS, J., ORTIZ, W. A., MOSHCHALOV, V. V., HACKENS, B., DELAMARE, R., VAN DE VONDEL, J., AND SILHANEK, A. V. Current crowding effects in superconducting corner-shaped Al microstrips. *Applied Physics Letters* 102, 052603 (feb 2013), 1–4. 161
- [3] ANISHCHANKA, A. *Proximity Effects in Superconductor-Ferromagnet Structures*. PhD thesis, 2008. 163
- [4] AQUINO, M. *Nonlinear magnetization dynamics in thin-films and nanoparticles*. PhD thesis, 2004. 115
- [5] BARDEEN, J., COOPER, L. N., AND SCHRIEFFER, J. R. Theory of superconductivity. *Phys. Rev.* 108, 5 (1957), 1175–1204. 2, 19
- [6] BEDNORZ, J. G., AND MÜLLER, K. A. Possible high  $t_c$  superconductivity in the ba-la-cu-o system. *Z. Phys.* 64, 2 (1986), 189–193. 2
- [7] BENDING, S. J. Local magnetic probes of superconductors. *Adv. Phys.* 48, 4 (1999), 449–535. 23

- [8] BERDIYOROV, G. R., HERNANDEZ, A. D., AND PEETERS, F. M. Confinement effects on intermediate-state flux patterns in mesoscopic type-i superconductors. *Phys. Rev. Lett.* *103* (Dec 2009), 267002. 58
- [9] BERDIYOROV, G. R., MILOŠEVIĆ, M. V., AND PEETERS, F. M. Spatially dependent sensitivity of superconducting meanders as single-photon detectors. *Applied Physics Letters* *100*, 262603 (jun 2012), 1–4. 161
- [10] BERKOV, D. V., AND MILTAT, J. Spin-torque driven magnetization dynamics: Micromagnetic modeling. *J. Magn. Magn. Mat.* *320* (2008), 1238–1259. 118
- [11] BERTOTTI, G. *Hysteresis in magnetism*. Academic Press, 1998. 106
- [12] BLOT, J., AND PELLAN, Y. Solving an old discrepancy: The  $g$ - $l$  parameter of al films. *Physics Letters A* *110*, 9 (1985), 465 – 466. 58
- [13] BLOT, J., PELLAN, Y., AND ROSENBLATT, J. Metastable states of superconducting indium films. *Journal of Low Temperature Physics* *30*, 5 (Mar 1978), 669–695. 58
- [14] BOBBA, F., DI GIORGIO, C., SCARFATO, A., LONGOBARDI, M., IAVARONE, M., MOORE, S. A., KARAPETROV, G., NOVOSAD, V., YEFREMENKO, V., AND CUCOLO, A. M. Vortex-antivortex coexistence in Nb-based superconductor/ferromagnet heterostructures. *Physical Review B* *89*, 214502 (jun 2014), 1–7. 113
- [15] BOGOMOLNY, E. B. *Sov. J. Nucl. Phys.* *24* (1976), 449–454. 27, 56, 68
- [16] BOTHNER, D., CLAUSS, C., KOROKNAY, E., KEMMLER, M., GABER, T., JETTER, M., SCHEFFLER, M., MICHLER, P., DRESSEL, M., KOELLE, D., AND KLEINER, R. The phase boundary of superconducting niobium thin films with antidot arrays fabricated with microsphere photolithography. *Supercond. Sci. Tech.* *25*, 6 (2012), 065020. 41

- [17] BOUTSIANIS, E., GUPTA, S., BOOMSMA, K., AND POULIKAKOS, D. Boundary conditions by schwarz-christoffel mapping in anatomically accurate hemodynamics. *Ann. Biomed. Eng.* 36, 12 (2008), 2068–2084. 27
- [18] BRANDT, E. H. The flux-line lattice in superconductors. *Rep. Prog. Phys.* 58, 11 (1995), 1465. 26
- [19] BRANDT, E. H. Precision ginzburg-landau solution of ideal vortex lattices for any induction and symmetry. *Phys. Rev. Lett.* 78 (Mar 1997), 2208–2211. 26
- [20] BUTENKO, A. B., LEONOV, A. A., BOGDANOV, A. N., AND RÖSSLER, U. K. Theory of vortex states in magnetic nanodisks with induced Dzyaloshinskii-Moriya interactions. *Physical Review B* 80, 134410 (oct 2009), 1–8. 103
- [21] CARBALLEIRA, C., MOSHCHALOV, V. V., CHIBOTARU, L. F., AND CEULEMANS, A. Multiquanta Vortex Entry and Vortex-Antivortex Pattern Expansion in a Superconducting Microsquare with a Magnetic Dot. *Physical Review Letters* 95, 23 (dec 2005), 1–4. 124
- [22] CARNEIRO, G. Tunable pinning of a superconducting vortex by a magnetic vortex. *Physical Review B* 75, 094504 (mar 2007), 1–9. 123
- [23] CARNEIRO, G. Moving vortex matter with coexisting vortices and anti-vortices. *Journal of Physics: Conference Series* 150, 052031 (mar 2009), 1–4. 136, 161, 182
- [24] CHANG, R., LI, S., LUBARDA, M. V., LIVSHITZ, B., AND LOMAKIN, V. Fastmag: Fast micromagnetic simulator for complex magnetic structures. *Journal of Applied Physics* 109, 7 (2011), 07D358. 112
- [25] CHEN, J. L., AND TSENG, T. Y. Interaction between a two-dimensional pancake vortex and a circular nonsuperconducting defect. *Phys. Rev. B* 54 (Jul 1996), 502–506. 59

- [26] CHEN, Q. H., CARBALLEIRA, C., AND MOSHCHALOV, V. V. Vortex matter in a hybrid superconducting/ferromagnetic nanostructure. *Physical Review B* 79, 104520 (mar 2009), 1–12. 123
- [27] CHEN, S., ZHANG, S., ZHU, Q., LIU, X., JIN, C., WANG, J., AND LIU, Q. Effect of Dzyaloshinskii-Moriya interaction on the magnetic vortex oscillator driven by spin-polarized current. *Journal of Applied Physics* 117, 17B720 (may 2015), 1–4. 103
- [28] CLEM, J. R., AND BERGGREN, K. K. Geometry-dependent critical currents in superconducting nanocircuits. *Physical Review B* 84, 174510 (nov 2011), 1–27. 161
- [29] CLEM, J. R., MAWATARI, Y., BERDIYOROV, G. R., AND PEETERS, F. M. Predicted field-dependent increase of critical currents in asymmetric superconducting nanocircuits. *Physical Review B* 85, 144511 (apr 2012), 1–16. 161
- [30] COOPER, L. N. Superconductivity in the neighborhood of metallic contacts. *Phys. Rev. Lett.* 6 (Jun 1961), 689–690. 163
- [31] DAS, P., TOMY, C. V., BANERJEE, S. S., TAKEYA, H., RAMAKRISHNAN, S., AND GROVER, A. K. Surface superconductivity, positive field cooled magnetization, and peak-effect phenomenon observed in a spherical single crystal of niobium. *Phys. Rev. B* 78 (Dec 2008), 214504. 41
- [32] DE GENNES, P. G. A. *Superconductivity of Metals and Alloys*. Advanced Book Classics. Addison-Wesley Publishing Company, 1966. 59
- [33] DE OLIVEIRA, I. G. The threshold temperature where type-i and type-ii interchange in mesoscopic superconductors at the bogomolnyi limit. *Physics Letters A* 381, 14 (2017), 1248 – 1254. 59

- [34] DE SOUZA, R. D. M. Estudo da densidade de corrente crítica para reversão da magnetização de nanoelementos ferromagnéticos. Master's thesis, Universidade Federal do Rio Grande do Norte, 2015. 104, 110
- [35] DE SOUZA SILVA, C. C., SILHANEK, A. V., VAN DE VONDEL, J., GILLIJNS, W., METLUSHKO, V., ILIC, B., AND MOSHCHALOV, V. V. Dipole-Induced Vortex Ratchets in Superconducting Films with Arrays of Micromagnets. *Physical Review Letters* 98, 11 (mar 2007), 1–4. 123
- [36] DEAVER, B. S., AND FAIRBANK, W. M. Experimental evidence for quantized flux in superconducting cylinders. *Phys. Rev. Lett.* 7, 2 (1961), 43–46. 17
- [37] DEO, P. S., SCHWEIGERT, V. A., PEETERS, F. M., AND GEIM, A. K. Magnetization of mesoscopic superconducting disks. *Phys. Rev. Lett.* 79 (Dec 1997), 4653–4656. 62
- [38] DIAS, F. T., PUREUR, P., RODRIGUES, P., AND OBRADORS, X. Paramagnetic effect at low and high magnetic fields in melt-textured  $\text{Yb}_2\text{Cu}_3\text{O}_{7-\delta}$ . *Phys. Rev. B* 70 (Dec 2004), 224519. 25
- [39] DOLL, R., AND NÄBAUER, M. Experimental proof of magnetic flux quantization in a superconducting ring. *Phys. Rev. Lett.* 7, 2 (1961), 51–52. 17
- [40] DONAHUE, M. J., AND PORTER, D. G. Oomf user's guide, version 1.0. *Interagency Report NISTIR 6376, National Institute of Standards and Technology* (1999). 105, 112
- [41] DORIA, M. M., DE C. ROMAGUERA, A. R., MILOŠEVIĆ, M. V., AND PEETERS, F. M. Threefold onset of vortex loops in superconductors with a magnetic core. *EPL (Europhysics Letters)* 79, 4 (2007), 47006. 124

- [42] DORIA, M. M., GUBERNATIS, J. E., AND RAINER, D. Virial theorem for Ginzburg-Landau theories with potential applications to numerical studies of type-II superconductors. *Physical Review B* 39, 13 (1989), 9573–9575. 97
- [43] DREWS, A., SELKE, G., ALBERT, C., GERHARDT, T., MEYER, J. M., DARSOW-FROMM, C., MENZEL, M., KRÜGER, B., AND MÖLLER, D. P. F. Micromagnum. 112
- [44] DRISCOLL, T. A., AND TREFETHEN, L. N. *Schwarz-Christoffel Mapping*. Cambridge University Press, 2002. Cambridge Books Online. 27
- [45] ENGBARTH, M. A., BENDING, S. J., AND MILOŠEVIĆ, M. V. Geometry-driven vortex states in type-i superconducting pb nanowires. *Phys. Rev. B* 83 (Jun 2011), 224504. 58
- [46] ESSMANN, U. Intermediate state of superconducting niobium. *Phys. Lett. A* 41, 5 (1972), 477 – 478. 41
- [47] ESSMANN, U., AND TRÄUBLE, H. The direct observation of individual flux lines in type {II} superconductors. *Phys. Lett. A* 24, 10 (1967), 526 – 527. 23
- [48] ESSMANN, U., AND TRÄUBLE, H. The flux-line arrangement in the “intermediate state” of type ii superconductors. *Phys. Lett. A* 27, 3 (1968), 156 – 157. 23
- [49] FEDER, J. Comments of the supercooling field for superconductors with  $k$  values near 0.4. *Solid State Communications* 5, 4 (1967), 299 – 301. 5, 57, 58
- [50] FERNÁNDEZ-PACHECO, A., STREUBEL, R., FRUCHART, O., HERTEL, R., FISCHER, P., AND COWBURN, R. P. Three-dimensional nanomagnetism. *Nature Communications* 8, 15756 (jun 2017), 1–14. 103
- [51] FERT, A., CROS, V., AND SAMPAIO, J. Skyrmions on the track. *Nature Nanotechnology* 8 (mar 2013), 152–156. 105

- [52] FINE, B., AND ROSENBERGER, G. *The Fundamental Theorem of Algebra*. Springer, 1997. 39
- [53] FINNEMORE, D. K., STROMBERG, T. F., AND SWENSON, C. A. Superconducting properties of high-purity niobium. *Phys. Rev.* *149* (Sep 1966), 231–243. 41
- [54] FISCHBACHER, T., FRANCHIN, M., BORDIGNON, G., AND FANGOHR, H. A systematic approach to multiphysics extensions of finite-element-based micro-magnetic simulations: Nmag. *IEEE Transactions On Magnetics* *43*, 6 (2007), 2896–2898. 112
- [55] FOMINOV, Y. V., AND FEIGEL'MAN, M. V. Superconductive properties of thin dirty superconductor-normal-metal bilayers. *Phys. Rev. B* *63* (Feb 2001), 094518. 159
- [56] GE, J., GUTIERREZ, J., CUPPENS, J., AND MOSHCHALOV, V. V. Observation of single flux quantum vortices in the intermediate state of a type-i superconducting film. *Phys. Rev. B* *88* (Nov 2013), 174503. 58
- [57] GE, J., GUTIERREZ, J., RAES, B., CUPPENS, J., AND MOSHCHALOV, V. V. Flux pattern transitions in the intermediate state of a type-i superconductor driven by an ac field. *New Journal of Physics* *15*, 3 (2013), 033013. 58
- [58] GE, J.-Y., GUTIERREZ, J., GLADILIN, V. N., DEVREESE, J. T., AND MOSHCHALOV, V. V. Bound vortex dipoles generated at pinning centres by Meissner current. *Nature Communications* *6*, 6573 (mar 2015), 1–8. xxvii, 168, 169, 187
- [59] GHINOVKER, M., SHAPIRO, I., AND SHAPIRO, B. Y. Creation of long living vortex-antivortex matter by laser pulse. *Journal of Low Temperature Physics* *116*, 1/2 (1999), 9–20. 160

- [60] GHINOVKER, M., SHAPIRO, I., AND SHAPIRO, B. Y. Explosive nucleation of superconductivity in a magnetic field. *Physical Review B* 59, 14 (1999), 9514–9521. 160
- [61] GILBERT, T. L., AND KELLEY, J. M. *Proc. Conf. Magnetism and Magnetic Materials A.I.E.E. Publ.* (1955), 253. 117
- [62] GINZBURG, V. L., AND LANDAU, L. D. *Zh. Eksp. ter. Fiz.* 20, 1064 (1950). 2, 19
- [63] GIORGIO, C. D., AGOSTINO, D. D., GIORGIO, D., IAVARONE, M., SCARFATO, M., AND MOORE, S. A. Superconducting Vortex-Antivortex Pairs: Nucleation and Confinement in Magnetically Coupled Superconductor-Ferromagnet Hybrids. In *Vortex Dynamics and Optical Vortices*. 2017, pp. 83–106. 113
- [64] GLADILIN, V. N., TEMPERE, J., DEVREESE, J. T., GILLIJNS, W., AND MOSHCHALCOV, V. V. Vortex-antivortex pair generation by an in-plane magnetic dipole on a superconducting film. *Physical Review B* 80, 054503 (aug 2009), 1–6. 123
- [65] GOA, P. E., HAUGLIN, H., BAZILJEVICH, M., IL'YASHENKO, E., GAMMEL, P. L., AND JOHANSEN, T. H. Real-time magneto-optical imaging of vortices in superconducting nbse 2. *Supercond. Sci. Tech.* 14, 9 (2001), 729. 24
- [66] GOMES, R. R., DORIA, M. M., AND ROMAGUERA, A. R. D. C. Paramagnetic excited vortex states in superconductors. *Phys. Rev. B* 93 (Jun 2016), 214518. 17, 184
- [67] GOR' KOV, L. P. *Sov. Phys. - JETP* 9, 1364 (1959). 19

- [68] GOR'KOV, L. P., AND ÉLIASHBERG, G. M. Generalizations of the ginzburg-landau equations for non-stationary problems in the case of alloys with paramagnetic impurities. *Zh. Eksp. Teor. Fiz.* 54 (1968), 612–626. 91
- [69] GRADSHTEYN, I., AND RYZHIK, I. *Table of Integrals, Series, and Products*. Academic Press, Elsevier, 2014. 212, 215
- [70] GROPP, W. D., KAPER, H. G., LEAF, G. K., LEVINE, D. M., PALUMBO, M., AND VINOKUR, V. M. Numerical simulations of vortex dynamics in type-ii superconductors. *Journal of Computational Physics* 123, 0022 (1996), 254–266. 94
- [71] GUBIN, A. I., IL'IN, K. S., VITUSEVICH, S. A., SIEGEL, M., AND KLEIN, N. Dependence of magnetic penetration depth on the thickness of superconducting Nb thin films. *Physical Review B* 72, 064503 (aug 2005), 1–8. 102
- [72] HAO, L., MACFARLANE, J. C., GALLOP, J. C., AND LAM, S. K. H. Direct measurement of penetration length in ultrathin and/or mesoscopic superconducting structures. *Journal of Applied Physics* 99, 12 (2006), 123916. 59
- [73] HAYASH, M., AND EBISAWA, H. Vortex nucleation and annihilation in superconducting corbino disks. *Journal of Physics and Chemistry of Solids* 66, 8 (2005), 1380 – 1383. Proceedings of the ISSP International Symposium (ISSP-9) on Quantum Condensed System. 9, 158, 186
- [74] HE, A., XUE, C., AND ZHOU, Y.-H. Dynamics of vortex-antivortex pair in a superconducting thin strip with narrow slits. *Chinese Physics B* 26, 4 (apr 2017), 1–8. 161
- [75] HERNÁNDEZ, A. D., AND DOMÍNGUEZ, D. Surface barrier in mesoscopic type-i and type-ii superconductors. *Phys. Rev. B* 65 (Apr 2002), 144529. 26

- [76] HERTEL, R., AND SCHNEIDER, C. M. Exchange Explosions: Magnetization Dynamics during Vortex-Antivortex Annihilation. *Physical Review Letters* 97, 177202 (oct 2006), 1–4. 103
- [77] IM, M.-Y., FISCHER, P., YAMADA, K., SATO, T., KASAI, S., NAKATANI, Y., AND ONO, T. Symmetry breaking in the formation of magnetic vortex states in a permalloy nanodisk. *Nature Communications* 3 (jul 2012), 1–6. 105, 114
- [78] IVANCHENKO, Y. M., AND MIKHEENKO, P. New mechanism of penetration of vortices into current-saturated superconducting films. *Soviet Physics Jetp* 58, 6 (1983), 1228–1234. 159
- [79] JUN, S.-H., SHIM, J.-H., OH, S.-K., YU, S.-C., KIM, D.-H., MESLER, B., AND FISCHER, P. Nonlinear motion of coupled magnetic vortices in ferromagnetic/nonmagnetic/ferromagnetic trilayer. *Applied Physics Letters* 95, 14 (2009), 142509. 114
- [80] KAKAY, A., WESTPHAL, E., AND HERTEL, R. Speedup of fem micromagnetic simulations with graphical processing units. *IEEE Transactions On Magnetics* 46, 6 (2010), 2303–23006. 112
- [81] KELLER, M. *Gilbert damping and noise in magnetic GMR multilayers*. PhD thesis, 2007. 115
- [82] KITTEL, C. *Introduction to Solid State Physics*. Wiley, 2004. 58
- [83] KOMENDOVÁ, L., MILOŠEVIĆ, M. V., AND PEETERS, F. M. Soft vortex matter in a type-I/type-II superconducting bilayer. *Physical Review B* 88, 094515 (sep 2013), 1–9. 99
- [84] LANDAU, L., AND LIFSHITZ, E. *Phys. Zeitsch der Sow* 8 (1935), 153–169. 115

- [85] LANGE, M., VAN BAEL, M. J., SILHANEK, A. V., AND MOSHCHALOV, V. V. Vortex-antivortex dynamics and field-polarity-dependent flux creep in hybrid superconductor/ferromagnet nanostructures. *Physical Review B* 72, 052507 (aug 2005), 1–4. 123
- [86] LASHER, G. Mixed state of type-i superconducting films in a perpendicular magnetic field. *Phys. Rev.* 154 (Feb 1967), 345–348. 58, 59
- [87] LEONOV, A. O., MONCHESKY, T. L., ROMMING, N., KUBETZKA, A., BOGDANOV, A. N., AND WIESENDANGER, R. The properties of isolated chiral skyrmions in thin magnetic films. *New Journal of Physics* 18, 065003 (may 2016), 1–16. 109
- [88] LI, G., URBANO, R. R., GOSWAMI, P., TARANTINI, C., LV, B., KUHN, P., REYES, A. P., CHU, C. W., AND BALICAS, L. Anomalous hysteresis as evidence for a magnetic-field-induced chiral superconducting state in lifeas. *Phys. Rev. B* 87 (Jan 2013), 024512. 25
- [89] LIMA, C. L. S., AND DE SOUZA SILVA, C. C. Dynamics of driven vortex-antivortex matter in superconducting films with a magnetic dipole array. *Arxiv preprint arXiv:0808.2421* 1 (2008), 1–5. 160
- [90] LITTLE, W. A., AND PARKS, R. D. *Phys. Rev. Lett.* 9, 9 (1962). 17
- [91] LIU, Y., AND DU, A. Effects of damping constant on gyrotropic motion and switching of vortex core in permalloy disk. *Journal of Magnetism and Magnetic Materials* 321 (oct 2009), 3493–3497. 105, 114
- [92] LONDON, F., AND LONDON, H. *Proc. Roy. Soc. A* 149, 71 (1935). 11
- [93] LOPEZ-DIAZ, L., AURELIO, L. T., MARTINEZ, E., HERNANDEZ-LOPEZ, M. A., GOMEZ, J., ALEJOS, O., CARPENTIERI, M., FINOCCHIO, G., AND

- CONSOLO, G. Micromagnetic simulations using graphics processing units. *Journal of Physics D: Applied Physics* 45, 323001 (2012). 112
- [94] LUO, Y. M., ZHOU, C., WON, C., AND WU, Y. Z. Effect of DzyaloshinskiiâMoriya interaction on magnetic vortex. *AIP Advances* 4, 047136 (apr 2014), 1–10. 114
- [95] MAKI, K. Vortex motion in type i superconductors. *Prog. Theor. Phys.* 42, 3 (1969), 448–460. 58
- [96] MALONEY, M. D., DE LA CRUZ, F., AND CARDONA, M. Superconducting parameters and size effects of aluminum films and foils. *Phys. Rev. B* 5 (May 1972), 3558–3572. 5, 57, 58
- [97] MARCHIORI, E., CURRAN, P. J., KIM, J., SATCHELL, N., BURNELL, G., AND BENDING, S. J. Reconfigurable superconducting vortex pinning potential for magnetic disks in hybrid structures. *Scientific Reports* 7, 45182 (mar 2017), 1–9. 122, 123
- [98] MCEVOY, J., JONES, D., AND PARK, J. Supercooling of superconductors below the surface nucleation field. *Solid State Communications* 5, 8 (1967), 641 – 644. 5, 57, 58
- [99] MEISSNER, W., AND OCHSENFELD, R. *Naturwiss.* 21, 787 (1933). 1
- [100] MEJÍA-LÓPEZ, J., ALTBIR, D., LANDEROS, P., ESCRIG, J., ROMERO, A. H., ROSHCHIN, I. V., LI, C.-P., FITZSIMMONS, M. R., BATLLE, X., AND SCHULLER, I. K. Development of vortex state in circular magnetic nanodots: Theory and experiment. *Physical Review B* 81, 184417 (may 2010), 1–8. 103

- [101] MEL'NIKOV, A. S., AND SAMOKHVALOV, A. V. Abrikosov vortex escape from a columnar defect as a topological electronic transition in a vortex core. *JETP Letters* *94*, 10 (jan 2011), 759–763. 161
- [102] MILOŠEVIĆ, M., AND PEETERS, F. Vortex-antivortex nucleation in superconducting films with arrays of in-plane dipoles. *Physica C* *437-438* (may 2006), 208–212. 124, 162
- [103] MILOŠEVIĆ, M. V. *Vortex Matter in Mesoscopic Superconductor / Ferromagnet Heterosystems*. PhD thesis, Universiteit Antwerpen, 2004. 161
- [104] MILOŠEVIĆ, M. V., BERDIYOROV, G. R., AND PEETERS, F. M. Stabilized vortex-antivortex molecules in a superconducting microdisk with a magnetic nanodot on top. *Physical Review B* *75*, 052502 (feb 2007), 1–4. 124
- [105] MILOŠEVIĆ, M. V., AND PEETERS, F. M. Interaction between a superconducting vortex and an out-of-plane magnetized ferromagnetic disk: Influence of the magnet geometry. *Physical Review B* *68*, 094510 (sep 2003), 1–12. 161
- [106] MILOŠEVIĆ, M. V., AND PEETERS, F. M. Vortex-Antivortex Lattices in Superconducting Films with Magnetic Pinning Arrays. *Physical Review Letters* *93*, 267006 (dec 2004), 1–4. 124
- [107] MILOŠEVIĆ, M. V., AND PEETERS, F. M. Field-enhanced critical parameters in magnetically nanostructured superconductors. *Europhysics Letters (EPL)* *70*, 5 (jun 2005), 670–676. 162
- [108] MILOŠEVIĆ, M. V., AND PEETERS, F. M. Vortex-Antivortex Nucleation in Magnetically Nanotextured Superconductors: Magnetic-Field-Driven and Thermal Scenarios. *Physical Review Letters* *94*, 227001 (jun 2005), 1–4. 124

- [109] MILOŠEVIĆ, M. V., PEETERS, F. M., AND JANKÓ, B. Vortex manipulation in superconducting films with tunable magnetic topology. *Supercond. Sci. Technol.* *24*, 024001 (2011). 123, 161
- [110] MOSHCHALOV, V., MENGHINI, M., NISHIO, T., CHEN, Q. H., SILHANEK, A. V., DAO, V. H., CHIBOTARU, L. F., ZHIGADLO, N. D., AND KARPINSKI, J. Type-1.5 superconductivity. *Phys. Rev. Lett.* *102* (Mar 2009), 117001. 6
- [111] MÜLLER, A., MILOŠEVIĆ, M. V., DALE, S. E. C., ENGBARTH, M. A., AND BENDING, S. J. Magnetization measurements and ginzburg-landau simulations of micron-size  $\beta$ -tin samples: Evidence for an unusual critical behavior of mesoscopic type-i superconductors. *Phys. Rev. Lett.* *109* (Nov 2012), 197003. 62
- [112] NAHRWOLD, G., SCHOLTYSEK, J. M., MOTL-ZIEGLER, S., ALBRECHT, O., MERKT, U., AND MEIER, G. Structural, magnetic and transport properties of permalloy for spintronic experiments. *Journal of Applied Physics* *108*, 013907 (2010). 105, 114
- [113] NIEDERMAYER, C., FORGAN, E. M., GLÜCKLER, H., HOFER, A., MORENZONI, E., PLEINES, M., PROKSCHA, T., RISEMAN, T. M., BIRKE, M., JACKSON, T. J., LITTERST, J., LONG, M. W., LUETKENS, H., SCHATZ, A., AND SCHATZ, G. Direct observation of a flux line lattice field distribution across an  $\text{YBa}_2\text{Cu}_3\text{O}_{7-\delta}$  surface by low energy muons. *Phys. Rev. Lett.* *83* (Nov 1999), 3932–3935. 24
- [114] NOVAIS, E. R. P., LANDEROS, P., BARBOSA, A. G. S., MARTINS, M. D., GARCIA, F., AND GUIMARÃES, A. P. Properties of magnetic nanodots with perpendicular anisotropy. *Journal of Applied Physics* *110* (sep 2011), 1–7. 114, 122

- [115] OLSEN, Å., HAUGLIN, H., JOHANSEN, T., GOA, P., AND SHANTSEV, D. Single vortices observed as they enter nbse2. *Physica C 408–410* (2004), 537 – 538. 24
- [116] ONNES, H. K. The superconductivity of mercury. *Commun. Phys. Lab. 12*, 120 (1911). 1
- [117] PANG, Z., YIN, F., FANG, S., ZHENG, W., AND HAN, S. Micromagnetic simulation of magnetic vortex cores in circular permalloy disks: Switching behavior in external magnetic field. *Journal of Magnetism and Magnetic Materials 324* (mar 2012), 884–888. 105, 114
- [118] PARKER, C. V., PUSHP, A., PASUPATHY, A. N., GOMES, K. K., WEN, J., XU, Z., ONO, S., GU, G., AND YAZDANI, A. Nanoscale Proximity Effect in the High-Temperature Superconductor. *Physical Review Letters 104*, 117001 (mar 2010), 1–4. 159
- [119] PEARL, J. Current distribution in superconducting films carrying quantized fluxoids. *Applied Physics Letters 5*, 4 (aug 1964), 65–66. 22
- [120] PEARL, J. Structure of superconductive vortices near a metal air interface. *Journal of Applied Physics 37*, 11 (1966), 4139–4141. 59
- [121] PEREIRA, P. J., MOSHCHALOV, V. V., AND CHIBOTARU, L. F. Solution of linearized ginzburg-landau problem for mesoscopic superconductors by conformal mapping. *J. Phys: Conf. Series 410*, 1 (2013), 012162. 28
- [122] PIANO, S. *Andreev Reflections and transport phenomena in superconductors at the interface with ferromagnets and normal metals Samanta Piano*. PhD thesis, Università degli Studi di Salerno, 2006. 113

- [123] PIÑA, J. C., ZORRO, M. A., AND DE SOUZA SILVA, C. C. Vortex-antivortex states in nanostructured superconductor-ferromagnet hybrids. *Physica C 470* (oct 2010), 762–765. 124, 137
- [124] PRIOUR, D. J., AND FERTIG, H. A. Vortex States of a Superconducting Film from a Magnetic Dot Array. *Physical Review Letters 93*, 5 (jul 2004), 1–4. 124, 161
- [125] RAYBOULD, T., FEDOTOV, V. A., PAPASIMAKIS, N., YOUNGS, I., AND ZHELUDEV, N. I. Exciting dynamic anapoles with electromagnetic doughnut pulses. *Applied Physics Letters 111*, 8 (2017), 081104. 125
- [126] SAINT-JAMES, D., AND GENNES, P. Onset of superconductivity in decreasing fields. *Physics Letters 7*, 5 (1963), 306 – 308. 3, 5, 57, 58
- [127] SAMPAIO, J., CROS, V., ROHART, S., THIAVILLE, A., AND FERT, A. Nucleation, stability and current-induced motion of isolated magnetic skyrmions in nanostructures. *Nature Nanotechnology 8* (nov 2013), 839–844. 105
- [128] SCHMID, A. A time dependent ginzburg-landau equation and its application to a problem of resistivity in the mixed state. *Phys. Konden. Materie 5* (1966), 302–317. 91
- [129] SCHOLZ, W., FIDLER, J., SCHREFL, T., SUESS, D., DITTRICH, R., FORSTER, H., AND TSIANTOS, V. Scalable parallel micromagnetic solvers for magnetic nanostructures. *Comput. Mater. Sci. 28* (2003), 366–383. 112
- [130] SHANENKO, A. A., MILOŠEVIĆ, M. V., PEETERS, F. M., AND VAGOV, A. V. Extended ginzburg-landau formalism for two-band superconductors. *Phys. Rev. Lett. 106* (Jan 2011), 047005. 59
- [131] SHAPOVAL, T., METLUSHKO, V., WOLF, M., NEU, V., HOLZAPFEL, B., AND SCHULTZ, L. Enhanced pinning of superconducting vortices at circular

- magnetic dots in the magnetic-vortex state. *Physica C* 470, 19 (oct 2010), 867–870. 123
- [132] SHINJO, T. Magnetic Vortex Core Observation in Circular Dots of Permalloy. *Science* 289, 5481 (aug 2000), 930–932. 122
- [133] SILHANEK, A. V., GLADILIN, V. N., VAN DE VONDEL, J., RAES, B., ATAKLTI, G. W., GILLIJNS, W., TEMPERE, J., DEVREESE, J. T., AND MOSHCHALCOV, V. V. Local probing of the vortex-antivortex dynamics in superconductor/ferromagnet hybrid structures. *Superconductor Science and Technology* 24, 024007 (feb 2011), 1–9. 123
- [134] SINGHA DEO, P., SCHWEIGERT, V. A., AND PEETERS, F. M. Hysteresis in mesoscopic superconducting disks: The bean-livingston barrier. *Phys. Rev. B* 59 (Mar 1999), 6039–6042. 26
- [135] SONIER, J. E., BREWER, J. H., KIEFL, R. F., BONN, D. A., DUNSIGER, S. R., HARDY, W. N., LIANG, R., MACFARLANE, W. A., MILLER, R. I., RISEMAN, T. M., NOAKES, D. R., STRONACH, C. E., AND WHITE, M. F. Measurement of the fundamental length scales in the vortex state of  $\text{YBa}_2\text{Cu}_3\text{O}_{6.60}$ . *Phys. Rev. Lett.* 79 (Oct 1997), 2875–2878. 24
- [136] STRAVER, E. W. J., HOFFMAN, J. E., AUSLAENDER, O. M., RUGAR, D., AND MOLER, K. A. Controlled manipulation of individual vortices in a superconductor. *Appl. Phys. Lett.* 93, 17 (2008). 24
- [137] SUDEROW, H., GUILLAMÓN, I., RODRIGO, J. G., AND VIEIRA, S. Imaging superconducting vortex cores and lattices with a scanning tunneling microscope. *Supercond. Sci. Tech.* 27, 6 (2014), 063001. 24
- [138] TAGIROV, L. Proximity effect and superconducting transition temperature in superconductor/ferromagnet sandwiches. *Physica C: Superconductivity* 307, 1-2 (oct 1998), 145–163. 163

- [139] THOMPSON, D. J., MINHAJ, M. S. M., WENGER, L. E., AND CHEN, J. T. Observation of paramagnetic meissner effect in niobium disks. *Phys. Rev. Lett.* 75 (Jul 1995), 529–532. 25
- [140] TINKHAM, M. *Introduction to Superconductivity*. Dover Books on Physics Series. Dover Publications, 1996. 5, 6, 57, 58, 62, 161
- [141] TREFETHEN, L. N. Numerical computation of the schwarz–christoffel transformation. *SIAM J. Sci. Sstat. Ccomp.* 1, 1 (1980), 82–102. 27
- [142] VAGOV, A., SHANENKO, A. A., MILOŠEVIĆ, M. V., AXT, V. M., AND PEETERS, F. M. Two-band superconductors: Extended ginzburg-landau formalism by a systematic expansion in small deviation from the critical temperature. *Phys. Rev. B* 86 (Oct 2012), 144514. 59
- [143] VAGOV, A., SHANENKO, A. A., MILOŠEVIĆ, M. V., AXT, V. M., VINOKUR, V. M., AGUIAR, J. A., AND PEETERS, F. M. Superconductivity between standard types: Multiband versus single-band materials. *Phys. Rev. B* 93 (May 2016), 174503. 59
- [144] VAGOV, A. V., SHANENKO, A. A., MILOŠEVIĆ, M. V., AXT, V. M., AND PEETERS, F. M. Extended ginzburg-landau formalism: Systematic expansion in small deviation from the critical temperature. *Phys. Rev. B* 85 (Jan 2012), 014502. 59
- [145] VAN BAELE, M. J., BEKAERT, J., TEMST, K., VAN LOOK, L., MOSHCHALOV, V. V., BRUYNSEAEDE, Y., HOWELLS, G. D., GRIGORENKO, A. N., BENDING, S. J., AND BORGHES, G. Local observation of field polarity dependent flux pinning by magnetic dipoles. *Phys. Rev. Lett.* 86 (Jan 2001), 155–158. 123

- [146] VAN BAEL, M. J., TEMST, K., MOSHCHALOV, V. V., AND BRUYNSE-  
AEDE, Y. Magnetic properties of submicron co islands and their use as artificial  
pinning centers. *Phys. Rev. B* 59 (Jun 1999), 14674–14679. 124
- [147] VAN DE VONDEL, J., SILHANEK, A. V., METLUSHKO, V., VAVASSORI, P.,  
ILIC, B., AND MOSHCHALOV, V. V. Self-organized mode-locking effect in  
superconductor/ferromagnet hybrids. *Physical Review B* 79, 5 (feb 2009), 1–9.  
113
- [148] VANSTEENKISTE, A., LELIAERT, J., DVORNIK, M., HELSEN, M., GARCIA-  
SANCHEZ, F., AND VAN WAEYENBERGE, B. The design and verification of  
MuMax3. *AIP Advances* 4, 107133 (oct 2014), 1–22. 105, 112, 118, 124, 160
- [149] VARGAS-PAREDES, A. A., DORIA, M. M., AND NETO, J. A. H. The  
lichnerowicz-weitzenböck formula and superconductivity. *J. Math. Phys.* 54, 1  
(2013). 30
- [150] VU, L. N., WISTROM, M. S., AND VAN HARLINGEN, D. J. Imaging of  
magnetic vortices in superconducting networks and clusters by scanning squid  
microscopy. *Appl. Phys. Lett.* 63, 12 (1993), 1693–1695. 24
- [151] WACHOWIAK, A. Direct Observation of Internal Spin Structure of Magnetic  
Vortex Cores. *Science* 298, 5593 (oct 2002), 577–580. 103
- [152] ZARZUELA, R., VÉLEZ, S., HERNANDEZ, J. M., TEJADA, J., AND NOVOSAD,  
V. Quantum depinning of the magnetic vortex core in micron-size permalloy  
disks. *Physical Review B* 85, 180401 (may 2012), 1–5. 122
- [153] ZHANG, S., PETFORD-LONG, A. K., AND PHATAK, C. Creation of artificial  
skyrmions and antiskyrmions by anisotropy engineering. *Scientific Reports* 6,  
31248 (nov 2016), 1–10. 105

- [154] ZHARKOV, G. F. Critical fields of a superconducting cylinder. *Central European Journal of Physics* 2, 1 (Mar 2004), 220. 58
- [155] ZHARKOV, G. F. Superconducting states of the cylinder with a single vortex in magnetic field according to the ginzburg-landau theory. *Central European Journal of Physics* 3, 1 (Mar 2005), 77. 58
- [156] ZHONG, H., HUANG, L., WEI, D., WANG, S., ZHU, Y., AND YUAN, J. Experimental determination of ultra-sharp stray field distribution from a magnetic vortex core structure. *Journal of Magnetism and Magnetic Materials* 321 (aug 2009), L37–L40. 122

# Appendix A

## The kinetic energy decomposition

Consider the term  $|D_+\psi|^2$ , which can be casted as,

$$\begin{aligned} |D_+\psi|^2 &= [(D_1\psi)^* - i(D_2\psi)^*][(D_1\psi) + i(D_2\psi)] \\ &= (D_1\psi)^*(D_1\psi) + (D_2\psi)^*(D_2\psi) \\ &\quad + i[(D_1\psi)^*(D_2\psi) - (D_2\psi)^*(D_1\psi)]. \end{aligned} \tag{A.1}$$

Expanding only the derivative  $D_1$ ,

$$\begin{aligned} (D_1\psi)^*(D_2\psi) &= \left(-\frac{\hbar}{i}\partial_1\psi^*\frac{q}{c}A_1\psi^*\right)(D_2\psi) \\ &= \partial_1\left[-\frac{\hbar}{i}\psi^*(D_2\psi)\right] \\ &\quad - \left(\frac{\hbar}{i}\psi^*\right)\partial_1 D_2\psi - \frac{q}{c}A_1\psi^* D_2\psi. \end{aligned} \tag{A.2}$$

Rearranging the terms, one obtains that,

$$(D_1\psi)^*(D_2\psi) = -\frac{\hbar}{i}\partial_1(\psi^* D_2\psi) + \psi^* D_1 D_2\psi. \tag{A.3}$$

In the same way, we obtain that,

$$(D_2\psi)^*(D_1\psi) = -\frac{\hbar}{i}\partial_2(\psi^* D_1\psi) + \psi^* D_2 D_1\psi. \tag{A.4}$$

The complex conjugate of these relations give us that,

$$(D_2\psi)^*(D_1\psi) = \frac{\hbar}{i}\partial_1[(D_2\psi)^*\psi] + (D_1D_2\psi)^*\psi, \quad (\text{A.5})$$

$$(D_1\psi)^*(D_2\psi) = \frac{\hbar}{i}\partial_2[(D_1\psi)^*\psi] + (D_2D_1\psi)^*\psi. \quad (\text{A.6})$$

At this point, we have two formulations for the same identity, where one relation is the complex conjugate of the second one. The expression

$$\begin{aligned} |D_+\psi|^2 &= |\vec{D}\psi|^2 \\ &+ i \left[ -\frac{\hbar}{i}\partial_1(\psi^*D_2\psi) + \psi^*D_1D_2\psi \right] \\ &- \left[ -\frac{\hbar}{i}\partial_2(\psi^*D_1\psi) + \psi^*D_2D_1\psi \right], \end{aligned}$$

becomes,

$$\begin{aligned} |D_+\psi|^2 &= |\vec{D}\psi|^2 + i\psi^*[D_1, D_2]\psi \\ &- \hbar\partial_1(\psi^*D_2\psi) + \hbar\partial_2(\psi^*D_1\psi). \end{aligned} \quad (\text{A.7})$$

The commutator,

$$\begin{aligned} [D_1, D_2] &= \left[ \frac{\hbar}{i}\partial_1 - \frac{q}{c}A_1, \frac{\hbar}{i}\partial_2 - \frac{q}{c}A_2 \right] \\ &= -\frac{\hbar q}{i c}(\partial_1A_2 - \partial_2A_1), \end{aligned} \quad (\text{A.8})$$

becomes,

$$[D_1, D_2] = -\frac{\hbar q}{i c}h_3. \quad (\text{A.9})$$

Then one obtains that,

$$\begin{aligned} |D_+\psi|^2 &= |\vec{D}\psi|^2 - i([D_1, D_2]\psi^*)\psi \\ &- \hbar\partial_1[(D_2\psi)^*\psi] + \hbar\partial_2(D_1\psi)^*\psi, \end{aligned} \quad (\text{A.10})$$

which gives expressions for  $|\vec{D}\psi|^2$ ,

$$\begin{aligned} |\vec{D}\psi|^2 &= |D_+\psi|^2 + \frac{\hbar q}{c} h_3 |\psi|^2 \\ &+ \hbar [\partial_1(\psi^* D_2\psi) - \partial_2(\psi^* D_1\psi)], \end{aligned} \quad (\text{A.11})$$

and

$$\begin{aligned} |\vec{D}\psi|^2 &= |D_+\psi|^2 + \frac{\hbar q}{c} h_3 |\psi|^2 \\ &+ \hbar \{ \partial_1 [(D_2\psi)^*\psi] - \partial_2 [(D_1\psi)^*\psi] \}. \end{aligned} \quad (\text{A.12})$$

We sum the two expressions and divide by 2 to obtain that,

$$\begin{aligned} |\vec{D}\psi|^2 &= |D_+\psi|^2 + \frac{\hbar q}{c} h_3 |\psi|^2 \\ &+ \hbar \left\{ \partial_1 \frac{\psi^* D_2\psi + (D_2\psi)^*\psi}{2} - \partial_2 \frac{\psi^* D_1\psi + (D_1\psi)^*\psi}{2} \right\}. \end{aligned} \quad (\text{A.13})$$

Introducing the definition of the current we obtain the desired dual formulation of the kinetic energy given by Eq.(2.8)

# Appendix B

## Calculation of the integrals

In this appendix we calculate the following integrals.

$$I_2 = \frac{R^2}{\Sigma} \int_0^R dr r f_2(r), \quad (\text{B.1})$$

$$f_2(r) = \int_0^{2\pi} d\theta \frac{r^2 + a_0^2 - 2 a_0 r \cos(\theta)}{R^4 + a_0^2 r^2 - 2 a_0 r R^2 \cos(\theta)}, \quad (\text{B.2})$$

$$I_4 = \frac{R^4}{\Sigma} \int_0^R dr r f_4(r), \quad (\text{B.3})$$

$$f_4(r) = \int_0^{2\pi} d\theta \frac{(r^2 + a_0^2 - 2 a_0 r \cos(\theta))^2}{(R^4 + a_0^2 r^2 - 2 a_0 r R^2 \cos(\theta))^2}, \quad (\text{B.4})$$

$$I_{\Upsilon} = \frac{1}{\Sigma} \int d^2x \vec{\partial}^2 f_{\Upsilon}(r, \theta) = \frac{1}{\Sigma} \oint_{\partial\Sigma} dl \hat{n} \cdot \vec{\partial} f_{\Upsilon}(r, \theta), \quad (\text{B.5})$$

$$f_{\Upsilon}(r, \theta) = R^2 \frac{r^2 + a_0^2 - 2 a_0 r \cos(\theta)}{R^4 + a_0^2 r^2 - 2 a_0 r R^2 \cos(\theta)}. \quad (\text{B.6})$$

The integral  $I_2$  is associated with the density of Cooper pairs. As shown in Eq.(B.1) and (B.2) the integral of  $|\psi|^2$  is obtained in two parts: first we integrate the angular part, that results in a function of the radius  $f_2(r)$  and after we integrate the function  $f_2(r)$  in the radial coordinate. The angular integral has a form with a well-known

result [69].

$$\int dx \frac{A + B \cos(x)}{a + b \cos(x)} = \frac{B}{b} x + \frac{A b - a B}{b} \int dx \frac{1}{a + b \cos(x)}, \quad (\text{B.7})$$

$$\int dx \frac{1}{a + b \cos(x)} = \frac{2}{\sqrt{a^2 - b^2}} \tan^{-1} \left( \frac{\sqrt{a^2 - b^2} \tan(x/2)}{a + b} \right) \\ , \text{ for } a^2 > b^2. \quad (\text{B.8})$$

To calculate this integral we consider separately the integration in the four quadrants, as shown below.

$$\int_0^{2\pi} dx \frac{A + B \cos(x)}{a + b \cos(x)} = \int_0^{\pi/2} dx \frac{A + B \cos(x)}{a + b \cos(x)} \\ + \int_{\pi/2}^{\pi} dx \frac{A + B \cos(x)}{a + b \cos(x)} + \int_{\pi}^{3\pi/2} dx \frac{A + B \cos(x)}{a + b \cos(x)} \\ + \int_{3\pi/2}^{2\pi} dx \frac{A + B \cos(x)}{a + b \cos(x)}. \quad (\text{B.9})$$

We make the following change of variables.

First quadrant:  $y = x$

$$\int_0^{\pi/2} dx \frac{A + B \cos(x)}{a + b \cos(x)} \rightarrow \int_0^{\pi/2} dy \frac{A + B \cos(y)}{a + b \cos(y)}. \quad (\text{B.10})$$

Second quadrant:  $y = x - \pi$

$$\int_{\pi/2}^{\pi} dx \frac{A + B \cos(x)}{a + b \cos(x)} \rightarrow \int_{-\pi/2}^0 dy \frac{A - B \cos(y)}{a - b \cos(y)}. \quad (\text{B.11})$$

Third quadrant:  $y = x - \pi$

$$\int_{\pi}^{3\pi/2} dx \frac{A + B \cos(x)}{a + b \cos(x)} \rightarrow \int_0^{\pi/2} dy \frac{A - B \cos(y)}{a - b \cos(y)}. \quad (\text{B.12})$$

Fourth quadrant:  $y = x - 2\pi$

$$\int_{3\pi/2}^{2\pi} dx \frac{A + B\cos(x)}{a + b\cos(x)} \rightarrow \int_{-\pi/2}^0 dy \frac{A + B\cos(y)}{a + b\cos(y)}. \quad (\text{B.13})$$

Inserting the variable changes in the original integral, we obtain a new interval of integration

$$\begin{aligned} & \int_0^{2\pi} dx \frac{A + B\cos(x)}{a + b\cos(x)} = \int_{-\pi/2}^{\pi/2} dy \frac{A + B\cos(y)}{a + b\cos(y)} \\ & + \int_{-\pi/2}^{\pi/2} dy \frac{A - B\cos(y)}{a - b\cos(y)}. \end{aligned} \quad (\text{B.14})$$

We calculate the integrals in the interval  $-\pi/2 < x < +\pi/2$

$$\begin{aligned} & \int_{-\pi/2}^{+\pi/2} dx \frac{A + B\cos(x)}{a + b\cos(x)} = \frac{B}{b}\pi \\ & + \frac{4(Ab - aB)}{b\sqrt{a^2 - b^2}} \tan^{-1} \left( \frac{\sqrt{a^2 - b^2}}{a + b} \tan\left(\frac{\pi}{4}\right) \right), \end{aligned} \quad (\text{B.15})$$

$$\begin{aligned} & \int_{-\pi/2}^{+\pi/2} dx \frac{A - B\cos(x)}{a - b\cos(x)} = \frac{B}{b}\pi \\ & + \frac{4(Ab - aB)}{b\sqrt{a^2 - b^2}} \tan^{-1} \left( \frac{\sqrt{a^2 - b^2}}{a - b} \tan\left(\frac{\pi}{4}\right) \right). \end{aligned} \quad (\text{B.16})$$

We obtain the expressions for the integral in the interval  $0 < x < 2\pi$

$$\begin{aligned} & \int_0^{2\pi} dx \frac{A + B\cos(x)}{a + b\cos(x)} = 2\pi \frac{B}{b} + \frac{4(Ab - aB)}{b\sqrt{a^2 - b^2}} \\ & \times \left[ \tan^{-1} \left( \frac{\sqrt{a^2 - b^2}}{a + b} \right) + \tan^{-1} \left( \frac{\sqrt{a^2 - b^2}}{a - b} \right) \right], \end{aligned} \quad (\text{B.17})$$

and verify that,

$$\begin{aligned}\frac{\sqrt{a^2 - b^2}}{a + b} &= \frac{\sqrt{(a + b)(a - b)}}{(a + b)^2} = \left(\frac{a - b}{a + b}\right)^{1/2}, \\ \frac{\sqrt{a^2 - b^2}}{a - b} &= \frac{\sqrt{(a + b)(a - b)}}{(a - b)^2} = \left(\frac{a + b}{a - b}\right)^{1/2}.\end{aligned}\tag{B.18}$$

Using the identity  $\tan^{-1}(x) + \tan^{-1}(1/x) = \pi/2$  if  $x > 0$ , we simplify the expression to obtain that,

$$\int_0^{2\pi} dx \frac{A + B \cos(x)}{a + b \cos(x)} = 2\pi \frac{B}{b} + 2\pi \frac{(A b - a B)}{b \sqrt{a^2 - b^2}}.\tag{B.19}$$

At this point we have a general result for the integral (B.7). The next step is to apply this result for integrand of  $f_2(r)$ . We consider the following identifications  $A = a_0^2 + r^2$ ,  $B = -2a_0r$ ,  $a = R^4 + a_0^2r^2$  and  $b = -2a_0rR^2$ . Inserting these expressions in the Eq. (B.19) we obtain

$$f_2(r) = \frac{2\pi}{R^2} - \frac{2\pi}{R^2} \frac{(R^2 - a_0^2)(R^2 - r^2)}{R^4 - a_0^2r^2}.\tag{B.20}$$

With the result obtained in Eq.(B.20), the integral  $I_2$  becomes,

$$\begin{aligned}I_2 &= \frac{R^2}{\Sigma} \int_0^R r f_2(r) dr \\ &= \frac{2\pi}{\Sigma} \int_0^R r dr - \frac{2\pi}{\Sigma} (R^2 - a_0^2) R^2 \int_0^R \frac{r dr}{R^4 - a_0^2 r^2} \\ &+ \frac{2\pi}{\Sigma} (R^2 - a_0^2) \int_0^R \frac{r^3 dr}{R^4 - a_0^2 r^2}.\end{aligned}\tag{B.21}$$

Next we calculate each one of the three integrals in Eq.(B.21)

$$\begin{aligned} \int_0^R r dr &= \frac{R^2}{2}, \\ \int_0^R \frac{r dr}{R^4 - a_0^2 r^2} &= \frac{1}{2a_0^2} \ln \left( \frac{R^4}{R^4 - a_0^2 R^2} \right), \\ \int_0^R \frac{r^3 dr}{R^4 - a_0^2 r^2} &= \frac{R^4}{2a_0^4} \ln \left( \frac{R^4}{R^4 - a_0^2 R^2} \right) - \frac{R^2}{2a_0^2}. \end{aligned} \quad (\text{B.22})$$

Inserting these results in Eq.(B.21) and considering that  $\Sigma = \pi R^2$  we have

$$I_2 = 2 - \frac{R^2}{a_0^2} - \left( \frac{R^2}{a_0^2} - 1 \right)^2 \ln \left( 1 - \frac{a_0^2}{R^2} \right). \quad (\text{B.23})$$

Next we calculate the surface integral defined in Eq.(B.5). The normal vector is the radial one,  $\hat{n} = \hat{r}$ , such that,  $f_{\Upsilon}(r, \theta): \hat{r} \cdot \vec{\partial} f_{\Upsilon} = \partial_r f_{\Upsilon}$ . To calculate the integral with the derivative,

$$\begin{aligned} &\frac{\partial f_{\Upsilon}(r, \theta)}{\partial r} \\ &= 2R^2(R^2 - a_0^2) \frac{(R^2 + a_0^2)r - a_0(R^2 + r^2) \cos(\theta)}{(R^4 + a_0^2 r^2 - 2a_0 r R^2 \cos(\theta))^2}, \end{aligned} \quad (\text{B.24})$$

we use the formula [69]

$$\begin{aligned} \int dx \frac{A + B \cos(x)}{(a + b \cos(x))^2} &= \frac{1}{a^2 - b^2} \left[ \frac{(a B - A b) \sin(x)}{a + b \cos(x)} \right. \\ &\quad \left. + \int dx \frac{A a - b B}{a + b \cos(x)} \right]. \end{aligned} \quad (\text{B.25})$$

To obtain the integral  $I_{\Upsilon}$ , we divide the interval  $0 < x < 2\pi$  into four quadrants and use the following changes of variable for each of them.

First quadrant:  $y = x$

$$\int_0^{\pi/2} dx \frac{A + B \cos(x)}{(a + b \cos(x))^2} \rightarrow \int_0^{\pi/2} dy \frac{A + B \cos(y)}{(a + b \cos(y))^2}. \quad (\text{B.26})$$

Second quadrant:  $y = x - \pi$

$$\int_{\pi/2}^{\pi} dx \frac{A + B \cos(x)}{(a + b \cos(x))^2} \rightarrow \int_{-\pi/2}^0 dy \frac{A - B \cos(y)}{(a - b \cos(y))^2}. \quad (\text{B.27})$$

Third quadrant:  $y = x - \pi$

$$\int_{\pi}^{3\pi/2} dx \frac{A + B \cos(x)}{(a + b \cos(x))^2} \rightarrow \int_0^{\pi/2} dy \frac{A - B \cos(y)}{(a - b \cos(y))^2}. \quad (\text{B.28})$$

Fourth quadrant:  $y = x - 2\pi$

$$\int_{3\pi/2}^{2\pi} dx \frac{A + B \cos(x)}{(a + b \cos(x))^2} \rightarrow \int_{-\pi/2}^0 dy \frac{A + B \cos(y)}{(a + b \cos(y))^2}. \quad (\text{B.29})$$

We collect these results together and we obtain a new integration interval  $-\pi/2 < x < \pi/2$ , and the original integral is rewritten in two parts, with positive and negative signs in the integrand, respectively.

$$\int_0^{2\pi} dx \frac{A + B \cos(x)}{(a + b \cos(x))^2} = \int_{-\pi/2}^{\pi/2} dy \frac{A + B \cos(y)}{(a + b \cos(y))^2} + \int_{-\pi/2}^{\pi/2} dy \frac{A - B \cos(y)}{(a - b \cos(y))^2}. \quad (\text{B.30})$$

For the integral with the positive sign we find that,

$$\int_{-\pi/2}^{\pi/2} dy \frac{A + B \cos(y)}{(a + b \cos(y))^2} = \frac{2(aB - Ab)}{a(a^2 - b^2)} + \frac{4(Aa - bB)}{(a^2 - b^2)^{3/2}} \tan^{-1} \left( \frac{\sqrt{a^2 - b^2}}{a + b} \right), \quad (\text{B.31})$$

and for the negative sign,

$$\int_{-\pi/2}^{\pi/2} dy \frac{A - B \cos(y)}{(a - b \cos(y))^2} = -\frac{2(aB - Ab)}{a(a^2 - b^2)} + \frac{4(Aa - bB)}{(a^2 - b^2)^{3/2}} \tan^{-1} \left( \frac{\sqrt{a^2 - b^2}}{a - b} \right). \quad (\text{B.32})$$

Summing the two integrals and using the same trigonometric property for  $\tan^{-1}(x)$  shown before, we obtain that,

$$\int_0^{2\pi} dx \frac{A + B \cos(x)}{(a + b \cos(x))^2} = 2\pi \frac{Aa - bB}{(a^2 - b^2)^{3/2}}. \quad (\text{B.33})$$

The surface integral can be written as,

$$\begin{aligned} I_\Upsilon &= \frac{1}{\Sigma} \oint_{\partial\Sigma} dl \frac{\partial f_\Upsilon}{\partial r} \\ &= \frac{1}{\Sigma} \int_0^{2\pi} R d\theta \left( \frac{\partial f_\Upsilon}{\partial r} \right)_{r=R}. \end{aligned} \quad (\text{B.34})$$

Next we insert the derivative of the function  $f_\Upsilon$  in the previous integral, and define the following parameters  $A = (R^2 + a_0^2)R$ ,  $B = -2a_0R^2$ ,  $a = R^4 + a_0^2R^2$  and  $b = -2a_0R^3$ . We consider the area  $\Sigma = \pi R^2$  to obtain that,

$$I_\Upsilon = \frac{4}{R^2}. \quad (\text{B.35})$$

The last integral to be calculated,  $I_4$ , defined in Eq.(B.3), is the square of the superconductor density over the entire area of the cross section of the cylinder. Similarly to  $I_2$ , first we calculate the angular integral and define the results as a function of the radius, as shown in Eq.(B.4). To calculate the latter integral we expand the numerator of the argument and divide the original integral in two parts,

defined as follows:  $f_4(r) = f_4^I(r) + f_4^{II}(r)$ , where the first part is given by,

$$f_4^I(r) \equiv \int_0^{2\pi} d\theta \frac{(r^2 + a_0^2)^2 - 4 a_0 r (r^2 + a_0^2) \cos(\theta)}{(R^4 + a_0^2 r^2 - 2 a_0 r R^2 \cos(\theta))^2}, \quad (\text{B.36})$$

and the second part is given by,

$$f_4^{II}(r) \equiv \int_0^{2\pi} d\theta \frac{4 a_0^2 r^2 \cos^2(\theta)}{(R^4 + a_0^2 r^2 - 2 a_0 r R^2 \cos(\theta))^2}. \quad (\text{B.37})$$

The integral (B.36) is of the same type of the calculated integral (B.33). We just need to do  $A = (r^2 + a_0^2)^2$ ,  $B = -4a_0 r (r^2 + a_0^2)$ ,  $a = R^4 + a_0^2 r^2$  and  $b = -2a_0 r R^2$ . The second integral we write as a derivative of an integral with a known result:

$$\int_0^{2\pi} dx \frac{B \cos^2(x)}{(a + b \cos(x))^2} = \frac{\partial}{\partial b} \int_0^{2\pi} dx \frac{-B \cos(x)}{a + b \cos(x)}. \quad (\text{B.38})$$

This integral is found in the right hand side of the previous equation and the result is given by,

$$\int_0^{2\pi} dx \frac{-B \cos(x)}{a + b \cos(x)} = 2\pi \frac{B}{b} + 2\pi \frac{a B}{b(a^2 - b^2)}, \quad (\text{B.39})$$

where  $A = 0$ . Calculating the derivative, one finds the expression,

$$f_4^{II} = 2\pi \frac{B}{b^2} - 2\pi \frac{a B (a^2 - 2 b^2)}{b^2 (a^2 - b^2)^{3/2}}, \quad (\text{B.40})$$

where the constants shown in the final result are related to the original expression for  $f_4^{II}$  by  $B = 4a_0^2 r^2$ ,  $a = R^4 + a_0^2 r^2$  and  $b = -2a_0 r R^2$ . The final result for Eq.(B.4)

is a function of the radius and is given by

$$\begin{aligned}
 f_4(r) &= \frac{2\pi}{R^4} + \frac{2\pi}{R^4} \frac{1}{(R^4 + a_0^2 r^2)^3} \\
 &\times \left[ - \left(1 - \frac{R^4}{a_0^4}\right) a_0^6 r^6 + \left(7R^4 - 8\frac{R^6}{a_0^2} + \frac{R^8}{a_0^4}\right) a_0^4 r^4 \right. \\
 &\left. + \left(7R^8 - 8a_0^2 R^6 + a_0^4 R^4\right) a_0^2 r^2 - R^8 (R^4 - a_0^4) \right]. \tag{B.41}
 \end{aligned}$$

To obtain  $I_4$  we insert the function  $f_4(r)$  and we consider the following change of variable  $x = a_0^2 r^2 / R^4$ . With this change of variable and some simplifications one obtains that  $I_4 = (R^2/a_0^2)(a_0^2/R^2 + \sum_{j=0}^3 d_j K_j)$ , where the  $d_j$  coefficients are defined as follows:

$$d_0 \equiv -1 + \frac{a_0^4}{R^4}, \tag{B.42}$$

$$d_1 \equiv 7 - 8\frac{a_0^2}{R^2} + \frac{a_0^4}{R^4}, \tag{B.43}$$

$$d_2 \equiv \frac{R^4}{a_0^4} - 8\frac{R^2}{a_0^2} + 7, \tag{B.44}$$

$$d_3 \equiv \frac{R^4}{a_0^4} - 1, \tag{B.45}$$

and the integrals in the new variable  $x$  are defined as

$$K_j \equiv \int_0^{a_0^2/R^2} \frac{x^j dx}{(1-x)^3}. \tag{B.46}$$

The calculated  $K_j$  integrals give the results

$$K_0 = \frac{1}{2} \left(1 - \frac{a_0^2}{R^2}\right)^{-2} - \frac{1}{2}, \quad (\text{B.47})$$

$$K_1 = \frac{1}{2} \left(1 - \frac{a_0^2}{R^2}\right)^{-2} - \left(1 - \frac{a_0^2}{R^2}\right)^{-1} + \frac{1}{2}, \quad (\text{B.48})$$

$$K_2 = \frac{1}{2} \left(1 - \frac{a_0^2}{R^2}\right)^{-2} - 2 \left(1 - \frac{a_0^2}{R^2}\right)^{-1} + \frac{3}{2} \\ - \ln \left(1 - \frac{a_0^2}{R^2}\right), \quad (\text{B.49})$$

$$K_3 = \frac{1}{2} \left(1 - \frac{a_0^2}{R^2}\right)^{-2} - 3 \left(1 - \frac{a_0^2}{R^2}\right)^{-1} + \frac{5}{2} \\ - \frac{a_0^2}{R^2} - 3 \ln \left(1 - \frac{a_0^2}{R^2}\right). \quad (\text{B.50})$$

Then the products  $c_j K_j$  are obtained and summed over in  $j$ . After some simplifications Eq.(2.68) is finally obtained.